

This item was submitted to Loughborough University as a PhD thesis by the author and is made available in the Institutional Repository (<https://dspace.lboro.ac.uk/>) under the following Creative Commons Licence conditions.



For the full text of this licence, please go to:
<http://creativecommons.org/licenses/by-nc-nd/2.5/>



Crystal-plasticity modelling of machining

By:

Abolfazl Zahedi

A doctoral thesis

Wolfson School of Mechanical and Manufacturing Engineering

Loughborough University

Supervisors: Prof. Vadim V. Silberschmidt – Loughborough University
Prof. Vladimir Babitsky– Loughborough University

March 2014

Abstract

A machining process is one of the most common techniques used to remove material in order to create a final product. Most studies on mechanisms of cutting are performed under the assumption that the studied material is isotropic, homogeneous and continuous. One important feature of material- its anisotropy- is linked to its crystallographic nature, which is usually ignored in machining studies. A crystallographic orientation of a workpiece material exerts a great influence on the chip-formation mechanism. Thus, there is a need for developing fundamental understanding of material's behaviour and material removal processes. While the effect of crystallographic orientation on cutting-force variation is extensively reported in the literature, the development of the single-crystal machining models is somewhat limited.

The main objective of this thesis is to develop a model of machining in a single-crystal f.c.c. structure to study the cutting-force variation affected by grain-level deformation processes. In this thesis, three common machining processes, including orthogonal cutting, turning and vibration-assisted machining were modelled. The obtained data can also be extended to milling machining operations. To overcome the problem of mesh distortion, which is common in modelling a machining process, a three-dimensional coupled FE/SPH model was developed for the first time for a single-crystal machining study. The mechanism of deformation in single-crystal machining is quite complex; for each incremental deformation, the number of active slip systems and amount of slip is identified uniquely in 12 slip systems available in the f.c.c. structure.

The crystal-plasticity formulation in terms of a VUMAT subroutine is implemented for single-crystal machining studies in ABAQUS/Explicit (v.6.11) software. High-purity copper and aluminium were considered for the simulation of machining operations. Between three selected grain orientations for orthogonal machining of single-crystals f.c.c. structure – (100), (101) and (111) –

the cutting-force variation on the (101) plane was observed to be larger than that for two other planes. By developing the turning model, it was possible to study the continues orientation for each fixed zone axis. The variation of the mean specific energy of selected zone axis reached 150%. This is an extremely important observation and provides information on the case of machinability in particular zone axes. This significant variation indicates the sensitivity of the process to material crystallography. The deviation (about the mean) of the specific energy with crystal orientation changed significantly with the positions of the zone axis. The minimum deviation was observed for the [111] zone axis, which is characterized by the maximum crystallographic symmetry while the maximum one was found in the [112] zone axis. The performed simulations demonstrated different values for cutting-force reduction in different orientation setups for VAM as compared to that of CM. The study of simulation results demonstrated that the (101) crystal orientation with 30° cutting direction had the highest reduction of cutting force for three common levels of amplitude and frequencies. Therefore, this orientation setup is the best choice for VAM.

Keywords: Single crystal; SPH; Crystal plasticity; Finite-element modelling

Acknowledgements

First of all, I would like to thank Prof. Vadim V. Silberschmidt and Prof. Vladimir Babitsky. I am greatly honoured for having had an opportunity to work with them. They constantly inspired and motivated me to achieve my academic goals. I would like to thank Dr Anish Roy. He extends my understanding in deformation of crystalline materials.

I would also like to thank my research colleagues Dr Murat Demiral, Dr Simin Li, Dr Riaz Muhammd, Dr Agostino Maurotto, Dr Farukh, Dr Vaibhav Phadnis, Dr Bentolhoda Ayati, Dr Vahid Nekouei and Dr Javad Falsafi for sharing their knowledge and research experience with me.

I want to express my respect to my family, especially to my father, sister and my brothers for their support and patience during my studies.

And most importantly, I would like to thank my wife, Fatemeh Vahidnia, for everything she has done for me. Throughout my life, she has supported me in all of my endeavours.

The support of Mechanics of Advanced Materials Research Group is also acknowledged.

Dedicated to my beloved mother

Fatemeh Sedgh

Publications

- 1) **S.A. Zahedi**, A. Roy, V.V. Silberschmidt (2013) "Modeling of Micro-machining Single-crystal f.c.c. Metals" *Procedia CIRP*, Vol. 8, pp 346–350.
- 2) **S.A. Zahedi**, Murat Demiral, Anish Roy, Vadim V. Silberschmidt, (2013) "FE/SPH modelling of orthogonal micro-machining of f.c.c. single crystal" *Computational Materials Science*, Vol. 78, pp 104–109.
- 3) **S.A. Zahedi**, S. Li, A. Roy, V. Babitsky, V. V. Silberschmidt (2012) "Application of smooth-particle hydrodynamics in metal machining", *Journal of Physics: Conference Series* 382(1).
- 4) **S.A. Zahedi**, M. Demiral, A. Roy, V. Babitsky, V. Silberschmidt (2012) "Indentation in f.c.c. single crystals", *Solid State Phenomena*, Vol. 188, pp. 219-225.
- 5) M. Demiral, **S.A. Zahedi**, A. Roy, V. V. Silberschmidt (2011) "Deformation mechanisms of advanced Ti-based alloy in nano-scale: A numerical study based on experiments", 2nd International Conference on Material Modelling, Paris, FRANCE, 31 August -2 September 2011.

Notation and abbreviations

V	Cutting velocity
h_c	Machining thickness
a, b, c	Lattice axial length
α, β, γ	Inter-axial angles
τ	Shear stress
σ	Applied stress
λ	Angle between the slip direction and the applied force
ϕ	Angle between the normal to the slip plane and the applied force
\mathbf{F}	Deformation gradient
\mathbf{F}^e	Deformation gradient for elastic stretching
\mathbf{F}^p	Deformation gradient for plastic stretching
\mathbf{L}^e	Elastic strain rate
$\dot{\mathbf{F}}^e$	Stress rate
\mathbf{C}	Tensor of elastic moduli
\mathbf{L}	Total strain rate
\mathbf{L}^p	Plastic strain rate
$\mathbf{C}_{11}, \mathbf{C}_{22}, \mathbf{C}_{44}$	Material constants for elastic moduli
$\dot{\gamma}^\alpha$	Shear rate
μ_{ij}^α	Schmid tensor
s_i^α	Slip direction
n_i^α	Slip plane normal
N	Total number of available slip systems
$\dot{\gamma}_0$	Reference strain rate
g^α	Current strength of that slip system
n	Rate sensitivity of the crystal
$\text{sgn}(*)$	Signum function
$h_{\alpha\beta}$	Slip-hardening moduli
W	Soothing (or kernel) function
h	Supporting radius
Ω	Volume of the integral

$\delta(x - x')$	Dirac delta function
Δt	Time increment
θ_1	Integration constant
Δt_{cr}	Critical time step
$\Delta \tau^{(\alpha)}$	Increments of resolved shear stress
$\Delta g^{(\alpha)}$	Current strength
h_0	Initial hardening modulus
τ_0	Initial value of current strength of the slip systems
τ_s	Resolved shear stress
g^α	Strength of each slip system α
$h_{\alpha\beta}$	Interaction strength between slip system α and β
[hkl]	Crystal direction
[uvw]	Crystal plane
[abc]	Fixed zone axes
θ	Angle of rotation
U, W	Cutting direction vector
μ	Coefficient of friction
r	Radius of cutting tool
a	Vibration amplitude
ω	Natural frequency
f	Frequency of vibration
$g_T^\alpha _{t=0}$	Incipient strength of slip systems
m	Slip-plane normal
q	Latent to the self-hardening ratio
s	Slip direction
P	Load

Table of contents

Certificate of originality	i
Abstract	ii
Acknowledgements	iv
Publications	vi
Notation and abbreviations	vii
Table of contents	ix
List of figures	xii
List of tables	xvii
1. Introduction of metal cutting	1
1.1 Metal-cutting process	1
1.2 Macro-and micro-machining	2
1.2.1 Differences between macro-and micro-machining	3
1.2.2 Importance of micro-machining processes	6
1.3 Research aim and objective.....	9
1.4 Outline of the thesis	10
2 Experimental studies of single-crystal machining	13
2.1 Basic crystal structure of solids	13
2.2 Descriptions of miller indices.....	17
2.3 Mechanism of plastic deformation in crystals	19
2.4 Single-crystal machining experiments	22
2.4.1 Machining force variation	23
2.4.2 Size effect.....	32
2.5 Summary.....	36
3 Modelling of machining in micro scale	37
3.1 Introduction	37
3.2 Analytical modelling	38
3.3 Numerical computation method.....	41
3.3.1 Lagrangian and updated Lagrangian schemes	42
3.3.2 Eulerian scheme	43
3.3.3 Arbitrary Lagrangian-Eulerian scheme (ALE).....	44
3.3.4 Molecular dynamic (MD) method.....	46
3.3.5 Smooth particle hydrodynamics (SPH) method	50
3.4 Coupling SPH and finite-element technique	52
3.5 Summary.....	55

4 Computational framework of crystal plasticity	57
4.1 Crystal plasticity theory	57
4.1.1 Kinematics	60
4.1.2 Hardening rule	63
4.2 Numerical implementation	66
4.2.1 SPH technique - theory and formulation	66
4.2.2 Incremental formulation of crystal-plasticity	72
4.3 Summary.....	76
5 Modelling of orthogonal single crystal machining	77
5.1 Introduction	77
5.2 Model descriptions and features	78
5.2.1 Geometry configuration.....	79
5.2.2 Orientation setup	80
5.2.3 Properties of workpiece material.....	83
5.2.4 Mesh technique	84
5.2.5 Contact algorithm.....	89
5.2.6 Sensitivity of model.....	91
5.2.7 Model validation	94
5.2.8 Shortcoming of model	95
5.3 Mechanism of deformation in single-crystal machining.....	96
5.4 Variation of cutting force and chip morphology	101
5.5 Effect of material property	105
5.6 Parametric study of orthogonal machining model.....	107
5.6.1 Effect of coefficient of friction	107
5.6.2 Effect of tool-edge radius.....	113
5.7 Summary.....	117
6 Modelling of single-crystal turning.....	119
6.1 Introduction	119
6.2 Model characteristics.....	121
6.2.1 Descriptions of turning geometry	121
6.2.2 Configuration of coordinate system	124
6.2.3 Contact and boundary conditions	127
6.2.4 Mesh.....	128
6.2.5 Experimental verification	129
6.2.6 Shortcomings of model.....	131
6.3 Cutting-force variation for fixed zone axis	133
6.4 Study of cutting parameters in turning.....	139
6.4.1 Effect of friction	141
6.4.2 Effect of cutting velocity	143
6.5 Summary.....	145
7 Vibration-assisted single-crystal machining model	147

7.1 Introduction	147
7.2 Modelling procedure	149
7.2.1 Geometry configuration.....	150
7.2.2 Orientation setup	150
7.2.3 Definition of material properties	151
7.2.4 Boundary conditions	151
7.2.5 Step selection.....	155
7.2.6 Mesh sensitivity	155
7.2.7 Distribution of Von-Mises stress in contact domain.....	157
7.2.8 Simulation verification	158
7.2.9 Shortcomings of model.....	159
7.3 Comparison of cutting force for CM and VAM	159
7.4 Parametric study of VAM	164
7.4.1 Effect of vibration amplitude	164
7.4.2 Effect of vibration frequency.....	169
7.5 Summary.....	173
8 Conclusions and future work.....	175
8.1 Concluding remarks.....	175
8.1.1 Orthogonal machining	177
8.1.2 Turning.....	178
8.1.3 Vibration-assisted machining	179
8.2 Impact of study.....	180
8.3 Recommendations for future work.....	181
References	183

List of figures

Figure 1:1 Workpiece microstructures in macro-machining (a) and micro-machining (b) after (Kota, 2011).....	4
Figure 1:2 Simplified model of orthogonal machining.....	4
Figure 1:3 Cutting model for macro-machining (a) and (b) micro-machining.....	5
Figure 1:4 Miniature micro-machine tools: (a) micro lathe; (b) portable micro-factory (Okazaki et al., 2004).....	7
Figure 1:5 Some examples of micro-machined products: (a) micro-end mill cutting (Wenda et al., 1999) ;(b) turning micro-lapping tool (Brinksmeier et al., 1998); (c) micro-gear pump rotors (Masaki et al., 1990); (d) ultra-precision milling (Masaki et al., 1990); (e) small statue by 5 axis control micro-machining (Tanaka, 2001).....	8
Figure 1:6 Thesis structure	11
Figure 2:1 Schematics of three general types of solids: (a) amorphous, (b) polycrystalline and (c) single crystal after (Azaroff, 1984)	14
Figure 2:2 Space lattice and unit cell (Campbell, 2008).....	14
Figure 2:3 14 Bravias lattices (Kittel, 1986).....	16
Figure 2:4 Three common crystal structures of metals (Kittel, 1986).....	17
Figure 2:5 Planes (a) and directions (b) in cubic unit cells (William and Javad, 2004)	18
Figure 2:6 Dislocation movement (Callister, 1997).....	20
Figure 2:7 12 slip systems in f.c.c. crystal (William and Javad, 2004).....	21
Figure 2:8 Chip-formation pattern of specimen in (100) plane with different cutting orientation angles: (a) -25°, (b) -15° (c) 0° (d) 25° (e) 45° (Ueda et al., 1980)	26
Figure 2:9 Chip-formation pattern of specimen in (101) plane with different cutting orientation angles: (a) -70°, (b) -45°, (c) 0°, (d) 35°, (e) 70°, (f) 90°, (Ueda et al., 1980)	27

Figure 2:10 Calculated slip lines and those observed on the side surface for (001) [110] (a) and (110) [001] (b) cutting orientations (Sato et al., 1979)	28
Figure 2:11 Variation of cutting force in cutting copper single crystal in different cutting directions in (110) (a) and (111) (b) planes (Yuan et al., 1994).....	29
Figure 2:12 Variation of cutting force in cutting aluminium single crystal in different cutting directions in (110) (a) and (111) (b) planes (Yuan et al., 1994).....	29
Figure 2:13 Cutting (C), thrust (T), and lateral (L) forces for: (a) (12 5 0) facet for 5 mm/s and 20 μm depth of cut; (b) (6 7 0) facet with 10 mm/s and 20 μm depth of cut; (c) (2 7 0) facet with 5 mm/s and 5 μm ; and (d) force components (Lawson et al., 2008).....	31
Figure 2:14 Chip formation through (a) shear and sliding along rake face of the tool, (b) negative rake angle and (c) effective negative rake angle with the edge radius of order of depth cut after Lucca et al., (1991).....	35
Figure 3:1 Cutting model for orthogonal machining: (a) Merchant theory and (b) rounded tool edge (Kim, 1996)	40
Figure 3:2 Primary shear zone after (Kiliçaslan, 2009)	41
Figure 3:3 Mesh motion in Lagrangian formulation (Simulia, 2011)	42
Figure 3:4 Mesh motion in eulerian formulation (Simulia, 2011).....	44
Figure 3:5 One-dimensional example of lagrangian, eulerian and ALE mesh (Donea et al., 2004).....	45
Figure 3:6 Mesh motion in Arbitrary Lagrangian-Eulerian formulation (Simulia, 2011)	46
Figure 3:7 MD simulations of nano metric cutting performed on ductile (a-c-e) and brittle (b-d-f) work material with various tool rake angles: (a) and (b) - 15°, (c) and (d) 0°, (e) and (f) 15 (Komanduri et al., 2001)	49
Figure 4:1 Relation between shear stress and normal stress.....	58
Figure 4:2 Lattice rotation in tension.....	59
Figure 4:3 Elsto-plastic deformation in crystal structure (Ellyin, 1996)	61
Figure 4:4 Geometry of neighbouring particle and weighing factor (Limido et al., 2007)	67
Figure 4:5 Relations between parameters x , h and r in SPH model	67

Figure 4:6 flow chart of VUMAT for crystal plasticity.....	75
Figure 5:1 Configuration of orthogonal micro-machining after (Kota, 2011).....	78
Figure 5:2 Geometry of orthogonal-machining model (dimension in μm)	80
Figure 5:3 Planner configuration setup.....	81
Figure 5:4 Meshing of continuum finite-element workpiece region.....	84
Figure 5:5 Changing the element shape	85
Figure 5:6 Three dimensional mesh of workpiece material	87
Figure 5:7 A 3D model of orthogonal machining.....	91
Figure 5:8 Four selected mesh configurations with (a) 2646, (b) 18491, (c) 71825 and (d) 137781 numbers of SPH particle for representative workpiece	92
Figure 5:9 Cutting-force evaluations for different numbers of SPH particles.....	93
Figure 5:10 Distributions of Von Misses stress along two paths in workpiece material in (010) plane.....	94
Figure 5:11 Shear strain distribution for 12 slip systems.....	100
Figure 5:12 Evolution of cutting forces for different cutting planes of 0° cutting direction	103
Figure 5:13 Chip morphologies in three planes-(100), (101) and (111)-in 0° cutting direction for different stages of machining (Sections I – III, see Figure 5:12)	104
Figure 5:14 Typical variation of cutting force for various cutting directions for copper single crystal machining	105
Figure 5:15 Typical variation of cutting force for various cutting directions for aluminum single crystal machining.....	106
Figure 5:16 Cutting force behaviour of different coefficients of friction in different orientations machining process.....	109
Figure 5:17 Cutting force pattern for different coefficients of friction	110
Figure 5:18 Distribution of flow stresses for different coefficients of friction: (a) $\mu=0$, (b) $\mu=0.12$ and (c) $\mu=0.4$	112

Figure 5:19 The force components tangential (a) and normal (b) for three h/cr value.....	114
Figure 5:20 Chip shape for various magnitudes of (a): $h/cr = 2$; (b): $h/cr = 1$; (c) $h/cr = 0.5$	116
Figure 6:1 Basic turning operation after Yang and Tarnng, (1998).....	120
Figure 6:2 Geometry of cutting process (dimension in mm)	123
Figure 6:3 Relations between cutting coordinate system and reference cutting frame.....	125
Figure 6:4 Standard-stereographic triangle for f.c.c. crystals.....	126
Figure 6:5 Boundary conditions.....	127
Figure 6:6 Comparison of model predictions and experimental data (Cohen, 1982) for [001] zone axis	130
Figure 6:7 Strain distribution over 12 slip systems	131
Figure 6:8 Fly off particles inside rectangular box.....	132
Figure 6:9 Variation of specific cutting energy in modelling of micro-machining for eight zone axis: (a) [101]; (b) [111]; (c) [213]; (d) [216]; (e) [212]; (f) [112] and (g) [102]	136
Figure 6:10 Milling operation.....	139
Figure 6:11 Effect of coefficient of friction on specific cutting energy pattern for (a) [001]; (b) [101] and (c) [111] zone axis-(case 1 to 9)	142
Figure 6:12 Variation on cutting speed in specific cutting energy for three different zone axes; (a) [001]; (b) [101]; (c) [111]- (case 10-18)	144
Figure 7:1 Schematic of vibration-assisted machining (VAM)	148
Figure 7:2 Three-dimensional FE/SPH model of VAM (dimensions in μm)	150
Figure 7:3 Cutting tool's displacement and velocity in CM model ((a) and (b)) and VAM model ((c) and (d)).....	153
Figure 7:4 Tool-workpiece contact zone for VAM.....	154
Figure 7:5 Workpiece constraints	154
Figure 7:6 Mesh sensitivity analysis of workpeice	156

Figure 7:7 Distribution of von Mises stress in contact domain for VAM.....	157
Figure 7:8 Specific cutting-energy magnitudes for presented model and experimental study by Lawson et al. (2008)	158
Figure 7:9 Cutting-force variations for VAM and CM (cutting speed 1 m/s and depth of cut 5 μm)	160
Figure 7:10 Shear strain distribution.....	162
Figure 7:11 Variation of cutting force for fixed frequency of 20 kHz and different vibration amplitudes in (100) crystal orientation with cutting directions: (a) 0°, (b) 30°, (c) 60° and (d) 90°	166
Figure 7:12 Variation of cutting force for fixed frequency of 20 kHz and different vibration amplitudes in (101) crystal orientation with cutting directions: (a) 0°, (b) 30°, (c) 60° and (d) 90°	167
Figure 7:13 Variation of cutting force for fixed frequency of 20 kHz and different vibration amplitudes in (111) crystal orientation with cutting directions: (a) 0°, (b) 30°, (c) 60° and (d) 90°	168
Figure 7:14 Variation of cutting force with constant vibration amplitude of 10 μm for different frequencies for (100) crystal orientation with cutting directions: (a) 0°, (b) 30°, (c) 60° and (d) 90°	170
Figure 7:15 Variation of cutting force with constant vibration amplitude of 10 μm for different frequencies for (101) crystal orientation with cutting directions: (a) 0°, (b) 30°, (c) 60° and (d) 90°	171
Figure 7:16 Variation of cutting force with constant vibration amplitude of 10 μm for different frequencies for (111) crystal orientation with cutting directions: (a) 0°, (b) 30°, (c) 60° and (d) 90°	172

List of tables

Table 2-1 Seven basic systems of crystal structure (Kittel, 1986).....	15
Table 2-2 Common slip planes and directions for different structures (William and Javad, 2004)	21
Table 2-3 Experimental study on single crystal machining from literature, and associated machining parameters	23
Table 2-4 Summary of experimental reports on size effect	33
Table 4-1 Hardening models	64
Table 5-1 Cutting directions (see Figure 5:3)	82
Table 5-2 Material parameters of single-crystal copper (Wang et al., 2004)	83
Table 5-3 Cutting forces normalised to cutting direction of 0° in modelling and experimental study of Zhou and Ngoi (2001)	95
Table 5-4 Values of Schmid factor for 12 slip systems for three cutting directions [100], [110] and [111].	98
Table 5-5 Shear-angle prediction for machining in cutting direction [100]	98
Table 5-6 Coefficient of friction of crystalline copper for different orientation sets (Zhou and Ngoi, 2001)	108
Table 5-7 Tangential to normal force ratio in different directions.....	117
Table 6-1 Turning simulation parameters	124
Table 6-2 Three orthonormal directions for eight zone axes (see Figure 6:3)	126
Table 6-3 variation of cutting energy versus θ°	138
Table 6-4 Simulation setups for study friction and cutting velocity in turning...	140
Table 7-1 Cutting force magnitudes (in N) for three basic orientations of f.c.c. in four cutting directions	163

Table 7-2 Cutting-force reduction for three amplitude (10, 20 and 30 μm).....168

Table 7-3 Cutting force reduction for three frequencies - 15, 20 and 25 kHz.....173

Introduction of metal cutting

1. Introduction of metal cutting

1.1 Metal-cutting process

The general idea of the metal cutting process is to remove unwanted material from a workpiece in order to produce a high-quality surface and a part with accurate dimensions and acceptable tolerances. Material removal from the bulk raw material, in the form of chips, is usually associated with large forces and thus requires robust machinery. Common examples of these machines are lathes, milling, drilling and grinding machines. These machines achieve material removal in a process of dynamic interaction between a piece of the cut material, called *workpiece*, and a cutting tool. A relative motion between the workpiece and the tool is called the *cutting velocity* or *speed* and extend of tool's penetration is characterized by uncut chip thickness. The relative motion can be provided by moving the workpiece, or the tool, or both.

Machining is the most commonly used process in production of industrial components production. One of its greatest advantages is the possibility to produce complex-shaped items, which cannot be created by casting or forging processes. Nowadays machining processes are used to make everyday products either directly or industrially. Merchant (1998) estimated that 15% of the value of all mechanical components manufactured worldwide is derived from machining operations. In the US, more than \$100 billion spent annually on the machining and related operations (Flom, 1985). Typically, a large popular-more than 80 percent-of all the machine tools used in the manufacturing industry are metal-cutting in nature (Trent and Wright, 2000). These facts show the importance of metal cutting in general manufacturing.

Industrial importance and economic significance of metal cutting need a comprehensive understanding of its fundamentals in order to enhance it. Without knowledge of machining, it is impossible to develop new cutting equipment or determine the optimum cutting conditions. Analytical and numerical models can be deduced from this fundamental knowledge to increase the efficiency of the process. Having this fundamental knowledge can help us to enable machining of new alloys, which are often more difficult to machine due to the pursuit of higher product properties (König *et al.*, 1990) and also improve dimensional accuracy of the machined products.

1.2 Macro-and micro-machining

The machining process can be classified broadly into a macro-and micro-cutting based on the interference between the tool and workpiece. If the interference is large ($>200 \mu\text{m}$), meaning that more material is being removed during a given motion or pass of the tool with regarded to the workpiece, then it is commonly regarded as *macro-cutting*; if the interference is small ($<200 \mu\text{m}$), it is called *micro-cutting* (Trent and Wright, 2000). The application of micro machining is not only limited to the micro size workpiece and cutting tool. The need to remove smaller

amounts of material to create the features, components and devices appear under three conditions:

1. making tiny parts and components,
2. making smaller, intricate features on larger parts, such as molds, and
3. creating a very fine smooth surfaces on larger, bulk parts.

Therefore, tools used to remove these small amounts of material may not necessarily involve micro-sized dimensions. The first two above cases largely involve cutting tools that have dimensions comparable to those of the desired features. Micro-cutting can also be achieved with normal macro-sized cutting tools, especially in the last case. Masuzawa and Tönshoff (1997) defined the range of uncut chip thickness for micro-cutting as 0.1 to 200 μm . Normally, larger interferences are used in *rough* machining operations to increase the material-removal rate in mass production, and smaller interferences are used in finishing operations after roughing ones remove most of the unwanted material from the bulk workpiece.

1.2.1 Differences between macro-and micro-machining

Micro-machining is fundamentally different from macro-machining while in terms of kinematics they are similar. Mechanics of machining at the micro-scale displays different characteristics due to its significant size reduction from that of the macro-scale. Thus, the fundamental difference between macro-and micro- machining arises due to the scale of the operation. These differences are broadly included in the effect of tool's geometry and workpiece parameters (Chae *et al.*, 2006).

An important difference is linked to the considerable effect of workpiece's microstructure on the micro-machining processes. Although in macro-machining a tool moves through many grains, in micro-machining a few grains –or a single grain- are engaged with the tool at the same time (see Figure 1:1). In this picture V is the cutting velocity and h_c is the machining thickness. A simplified relation for rake angle, tool edge radius and shear angle presented in Figure 1:2 for two-

dimension-orthogonal cutting. Rake angle describes the angle between the leading edge of a cutting tool and a perpendicular to the surface being cut. Shear angle is the angle of shearing surface measured from tool direction.

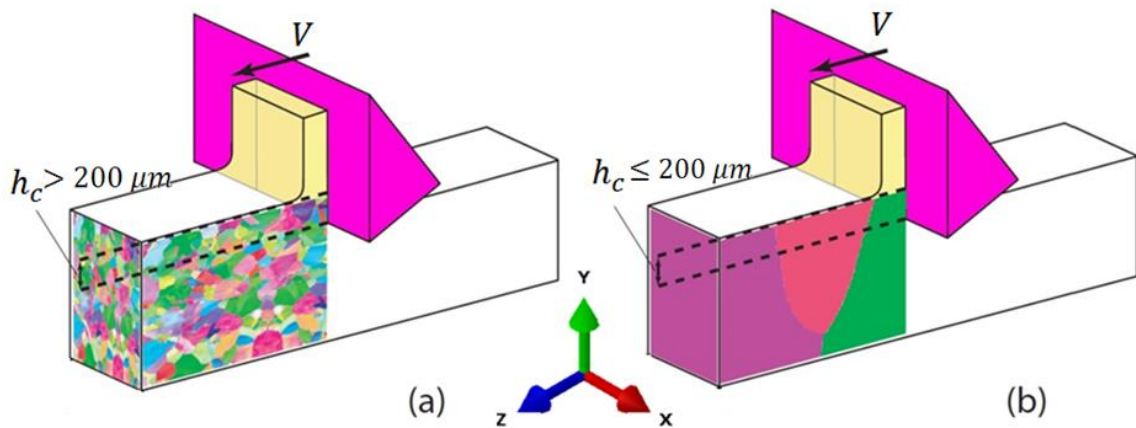


Figure 1:1 Workpiece microstructures in macro-machining (a) and micro-machining (b) after (Kota, 2011)

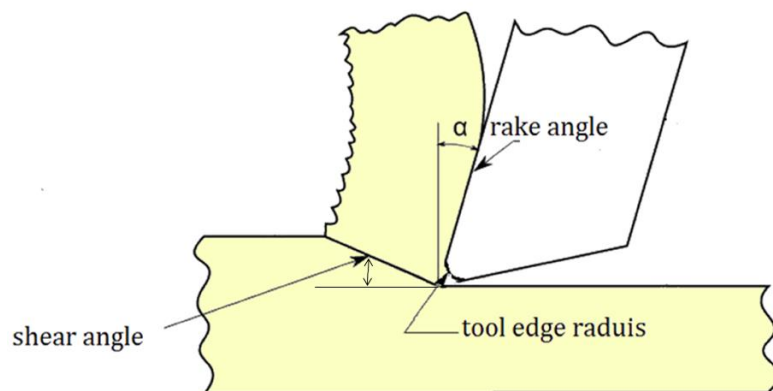


Figure 1:2 Simplified model of orthogonal machining

Characteristic dimensions of grains in metals are commensurate with the values of uncut chip thickness typical for micro-machining. Therefore, the process takes place within individual crystals or within a few crystals at the time. Since elastic

and plastic behaviours of individual crystals (grains) are anisotropic, the mechanical response to cutting varies when passing through different grains. Therefore, the machining response, including forces, a chip-thickness ratio, lamellae structure, surface finish, built-up edge and side flow varies during the process (Kota, 2011). In contrast, since a large number of grains are encountered during a macro-scale cutting process, an averaged effect of the workpiece's microstructure is experienced, and the material can usually be assumed to behave isotropically.

In addition to workpiece parameters, tool geometry also has an important effect on micro-machining. The principles of micro-machining are similar to those of conventional cutting operations. In micro-machining the edge radius of the tools is larger than the chip thickness while in macro-machining, chip shear occurs along the rounded tool edge (see Figure 1:3). In micro-machining, material removed by cutting tool with a large negative rake angle, which affects the magnitude of the shearing forces. Therefore, a relatively large volume of material has to become fully plastic for a relatively small amount of material to be removed, resulting in a significant increase in specific energy (Shaw, 1995). The increase in the cutting forces leads to accelerated tool wear, large tool deflection, and a built-up edge. Further, when the chip thickness is below critical values, chips may not be generated during the cutting process; instead, the workpiece material deforms elastically.

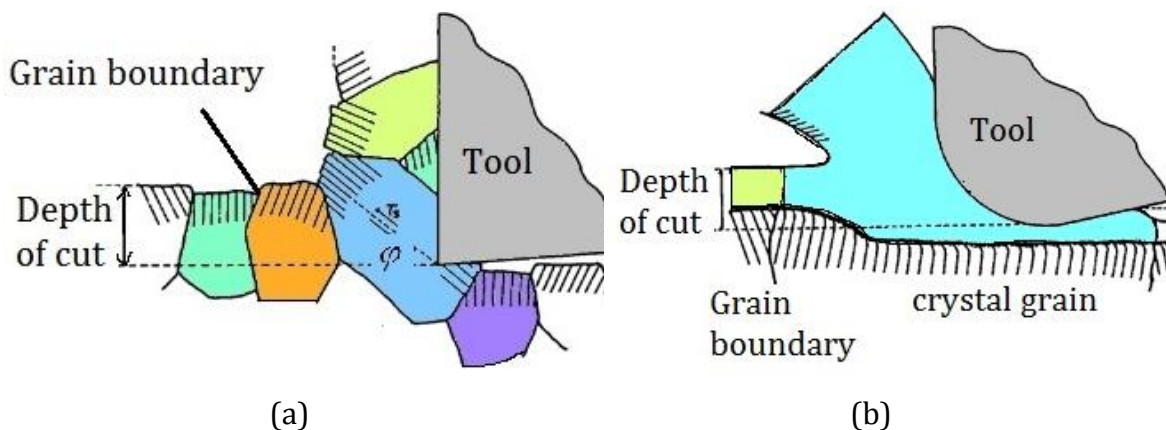


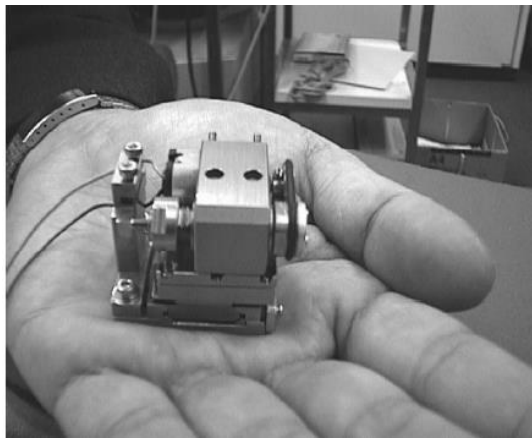
Figure 1:3 Cutting model for macro-machining (a) and (b) micro-machining

1.2.2 Importance of micro-machining processes

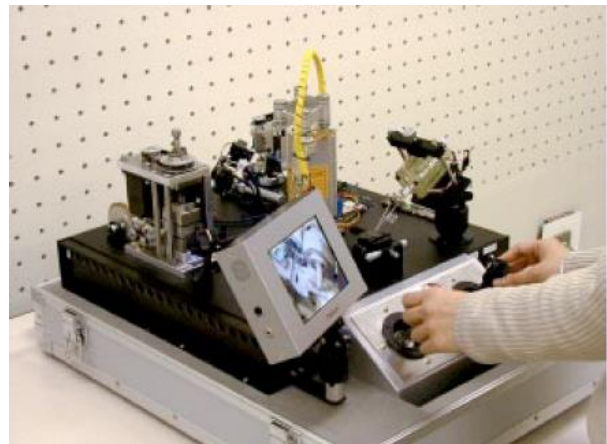
Micro-cutting processes have proven to provide a good possibility for manufacturing micro-structured parts or micro-parts in small quantities. This process is getting more attention from researchers and industry due to the increasing need for miniaturization of components, features and devices. The forerunner of this technology was mostly the electronics industry with its need to manufacture electronic components, like printed circuit boards and integrated circuits (Khandpur, 2005).

Micro-machining can be used in many different ways depending on the industry, feature size, and focus of interest. It is widely used in the aerospace, biomedical, automotive and microelectronics industry in production of electric, piezoelectric, semiconductors, magnetic and optical components for high-performance systems such as transducers, resonators, actuators and sensors. Possible applications include micro-holes in circuit boards, micron-sized devices in IC-packages, micro-scale fuel cells, micro-fluids systems, micro-holes in fuel-injection nozzles for automobiles, and fibre optics are a few samples of micro-machining production (Masuzawa, 2000). Among other applications, there are high-temperature jets, cell-and tissue- handling devices in bio-technology, inspection and surgical devices for in the medical industry, deep X-ray lithography and more.

Micro-machine tools are cost-effective when compared with macro-machine tools and require smaller amounts of materials when fabricated. Therefore, machining centers can be constructed with more expensive materials that exhibit better engineering properties. Micro-machine tools have higher natural frequencies compared with conventional macro-machines, due to substantially smaller mass. Figure 1:4 illustrated miniature micro-machine tools and Figure 1:5 shown some products to demonstrate the range of sizes and accuracies in micro-machining.

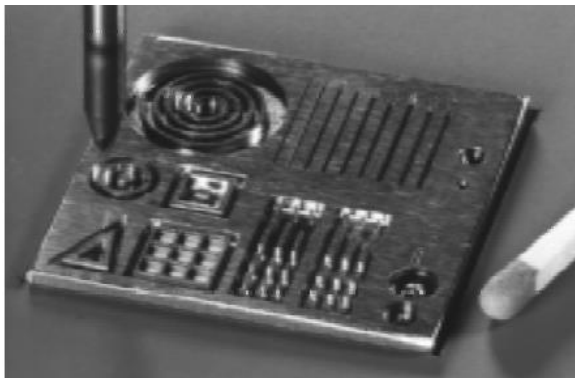


(a)

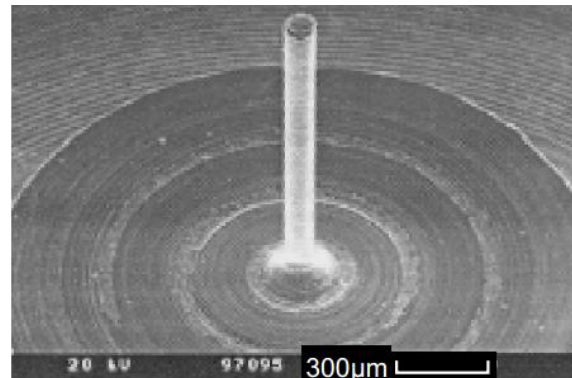


(b)

Figure 1:4 Miniature micro-machine tools: (a) micro lathe; (b) portable micro-factory (Okazaki *et al.*, 2004)



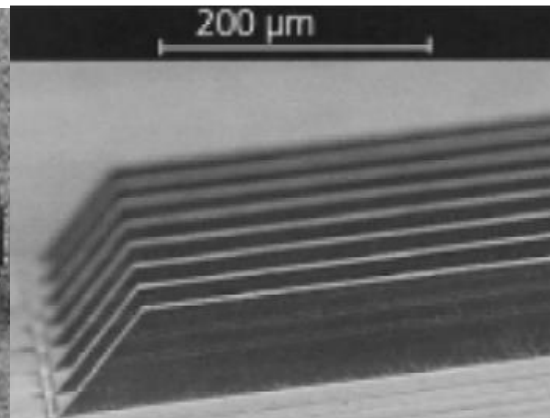
(a)



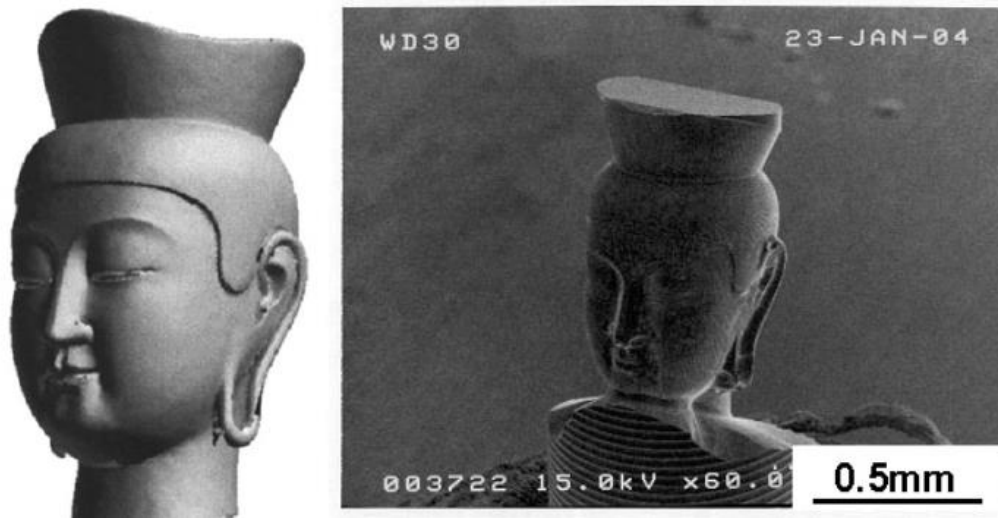
(b)



(c)



(d)



(e)

Figure 1:5 Some examples of micro-machined products: (a) micro-end mill cutting (Wenda *et al.*, 1999) ;(b) turning micro-lapping tool (Brinksmeier *et al.*, 1998); (c) micro-gear pump rotors (Masaki *et al.*, 1990); (d) ultra-precision milling (Masaki *et al.*, 1990); (e) small statue by 5 axis control micro-machining (Tanaka, 2001)

As current trends toward miniaturization accelerate and ever more applications are realized, comprehensive understanding of micro-manufacturing processes becomes important for optimization of current technologies and developing future ones. Getting higher accuracy is always a challenging task in micro-machining. As unit removal size decreases, issues of tool edge geometry, grain size and orientation, etc. become dominant, with strong influences on resulting accuracy, surface quality and integrity of machined components. These factors have little or no influence at larger scales.

The tool-workpiece interaction in single grains highlighted a need for developing fundamental understanding of material's behaviour and material removal processes in single crystals machining process. All the crystalline materials are composed of grains and grain boundaries, which, to a large extent, dictate their mechanical properties. Even though the single-crystal machining process currently draws a lot of attention in research, our current knowledge regarding the effects of

crystallographic orientation on the machining process is very limited. Thus, there is an industry need for robust modelling tools with predictive capability to characterize a component's response to thermo-mechanical loading states. This would reduce the need for extensive experimental studies, which are expensive, and also help to extend the usability envelope of next-generation components to untried levels of load and environment conditions. These simulations will support of research studies undergoing at deformation mechanisms at micro scale to select the best possible choices of cutting direction. The main aim of the modelling is to approach model capable of predicting the response of the material to cutting as well as a load on the cutting tool at various conditions.

1.3 Research aim and objective

The material behaviour is known to depend on many factors. These factors can be divided into those dependent and independent of the cutting process. The main factors defined by the cutting process are: depth of cut, cutting velocity and feed rate. Examples of factors being independent of the cutting process are: initial crystal orientation, initial crystal size, etc. (Trent and Wright, 2000). The aim of this study is to develop a robust modelling approach to further understanding the effect of crystalline material in machining processes.

The machining models need to simultaneously incorporate both the effects of crystallographic anisotropy and kinematics of the machining process. For this aim the crystal-plasticity theory implemented for three machining schemes, name as orthogonal cutting, turning and vibration-assisted machining, to study the material behaviour in cutting processes. A three-dimensional FE/SPH model was developed in order to address concerns of ultra-precision modelling of material.

The following specific objectives will be implemented to achieve this aim.

- To develop physically realistic machining model incorporating anisotropy for f.c.c. crystal structures.
- To predict the cutting force and its variation in machining processes as well as chip morphology depending on crystal orientation.

- To study the effect of cutting parameters such as tool's edge radius, friction, cutting speed in the machining of single crystals.

1.4 Outline of the thesis

The present thesis consists of an introduction and seven chapters. The structure of chapters is shown in Figure 1:6 and summarized below.

Chapter 2 covers experimental research studies in the literature on the single-crystal machining process. For better understanding of crystal structure, this chapter starts with basic information about crystalline materials followed by a slip system mechanism in a single crystal. It concludes that a large body of experimental evidence suggests a strong dependence of machining response on crystallographic orientation.

The common metal-cutting models in the literatures are presented in Chapter 3. In order to overcome limitations of analytical models, finite-element modelling schemes were developed recently to provide a valuable insight into the cutting process. Numerical simulations of machining processes have been a significant challenge for many numerical methods. This process often breaks down due to severe mesh distortion. The Lagrangian, updated-Lagrangian, Eulerian, Arbitrary Lagrangian-Eulerian (ALE) and mesh-free techniques are briefly introduced and their disadvantages are discussed in this chapter. At the end of this chapter, a three-dimensional FE/SPH method is recommended for modelling of single-crystal machining.

In Chapter 4, the crystal-plasticity formulation used in this thesis is introduced. The mathematical description of crystal plasticity is discussed, followed by a discussion of mechanisms in the f.c.c. structure. The crystal-plasticity- based finite-element method is used as a numerical means to solve the field equations of elasticity and plasticity. This chapter focuses on fundamentals of the SPH formulation and describes a VUMAT subroutine used to implement the single-crystal-machining model in simulations.

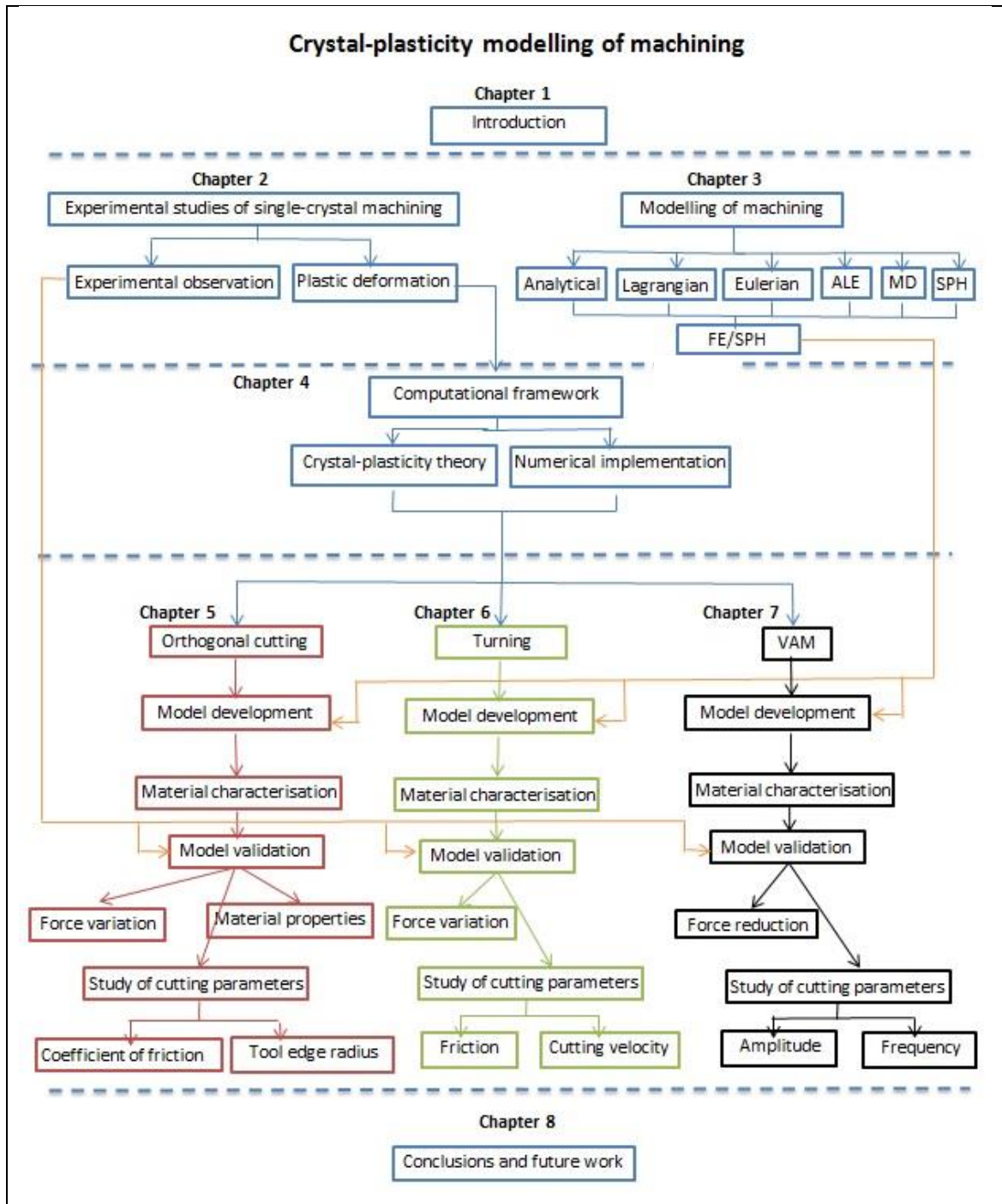


Figure 1:6 Thesis structure

Chapter 5 gives details of the three-dimensional FE/SPH modelling scheme of orthogonal cutting, which is the simplest geometric configuration of the cutting process. All parameters that are employed in simulations, such as the material

properties and modelling geometry, are obtained based on an experimental study found in the literature. The cutting force, which is one of the governing parameters defining efficiency of the cutting process, used for comparison of cutting in different orientations. The mechanism of deformation in single crystal is illustrated and the cutting force is presented with three crystal orientations and four cutting directions. The influence of important factors such as friction and tool edge radius in orthogonal machining is discussed in the final part of this chapter.

While the orthogonal modelling provides detailed data in terms of cutting energy (force) only for one specific crystal orientation at a time, the use of a turning configuration provides near-continuous data for the entire range of cutting directions for a given zone axis. Therefore, in Chapter 6, the turning model is presented. The cutting-force energy is obtained for eight orientations of the zone axis, and the influence of cutting parameters like cutting speed and friction is discussed in this chapter. This scheme can be extended to milling as well. The obtained results are compared to the previously published experimental data.

Vibration-assisted machining can potentially offer improved machinability for difficult-to-cut materials. Hence, Chapter 7 gives details of a simple orthogonal simulation with single-crystal models for both conventional and vibration-assisted machining. A comparative study of conventional and vibration-assisted machining in terms of frequency and amplitude is presented in this chapter.

Chapter 8 includes an attempt to summarize the capabilities of different developed models for each of the studied machining processes. It is followed by a list of recommendations for future work.

Experimental studies of single-crystal machining

2 Experimental studies of single-crystal machining

2.1 Basic crystal structure of solids

Solid materials are generally divided into three main types: amorphous, polycrystalline and single crystals (See Figure 2:1) (Azaroff, 1984). Each type is characterized by the size of an ordered region within the material. While polycrystalline materials have a high degree of order over many atomic or molecular dimensions, amorphous materials have ordered only within a few atoms or molecular dimensions. The ordered regions, or single crystals, vary in size and orientation with respect to one another. The single-crystal regions are called *grains* and are separated from one another by grain boundaries. Single-crystal materials, ideally, have a high degree of order, or regular geometric periodicity, throughout their entire volume.

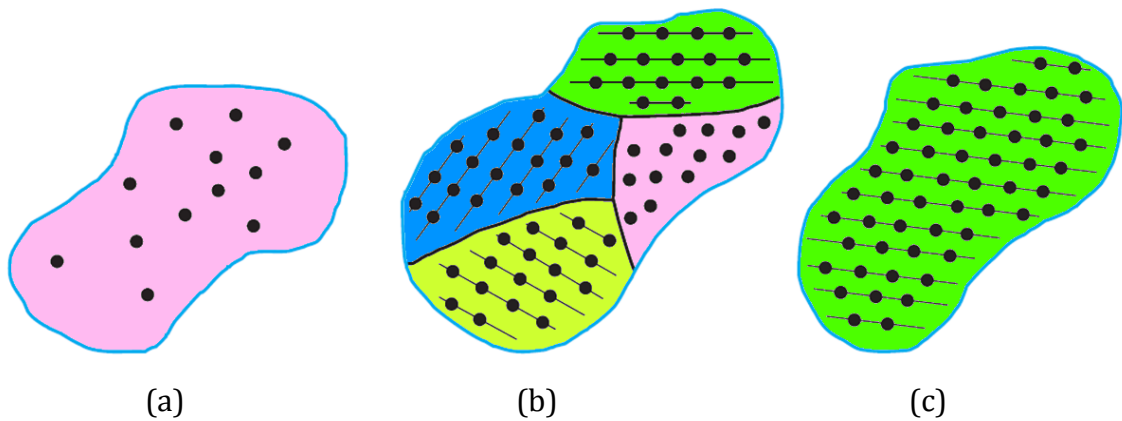


Figure 2:1 Schematics of three general types of solids: (a) amorphous, (b) polycrystalline and (c) single crystal after (Azaroff, 1984)

A crystal structure can form by solidification of a melt at a normal cooling rate. Pure metals can have structures with varying levels of complexity and symmetry. A number of examples of crystalline materials are metal, alloys and some ceramic materials. A crystalline structure consists of atoms, or molecules, arranged in a pattern that is repetitive in three dimensions. The unit cell of a crystal is the smallest pattern of arrangement. The geometry of a space lattice is completely specified by the lattice constants a , b , and c and the inter-axial angles α , β , and γ (see Figure 2:2) (Campbell, 2008). It is usually assumed that the space lattice continues to infinity in all directions. The intersections of lines, called *lattice points*, represent locations in space that contain the same kind of atoms or group of atoms of an identical composition, arrangement, and orientation.

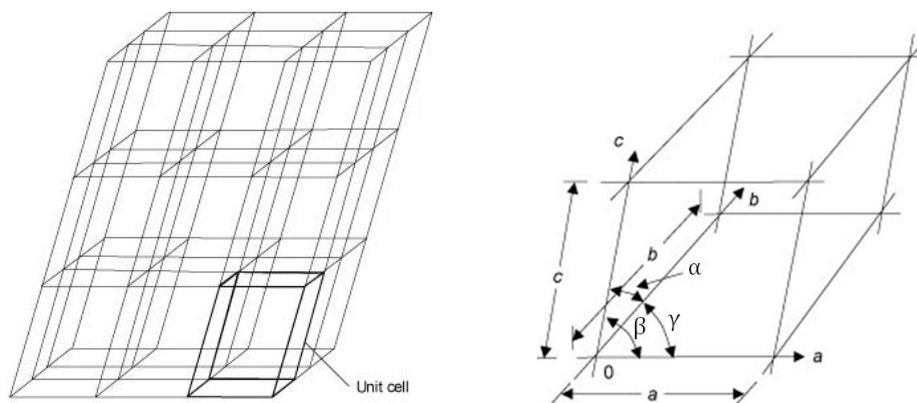
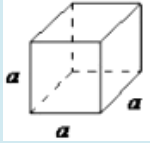
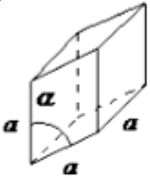
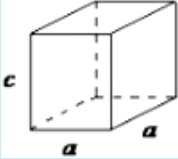
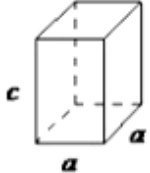
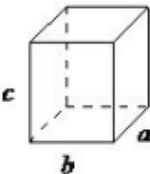
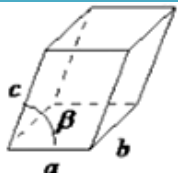
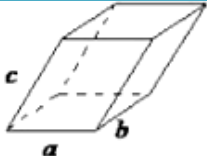


Figure 2:2 Space lattice and unit cell (Campbell, 2008)

All crystal systems can be grouped into one of seven basic systems. These seven basic, shown in Table 2-1, can be arranged in 14 different ways (see Figure 2:3), called *Bravais lattices*.

Table 2-1 Seven basic systems of crystal structure (Kittel, 1986)

Crystal system	Edge length	Interaxial angle	Unit cell geometry
Cubic	$a = b = c$	$\alpha = \beta = \gamma = 90^\circ$	
Rhombohedral	$a = b = c$	$\alpha = \beta = \gamma \neq 90^\circ$	
Hexagonal	$a = b \neq c$	$\alpha = \beta = \gamma \neq 90^\circ$	
Tetragonal	$a = b \neq c$	$\alpha = \beta = \gamma = 90^\circ$	
Orthorhombic	$a \neq b \neq c$	$\alpha = \beta = \gamma = 90^\circ$	
Monoclinic	$a \neq b \neq c$	$\alpha = \gamma = 90^\circ, \beta \neq 90^\circ$	
Triclinic	$a \neq b \neq c$	$\alpha \neq \beta \neq \gamma \neq 90^\circ$	

Most elemental metals (about 90%) crystallize upon solidification into three densely packed crystal structures: body-centered cubic (b.c.c.), face-centered cubic (f.c.c.) and hexagonal close-packed (h.c.p.) (See Figure 2:4). In terms of material structure, copper and aluminum have f.c.c. system and used in this thesis.

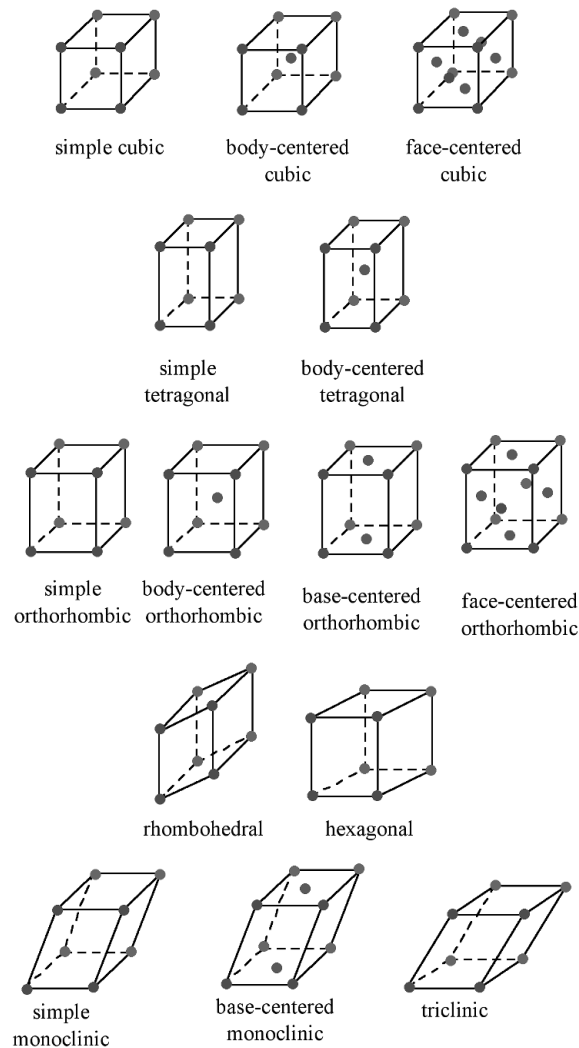


Figure 2:3 14 Bravais lattices (Kittel, 1986)

In f.c.c. system, atoms are centrally located on each face. Since the atom located on the face belongs to two unit cells and each of the eight corner atoms belongs to eight unit cells, four atoms belong to the unit cell. In the crystalline structure the volume of atoms belonging to the unit cell divided by the volume of the unit cell

called an atomic packing factor. This factor for the f.c.c. structure is 0.74; it is the densest obtainable extent of packing.

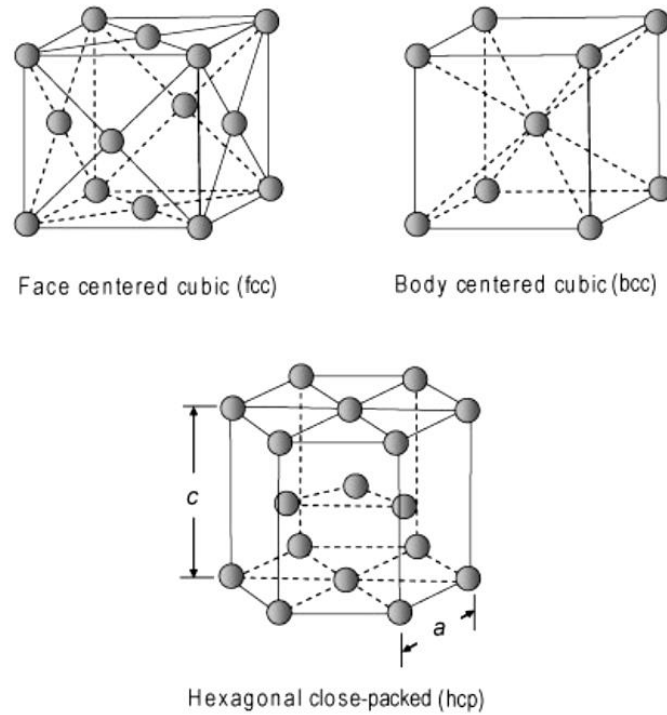


Figure 2:4 Three common crystal structures of metals (Kittel, 1986)

In the next section, the miller indices which are the way for the nomination of orientation an atomic plane in a crystal lattice is presented.

2.2 Descriptions of miller indices

Miller indices are a symbolic vector representation to describe the orientation of a plane or set of planes. These indices are useful to understand many phenomena in materials science, such as explaining the shapes of single crystals, the form of some materials' microstructure and the movement of a dislocation, which may determine the mechanical properties of the material (Ziman, 1972). This mathematical description allows us to define accurately, planes or directions within a crystal.

Miller indices are represented by a set of 3 integer numbers. In order to obtain the orientation of a crystal plane based on miller indices notation the following steps should be considered.

- 1- The fractional intercepts the plane with the crystallographic axes.
- 2- Taking the reciprocal of the fractional intercept of each unit length for each axis.
- 3- Cleared the fractions.
- 4- The parenthetically integer numbers

Figure 2:5 presents how directions and planes are defined based on miller indices in the cubic unit cells (William and Javad, 2004). Since the unit cell repeats in space, the notation actually represents a family of planes, all with the same orientation. In the cubic system directions having the same indices regardless of order or sign are equivalent. For example, these directions- $[123]$, $[213]$, $[312]$, $[132]$, $[231]$, $[321]$ - are the family of direction of $\langle 123 \rangle$.

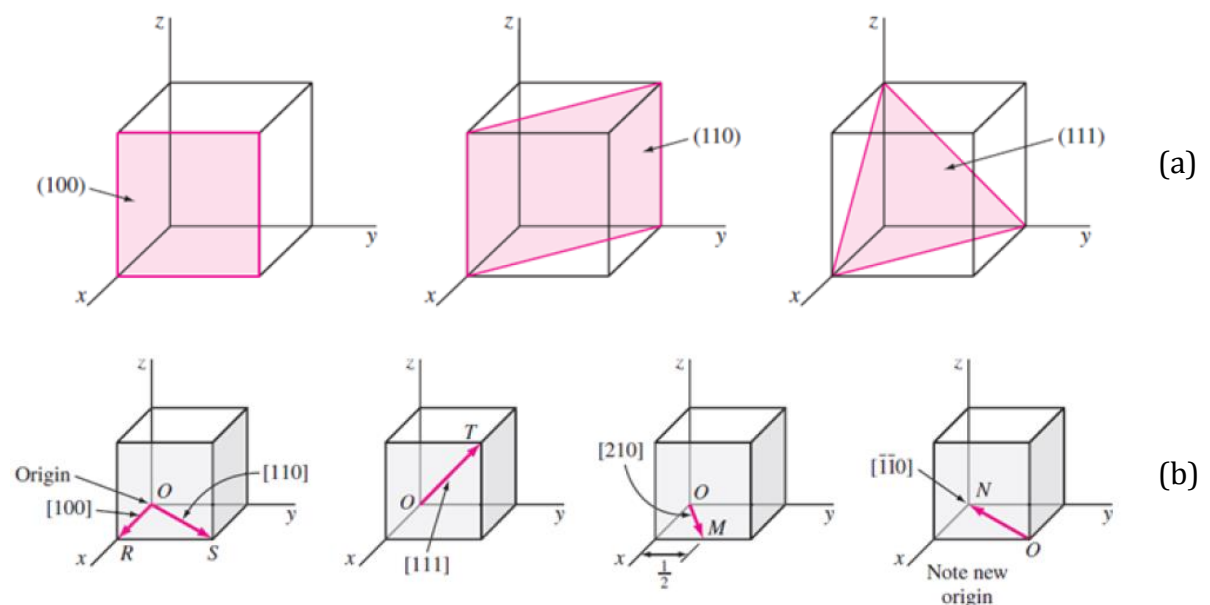


Figure 2:5 Planes (a) and directions (b) in cubic unit cells (William and Javad, 2004)

It is noted that the following conventions roles are considered for naming the miller index in the present thesis.

- 1- $[hkl]$ represents a direction, $\langle hkl \rangle$ represents a family of directions, (hkl) represents a plane and $\{hkl\}$ represents a family of planes.
- 2- The Negative numbers/directions are denoted with a bar on top of the number.

This symbolic vector is used to understand the deformation mechanism of f.c.c. crystalline materials which are described in the next section.

2.3 Mechanism of plastic deformation in crystals

Mechanical properties of metals depend on their crystalline structure. In a real crystal the lattice is not perfect and contains imperfections, or defects. Therefore, the perfect geometric periodicity is disrupted in some manner. Crystallographic slip is the governing mechanism of plastic deformation in metals and alloys driven by the motion of dislocations (Callister, 1997). The Figure 2:6 is shown a schematic of dislocation movement resulting from the application of a τ as shear stress. Dislocations are crystallographic defects, or irregularities, within a crystal structure, which can be introduced in materials either during plastic deformation, during solidification or as a result of thermal stresses.

The movement of dislocations is not with the same degree of ease on all crystallographic planes of atoms and in all crystallographic directions. Slip occurs on the planes of the densest packing of atoms and in the direction of the smallest distance between atoms since this requires the least amount of energy. The atoms primarily move on a specific plane called a *slip plane*. In that plane there are specific directions, along which dislocation motion occurs, called *slip directions*. The combination of the slip plane and the slip direction is called *slip system*. Therefore, a slip system is defined by two main factors:

1. The slip-plane normal, a normal to the plane that contains the slip direction.
2. The slip direction, a direction along which the material slips if the slip system is activated.

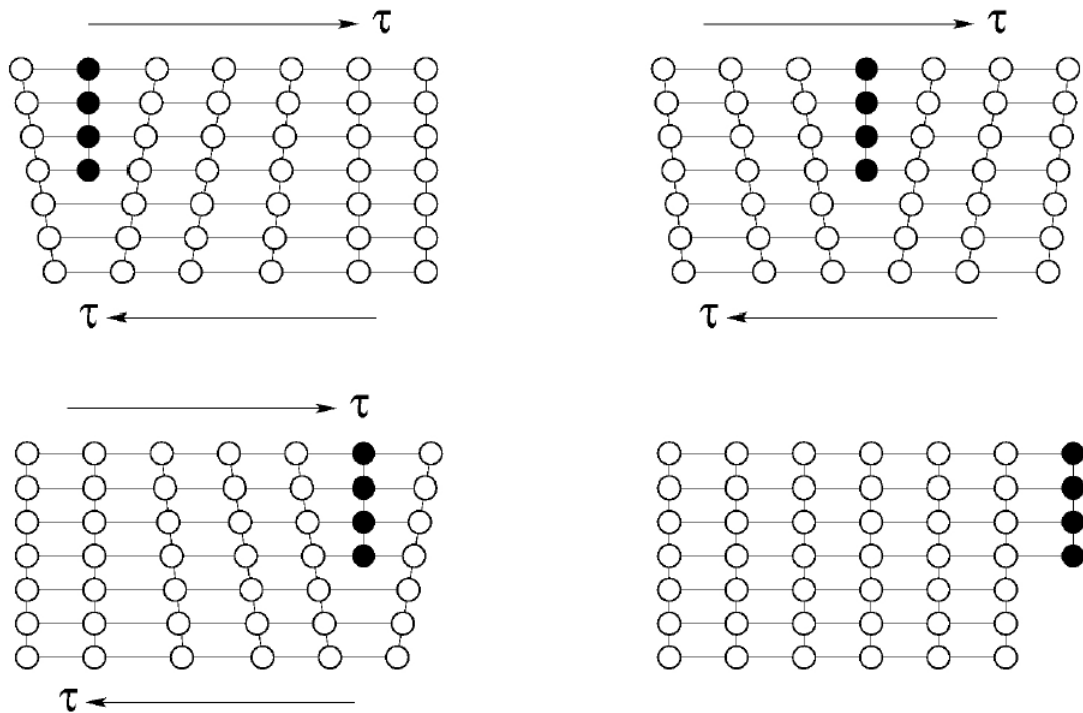


Figure 2:6 Dislocation movement (Callister, 1997)

Slip-system parameters are determined by packing of individual atoms within the material. Thus, the slip-system parameters for f.c.c. materials are rather different from those for b.c.c. and h.c.p. structure. Slip planes and directions for three common crystal structures (f.c.c., b.c.c. and h.c.p.) are listed in the Table 2-2 (William and Javad, 2004).

Table 2-2 Common slip planes and directions for different structures (William and Javad, 2004)

Structure	Slip direction	Slip plane
f.c.c.	$\langle 110 \rangle$	$\{111\}$
b.c.c.	$\langle 111 \rangle$	$\{110\}, \{112\}$
h.c.p.	$\langle 11\bar{2}0 \rangle$ $\langle 11\bar{2}3 \rangle$	$\{0001\}, \{1\bar{1}11\}, \{1\bar{1}01\}, \{1\bar{1}0\bar{1}\}$

The 12 slip systems are available for f.c.c. structure, resulting from 4 slip planes and 3 slip directions in each of those four planes. The slip-plane normal belongs to the $\{111\}$ and the slip directions belong to the $\langle 110 \rangle$ (see Figure 2:7).

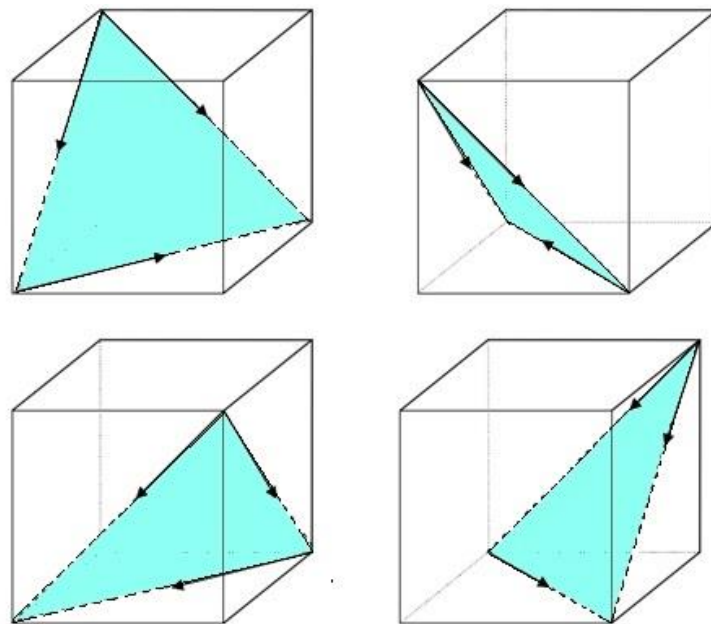


Figure 2:7 12 slip systems in f.c.c. crystal (William and Javad, 2004)

In general, the applied plastic strains are accommodated by the material through a combination of slipping action on multiple systems (Patwardhan, 2003). The amount of work required in deforming of f.c.c. crystals can vary significantly

depending on the crystal orientation. Hence, the single-crystal machining has more complicated mechanisms than those in cutting at the macro scale, which is mainly shearing of the material to forming a chip in front of the tool tip. Material's micro-structure in single crystals plays a significant role in the machining deformation processes. A study of small-scale deformation in machining makes it possible to gain a greater qualitative understanding of deformation processes. In the next section the brief overview of published papers dealing with experimental observations of machining in micro scale is presented.

2.4 Single-crystal machining experiments

Machining of single-crystal or conventional polycrystalline materials with small depths of cut (of an order of a few micro-metres) basically involves cutting within a single grain or multiple grains with interruptions at the grain boundaries. Since the grain orientation changes from one crystal to another in a polycrystalline aggregate, the cutting tool in a micro scale cutting process has experienced a workpiece with different crystallographic orientations. In the past few years, deformation of miniaturized single-crystal samples was frequently investigated to examine the processes governing deformation on the micro-metre and nano-metre length scales.

Table 2-3 shows briefly the cutting conditions and materials selection in some of the high cited publications related to single-crystal machining process. These papers investigated that the machining response, including machining forces and chip formation for single crystal machining strongly depended on the crystallographic orientation for a wide range of cutting parameters. In the case of selecting materials for single-crystal machining studies, mainly copper and aluminium have been preferred in literatures. In the presented thesis, both copper and aluminium are examined for orthogonal process while copper is selected for turning, and aluminium is considered for vibration-assisted machining material.

Table 2-3 Experimental study on single crystal machining from literature, and associated machining parameters

Papers	Material	Rake angle	Feed (μm)	Speed (mm/s)
(Ramalingam and Hazra, 1973)	Al	40°	127	0.27
(Williams and Gane, 1977)	Cu	40°	1-100	0.1-1
(Ueda <i>et al.</i> , 1980)	β -brass	0° , 20°	0.1-200	0.0025
(Williams and Horne, 1982)	Cu	40°	100	20
(Cohen, 1982)	Cu, Al	0° -50°	114.3	0.44
(Sato <i>et al.</i> , 1983)	Al	35°	100	1.66
(Moriwaki, 1989)	Cu	0° , 5°	0.01-3	8833.33
(Sato <i>et al.</i> , 1991)	Al	3°	0.5-3	16.66
(Yuan <i>et al.</i> , 1994)	Cu, Al	0°	1-10	0.16-0.83
(To <i>et al.</i> , 1997)	Al	0°	1-10	0.16-0.83
(Zhou and Ngoi, 2001)	Al, Cu	0°	5-10	1300
(Lawson <i>et al.</i> , 2008)	Al	0°	5-20	5-15

When cutting a single crystal materials, the specific orientation of the material with respect to the cutting direction will have a significant impact on the resulting force. Therefore, unlike conventional metal cutting, the cutting mechanism in single crystal machining is more influenced by the crystallography and active slip systems within the workpiece material. Two main aspects- cutting force variation and size effect- are stressed in single crystal machining studies. In the following sections the details of experimental studies of cutting force variation and the size effect involved in the machining of single crystals are present.

2.4.1 Machining force variation

The cutting force is one of the governing parameters defining efficiency of the cutting process. The workpiece material, cutting parameters, tool geometry, type of cutting process, etc. are the factors involved in cutting force in machining study.

In the single-crystal machining by having the same cutting parameters and only changing the direction of cutting, force will be changed. The experimental data obtained by Ramalingam and Hazra, (1973) showed that cutting force variation for single crystals aluminum arise from the need to maintain a constant dynamic shear stress on the bulk shear plane that operates during chip formation. They found that the dynamic shear stress was independent of crystal orientation and in good agreement with the value calculated for polycrystalline materials using a dislocation model. This observation was also proved by Williams and Gane (1977). Calculation of the shear stress on the shear plane during cutting showed that this was approximately constant for a copper and did not depend on the cutting machine used or the prior condition of the specimen.

The chip formation and separation are considered as an important factor which directly involved in the cutting force. The different chip formations were reported by Ueda *et al.*, (1980) on orthogonal cutting of a single crystal of β -brass. They used scanning electron microscopy for machining with cutting speed of 2.5 $\mu\text{m/s}$. These in-situ observations revealed significant variations in the chip formation mechanism at different crystallographic orientations (see Figure 2:8 and Figure 2:9).

Two different types of chips were observed- fractured and lamellar. They found that the specific energy has changed by machining along different workpiece orientations. The variation of chip formation was studied by trying to define the mechanisms of chip formation. The cutting force was correlated to chip morphology. Fracture in deformation of chips caused a fluctuation by cutting force, while a more regular, lamellar chip formed resulted in a smoother force. The variation of chip morphology in cutting single-crystal materials at different cutting direction was studied in greater detail by various researchers (Clarebrough and Ogilvie, 1950, Von and Black, 1970, Black, 1971, Williams and Horne, 1982). A series of experiments on the single crystals of copper showed by Williams and Horne, (1982) described that forces and chip morphology are highly orientation dependent. When the major slip plane was coincident with the cutting direction dislocation glide does not significantly contribute to material removal; chips are

formed by fracture along the direction of maximum shear stress. Most of the work used a sharp-edge diamond tool to investigate the force variation. This helped to isolate the machining force from the effect of the tool tip. Further geometric simplification was realized by utilizing an orthogonal machining process, which is the simplest geometric configuration with a zero rake angle.

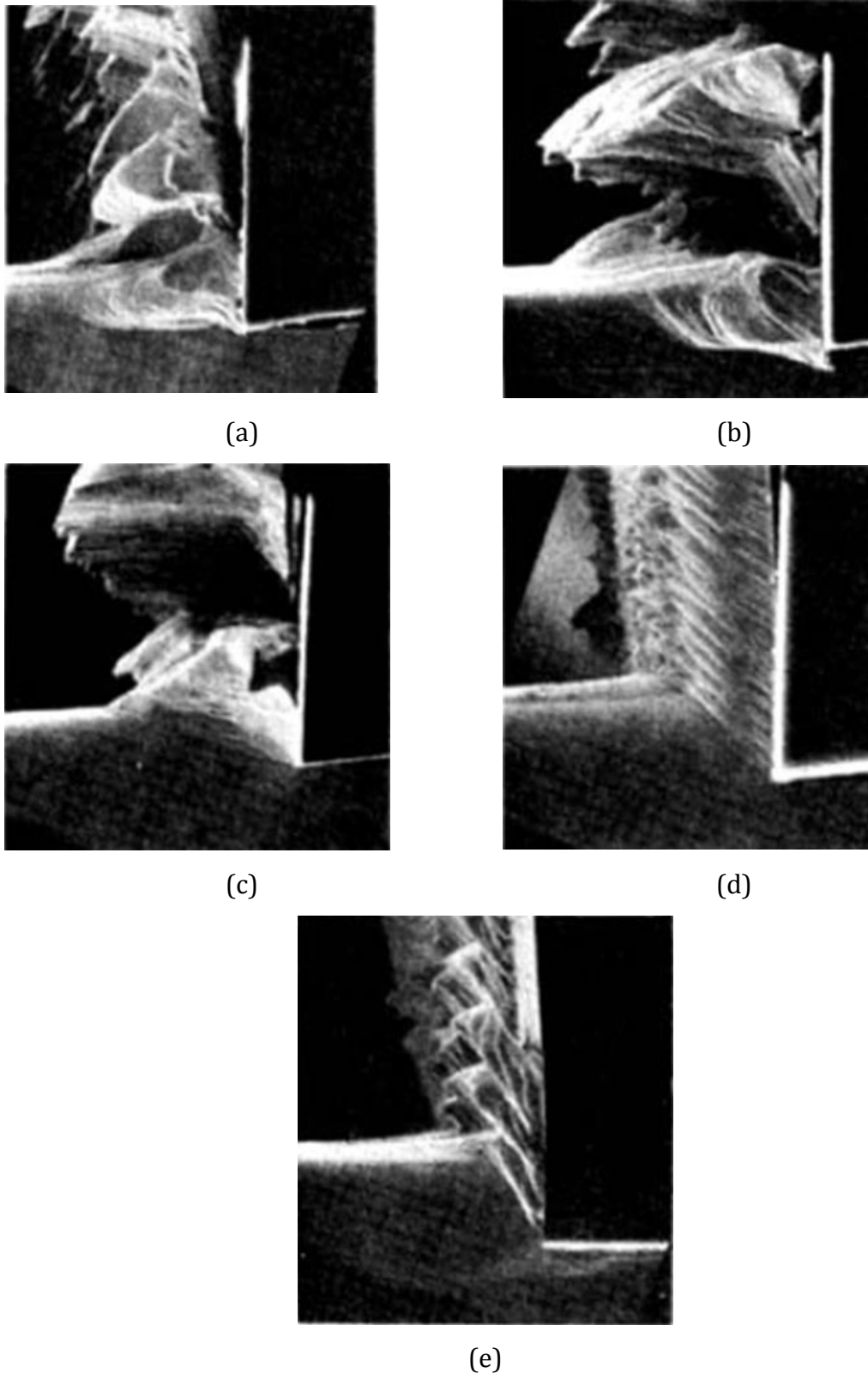


Figure 2:8 Chip-formation pattern of specimen in (100) plane with different cutting orientation angles: (a) -25° , (b) -15° (c) 0° (d) 25° (e) 45° (Ueda *et al.*, 1980)

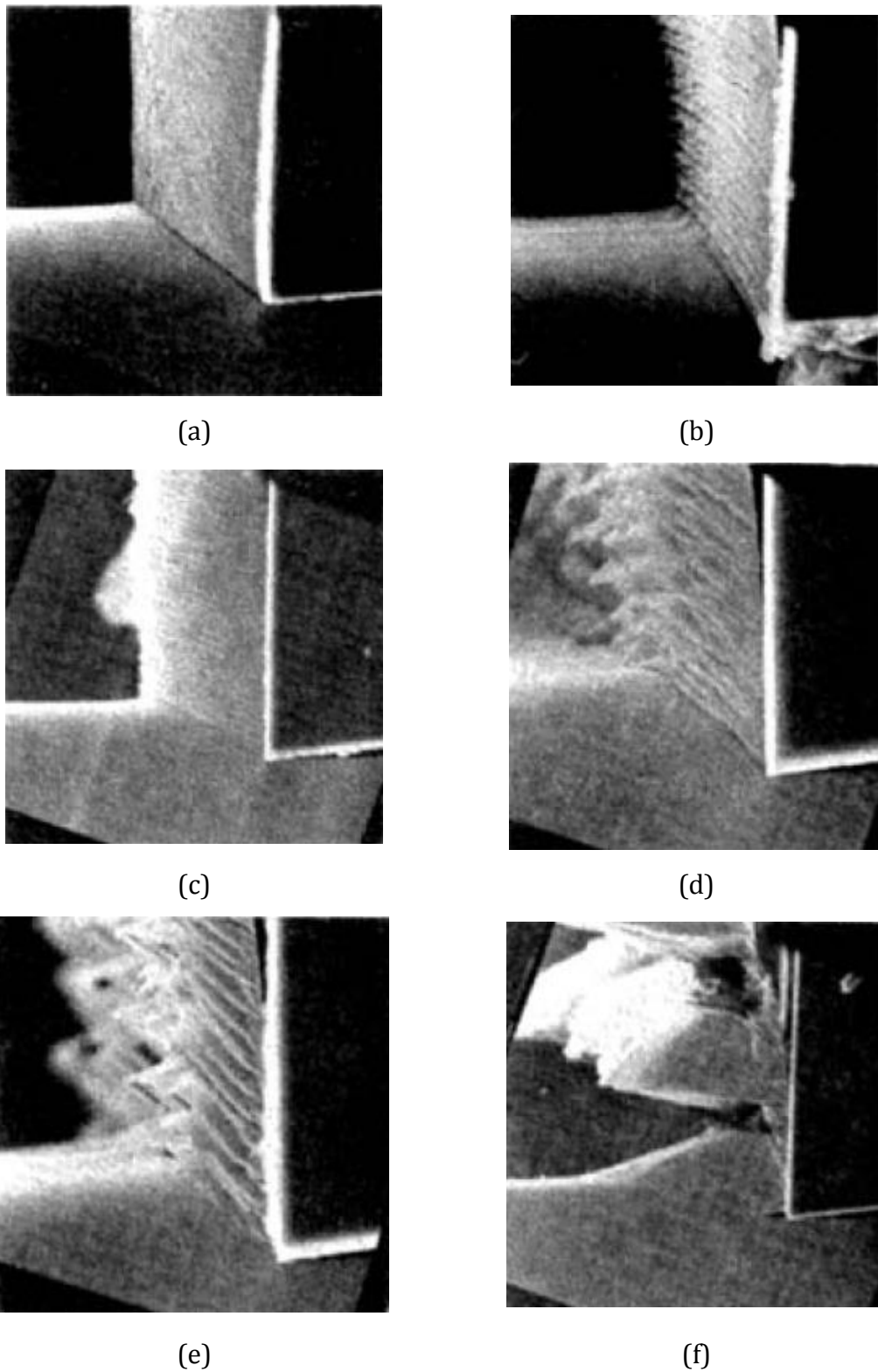


Figure 2:9 Chip-formation pattern of specimen in (101) plane with different cutting orientation angles: (a) -70° , (b) -45° , (c) 0° , (d) 35° , (e) 70° , (f) 90° , (Ueda *et al.*, 1980)

Another important observation in the literature was reported by Sato *et al.*, (1979). They performed machining experiments on (001) and (110) planes of aluminium single crystal with varying sets of cutting direction angles for the [001] direction. Their SEM images (Figure 2:10) showed a good agreement between the observed slip line and theoretical one, which was determined on the assumption of a slip-system mechanism. The theoretical slip line observed on the side surface of workpiece was calculated by the intersection of slip plane vector on crystal and cutting side plane vector. It was clarified that the mechanism of deformation of the finished surface could be explained reasonably based on the slip system of crystal.

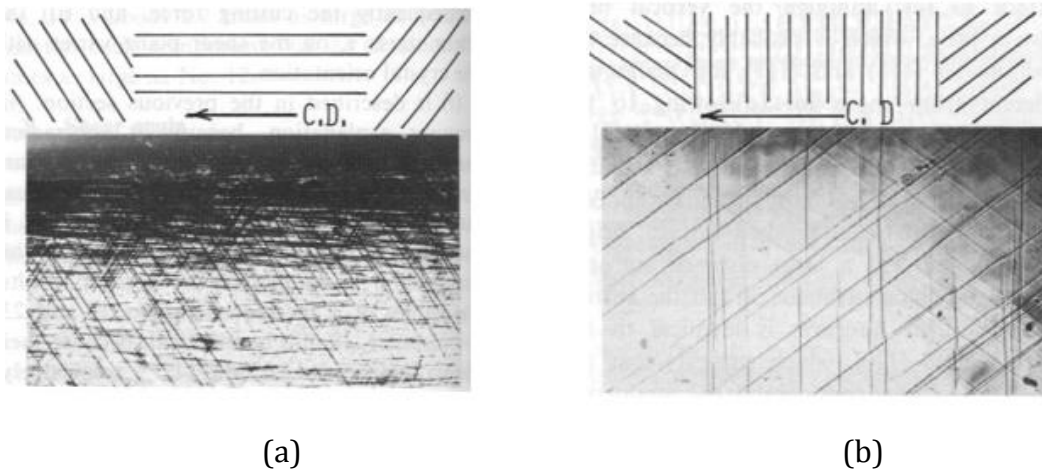


Figure 2:10 Calculated slip lines and those observed on the side surface for (001) [110] (a) and (110) [001] (b) cutting orientations (Sato *et al.*, 1979)

As the chip variation in single crystal machining directly affects the cutting force, some of the researchers implemented machining process on single-crystal copper or aluminium or both to study the cutting force variation. A convenient way to represent the crystallographic orientations is to specify the angle of rotation of each plane normal from a specific direction. Yuan *et al.*, (1994) used a diamond cutting test of single-crystal copper and aluminium in order to investigate the effect of crystallographic orientation on (110) and (111) planes in different cutting orientations. The cutting-force results for single crystals of copper and aluminium are shown in Figure 2:11 and Figure 2:12, respectively. Generally, the variation of

cutting force in the (111) plane is less than in (110). In the case of cutting on the (110) plane, the cutting-force value in the $[1\bar{1}0]$ direction was largest, while the cutting force reached a minimum value in the $[001]$ direction.

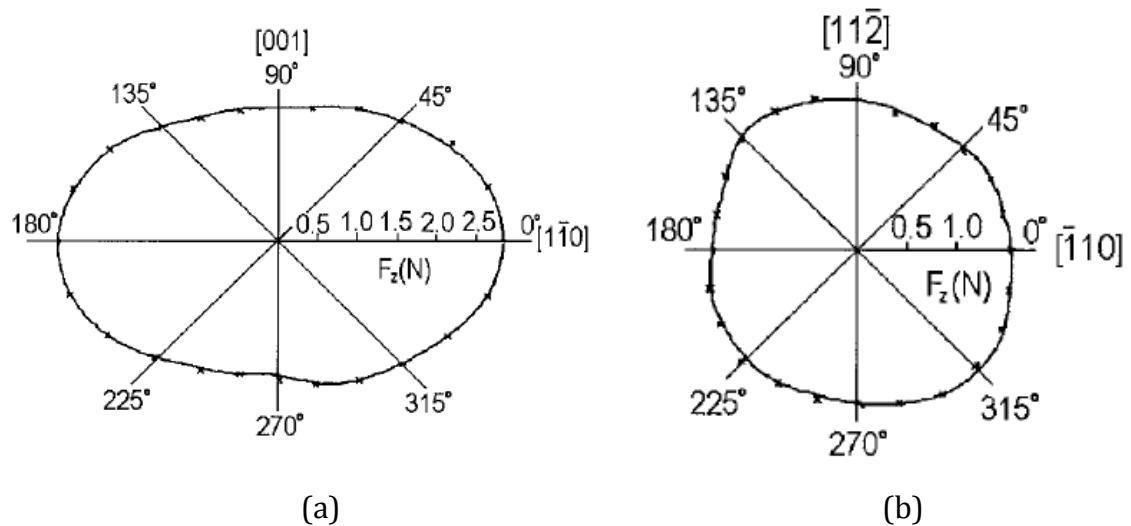


Figure 2:11 Variation of cutting force in cutting copper single crystal in different cutting directions in (110) (a) and (111) (b) planes (Yuan *et al.*, 1994).

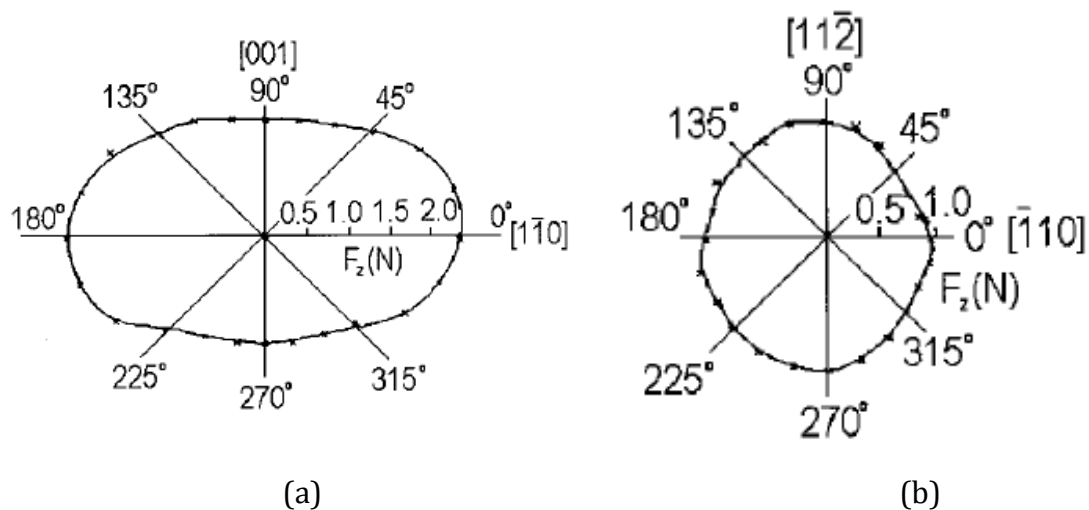


Figure 2:12 Variation of cutting force in cutting aluminium single crystal in different cutting directions in (110) (a) and (111) (b) planes (Yuan *et al.*, 1994).

Some of researchers showed that in addition to force variation in terms of magnitude, different cutting-force signatures were observed in the machining of a

specimen in the same crystal plane with different cutting directions. Lawson *et al.*, (2008) presented an experimental investigation of orthogonal machining of single-crystal aluminium at different crystallographic orientations for varying uncut chip thicknesses and cutting speeds using a diamond tool. Three distinct types of force patterns were observed (Figure 2:13); It included a stable signature (a), bi-stable behaviour (b) and increases with periodical fluctuation (c) during the process. The cutting force is the main component of the total force and used to calculate the power required to perform the machining operation. The thrust force is in the direction of feed motion in the orthogonal cutting and used to calculate the power of feed motion. In three-dimensional cutting, one more force component appears along the third axis called lateral force. The force components- cutting, thrust and lateral- and geometric relationships are described in (d).

They link these signatures to the activation different slip systems accumulated from the beginning of the cutting process. The causes of the observed bi-stable and fluctuating force signatures are the unsteady slip behaviour of the single crystals and the changes in frictional characteristics on the rake face.

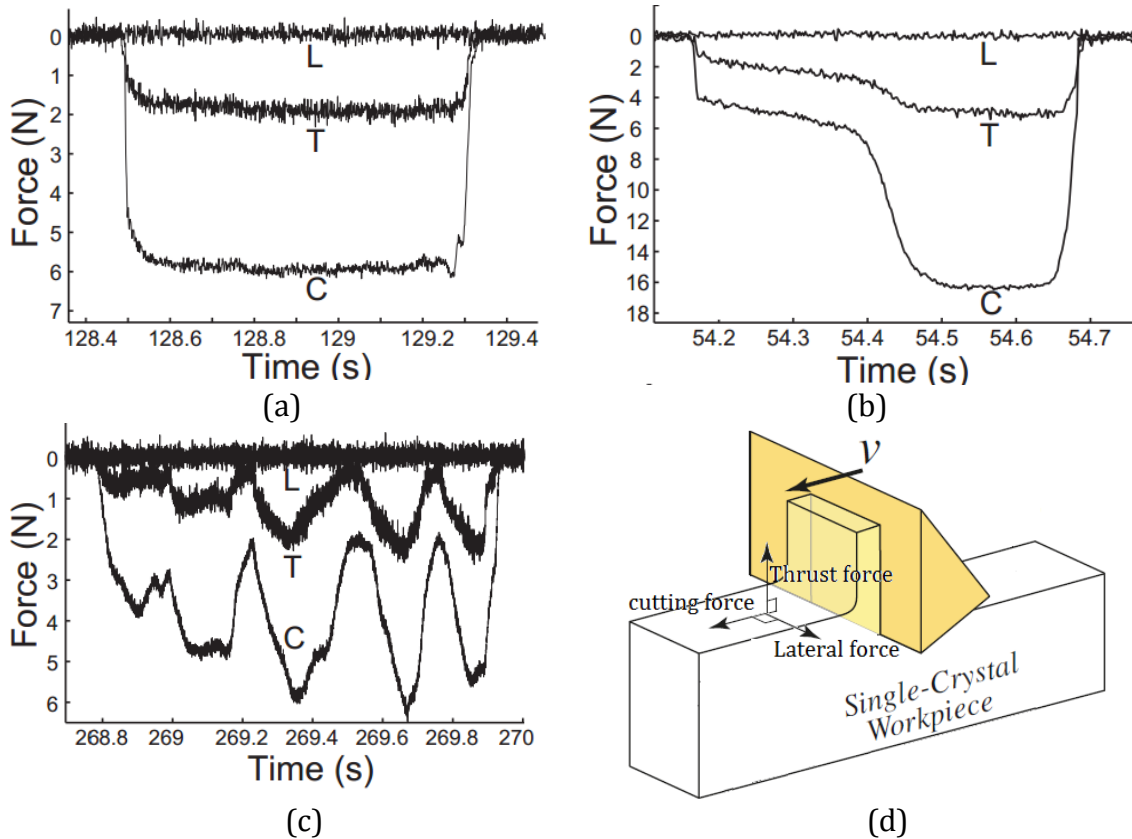


Figure 2:13 Cutting (C), thrust (T), and lateral (L) forces for: (a) (12 5 0) facet for 5 mm/s and 20 μm depth of cut; (b) (6 7 0) facet with 10 mm/s and 20 μm depth of cut; (c) (2 7 0) facet with 5 mm/s and 5 μm ; and (d) force components (Lawson *et al.*, 2008).

The above experimental studies demonstrated that the machining force had varied for different crystallographic orientations. This variation extended to 312% (Lawson *et al.*, 2008) in some cases (see Figure 2:13 b) and cannot be neglected. Although a number of studies were performed through the years, our fundamental understanding of machining force magnitudes and signatures, friction, cutting velocity, as well as amount of elastic recovery on single-crystal machining has not advanced. Analysing of single crystal machining study by means of experimental observation is expensive and time consuming since a wide range of parameters are involved in cutting process such as contact conditions, tool's geometry, friction, material's non-linearity, heat transfer and lubrication. It is challenging to conduct experiments, make in-situ observations and analysis of the results to study the

effect of each parameter. These limitations led to implement the pure modelling approach calibrated with experimental data to fully understand the cutting phenomena under various cutting conditions. To develop a robust modelling by accumulating enough knowledge on this issue should be a key parameter to achieve more understating in single-crystal machining.

In addition to a large force variation in micro-scale machining, the size effect has not had any unique phenomenological explanation. The size effect in micro machining scale means increases in nonlinearity of the amount of energy required for removing unit volume of material when the uncut chip thickness decreases from a few hundred microns to a few microns. The next section reviewed the size-effect experimental observation in single-crystal machining.

2.4.2 Size effect

When metal is removed by a machining process, there is a substantial increase in the specific energy required to decrease in a chip size. The size effect simply means that more energy should be used, and, hence, a higher cutting force than normally expected has to be exerted, in removing smaller amounts of material (Kopalinsky and Oxley 1984). A development of the unique explanation for the size effect has challenged researchers for well over the past fifty years. Although different explanations of this extra energy have been proposed in the literature, these are mainly divided into two main independent categories: tool's edge radius effects and strength of the material. In the single-crystal-machining process, the size effect is mainly related to a small ratio of un-deformed chip thickness to the tool edge radius. The next reason which is the nonlinearly increases strength of materials as a function of strain, strain rate and strain gradient is out of scope of present thesis and recommended as future works.

Experimental observations of the size effect associated with different materials under different cutting condition were reported in Table 2-4. This scaling in specific cutting energy reported while cutting several materials at varying cutting conditions of speeds, uncut chip thickness values and edge radii. Observations

based on experimental studies for both isotropic and anisotropic cutting indicate that the ratio of the depth of cut to the effective cutting-tool edge radius has a great influence on the realisation chip formation.

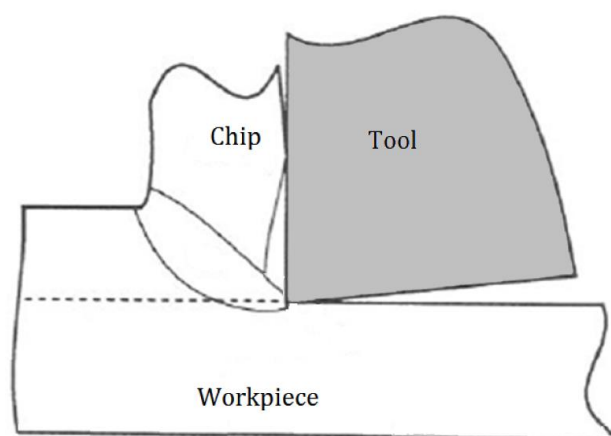
Table 2-4 Summary of experimental reports on size effect

Papers	Cutting speed (m/min)	Chip thickness (μm)	Edge radius (μm)	Material
(Nakayama and Tamura, 1968)	0.1	2 to 42	3 to 4 μm	Brass
(Lucca <i>et al.</i> , 1991)	6 to 108	0.025 to 20	0.01 to 0.30	Cu
(Liu and Melkote, 2006)	10,200	0.5-10	0.065 to 0.1	Al-5083
(Wu and Liu, 2010)	15.7 to 141.3	1 to 10	16	AISI 1045

Nakayama and Tamura (1968) observed that the sources of size effect relative to cutting forces were due to the fact that the energy consumed in plastic flow in the subsurface layer was not proportional to the undeformed chip thickness. The shear angle decreases with a decrease in the undeformed chip thickness. Though the minimum depth of cut in their experiments was as small as 2 μm , the increased of cutting force relative to size effect was about four times larger than the normal cutting force used in machining of brass. This result obtained from the small rake angle, the rounded character of the cutting edge, the slow cutting speed, and the relatively wide width of cut in the experimental studies. When the edge radius of the tool tends to be on the same order of magnitude as the chip thickness, the effective rake angle becomes negative and results in plowing as a material removal mechanism (Lucca *et al.*, 1991) (Figure 2:14). The nominal rake angle has a great influence on the specific cutting energy and cutting mechanisms. Lucca *et al.*, (1993) experimentally investigated the effect of the geometry of a single-crystal diamond tool's edge on forces and energies consumed in ultra-precision orthogonal cutting of copper material. Generally increasing around 10 times in cutting force observed in their experiments over uncut chip thicknesses from 20 μm down to 25 nm. Both the nominal rake angle and effective rake angle were

found to have significant effects on the resulting forces and energy dissipated. They noticed that the specific cutting energy required to machine at a very low chip thickness could not be explained by the energy required for shearing and overcoming friction on the rake face of the tool. The dominance of ploughing under these conditions was used to explain the increase in specific cutting energy. To estimate the effective rake angle at a given uncut chip thickness, a point was identified on the tool's edge profile, at a distance $1/2$ of the uncut chip thickness up from the workpiece surface.

The concept of a minimum chip thickness, below which no chip will form, or a minimum depth of cut below which no material removal will occur, was investigated by a few researchers. This was an attempt to understand the necessary minimum chip thickness to ensure proper cutting and avoid plowing and sliding of the tool. Kim *et al.* (2004) observed plowing under a certain depth of cut indicating that there exists a minimum chip thickness for chip formation. They found in their experiments with aluminum alloys that the minimum chip thickness was between 20 to 40% of the cutting edge radius. Hence, the value of minimum chip thickness varies with the cutting-edge radius, workpiece material and cutting processes.



(a)

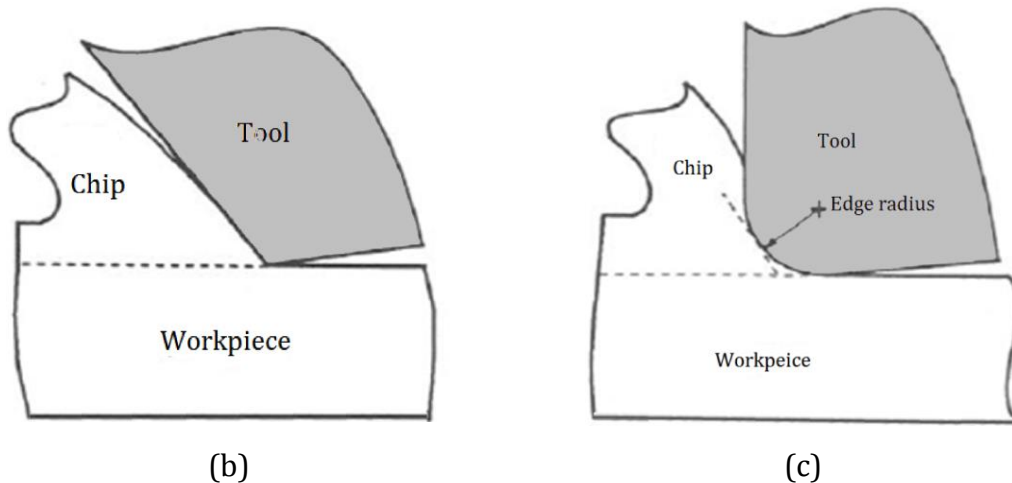


Figure 2:14 Chip formation through (a) shear and sliding along rake face of the tool, (b) negative rake angle and (c) effective negative rake angle with the edge radius of order of depth cut after Lucca *et al.*, (1991)

In metal cutting, the meaning of chip formation is the chip which just left the tool/chip interface and has not yet to be broken. Therefore, the main attention was paid to the cutting force and contact process at the tool-chip interface. The patterns of chip vary significantly with tool configuration/geometry, cutting conditions and workpiece material properties. Understanding the chip formation is the first step to good chip control, results in the prediction of chip breakability for a wide range of machining conditions. A lack of chip control often leads to coarse surface finish, poor machining accuracy, and problems with chip removal from the machining zone.

The tool-edge radius is an important parameter for surface quality in machining at micro scale. A small change of it significantly influences surface roughness. Weule *et al.* (2001) explained achieved surface roughness in terms of minimum depth of cut. They found that the minimum cutting depth depends primarily on the sharpness of the tool and, secondarily, on material properties of the workpiece. They used a homogeneous, hard workpiece material (SAE HI3) with no internal stresses which is used quite commonly for dies and molds.

The few studies, like Liu and Melkote (2006) and Wu and Liu (2010) has been reported that the specific cutting energy in machining increases nonlinearly with a

decrease in uncut chip thickness due to material strengthening. They concluded this increase in strength has been attributed to various factors such as strain rate, strain gradient, and temperature effects. A flow stress model based on strain gradient plasticity theory have been analysed for the micro-cutting process. The proposed models relate the flow stress in micro-cutting tool geometry (edge radius, rake angle, and clearance angle) and cutting condition (undeformed chip thickness, cutting width). The strain gradient strengthening presented in their studies contribute significantly to the size effect at low cutting speed and small uncut chip thickness. The existence and importance of strain gradient in single crystal machining is still a challenging task and out of scope of this thesis.

2.5 Summary

The previous studies demonstrated a significant variation in cutting force and chip topology in single crystal machining as a function of crystallographic orientations. These experimental observations demonstrated that the machining force had varied for different crystallographic orientations extended to 312% in some cases and cannot be neglected. Single crystal machining is more influenced by the crystallography and active dislocation slip systems within the workpiece. The contact phenomenon during single crystal machining is complicated due to the tool-edge-radius interface with single grain and requires a more fundamental investigation. Although a number of experimental studies were performed through the years, our fundamental understanding of single-crystal machining has not advanced because the experimental analysis of micro-machining interfaces with some limitations in terms of small size. These limitations led to implement the pure modelling approach calibrated with experimental data to fully understand the cutting phenomena under various cutting conditions. Develop a robust modelling by accumulating enough knowledge on this issue should be a key parameter to achieve more understating in single-crystal machining. In the next chapter the available modelling efforts to machining study is discussed.

Modelling of machining in micro scale

3 Modelling of machining in micro scale

3.1 Introduction

Analysing any machining technique by means of experimentations is expensive and time consuming since a wide range of parameters is involved in machining processes. These factors include contact conditions, friction, material's anisotropy, heat transfer, lubrication, etc. The microscopic level of phenomena in single crystal machining is one of the difficulties preventing the full understanding of the fundamentals of the process. It is challenging to conduct experiments, make *in-situ* observations and measure results after the experiment.

A unique solution for modelling, validation for all the types of sizes (macro-meso-micro) and a wide range of cutting conditions has not been found until now. Before creating a metal-cutting model, an understanding and configuration of the process need to be addressed. A variety of input parameters to the analysis processes must be known. A review of literature shows that cutting processes are generally dependent on:

- 1) workpiece parameters including the material type, crystallography, temperature and pre-deformation.
- 2) cutting-tool parameters that include tool design and geometry, materials of the tool etc.
- 3) cutting parameters including the speed, feed, depth of cut and the environment (Dornfeld *et al.*, 2006).

Some researchers studied an effect of few specific factors like speed and depth of the cut while in more advanced studies a complex physical behaviour underlying the machining process, was analysed. The modelling was used primarily for isotropic micro-machining where no crystallographic effects were considered. A physical understanding of single-crystal machining is necessary for developing and improving processes of ultra-precision metal-cutting technology. A combination of computer technology and a plasticity processing of a material theory provided a direction to enhance knowledge in metal machining. The rapid improvement in computational power caused a great advance in simulation of materials processing.

In terms of modelling, analytical approach is one type of analysis which involved some assumptions. Among the numerical techniques, finite-element analysis is one of the most frequently used methods to simulate machining processes. All the modelling involves a prediction of the machining forces under various cutting conditions. The predictability and validity of each developed model should be verified by experimental results in many cases and then could be an alternative way to fully understand the mechanism of machining in micro scale. In this chapter the available tools for modelling of the machining process are presented in more detail.

3.2 Analytical modelling

The effect of material anisotropy is often not included in the theoretical analysis. In order to study the effect of anisotropic material behaviour in the modelling, the underlying physical phenomenon causing this anisotropy need to be addressed.

The anisotropy observed in machining is the result of plastic deformation of metallic crystals. The machining response is determined by the orientations of the plane and directions with respect to the cutting geometry.

Sato *et al.*, (1983), used the Schmid factor value to obtain the active slip systems during machining. The amount of slips on each slip system was assumed to be proportional to the Schmid factor value. The shear angle was then calculated from sum of slip directions vector on active slip systems. Micro plasticity modelling of machining proposed by Lee and Yang (1993) is another limited analytical research available in literature to analyse the variation of cutting force for different orientations. This model was applied to the machining of single crystals by considering multiple active slip systems. Yuan *et al.* (1994) was assumed plane-strain orthogonal cutting in his analysis with a zero tool rake angle. This model allows prediction of cutting forces for a variety of cutting conditions.

Additional complications in analytical modelling of single-crystal machining arise from the actual amount of deformation happening, which is often characterized by the shear angle. As a consequence, strategies for incorporating the effects of anisotropy must firstly include determination of shear angle. Although the shear direction was shown to be very sensitive to the crystallographic orientation, the simple analytical relationship between the shear direction and crystallographic orientation is still a challenge for introduction into analytical modelling. Due to this limitation, while the numerous analytical researchers reported different aspects of cutting processes at the macro scale over the years, a few of them investigated the single crystal machining material.

Most of the analytical models of micro cutting in terms of size effect are based on the Merchant's theory by considering a rounded tool edge (Ko and Kim, 1999, James *et al.* 2012, Pearlman and Saigal, 2012, Kim, 1996)(see Figure 3:1).

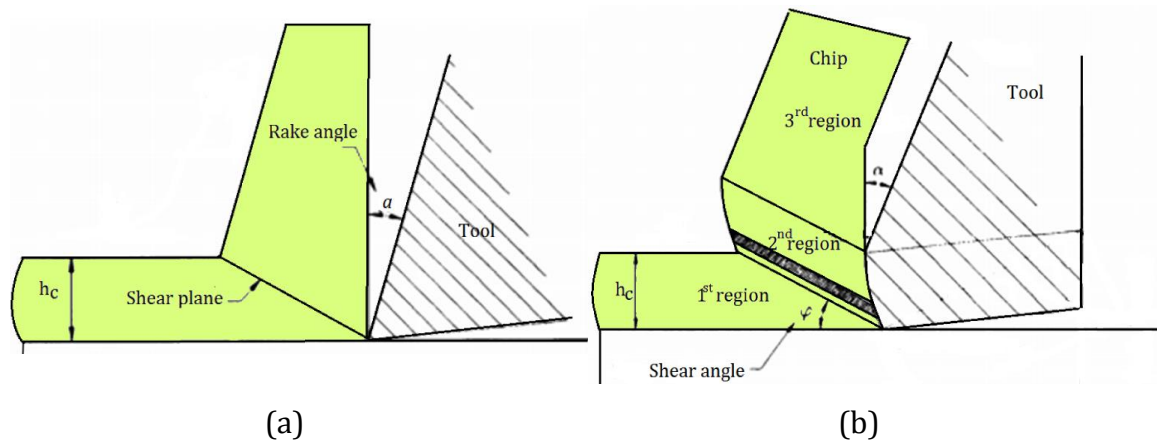


Figure 3:1 Cutting model for orthogonal machining: (a) Merchant theory and (b) rounded tool edge (Kim, 1996)

They proposed an orthogonal cutting model of micro machining with a rounded cutting tool to study sliding along the clearance face of the tool due to elastic recovery and ploughing caused by a relatively large edge radius of the tool. They found that the tool clearance face contributes significantly to the overall cutting force. The applicability and accuracy of these models for single-crystal machining are subject to many limitations.

The analytical techniques used to assess forces and stresses in the single crystal machining process are usually limited to one crystal plane and direction. Real machining is more complicated and, hence, require the use of other techniques for finding the machining forces and stresses involved. Numerical computation methods have become a tool for investigation of single-crystal machining. It is a good complement to experimental approaches as it can overcome some of the limitations in analytical techniques, if correctly done. It is not a perfect solution because it also involves many of the same assumptions as in analytical modelling. The computer-based models can offer a reasonable insight into certain verifiable trends or guidance on empirical research to assist further understanding of the process. The numerical computation methods like lagrangian, eulerian, arbitrary lagrangian eulerian, molecular dynamic and smooth particle hydrodynamic are known as robust schemes for modelling of machining and reviewed in the next section of this chapter.

3.3 Numerical computation method

A bibliographical review of the finite-element methods applied to the analysis and simulation of micro scale cutting was done by Mackerle (2003). Numerical simulations of metal-cutting processes are a significant challenge in terms of difficulty in modelling large-deformation at high strain rates in a numerically robust way. A primary shear zone is one of the most critical regions for metal-cutting simulations (Kiliçaslan, 2009). The deformation zone in the cutting process is shown in Figure 3:2. This zone extends from the tip of cutting tool and has high stress distribution predicted by modelling simulation. However the current developed model is also capable to predict the primary shear zone, this is beyond the scope of thesis. Due to high contact stresses along the chip-tool interface in this zone, high fluctuations from one node to another can occur in numerical method. Therefore, this process often breaks down due to severe mesh distortion and needs a reasonable type of mesh to be employed at this zone.

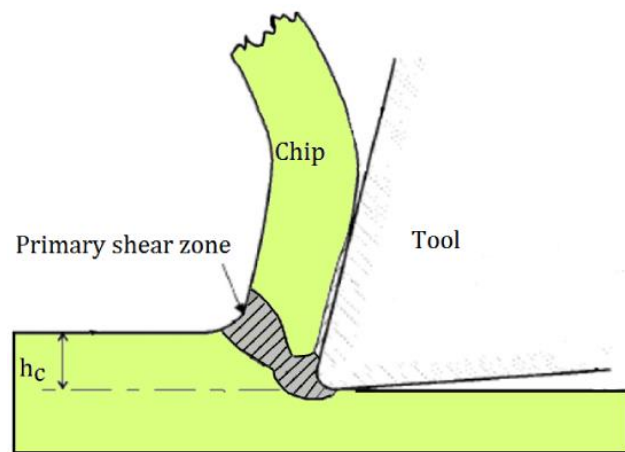


Figure 3:2 Primary shear zone after (Kiliçaslan, 2009)

In order to apply any type of FEM for complex problem like machining process, an understanding of various types of mesh, density (coarse or fine), re-meshing, adaptive mesh techniques, etc., is required. Typical finite-element formulations used for the metal-cutting process are Lagrangian, Eulerian, Arbitrary Lagrangian-

Eulerian (ALE), Molecular dynamic (MD) method and smooth particle hydrodynamic (SPH) techniques. The advantages, disadvantages and application of each scheme in machining simulation are discussed in the next section.

3.3.1 Lagrangian and updated Lagrangian schemes

In the Lagrangian and also the updated lagrangian formulations the mesh is fixed with regard to the geometry and moves with the deformed material. Re-meshing is the only difference between these two methods. The meaning of re-meshing is replacing the old mesh with a new one during the solution procedure to achieve mesh-distortion reduction (Shet and Deng, 2000). The Lagrangian description is shown in Figure 3:3 (Simulia, 2011). The numerical grid distorts with the material interface, and deformation happens by increments in time. After each increment, the reference domain is updated based on material coordinates. This behaviour gives a good representation of material interface and being computationally efficient is known as an advantage of this scheme (Shih, 1995). It presents no convective effects so that the boundary conditions at free surfaces, moving boundaries and material interfaces are automatically imposed. These FE methods are ideal for history-dependent material.

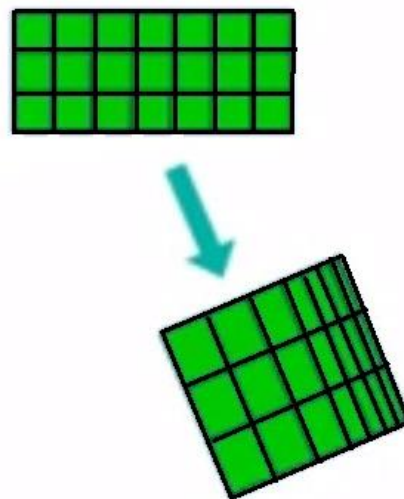


Figure 3:3 Mesh motion in Lagrangian formulation (Simulia, 2011)

Many researchers have implemented the lagrangian formulation for two-dimensional-metal-cutting cases, e.g. Balihodzic, (2002) and a few for three dimensional case (Ng *et al.*, 2002, Guo and Liu, 2002). The updated-lagrangian formulation was first used for modelling of machining by Klamecki (1973). The model of Shaw (1995) for metal cutting based on the updated-lagrangian formulation was included the effect of elasticity, visco-plasticity, temperature, strain rate and frictional force. In a recent publication with the updated-Lagrangian formulation, Özel (2006) simulated a continuous chip-formation process in orthogonal cutting by presenting different friction models based on the experimental data.

When deformation is very large like in machining applications, a distorted mesh and element entanglement caused to limit the application of lagrangian description. For this kind of modelling, the grid quickly distorts the mesh in the primary-shear zone. To overcome the mesh-distortion problem in a typical orthogonal metal-cutting simulation with the lagrangian schemes, a layer of elements is modelled as a cutting layer. This layer will be deleted after reaching the distortion level expected. It is usually a very small layer and is considered that the amount of volume lost is negligible for the solution. The loss of data in the thin layer is a great disadvantage of this scheme which cannot be implemented in single-crystal machining.

3.3.2 Eulerian scheme

The Euler process, in which the material grid remains fixed in space and the material flows through the grid, has the advantage of being able to deal with large deformations like machining processes without the use of small-time steps (Simulia, 2011) (see Figure 3:4). However, it completely avoids element distortions which include some limitations in dealing with material interfaces. Machining simulations with the Eulerian schemes have difficulties in tracking the deformation history of the material modelled.

This process is computationally less efficient than lagrangian one. The representation of material interfaces is not as good as lagrangian schemes and the implementation of complex constitutive models can be rather difficult. Another drawback is that the geometry must be well defined in a steady-state representation. In the case of orthogonal machining, the steady-state chip geometry and chip-tool contact length should be defined at the initial stage of modelling (Haglund, 2005). Having such a limitation has caused the use of eulerian technique for single crystal machining impossible.

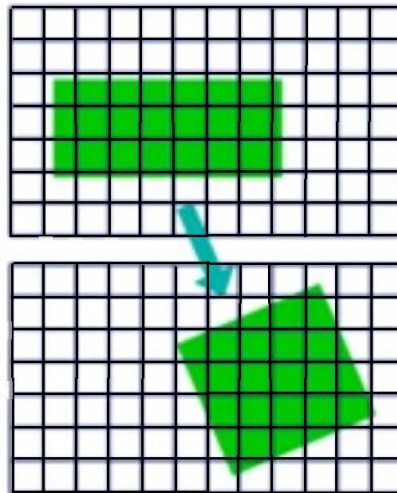


Figure 3:4 Mesh motion in eulerian formulation (Simulia, 2011).

3.3.3 Arbitrary Lagrangian-Eulerian scheme (ALE)

To combine the advantages of lagrangian and eulerian descriptions and to avoid their disadvantages, researchers have developed the Arbitrary Lagrangian-Eulerian (ALE) formulation recently. Figure 3:5 shows the comparison of lagrangian, eulerian and ALE mesh motion in one dimension (Donea *et al.*, 2004). The ALE method is a popular tool for simulation of continuum-mechanics problems with large shear deformations like phenomena happen in the machining process and metal forming (Khoei *et al.*, 2008). In the ALE description, the nodes of the computational mesh may be moved along the continuum in a normal

lagrangian fashion, or be held fixed in the eulerian manner, or be moved in some arbitrarily specified way to give a continuous reasoning capability.

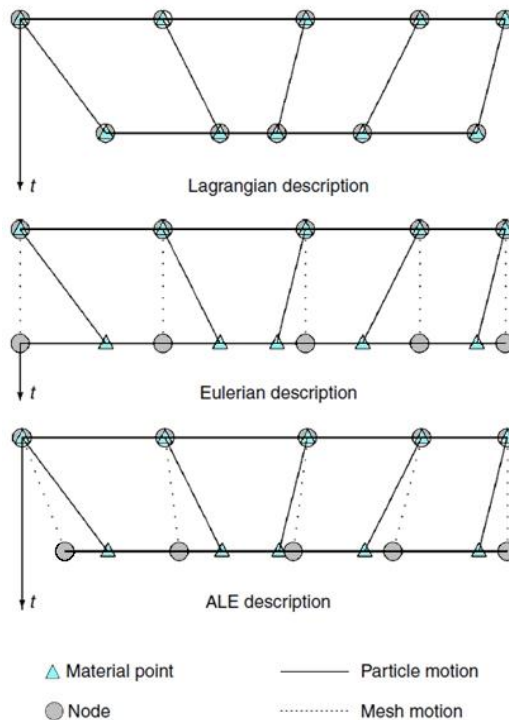


Figure 3:5 One-dimensional example of lagrangian, eulerian and ALE mesh (Donea *et al.*, 2004)

The Figure 3:6 compares the mesh motion for lagrangian formulation and ALE in two dimension (Simulia, 2011). Due to freedom in computational mesh moving in ALE description, greater distortions of continuum can be handled that would be possible with a purely lagrangian method, with more resolution than that afforded by a purely eulerian approach (Donea *et al.*, 2004).

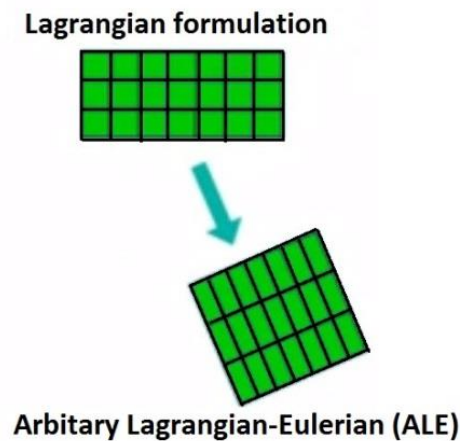


Figure 3:6 Mesh motion in Arbitrary Lagrangian-Eulerian formulation (Simulia, 2011)

The successful results of the ALE description motivated many researchers. The majority of them have followed the ALE technique to build new ideas into their research. In terms of cutting simulation, Childs (2006) developed a model by using the ALE formulation. His model does not suffer from the element distortion at the tool tip. Movahhedy *et al.* (2000) has shown that the ALE formulation offers the most efficient modelling approach compared to lagrangian and eulerian methods for cutting process. The main disadvantage of ALE is to design an efficient and effective mesh-moving algorithm to maintain mesh regularity for three-dimensional complicated material domain (Ma *et al.*, 2009). Having such limitation results in mesh distortion happens for three dimensional single-crystal machining model which has a more complicated deformation mechanism than shearing of material around the tool tip.

3.3.4 Molecular dynamic (MD) method

Severe mesh distortion occurs due to large strains and strain rates generated in the material ahead of the tool tip in a machining model. Application of atomic models for simulation of the metal-cutting process is important since these models are capable of modelling large deformation observed in the machining process without facing numerical problems caused by element distortion. Furthermore, in

the application of these techniques in metal cutting, there is no need to determine physical or geometrical element-separation criteria to model chip formation other than material deformation behaviour defined by material properties.

MD simulation is a very powerful modelling toolbox to follow and understand structure and dynamics. It enables studies in extreme detail literally at scales where motion of individual atoms can be tracked. The molecular-dynamics simulation method is based on the Newton's second law, $F = ma$, where F is the force exerted on the particle, m is its mass and a is its acceleration (Inamura and Takezawa, 1991). It is possible to determine the acceleration of each atom in the system by having knowledge of the force on each atom. Integration of the equations of motion, then yields a trajectory that describes positions, velocities and accelerations of the particles as they vary with time. From this trajectory, the average values of properties can be determined. The method is deterministic; once the positions and velocities of each atom are known, the state of the system can be predicted at any time in the future or the past.

Research involving MD simulations of cutting process can be traced back to early 1990s. Inamura *et al.* (1992) reported the cutting simulations based on MD with a couple of potential functions. This computational study showed that MD is a potential-modelling tool for the micro cutting process. They reported that the rate of energy dissipation in plastic deformation at this scale was larger than in macro cutting since concentrated shear zone did not appear, contrary to what is normally observed in macro scale machining.

Ikawa *et al.* (1991) developed a MD model for understanding of the chip-removal mechanism of copper in nano scale with depths of cut down to 1 nm. The model was able to continuously generate dislocations in front of the tool tip and produced chip morphology showing a very good agreement with experimental results. In another work, Shimada and Ikawa (1992) investigated the effect of crystallographic orientation on plastic deformation of single-crystal copper by using MD simulations. They studied the effect of tool geometry using several ratios

of the tool edge radius to the depth of cut with various parameters such as cutting force, specific energy, and subsurface damage.

Komanduri *et al.* (1998) and their further research (Komanduri *et al.*, 2001), investigated the effect of crystal orientation and direction of cutting for single-crystal aluminum and silicon. They also applied MD simulations to analysis of exit failure and burr formation in ductile and brittle materials with a f.c.c. structure. The sample of their simulation was shown in Figure 3:7. They successfully simulated burr formation in a ductile material and crack propagation in a brittle work material.

Many researchers have turned to MD for single crystal machining studies since the MD simulation technique is based on interatomic force calculations, it can accommodate micro-material characteristics as well as dislocations, crack propagation, specific cutting energy, etc. There is a major obstacle in MD modelling caused to ignore this method in the present thesis. Since MD calculates the interatomic forces between all atoms within a certain boundary, it requires a significant computational power in order to model the cutting process, e.g. the computational time for 6881 workpiece atoms by use of digital workstation with a clock speed of 600 MHz take a few weeks (Komanduri et al., 2001). Hence, many MD models were applied in two-dimensional cases with a very small model size, such as nano meter or angstrom level, with unrealistically high cutting speed. These limitations led to using smooth particle hydrodynamic for the single-crystal machining model.

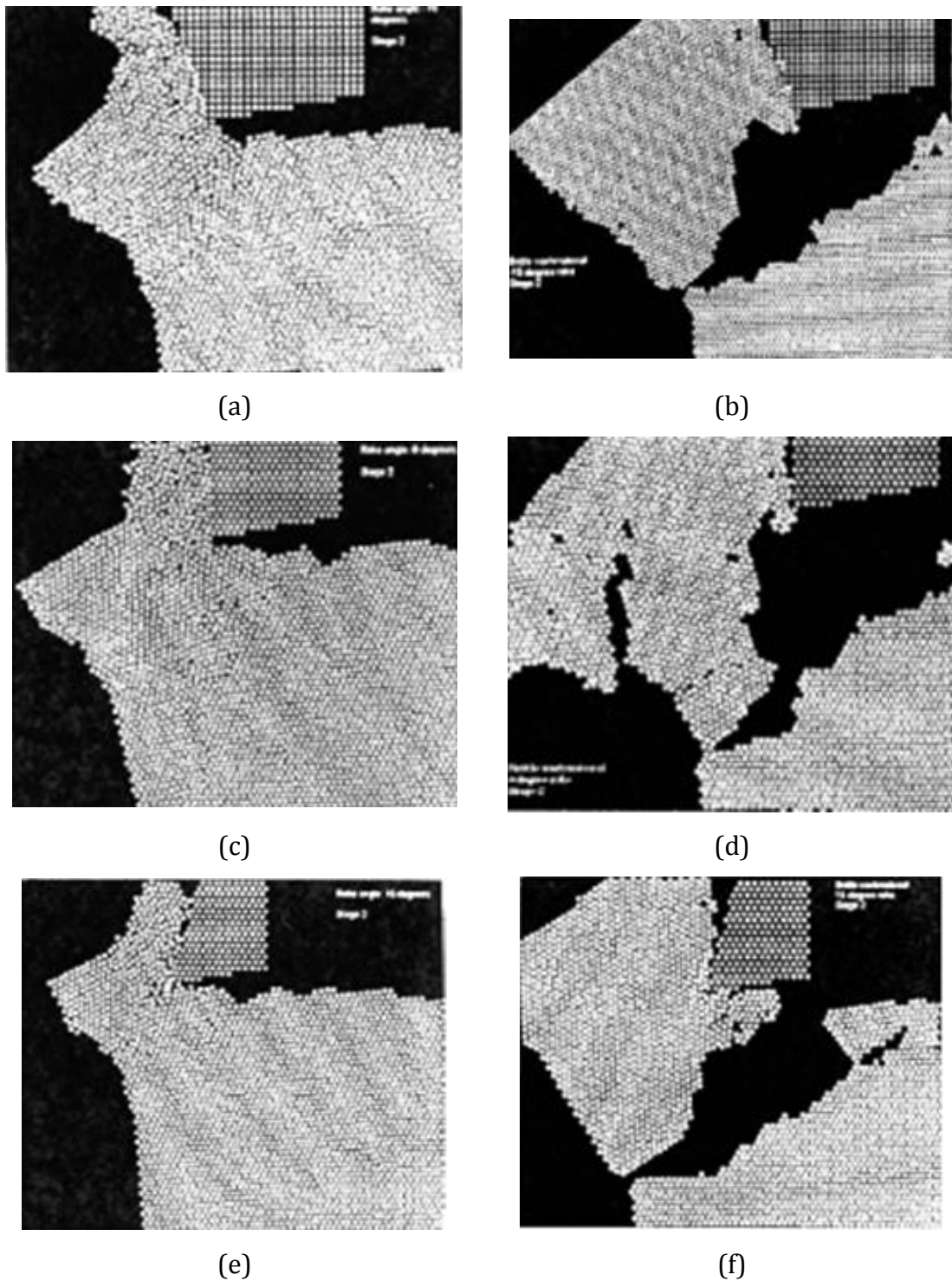


Figure 3:7 MD simulations of nano metric cutting performed on ductile (a-c-e) and brittle (b-d-f) work material with various tool rake angles: (a) and (b) -15° , (c) and (d) 0° , (e) and (f) 15° (Komanduri *et al.*, 2001)

3.3.5 Smooth particle hydrodynamics (SPH) method

SPH is a part of a larger family of mesh-free methods. These methods eliminate some or all of the traditional mesh-based views of computational domain and rely on a particle instead (Bagci, 2011). SPH which is the lagrangian based method provides an alternative methodology to eliminate most of the common difficulties in simulation of cutting processes. SPH employs the particles move relatively to each other in a disordered way during the deformation. The particle-based nature of the method also gives it the ability to track history-dependent properties such as surface formation and plastic strain in a node by node basis even during very large deformations (Limido *et al.*, 2007).

This technique used to simulate N-body problems, including complex fluid flows and large-strain solid-mechanics problems. It is a very important tool for resolving various physical problems related to continuum mechanics, crash simulations, ductile and brittle fracture in solids (Cossins, 2010). Hydro-dynamical parameter such as pressure, velocity, density, etc. can be tracked at finite particles, which move with material deformation. For a given spatial distribution of these points/particles, spatial derivatives may then be evaluated without the need for an underlying grid, which is one of the major advantages of SPH.

SPH uses a kernel approximation based on randomly distributed interpolation points, with no assumptions about which points are neighbours to calculate spatial derivatives. The calculation cycle is similar to that for a lagrange zone, except for the steps, where the kernel approximation is used. SPH requires the particles to be sorted at least once every cycle in order to locate current neighbouring particles (Agertz *et al.*, 2007). In SPH a set of discrete points used to construct trial functions, so that the difficulties associated with mesh distortion can be avoided or alleviated.

This method is the topic of recent research in many areas of computational science like cutting processes. In terms of machining simulation, the chip separation can be easily managed with this formulation. Application of SPH performed well in machining of some recent research (Limido *et al.*, 2011, Akarca *et al.*, 2008, Islam

et al., 2012). Generally, in the machining simulation the material failure modelling needs to be used. Calculating separation through material failure modelling is a difficult issue in cutting simulation. One method used in finite element analysis to address this issue is to evaluate the damage on each element and to remove those that suffer damage beyond some specified level. The obvious deficiency of this approach is that a significant part of the material volume is removed from the calculation unless an excessively fine mesh is used. Another method used to attempt to capture material failure requires postulating the locus of material separation. A special layer of contact elements is placed on that path, and separation is permitted as some break-away load is achieved. The deficiencies of this approach are not only that it lacks theoretical rigour, but that implementation of it in the context of large-deformation plasticity is a logistical ordeal.

SPH method underestimates the chip curve. The particles move relatively to each other in a disordered way during the deformation. This can be considered as a particle rearranging without topological restriction, thus high strains are easily handled, no remeshing is needed and natural chip/workpiece separation happens. The relative motion of the particles creates the opening. The new free surfaces are given by the particles's positions. The particle located on a free edge only interacts with existing particles located on one side of the free edge. Thus, the workpiece matter flows naturally around the tool tip. If the metal cutting should be simulated using the FEM method, it is necessary to set up parameters allowing the material failure and separation caused by the cutting tool. Material properties and state variables are approximated by their values on SPH particles. This avoids the severe problems of mesh tangling and distortion, which usually occur in Lagrangian analyses involving large deformation.

The SPH methods suffer from a higher computational cost, and the accuracy of it is still dependent on the node regularities to some extent. Some strategies have been developed for alleviation of the above-mentioned problems, but improvement of efficiency of mesh-free methods are still a challenge. Coupling of this technique with lagrange schemes suggested as a robust modelling tool for single crystal modelling is presented in this thesis.

3.4 Coupling SPH and finite-element technique

Different numerical solvers have certain advantages and limitations. It is critical that an analyst understands which solvers or combination of solvers is best suited to modelling the problem of interest. For example, lagrangian schemes are often difficult (or even impossible) to simulate some problems such as large-deformation problems, but mesh-free methods have recently become attractive alternatives for problems in computational mechanics, as they do not require a mesh to discrete the problem. In contrast, modelling with a SPH technique needs more computational memory. Although the weight of the computational cost is lightened due to the development of computer technologies, improvement of computational efficiency is still a key factor for simulations of many practical problems, like single crystal machining process.

The ability to model different regimes of physical events using different numerical techniques has a number of advantages. Instead of applying the same general solver to all domains of a problem, a solver optimized for a particular region of material behaviour can be used. The variation domains in the problem are then coupled together in space and time to provide an efficient and accurate solution. Coupling mesh-free method with FEM is a possible solution to modelling of single crystal machining. This approach allows for the use of accurate and efficient finite elements in the lower distortion regions, and for the use of SPH particles in the high distortion regions.

Although the SPH approach can be applied to severe distortions, it is generally not as good as standard finite elements for structural response applications. The important advantage of SPH, however, it's lagrangian formulation allows it to be linked straightforwardly to the standard finite-element lagrangian formulations. Therefore, it is possible to computations of both severe distortions and structural responses to be performed with a single lagrangian code.

It proposes that the most efficient and accurate methodology for the simulation of single crystal machining, is to couple two numerical techniques -FEM and SPH- together in one simulation. The region of the tool penetration at experiences large

distortions should be represented using mesh-free SPH scheme. Regions of the workpiece that experience only low levels of stresses and deformations can be represented using the FEM approach, because it is efficient. A zoning transition is used to reduce the number of cells at the distances furthest from penetration. To achieve this configuration for the modelling of the machining process, methodologies for coupling of FE and SPH processors should be addressed.

Different contact algorithms have been used with SPH to combine with the FE method, and the only purpose of these algorithms was to allow SPH nodes to interact with FE mesh. The earliest attempts were reported by Attaway *et al.* (1994). They determined the subset of particles interact with the boundary of the finite elements. To search which of a given set of particles lie inside a box, an ordered list of points was constructed by sorting the points on each rectangular coordinate value. The search algorithm was economical in its use of memory. Johnson *et al.* (1996) developed a rigid coupling method with SPH particles fixed with FE nodes in the interface zone. They suggested that contact between SPH particles and finite elements should be calculated according to the application field.

Fernández *et al.* (2005) developed a transition region between SPH and FE domains, and a shape function of the coupled SPH and FE interpolations was used. In the transition region, where both particles and nodes have an influence, a coupled interpolation was used. This coupled approximation formulated for a Galerkin formulation with accurate integration. However, this technique can easily be used for particle integration, in many applications first-order reproducibility is required only for the approximation of the derivatives.

For the contact between SPH particles and finite elements, Johnson *et al.* (2002) developed a master-slave method to describe the contact between SPH particles and finite elements. The interface node simply accepts forces from both the neighbouring nodes and the attached finite elements. The particle node was assumed to be in contact with the finite-element grid when the equations of motion cause the edge of the circular particle to cross over the master surface. If

the surface was frictionless, the nodal equations of motion are unaffected in the direction parallel to the master surface, and this allows for sliding between the particle and the finite element grid. Frictional effects can also be included and they were constrained to the direction parallel to the master surface. All of their results shown a slightly increased pressure designated as a reflection from the interface. This probably occurs because there was not a uniform node spacing and mass distribution at the interface.

Recently, a rather complete and rigorous study of FE–SPH coupling was performed by Sauer (2000) who also used a master–slave algorithm to validate his adaptive FE–SPH algorithm. The principle of the coupling was the extension of the SPH summation on all parts of FE discretization inside the approximation radius. This can be easily done by replacing particle sums by numerical evaluation integrals over the elements. His implementation of the contact algorithm is based on a gap function. This means that the particle, moving towards the master segment, experiences a contact force before it penetrates the master segment. The gap size is chosen as one-half of a distance between particles. This was the principal advantage of the coupling approximation over other approaches for FE/SPH presented in the past.

An important effort has been dedicated to the coupling of SPH and FEM in Zhang *et al.*, 2011. Their algorithm for the SPH particles far from the coupling interface, pure SPH approximation was used, and pure FEM approximation was implemented in the finite elements domain. For the SPH particles near the coupling interface, the FE nodes in the support domain were added to the SPH summation in the mode of background particles. Therefore, the smoothing function, W , was not truncated by the boundary. At the start of each time step, all the relative data to SPH approximation were transferred from FE nodes to the corresponding background particles. The background particles only increase the particle number in the support domain, and they were only passively searched by other SPH particles. At the end of each time step, the relative data were transferred from SPH particles to the corresponding FE nodes in the interface, updating the FE data. However, in this FE/SPH coupling algorithm, contact occurs once the distance

between two bodies was smaller than two times the smoothing length, which is not in agreement with reality and could be caused the error.

The algorithm used in this thesis is based on a master–slave algorithm to account for the contact interaction of FE elements and SPH particles. Discrete particles of SPH domain and solid elements of FE were coupled with a tie contact algorithm that allowed stable computations without distortion. In this algorithm, the nodes on both domains have same displacement and no relative movement between them. This is convenient since from experience using the SPH method, the size (smoothing length) of the SPH particle should be approximately half that of a Lagrange cell to give the same accuracy. Therefore, particles behave as spheres with radii equal to the radius of a sphere inscribed in the small cube associated with the particle volume. In the contact domain the same number of elements is implemented. Since PC3D elements do not have faces or edges, an element-based surface cannot be defined using these elements. Consequently, the constraint node-based surfaces are defined to particles.

3.5 Summary

The overview of modelling used for simulation of large-deformation-material responses in the machining process presented in this chapter. The common methods used in modelling of metal cutting included;

- 1) Lagrangian formulation, where the grid is attached to the material, requires updating of the mesh (remeshing algorithm) or the use of a chip-separation criterion to separate the chip from the workpiece.
- 2) Eulerian formulation, where the grid is not attached to the material and fixed in the space, is computationally efficient but cannot predict chip geometry.
- 3) Arbitrary-Lagrangian-Eulerian (ALE) formulation, where the grid is not attached to the material and move to avoid distortion, is destroyed due to a moving mesh algorithm for single crystal machining.

- 4) Molecular dynamic (MD) method, were based on interatomic force calculations, is used for two dimensional model in the range of nano size.
- 5) Smooth particle hydrodynamics (SPH) method, where is lagrangian based model, is effective in modelling but need much computational time.

Coupling FE/SPH formulation is found to be a very useful technique in solving high-deformation in single crystal machining. It can include material flow directly in front of the tool tip in its formulation without extensive element distortion. It also runs in sensible time. By using the FE/SPH technique, two sets of meshing systems are set in one model with SPH formulation implemented in a tool penetration area which experiences large distortions while FE is set in rest of the model. Combining these two methods result in an ideal analysis of the metal-cutting process.

Computational framework of crystal plasticity

4 Computational framework of crystal plasticity

4.1 Crystal plasticity theory

In general, deformation of a single crystal in tension or compression slip occurs in response to shear stress applied along a slip plane and in a slip direction. The shear component of applied stress is called *shear stress* and depends on the level of applied stress and orientation of the slip system. Slip begins when this value reaches a threshold value known as critical resolved shear stress (CRSS). The Schmid's law defines a relationship between the levels of shear stress, and applied stress as well as the orientation of the slip system. In Figure 4:1, shear stress is resolved on a slip system due to applied force \mathbf{F} , defined by a slip direction, \mathbf{s} , and a slip plane normal, \mathbf{n} . Note that angles λ and φ are, in general, not in the same plane.

To define shear stress in the slip plane for the given axial force and angle of the slip plane, the following equation can be written:

$$\tau = \sigma \cos\phi \cos\lambda. \quad 4-1$$

Here, σ is the applied stress, λ is the angle between the slip direction and the applied force, and ϕ is the angle between the normal to the slip plane and the applied force. The product $\cos\phi \cos\lambda$ is called *Schmid factor* (Blochwitz *et al.*, 1996). In a given crystal, there may be many available slip systems. During plastic deformation of a single-crystal, each existing slip system has a potential to be activated. As the tensile load is increased, the resolved shear stress on each system increases until eventually τ_c is reached on set of slip systems. These slip systems are generally oriented most favourably and have the largest Schmid factor, known as *primary slip system*.

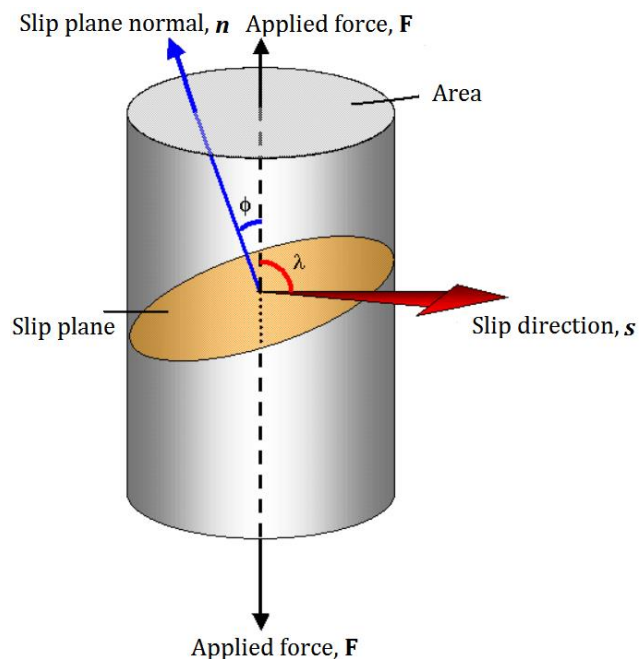


Figure 4:1 Relation between shear stress and normal stress

A single crystal undergoes constant orientation change when subjected to load. For example, under tension, slip planes orient themselves parallel to the loading direction; this is illustrated in Figure 4:2. Tensile loading of the crystal causes the planes to rotate towards the loading direction and leading to initiation of slip on a different system (Haasen *et al.*, 1974).

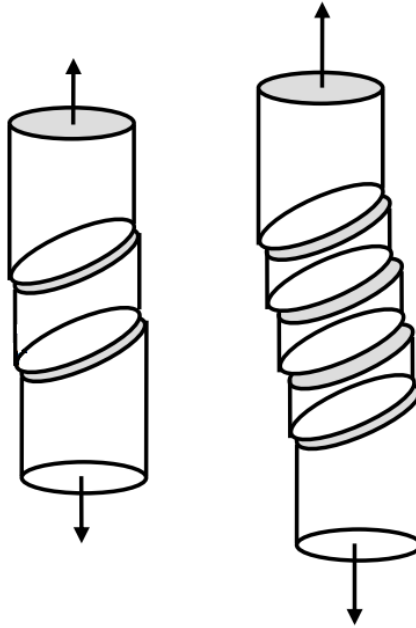


Figure 4:2 Lattice rotation in tension

For a slip system to be activated, the projected stress must exceed the CRSS for that slip system. The CRSS required for activation of a slip system is not a constant value, but evolves with an increase in deformation, known as *strain-* or *work-hardening*. Strain-hardening is caused basically by the interaction of dislocations in different slip systems. An extended discussion regarding this phenomenon is presented in Section 4.1.2.

The foundations of single-crystal plasticity theory may be traced to the papers by many researchers, including Bragg *et al.* (1938), Taylor (1934), Hill (1966) and Levy *et al.* (1971). The behaviour, accuracy, and efficiency of some of the above-mentioned crystal-plasticity models were examined by several investigators like Ling *et al.* (2005) and Kuchnicki *et al.* (2006). The crystal-plasticity framework has proven to be a robust approach for predicting the mechanical behaviour of, and

texture evolution in f.c.c. materials. This theory takes into account the initial texture of the material and its evolution with deformation for complex problem like machining (Lee and Yang 1993).

Two building blocks upon which all crystal-plasticity theoretical models are built are kinematics and the hardening rule. Numerical implementation is also important while not being a part of the crystal-plasticity theory. In the following section, these subjects are investigated.

4.1.1 Kinematics

A deformation gradient tensor \mathbf{F} at the continuum level can be used to express physical deformation processes in a material body mathematically. The mathematical definition of \mathbf{F} at a material point depends only on its initial and current positions. The total deformation gradient can be decomposed into multiple components in many different ways, with each component representing a different deformation mechanism or a micro-structural feature. One possibility is multiplicative decomposition into an elastic deformation gradient \mathbf{F}^e and plastic deformation gradient \mathbf{F}^p , according to (Nemat-Nasser, 1979):

$$\mathbf{F} = \mathbf{F}^e \mathbf{F}^p. \quad 4-2$$

Complexity of physical deformation processes makes it possible to have a large number of terms in the deformation-gradient decomposition in order to account for each deformation mechanism. However, each additional component adds a layer of complexity to the model, making it uncommon for a model to have more than three components. In fact, most models are based on two-term decompositions. \mathbf{F}^e and \mathbf{F}^p are commonly used to model an elastic-plastic behaviour of metals. Here, the inelastic deformation \mathbf{F}^p of a single crystal is assumed to arise deformation only from crystalline slip through the crystalline structure via dislocation motion. \mathbf{F}^e accounts for stretching and rotation of the lattice. Thus, \mathbf{F}^e does not necessarily represent a reversible elastic deformation and are assumed to be unaffected by slip.

While both the additive and multiplicative decompositions are mathematically acceptable, there is criticism in the literature regarding the physics of additive elastic/plastic decomposition. The additive deformation model decouples the elastic and plastic deformation processes, resulting in two-step deformation as shown in Figure 4:3 while in reality elastic and plastic deformation occurs simultaneously (Ellyin, 1996).

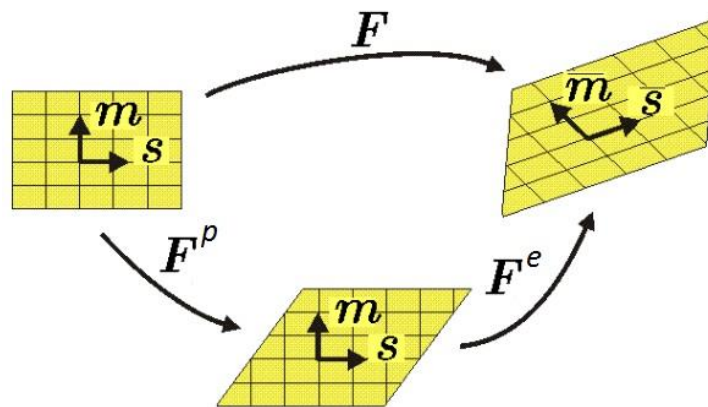


Figure 4:3 Elsto-plastic deformation in crystal structure (Ellyin, 1996)

In the constitutive model, the stress rate $\dot{\sigma}$ is related to the elastic strain rate L^e as:

$$\dot{\sigma} = C L^e = C(L - L^P), \quad 4-3$$

where C is the fourth-order elasticity tensor and L and L^P are the total strain rate and plastic strain rate, respectively. The f.c.c. metals have cubic symmetry. The elastic moduli for such crystals is particularly simple, and can be parameterized by only 3 material constants, C_{11} , C_{12} , C_{44} . The following matrix expresses the elastic moduli of such materials:

$$C = \begin{bmatrix} C_{11} & C_{12} & C_{12} & 0 & 0 & 0 \\ C_{12} & C_{11} & C_{12} & 0 & 0 & 0 \\ C_{12} & C_{12} & C_{11} & 0 & 0 & 0 \\ 0 & 0 & 0 & C_{44} & 0 & 0 \\ 0 & 0 & 0 & 0 & C_{44} & 0 \\ 0 & 0 & 0 & 0 & 0 & C_{44} \end{bmatrix} \quad 4-4$$

The plastic deformation, \mathbf{F}^P , represents material's plastic shear and corresponds to the amount of deformation that remains in the crystal after the load has been removed. According to the flow rule:

$$\dot{\mathbf{F}}^P = \mathbf{L}^P \mathbf{F}^P, \quad 4-5$$

with \mathbf{L}^P being the plastic strain rate. It is assumed to consist of the sum of the shear strain rate, $\dot{\gamma}^\alpha$, over the number of considered slip system. Therefore,

$$\mathbf{L}^P = \sum_{\alpha=1}^N \mu_{ij}^\alpha \dot{\gamma}^\alpha, \quad 4-6$$

with μ_{ij}^α as the Schmid tensor that equals to a dyadic product of the slip direction s_i^α and the slip plane normal n_j^α and N is the total number of available slip systems.

$$\mu_{ij}^\alpha = s_i^\alpha \times n_j^\alpha \quad 4-7$$

In Eq. 4-6 the superscript α specifies the slip system.

The shear strain rate $\dot{\gamma}^\alpha$ of the α th slip system in a rate- dependent crystalline solid is determined by visco-plastic flow rule as,

$$\dot{\gamma}^\alpha = \dot{\gamma}_0 f \left(\frac{\tau^\alpha}{g^\alpha} \right)^n, \quad 4-8$$

where the constant $\dot{\gamma}_0$ is the reference strain rate on the slip system α , g^α is the variable, which describes the current strength of that slip system α at the current time, τ^α is the shear stress on slip system α and the non-dimensional function f is a general function describing the dependence of strain rate on the stress.

The simplest flow rule is the visco-plastic power-law expression proposed by Hutchinson, (1976) to describe $\dot{\gamma}^\alpha$ in the following form:

$$\dot{\gamma}^\alpha = \dot{\gamma}_0 \operatorname{sgn}(\tau^\alpha) \left| \frac{\tau^\alpha}{g^\alpha} \right|^n, \quad 4-9$$

where n is the material's rate sensitivity and $\text{sgn}(\ast)$ is the signum function of \ast . It is worth mentioning that the reference strain-rate $\dot{\gamma}_0$ in this equation is taken as 10^{-4} 1/s. The strength of material g^α , is obtained based on hardening rule which is presented in the next section.

4.1.2 Hardening rule

Higher deformation of crystals requires more work to be done on it. Several attempts have been made to explain why plastic deformation increases the strength of metals, and as a result, various work-hardening models have been proposed that are applicable to f.c.c. as well as other materials. These explanations are principally divided into three types. The first type is based on the observed fact that, when a single crystal failed under load, small parts of it are rotated and having an orientation different from the main body of the crystal. It is supposed that the perfect crystal can slip under the action of a very small stress, but that the parts of the crystal rotated relative to its main part act as locking keys and prevents the slipping of the surrounding crystal, enabling the whole system to withstand a much greater load than the perfect crystal can support (Weng, 1979).

The second type of explanation is based on the fact that real crystals contain surfaces of misfit. These surfaces are supposed to hold up slipping to an increasing extent as the amount of distortion increases (Taylor, 1934). The third type of explanation is the opposite of the first two. A perfect crystal is supposed to be capable of withstanding a very large stress. The observed weakness of metal crystals is attributed to concentrations of stress due to internal surfaces of misfits or dislocations, and the increasing strength with increasing plastic strain is attributed to an increase in the number of dislocations or faults (Taylor, 1934). As the number of such faults increases the ratio of maximum stress in a region of stress concentration to mean stress in the material would be expected to increase.

The theory of dislocations gives a scientific explanation to many mechanical phenomena and even quantifies some mechanical properties. The motion of dislocations produces plastic deformation. It starts by application of the external

stress higher than a certain level. This build-up gives a rise to a phenomenon known as *work hardening* (Atkins, 2003). As dislocations pile up along a slip system, a greater stress must be applied in order to activate it; that is, CRSS of the slip system.

Strain-hardening of each slip system is characterized by the evolution of strengths through the incremental relation:

$$g^{(\alpha)} = \sum_{\beta} h_{\alpha\beta} \dot{\gamma}^{(\beta)}, \quad 4-10$$

where $\dot{\gamma}^{(\beta)}$ is the shear strain rate and $h_{\alpha\beta}$ is the slip-hardening moduli with diagonal terms related to self-hardening ($h_{\alpha\alpha}$) and non-diagonal terms $h_{\alpha\beta}$ ($\alpha \neq \beta$) related to latent hardening. Increase of its own strength $g^{(\alpha)}$ by shearing on the α th system is known as self-hardening. *Latent hardening* refers to the influence of the active slip system on hardening of the inactive slip systems and is an important concept in crystal plasticity to control the shape of the single crystal yield surface. Self-hardening can be measured using single-slip tests while for calculation of latent hardening the material deformed in single slip, then re-loading the specimen to activate a second slip system. It is often quantified as latent hardening ratio $q^{\alpha,\beta} = \frac{g^{(\alpha)}}{g^{(\beta)}}$.

Details of the hardening behavior of single crystals are very complex, and at present there is no consensus on the best way to measure or characterize hardening. Different hardening models used in crystal-plasticity are presented in Table 4-1.

Table 4-1 Hardening models

Hardening model	Description	Observation
(Taylor, 1938)	Isotropic hardening	No information about latent hardening
(Havner and	Latent hardening is	Predicts strong latent hardening

Shalaby, 1978)	incorporated.	
(Peirce <i>et al.</i> , 1982)	A modified model of latent hardening is suggested.	More in accord with experimental results, but Bauschinger effect is neglected
(Wu <i>et al.</i> , 1991)	Three-stage hardening of crystalline materials is described.	An explicit expression of slip interactions between slip systems
(Hutchinson, 1976)	An equal hardening rate for all slip systems	

In the present study the hardening model by Peirce *et al.*, (1982) is used to represent the hardening behaviour of each slip system described by the following equations:

$$g^\alpha = g^\alpha|_{t=0} + \Delta g^\alpha;$$

$$\Delta g^\alpha = \sum_{\beta=1}^N h_{\alpha\beta} \Delta \gamma^\beta, \text{ CRSS} = g^\alpha|_{t=0}. \quad 4-11$$

The hardening moduli $h_{\alpha\beta}$ in Eq. 4-11 are evaluated using the hardening model proposed by Peirce *et al.* (1982) as follows:

$$h_{\alpha\alpha} = h_0 \operatorname{sech}^2 \left| \frac{h_0 \gamma}{\tau_s - \tau_0} \right|, \quad 4-12$$

$$h_{\alpha\beta} = q h_{\alpha\alpha} (\alpha \neq \beta),$$

where h_0 is the initial hardening parameter, q is the latent hardening ratio and assumed to be 1, τ_0 is the yield stress equivalent to the initial value of current strength of the slip systems $g^\alpha|_{t=0}$, τ_s is the break-through stress, where large plastic flow initiates and γ corresponds to cumulative shear-strain on all slip systems and is described by

$$\gamma = \sum_{\alpha} \int_0^t |\dot{\gamma}^\alpha| dt, \quad 4-13$$

To describe plastic deformation in terms of crystallographic slip, three successive steps must be accomplished: (i) determination of active slip systems, (ii) determination of the increments of shear stress on the active slip systems and (iii) an update of the state of the material after a time step Δt . In the following section numerical implementation followed by complete algorithm of the crystal-plasticity theory are discussed.

4.2 Numerical implementation

There are a variety of approaches for merging finite-element formulations and crystal-plasticity models. One possibility is to embed a crystal-plasticity theory within a finite-element formulation as a constitutive theory. A theory developed to compute plastic deformation within a single crystal is called the *crystal plasticity finite element method* (CPFEM). The CPFEM uses the basic principles of mechanics to represent a transition from the microscopic scale to the macroscopic scale (Roters *et al.*, 2010). It is a useful tool for detailed simulation studies of texture evolution under realistic mechanical boundary conditions and under consideration of texture update.

The SPH technique allows the resolution of many problems that are generally difficult with regular mesh methods. This method is selected for the solution of crystal plasticity theory in the high distorted area in the single crystal machining model. An extended theory of SPH is highly presented in the next section.

4.2.1 SPH technique - theory and formulation

SPH formulation started with kernel approximation. To illustrate this, consider a continuum represented by a set of interacting particles, as shown in Figure 4:4. each particle i interacts with all other particles j that are within a given distance (usually assumed to be $2h$) from it. The distance h is called the *smoothing length*. The interaction is weighted by the function W which is called the *smoothing* (or *kernel*) function (Limido *et al.*, 2007).

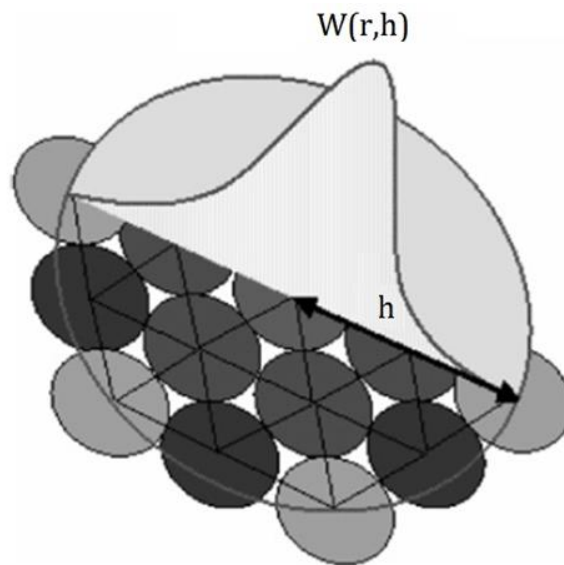


Figure 4:4 Geometry of neighbouring particle and weighing factor (Limido *et al.*, 2007)

The SPH theory presented here is taken from Cossins (2010). Relations between evaluation point x , distance between two particles r , and supporting radius h , are shown in Figure 4:5.

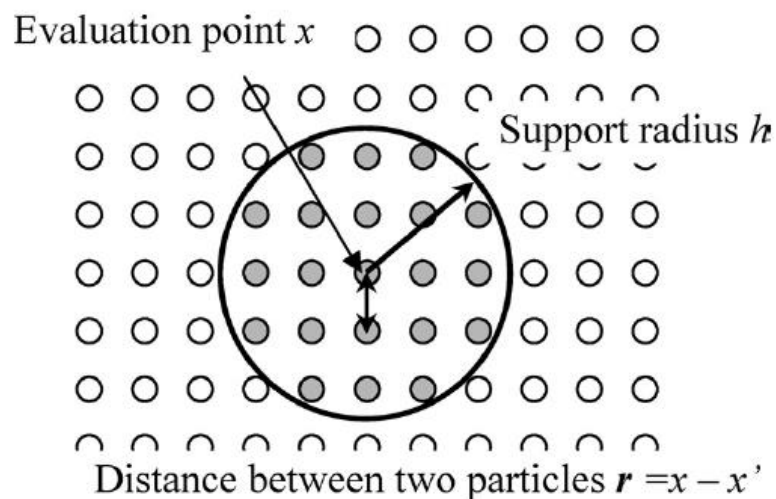


Figure 4:5 Relations between parameters x , h and r in SPH model

The concept of integral representation of a function $f(x)$ used in the SPH method starts from the following equation:

$$f(x) = \int_{\Omega} f(x')\delta(x - x')dx'. \quad 4-14$$

Following identity where $f(x')$ is the scalar function of the three-dimensional position vector x , Ω is the volume of the integral that contains x and $\delta(x - x')$ is the Dirac delta function that is commonly seen as

$$\delta(x - x') = \begin{cases} 1 & x = x' \\ 0 & x \neq x' \end{cases} \quad 4-15$$

In Eq. 4-14, the delta function supports, only a “point” and is zero for all $x \neq x'$ while the integration yields the value of the function where $x = x'$. In numerical integration, the delta function is impossible to use in its current form due to the fact that its value goes to infinity, so it must be approximated with another function. If the Delta function kernel $\delta(x - x')$ is replaced by a smoothing function $W(x - x', h)$, the integral representation of $f(x)$ is given by

$$f(x) = \int_{\Omega} f(x')W(x - x', h) dx' \quad 4-16$$

where $W(x - x', h)$ is called the *smoothing kernel function* or *smoothing kernel* or simply *kernel*. To express W , let us introduce an auxiliary function of δ . The most commonly function used by the SPH community is the cubic B-spline, which has some good properties of regularity (Michel *et al.*, 2006).

$$W(x - x', h) = \frac{1}{h^D} \delta\left(\frac{|x - x'|}{h}\right) \quad 4-17$$

with

$$\delta(y) = T \times \begin{cases} 1 - \frac{3}{2}y^2 + \frac{3}{4}y^3 & \text{for } y \leq 1 \\ \frac{1}{4}(2-y)^3 & \text{for } 1 < y \leq 2 \\ 0 & \text{for } y > 2 \end{cases} \quad 4-18$$

T is the constant of normalization that depends on the space dimension D . The T value is expressed as

$$T = \begin{cases} \frac{2}{3} & \text{for 1 - dimention;} \\ \frac{10}{7\pi} & \text{for 2 - dimentions;} \\ \frac{1}{\pi} & \text{for 3 - dimentions.} \end{cases} \quad 4-19$$

In the smoothing function, h is the smoothing length defining the influence area of the smoothing W . Note that as long as W is not the Diract function, the integral representation in Eq. 4-14 can only be an approximation. This is the origination of kernel approximation and is represented by an angle bracket $\langle \rangle$ and written as

$$\langle f(x) \rangle = \int_{\Omega} f(x')W(x - x', h) dx' \quad 4-20$$

Like in a finite-element method which continuous models are approximated using information at a finite number of discrete locations, in SPH method consists of a collection of particles each having physical degrees of freedom used for definition of physical quantity. Dividing the structure into discrete particles is called discretization. Interpolation within particles in SPH method is achieved through Kernel function. When we move from two particles the physical quantity is quite different. One way to try and fix this is by making the transition smoother. That's one of the main goals of kernel smoothers. Local average for any quantity can be obtained by the appropriate smoothing function.

One of the central issues of the mesh-free methods is how to effectively construct a proper shape function using only nodes scattered in an arbitrary manner without using a predefined mesh that provides the connectivity of the nodes. These particles have a spatial distance known as the smoothing length, over which their properties are smoothed by a kernel function. This means that the physical quantity of any particle can be obtained by summing the relevant properties of all the particles which lie within the range of the kernel. By fulfilling condition, solving system which is determining the displacement vector with consideration to the boundary conditions and remembering that the problem in concern is changing in time, SPH method solved the problem.

The smoothing function W should satisfy a number of conditions. The first one is the normalization condition that states

$$\int_{\Omega} W(x - x', h) dx' = 1. \quad 4-21$$

This condition is also termed as a *unitary condition* since the integration of the smoothing function produces the unity.

The second condition is the Delta-function property that is observed when the smoothing length approaches zero:

$$\lim_{h \rightarrow 0} W(x - x', h) = \delta(x - x'). \quad 4-22$$

The third condition is the compact condition:

$$W(x - x', h) = 0 \quad 4-23$$

When

$$|x - x'| > kh, \quad 4-24$$

where k is a constant related to the smoothing function for a point at x , and defines the effective (non-zero) area of the smoothing function called the *support domain* of that point. Using this compact condition, integration over the entire problem domain is localized as integration over the support domain of the smoothing function.

The Taylor expansion of $f(x)$ that is differentiable at the point $x=a$ is used in the following equation:

$$f(x) = f(a) + \hat{f}(a)(x - a) + \dots + \frac{f^n(a)(x - a)^n}{n!} \quad 4-25$$

So by considering the one-dimensional case of Eq. 4-20, the Taylor expansion of the function $f(x)$ around the point \hat{x} is

$$\begin{aligned} \langle f(x) \rangle &= \int_{\Omega} [f(x') + \hat{f}(x')(x - x') + O(|x - x'|^2)]W(x - x', h)dx' \\ &= f(x') \int_{\Omega} W(x - x', h)dx' \\ &+ \hat{f}(x') \int_{\Omega} (x - x')W(x - x', h)dx' \\ &+ \int_{\Omega} O(|x - x'|^2)W(x - x', h)dx' = f(x') \int_{\Omega} W(x - x', h)dx' \\ &+ \hat{f}(x') \int_{\Omega} (x - x')W(x - x', h)dx' + O(h^2), \end{aligned} \quad 4-26$$

where $O(h^2)$ is the limiting behaviour of the Taylor-expanded function that is truncated at its linear term. In Eq.4-26, the integral in the first term is equal to 1 by the normalization condition (Eq. 4-21). The integrand in the second term is a product of an odd and an even function (assuming W is chosen to be even); therefore, the integration over the domain will reduce to zero, and the function approximation reduces to

$$\langle f(x') \rangle = f(x') + O(h^2).$$

4-27

As can be seen from the above equation, the integral approximation using the smoothing function, in replacement of the delta function, has second-order accuracy. Hence, it can be seen that, integral representation or kernel representation of the SPH method is of second-order accuracy under a condition that the smoothing function is an even function. If the smoothing function is not even then the kernel approximation is not necessarily of second-order accuracy (Liu, 2004).

Many researchers have conducted investigations on the numerical aspects in accuracy, stability, convergence and efficiency of the SPH method (Liu, 2004). In the next section, the incremental formulation and complete algorithm of the crystal-plasticity theory discussed. The material nonlinearity in crystal-plasticity requires an incremental approach for integration of equilibrium equations.

4.2.2 Incremental formulation of crystal-plasticity

Many different integration schemes have been applied to, and developed for, crystal plasticity. These schemes fall broadly into two main categories: explicit integration or implicit integration. A plastic shear-strain increment in the slip system α for the time increment Δt is defined as

$$\Delta \gamma^{(\alpha)} = \Delta t [(1 - \theta_1) \dot{\gamma}_t^{(\alpha)} + \theta_1 \dot{\gamma}_{t+\Delta t}^{(\alpha)}],$$

4-28

where θ_1 is the integration constant, ranging from 0 to 1 depending on the implicit or explicit method. $\theta_1 = 0$ corresponds to the explicit method while θ_1 varies between 0 and 1 for the implicit method. The explicit approach was used in the present thesis since the implicit one has convergence difficulties and needs enormous computational time. Of course, very fine time increments are needed in

an explicit analysis of a model having rather small element sizes, which, in turn, leads to longer computational times. In this approach, the quantities associated with the material state at time t , are used to update the quantities associated with the state at $t + \Delta t$. The well-known explicit methods are a simple/forward Euler method and Runge-Kutta method (Sun *et al.*, 2000). The downside is that this approach is numerically unstable when Δt is larger than some critical time step Δt_{cr} . Δt_{cr} is linked to stiffness by means of a non-linear equations and is usually small. A small time step must be taken to prevent oscillation in the predicted stress state in most crystal-plasticity models.

The Taylor expansion of the slipping rate gives

$$\dot{\gamma}_{t+\Delta t}^{(\alpha)} = \dot{\gamma}_t^{(\alpha)} + \frac{\partial \dot{\gamma}^{(\alpha)}}{\partial \tau^{(\alpha)}} \Delta \tau^{(\alpha)} + \frac{\partial \dot{\gamma}^{(\alpha)}}{\partial g^{(\alpha)}} \Delta g^{(\alpha)}, \quad 4-29$$

where $\Delta \tau^{(\alpha)}$ and $\Delta g^{(\alpha)}$ are the increments of resolved shear stress and current strength in the slip system α within the time increment Δt , respectively. The following incremental relation is obtained by combining Eq. 4-28 and Eq.4-29.

$$\Delta \gamma^{(\alpha)} = \Delta t \left[\dot{\gamma}_t^{(\alpha)} + \theta_1 \frac{\partial \dot{\gamma}^{(\alpha)}}{\partial \tau^{(\alpha)}} \Delta \tau^{(\alpha)} + \theta_1 \frac{\partial \dot{\gamma}^{(\alpha)}}{\partial g^{(\alpha)}} \Delta g^{(\alpha)} \right], \quad 4-30$$

The user-defined material subroutine (VUMAT), initially developed by Huang (1991), modified by Kysar (1997) and further developed by Demiral (2012) was used to implement the single-crystal plasticity formulation. This code is further developed by the author with regard to implement two coordinate systems, crystal and reference coordinate system. The three vectors of crystal coordinate system need to be calculated based on the desired cutting plane normal. In the subroutine, the lattice deformation and rotation are fully characterized by reciprocal vectors coinciding with slip directions and normal to slip planes in the deformed configuration.

The τ_s , τ_0 , h_0 , C_{11} , C_{22} , C_{44} , n were the input material parameters. Taking into account the lack of appropriate experimental data for latent hardening, the

interaction matrix $h_{\alpha\beta}$ was set to one for diagonal terms, so only self-hardening and no cross hardening was considered. Knowing the strain, grain orientation, current strength of a slip system and resolved shear stress at time t , the Schmid tensor and the shear-strain-rate are calculated using Eq. 4-7 and Eq. 4-9 and after that the new increments for slipping rate was calculated with Eq. 4-29. More details of VUMAT subroutine in the form of flow charts is shown in Figure 4:6.

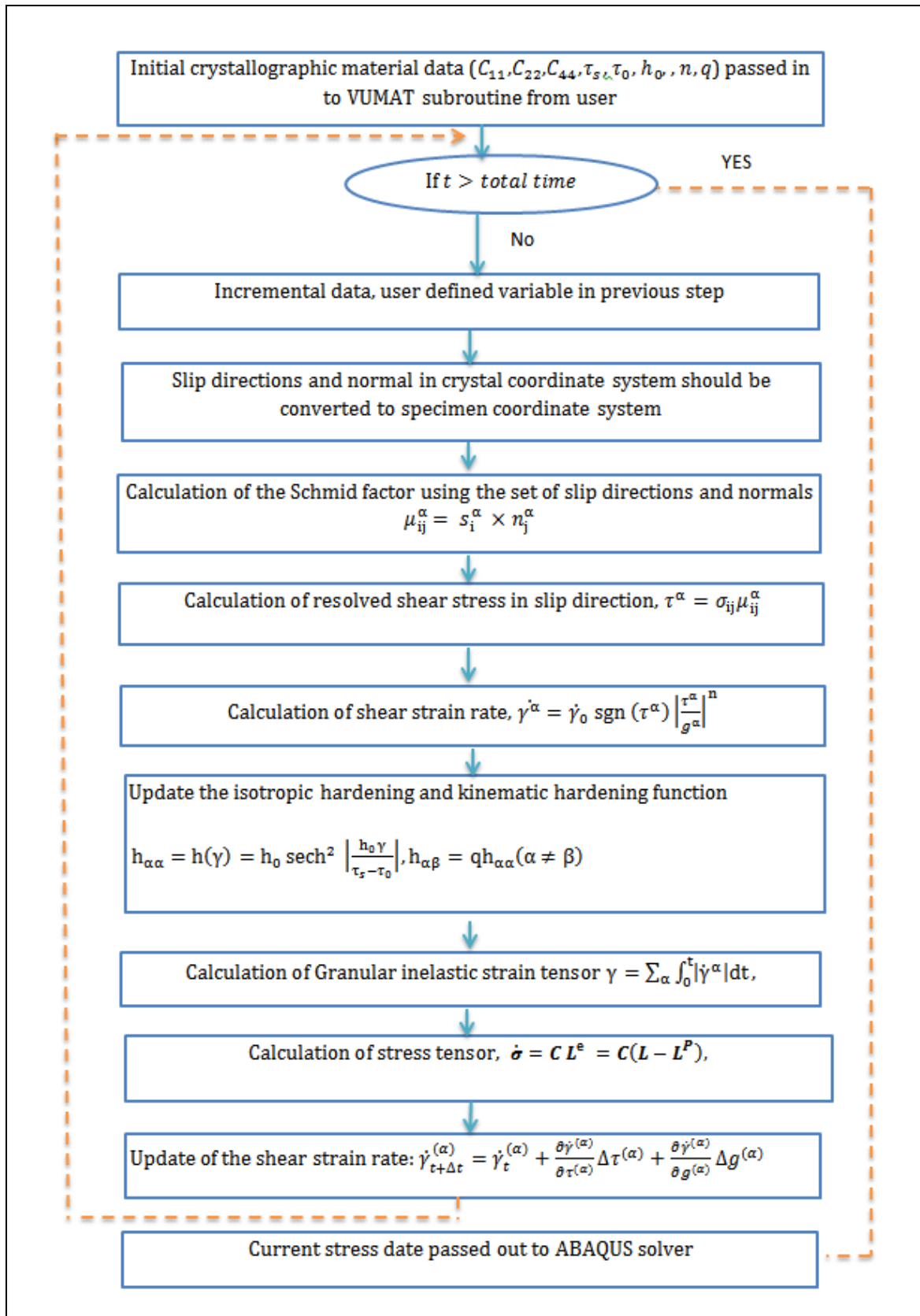


Figure 4:6 flow chart of VUMAT for crystal plasticity

4.3 Summary

The main aim of this chapter was to present a crystal plasticity theory in a continuum framework. The plastic deformation is assumed to be due to resolved shear stress on a slip system. The Schmid factor is assumed here to be the driving direction for activation of a slip system. Implementation of VUMAT subroutine makes it possible to use ABAQUS/Explicit with SPH technique for stress analyses of single crystals. The SPH theory uses particles based on quadratic formulation for moving them to represent a material. By applying a sampling kernel, the code can estimate the characteristic property at any position based on the locations of nearby particles in 3D space. This method is very straightforward, versatile, and robust for solving the distortion problem in the single crystal machining model.

The crystal plasticity theory has been implemented numerically within the VUMAT subroutine. In this subroutine, h_0 is the initial hardening modulus, τ_0 is the initial yield stress, τ_s the resolved shear stress, g^α the current strength of slip system α , $h_{\alpha\alpha}$, the self-hardening modulus and $h_{\alpha\beta}$ the interaction strength between slip system α and β . These parameters are defined as the material parameters and are imported as input of the subroutine. The SPH technique is used for the approach to incorporate the yield function and the method to obtain the true solution and the way to update state variables in the presented thesis.

Modelling of orthogonal single-crystal machining

5 Modelling of orthogonal single crystal machining

5.1 Introduction

The metal-cutting processes include different types of machining such as grinding, turning, milling, etc. Although the actual machines and tools for cutting processes look very different, the basic mechanism of chip formation can be understood with the use of a simple process called *orthogonal cutting*. This process is illustrated schematically in Figure 5:1. In the model of orthogonal cutting, the tool edge is kept normal to both cutting and feed directions. This process removes metal to create high quality and precise surface shapes.

This deceptively simple orthogonal single crystal machining process actually involves complex phenomena crossing the fields of elasticity and plasticity. The aim of this chapter is to derive a computational model that accurately predicts the deformations, stresses, plastic strain distribution in the f.c.c. crystalline structure

workpiece material. The simplest shape of orthogonal machining widely used in this chapter to understand the deformation mechanisms of the machining process.

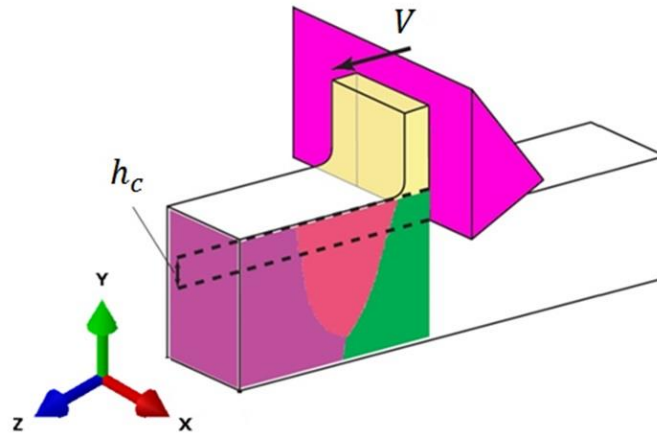


Figure 5:1 Configuration of orthogonal micro-machining after (Kota, 2011)

The computational single crystal machining model consumes much less effort and cost than an experimental test procedure. The trend of predicted results leads to new designs of the process and tool machines. In the next section the model configuration is discussed in more details.

5.2 Model descriptions and features

In this chapter, a hybrid modelling approach for tool penetration into single crystal of copper based on a combination of SPH and continuum finite element is presented. The philosophy of this approach is to use a mesh-free technique in the process zone, which undergoes high- strain and- strain-rate deformations with material separation, with a continuum FE formulation being used for the rest of a workpiece volume to reduce computational cost. To gain a physical comprehension of the cutting process at the micro level, a material model based on crystal plasticity described in Section 4.1 is implemented.

An explicit dynamics procedure is used in this work to build a numerical model and analyse the machining process. This is an effective method to solve a wide

range of nonlinear problems in material science and solid mechanics (Halloran *et al.*, 2005). Explicit algorithms use a large number of very small time increments to attain a solution. The computational cost of each increment is very small as opposed to implicit algorithms where increment sizes may be comparatively large. The explicit method proved to be the preferable choice in the case of loading conditions and contact condition involved in machining process (Harewood and Mchugh, 2007).

The software package for numerical simulations was ABAQUS/Explicit (v.6.11). This is a commercial software package, which utilizes descriptive commands in an input file to drive the FE solution procedure. The input file contains a description of the problem in terms of geometry, nodal and elemental definitions, and details of interfacial contact. In addition, the package also offers post-processing capabilities that simplifies the analysis of results. A user-defined subroutine (VUMAT) described in Section 4.2 was used for implementation of material properties. The following sections describe the FE model development in ABAQUS/Explicit (v.6.11).

5.2.1 Geometry configuration

A 3D workpiece with dimensions of $500\ \mu\text{m} \times 500\ \mu\text{m} \times 50\ \mu\text{m}$ was selected as an appropriate representation of a crystalline continuum. The workpiece was divided into two regions; one representing the SPH domain ($200\ \mu\text{m} \times 200\ \mu\text{m} \times 50\ \mu\text{m}$) and the remaining part being a continuum FE domain (Figure 5:2). By using this technique the unnecessary large dimension geometry that might be computationally very expensive modelled with the continuum FE domain. Therefore, the computational time will reduce significantly.

To have a match between the experimental study and simulation results, the same cutting tool geometry of Zhou and Ngoi (2001) was selected for current model. Generally, to optimize a 3D workpiece dimension for the single crystal machining study needs to have a wide range of knowledge about the material behaviour and

boundary conditions during the process. It has been reported by Lie *et al.* (2005) that the minimum thickness of the workpiece in machining study must be considered the same or bigger than cutting depth to determine the three dimensional mechanical responses of the material during a micro machining process. The geometry workpiece dimensions are selected to represent the single copper grain size.

A tool rake angle was 0° and a clearance angle 5° . Selecting of zero rake angles is based on eliminating of the effect of rake angle in the machining process and smaller clearance angle reduced the friction between the clearance face and workpiece. By this consideration the cutting tool geometry parameters are isolated in the model and the study focuses only on the effects of the plasticity of workpiece materials.

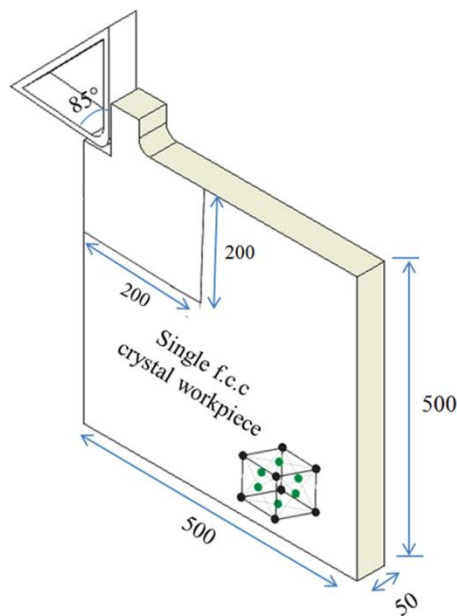


Figure 5:2 Geometry of orthogonal-machining model (dimension in μm)

5.2.2 Orientation setup

The crystallographic orientation refers to a relative position of atomic planes in the volume of a crystal with regard to a fixed reference frame. For this purpose, two

coordinate systems are defined, one linked to the crystal and the other acting as a reference frame. Both coordinate systems are usually defined employing three orthonormal directions. The crystal coordinate system specifies the directions of single crystal compare to reference frame. The choice of directions in crystal frame is quite arbitrary, although it is convention to adapt it to the crystal symmetry. For example, for a f.c.c. crystal structure with orthogonal symmetry the axes $[100]$, $[010]$, $[001]$ are chosen as the crystal's coordinate system. These three orthonormal directions initially serve as the reference system.

To study the influence of the cutting direction and crystallographic orientation on cutting forces, four cutting directions on three crystal orientations were chosen. In this analysis, a planner configuration was used, in which the tool cuts along a particular crystal direction $[hkl]$ on a chosen crystal plane normal $[uvw]$ (Figure 5:3).

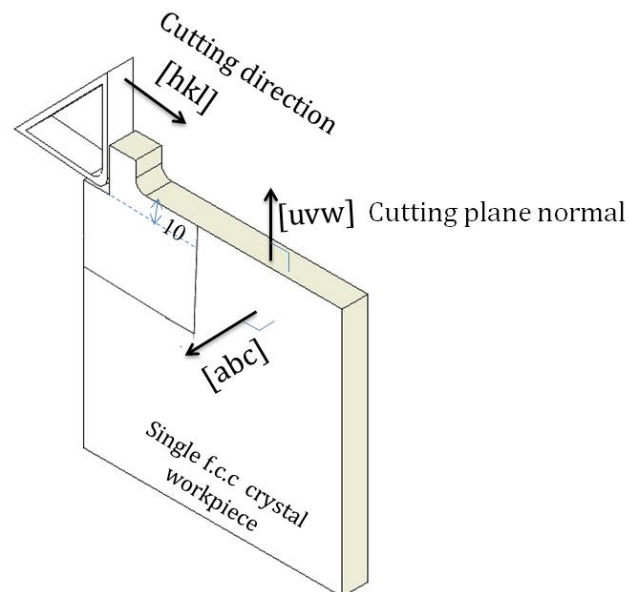


Figure 5:3 Planner configuration setup

For simulations, appropriate crystal orientations were selected so that the cutting operation was carried out on the $[010]$, $[101]$ and $[111]$ cutting planes normal. Four cutting directions were chosen for each cutting plane: 0° , 30° , 60° and 90° . In

order to define the crystal coordinate system vectors for each cutting direction a code in MATLAB software was developed. Actually, by changing the crystal frame compare to reference frame the single crystal are machined in different orientations.

There are some key points for calculation of the cutting directions in a new crystal frame.

- 1- The direction corresponding to the normal cutting plane is always perpendicular to other two directions. The cutting plane normals in these simulation setups are served as [010], [101] and [111].
- 2- The rotation of cutting directions (0°, 30°, 60° and 90°) is always considered in cutting plane. The following equation describes the relation between directions and angle of rotation.

$$\cos \theta = \frac{\mathbf{U} \cdot \mathbf{W}}{|\mathbf{U}| |\mathbf{W}|} \quad 5-1$$

where \mathbf{U} and \mathbf{W} were the cutting direction for chosen cutting plane before and after rotation.

By doing some calculations the corresponding cutting directions and orientations used in the simulations are obtained and listed in Table 5-1. For each simulation setup the [uvw], [abc] and [hkl] vectors were used as input parameters in VUMAT subroutine for definition of crystal orientation and cutting direction.

Table 5-1 Cutting directions (see Figure 5:3)

0°			30°		60°		90°	
[uvw]	[abc]	[hkl]	[abc]	[hkl]	[abc]	[hkl]	[abc]	[hkl]
[010]	[100]	[001]	$[\sqrt{3} \ 0 \ \bar{1}]$	$[1 \ 0 \ \sqrt{3}]$	$[1 \ 0 \ \sqrt{3}]$	$[\sqrt{3} \ 0 \ 1]$	$[00\bar{1}]$	[100]
[101]	$[\bar{1}01]$	[010]	$[\bar{3} \ \sqrt{6} \ 3]$	$[1 \ \sqrt{6} \ \bar{1}]$	$[\sqrt{2} \ 2\sqrt{3} \ \sqrt{2}]$	$[\sqrt{6} \ 2 \ \sqrt{6}]$	[010]	$[10\bar{1}]$
[111]	$[\bar{1} \ 01]$	$[\bar{1} \ 2 \ \bar{1}]$	$[\bar{1} \ \bar{1} \ 2]$	$[\bar{1} \ 1 \ 0]$	$[0 \ \bar{1} \ 1]$	$[\bar{1} \ 2 \ \bar{1}]$	$[\bar{1} \ 2 \ \bar{1}]$	$[10 \ \bar{1}]$

5.2.3 Properties of workpiece material

In the current work the tool is defined as a rigid body and the workpiece material is simulated by employing the crystal-plasticity parameters. In a f.c.c. single crystal of copper, slips may occur on 12 individual slip systems, with the slip planes belonging to type $\{111\}$ and the slip directions to type $\langle 110 \rangle$ (see Section 2.3). The plastic properties of single crystals are strongly sensitive to the material's crystal structure and composition. The representative parameters for a copper single crystal are listed in the Table 5-2 where each slip system assumed to have the same values of plastic parameters (Wang *et al.*, 2004).

Table 5-2 Material parameters of single-crystal copper (Wang *et al.*, 2004)

Elastic parameters	Parameters of slipping rate	Parameters of hardening
$C_{11} = 168$ GPa	$\dot{\gamma}_0 = 0.001$ S ⁻¹	$h_0 = 180$ MPa
$C_{12} = 121.4$ GPa	$n = 20$	$\tau_s = 148$ MPa
$C_{44} = 75.4$ GPa		$\tau_0 = 16$ MPa

Smaller values of n such as 1, 2 or 5 represent a rate deformation sensitive, whereas larger values such as 20, 50, 100 correspond to a rate-insensitive model. By selecting n equal to 1 the shear stress has relation with shear strain which is not right in crystal plasticity theory while selecting of the rate sensitivity parameter equal to infinity was required very long computational times due to convergence problems. This is due to the fact that when the value of τ^α becomes slightly larger than the strength of the slip system g^α as a result of a finite strain increment in FE calculations, $\dot{\gamma}^\alpha$, becomes almost infinite causing termination of the analysis. To avoid this, finer strain increments, and, hence, ultra-fine time increments, should be used, leading to dramatically long computational times. The computational analysis of Wang *et al.*, 2004 selected n equal to 20 and this value corresponds to the deformation rate insensitive material's behaviour of the single-crystal copper.

5.2.4 Mesh technique

In order to save computational time and better efficiency of simulations, the workpiece is divided into four domains in terms of mesh configuration. Schematic of the final workpiece mesh is shown in the Figure 5:4. The SPH domain and the continuum finite-element domain close to the SPH area was meshed finer than its remaining part. The transitional meshes with the same element type (C3D8R) and different shape was used between the fine and coarse domains.

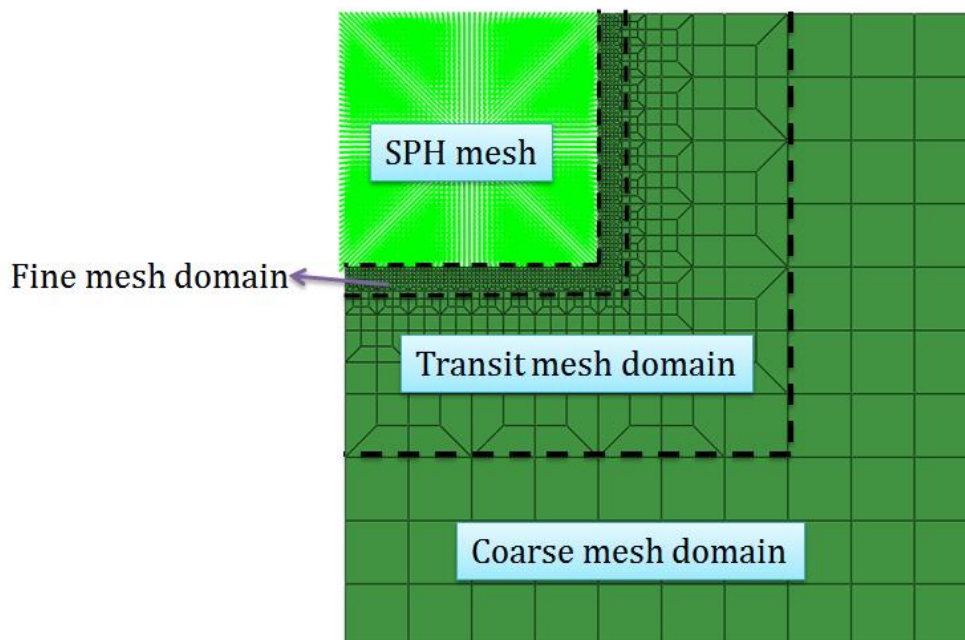


Figure 5:4 Meshing of continuum finite-element workpiece region

The transit mesh shape was not included in the Abaqus/CAE database originally and need to be generated by changing the input file. For this matter, the edit mesh toolset was used to manipulate the elements. In order to create this appropriated mesh shape, four quadrilateral shell elements with reduced integration (S4R) type should be reduced to three elements. In order to this case, two elements and any nodes that would be left unassociated with these two elements were deleted from S4R element (See Figure 5:5). This procedure is continued for the whole mesh in the transit domain.

This domain is used to construct a gradient of mesh refinement. Large element sizes in FE domain are linked to fine element sizes in SPH area. By considering the proper particle size in SPH and coarse mesh domain the element size in transit domain is limited. Sensitivity analysis of workpiece mesh domain is presented in Section 5.2.6.

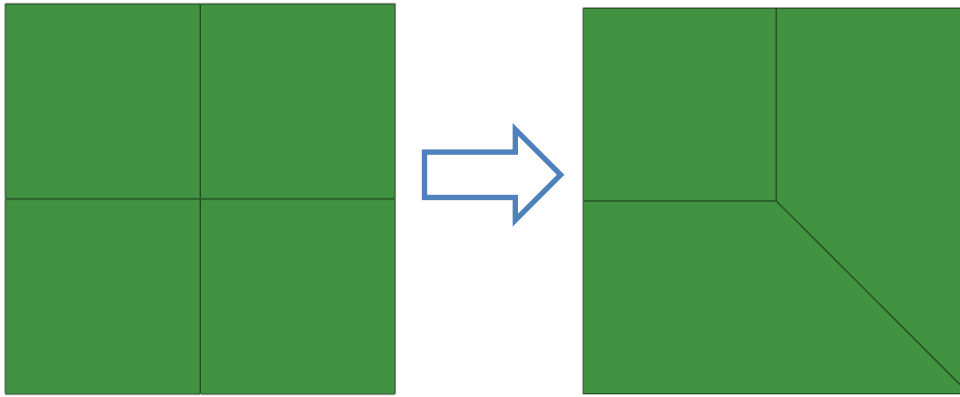


Figure 5:5 Changing the element shape

The technique for creating the proper mesh workpiece used in this thesis is presented in Figure 5:6. By importing the initial-mesh model of workpiece from an output database in the form of an orphan mesh (Figure 5:6. a), the elements of close domains to the SPH area were split in two (Figure 5:6. b). The orphan mesh part contains the output database as a collection of nodes, elements, surfaces, and sets with no associated geometry. In effect, the mesh information has been orphaned from its parent geometry. The same modification of element (see Figure 5:5) would be implemented on the subdivided domain element. The technique was continued to reach the appropriated element size close to SPH domain. After creating a layer of shell elements (Figure 5:6 c), the offset ability was used in normal plane direction to create a unique solid layer (Figure 5:6 d). These elements that compose of the new subdivided shape domains are printed to the new data (.inp) file and consider as workpiece mesh.

The FE domain was meshed with eight-node brick elements with reduced integration (C3D8R) while SPH was implemented via the formulation associated with PC3D elements. The PC3D elements are used to define particles in space that model a particular area of workpiece. These are not hourglass or distortion control forces element. Even though particle elements are defined in simulations using one node per element, the SPH computes contributions for each element based on neighbouring particles that are within a sphere of influence, which radius is a smoothing length. By default, the smoothing length is computed automatically: as deformation progresses, particles move with respect to each other, and the neighbours of a given particle can change.

The SPH computational framework is available in ABAQUS/Explicit (v.6.11) and was readily used in this thesis. The simulated region is represented by particles which carry a certain mass and move with Lagrangian in nature. It uses a cubic spline as the interpolation polynomial, and work based on the classical SPH theory described in Section 4.2.1. The smoothed part is introduced, according to the desire to represent the particles as a continuum, rather than individual points in space. In SPH formulation exists an interpolating function, which is used to estimate the physical quantities and their derivatives at any point in space from disordered particles. The purpose of the kernel is to transform the representation of a particle from a point mass one, to a spatially spread one. More specifically, the kernel is a bell shaped function which has a smooth and continuous first (and usually second) derivative, and is smooth and continuous itself. This function is used to spread the mass (and other properties) of the particles in space, and is normalised so as to conserve the physical quantities in the system. Usually when this kernel is utilised, the contribution is assumed to be zero when the distance from the particle is greater than $2h$. Nevertheless, a lot of particles still have to contribute to the calculation for the sampling to be adequate, which leads to an increased computational effort.

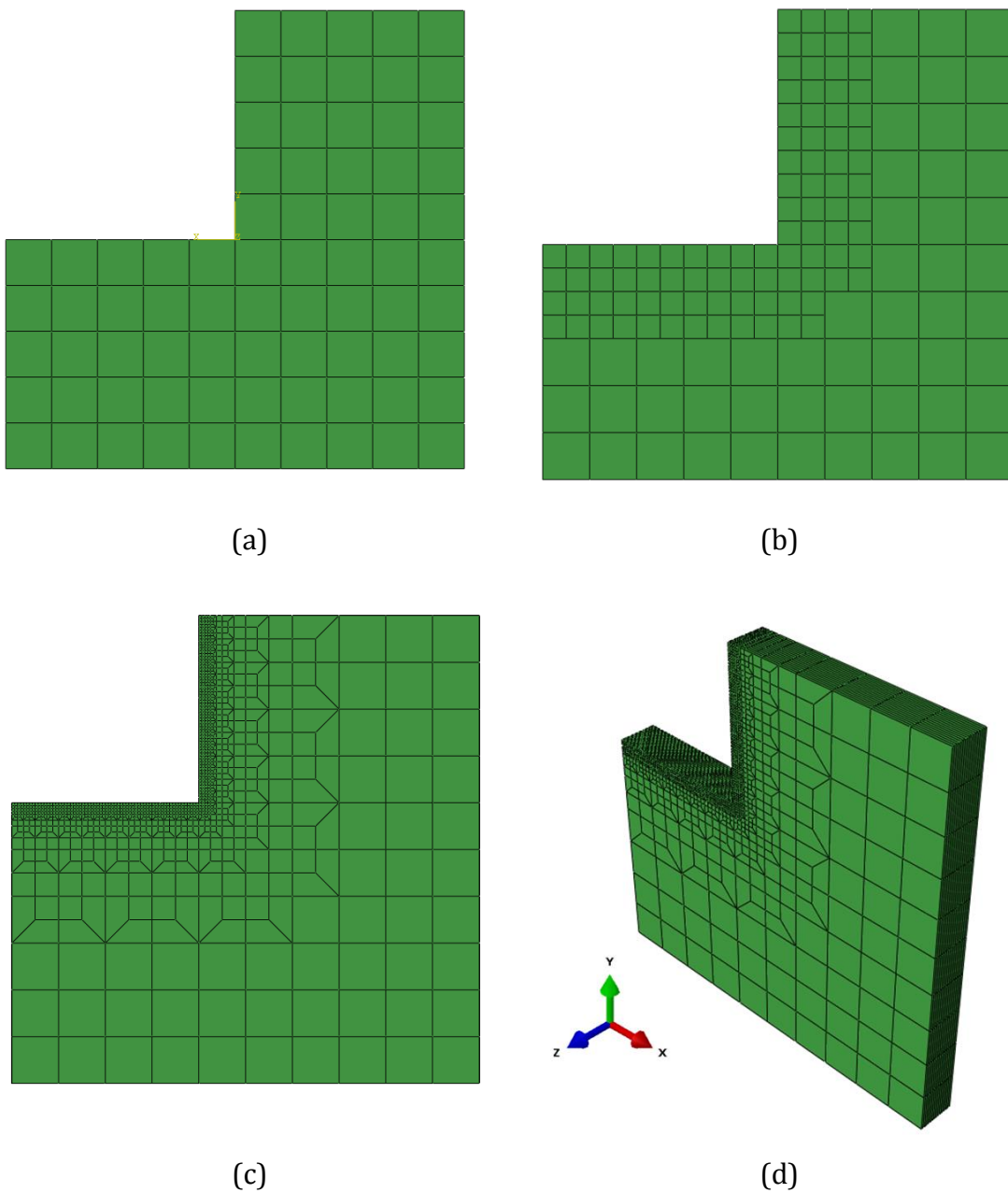


Figure 5:6 Three dimensional mesh of workpiece material

Forces are a function of position and smoothing length. If the system is split up into N discrete bodies, as in SPH, the combined forces act on the matter of the system, and if not in balance cause it to accelerate according to Newton's second law of motion. In SPH, the forces are centred on the particles, such that is the mass of a particle, and the associated acceleration of the particle is along the direction of the combined forces. In this implementation of SPH, there are three intrinsic

properties of the particles that must be followed in time: Position, velocity and the internal energy of the particles. Differential equations for updating the velocity have already been derived from the forces. The change in internal energy per unit mass can be derived from the first law of thermodynamics, applied to an adiabatic process. This essentially says that the change in volume is proportional to the change in internal energy of the particles.

For every increment, the SPH method in ABAQUS/Explicit (v.6.11) recomputed the local connectivity internally and calculates kinematic quantities based on contributions from this cloud of particles centered at the particle of interest. The stresses are then computed in a similar fashion as for reduced integration brick elements, which are in turn used to compute element nodal forces for the particles in the cloud based on the SPH formulation.

By default, ABAQUS/Explicit (v.6.11) computes a smoothing length at the beginning of the analysis so that the average number of particles associated with an element is roughly between 30 and 50 (Simulia, 2011). The smoothing length is kept constant during the analysis. Therefore, the average number of particles per element can either decrease or increase during the analysis depending on whether the average behaviour in the model is expansive or compressive, respectively. By default, the maximum number of allowed particles associated with one element is 140 (Simulia, 2011).

Output available for PC3D element includes all mechanics-related output for continuum elements includes: stress, strain, energies and the values of state, field and user- defined variables. Particles can be visualized in ABAQUS/CAE using a circular shape. In contour plots the values of field output variables are shown as circular patches of colour. This is convenient since from experience using the SPH processor, the characteristic length should be approximately half that of a lagrange cell to give the same accuracy.

The user subroutines in Abaqus allow the program to be customized for particular applications. The crystal plasticity user subroutine VUMAT in Abaqus/Explicit

allows the crystal plasticity formulation as constitutive models to be added to the material definition of workpiece domain. There is no difference to the implication of a user subroutine for FE and SPH domain.

5.2.5 Contact algorithm

From the literature survey in Section 3.4 and experience in dealing with the contact problem in the finite-element method, it was concluded that the glue contact would be a good starting point for contact FE/SPH due to its simplicity and efficiency. Discrete particles and solid elements were coupled with a kinematic-tie contact algorithm that allowed stable computations without distortion. Since PC3D elements do not have faces or edges, an element-based surface cannot be defined using these elements. Consequently, the constraint node-based surfaces are defined to particles. For contact purpose, particles behave as spheres with radii equal to the radius of a sphere inscribed in the small cube associated with the particle volume.

The master–slave algorithm accounts for the contact interaction of cutting tool and SPH particles. The friction force in contact regions between the chip and the tool is difficult to determine and influenced by many factors such as cutting speed, depth of cutting, cutting tool geometry, workpiece anisotropy, etc (Özel, 2006). Frictional behaviour at the chip tool interface is one of the most difficult areas to model due to its uncertainty to predict. The basic Coulomb friction model relates the maximum allowable frictional shear stress across the chip tool interface to the contact pressure between the contacting bodies. The critical shear stress upon which sliding of the surfaces starts, is defined as $\tau = \mu p$, where μ is the coefficient of friction and p is the contact pressure between the surfaces. The typical Coulomb friction law with a constant coefficient of friction $\mu = 0.12$, was used this represents a simplistic model of frictional behaviour along the chip-tool and workpiece- tool interface. This number is the most widely used coefficient for implementation of a constant coefficient of friction in the simulation of metal-

cutting processes (Haglund, 2005). And also the average value of coefficient parameters for micro-machining of single crystalline copper at different orientations in Table 5-6 are equal to 0.12.

Another important parameter in machining simulation is the temperature. Heat has critical influences on the machining process. There are several types of heat source in machining like plastic work deformation; work done by friction and etc. Increased the temperature growth tool wear and then reduce tool life, get a rise to thermal deformation and cause to environmental problems. Due to the complexity of machining mechanics, it's hard to predict the intensity and distribution of the heat sources in an individual machining operation. Especially, because the properties of materials in machining vary with temperature, the mechanical process and the thermal dynamic process are tightly coupled together.

Effect of temperature is not considered in this thesis. Reducing the machining time through lower cutting length, using lower cutting speed and depth of cut in single crystalline copper and aluminium with high thermal conductivity were the main issues to minimize the effect of temperature.

In terms of boundary condition, the right and bottom faces of the workpiece were fixed with regard to linear displacements and rotations. To prevent the tool tip from touching the workpiece in the initialization process of simulations, the initial offset distances equal to 5 μm , namely the distance between the cutting tool tip and workpiece in the X-axis direction, was kept. A 3D model of orthogonal machining is shown in Figure 5:7.

A rectangular region was computed at the beginning as the bounding box, within which the particles would be tracked. This fixed rectangular box was 10% larger than the overall dimensions of the whole model, and it was centered at the geometric center of the model. As the analysis progressed, if a particle was outside the box, it behaved like a free-flying point mass and did not contribute to SPH calculations. The particles returning into the box at a later stage were once again included in the calculations.

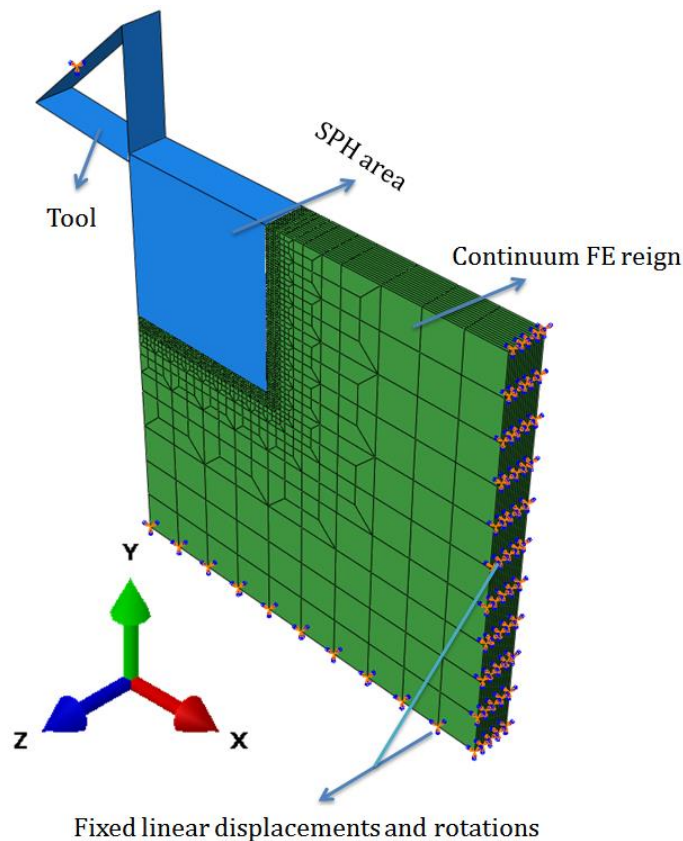


Figure 5:7 A 3D model of orthogonal machining

5.2.6 Sensitivity of model

To find a compromise between the conflicting requirements of accuracy and computational cost, a mesh-sensitivity analysis of the model was undertaken before performing planned simulations. Four selected mesh configurations for the workpiece are shown in Figure 5:8. The evaluation of cutting forces for various numbers and sizes of elements are shown in Figure 5:9. Apparently, no significant variation was observed for cutting either with 71825 or 137781 SPH particles, while the running time difference was about five times. Therefore, the minimum element size of $3.1\ \mu\text{m}$ in the region of tool penetration gives reasonably accurate results. Based on the initial mesh-sensitivity analysis, the optimum number of particles in the SPH domain was determined to be 71825. The mesh-sensitivity analysis was performed in the 0° direction for (010) crystallographic orientation of

copper for frictional conditions, with $\mu = 0.12$. The depth of cut was set at $10 \mu\text{m}$, and the tool moved in the positive x direction with velocity of 1300 mm/s .

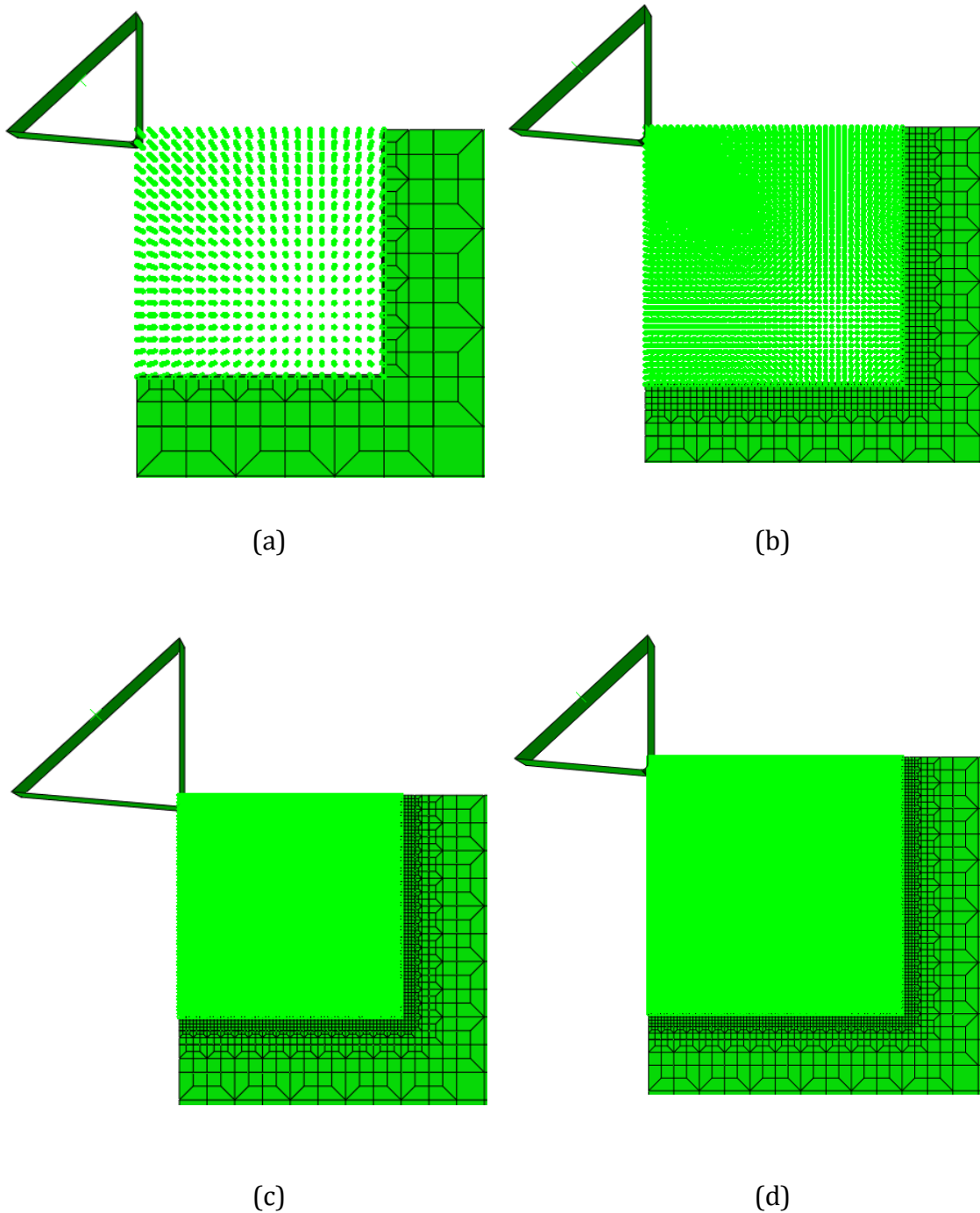


Figure 5:8 Four selected mesh configurations with (a) 2646, (b) 18491, (c) 71825 and (d) 137781 numbers of SPH particle for representative workpiece

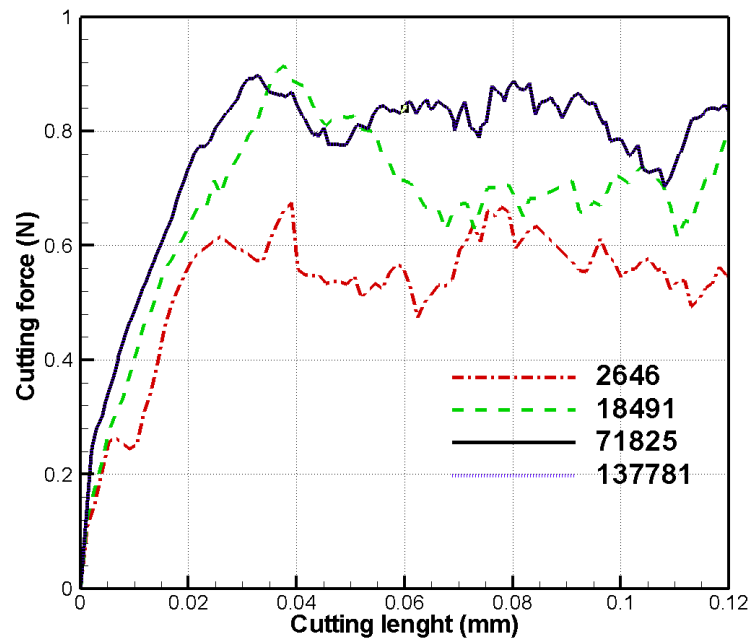


Figure 5:9 Cutting-force evaluations for different numbers of SPH particles

It is well known that spurious ‘ghost’ forces often get introduced when modelling domains of different scales. The ghost force is an unbalanced force and the principal reason for this force is the fact that the SPH method has focussed on approximating the energy and not the forces. In order to avoid the ghost forces, the forces acting on atoms in the transition zones need to be corrected. This is achieved by demanding that right contact algorithm. (Shenoy *et al.*, 1999). In this model, there is no explicit characterisation of length scales, and the underlying physics in both the SPH and FE domains is the same. Still, the validity of the developed model was evaluated by checking of the consistency of the computed fields at the interface of the two domains. Figure 5:10 demonstrates the distribution of Von Mises stresses along the vertical (A-B-C) and horizontal (D-E-F) paths in the entire model at the maximum cutting length. It was observed that at points B and E, representing the boundary between SPH and FE domains, the stress values are continuous, without any abrupt change (only with some small-scale fluctuations) proving that the combination of modelled domains was appropriate. The Coulomb’s law of friction with a co-efficient of friction of $\mu = 0.12$

was used to model the frictional interaction between the tool and the workpiece material. The maximum cutting length of 120 μm was considered in the simulations. The analysis was performed in the 0° direction for (010) crystallographic orientation with depth of cut set at 10 μm , tool velocity of equal to 1300 mm/s. For continuous machining problems, the SPH domain should be extended to span the entire workpiece length to take advantage of the ease of modelling material separation in the form of chips. This configuration setup is implemented in Chapter 7 to study vibration-assisted machining.

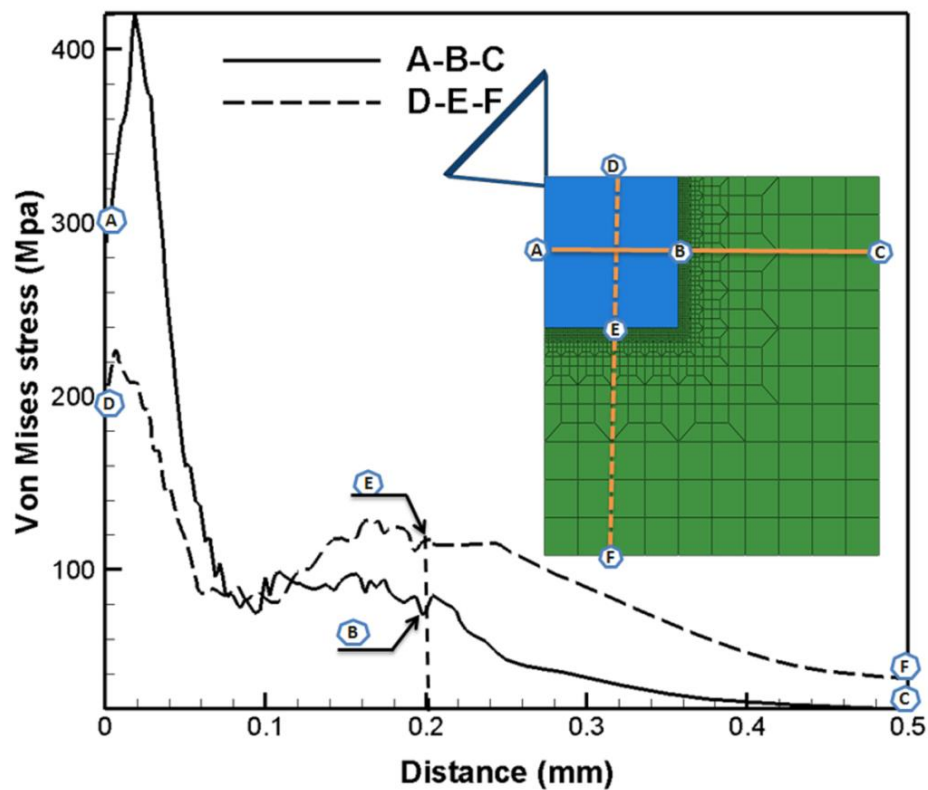


Figure 5:10 Distributions of Von Mises stress along two paths in workpiece material in (010) plane

5.2.7 Model validation

In Table 5-3, the calculated cutting forces normalised to the cutting force in the 0° cutting direction, are compared with experiments of Zhou and Ngoi (2001). It

means that cutting force in 30°, 60° and 90° cutting direction divided by cutting force in 0° cutting direction for experimental study and current model. Implementation of this approach is kept a better comparison of cutting force patterns than the exact value. The results of the modelling efforts are in good agreement with the experimental data. Exact comparisons of cutting forces with experiments in Zhou and Ngoi, (2001), are impossible, since some parameter like coefficient of friction and tool-tip radius used in the experimental study was not defined.

Table 5-3 Cutting forces normalised to cutting direction of 0° in modelling and experimental study of Zhou and Ngoi (2001)

Cutting plane	Cutting direction			
		30°	60°	90°
(101)	Experimental	0.80	0.71	0.65
	Modelling	0.79	0.73	0.64
(111)	Experimental	0.91	0.90	0.93
	Modelling	0.89	0.91	0.94

5.2.8 Shortcoming of model

The developed model presented in this chapter is subject to the few limitations as follows:

- 1- The functionality of changing C3D8R elements to particles is not supported automatically in Abaqus/CAE (v.6.11). The PC3D elements (SPH particle) should manually be added to the input file in the specific domain and so the relative changes of the writing element in Abaqus file are needed to implement manually for each modelling. This limitation increased the time to prepare models for each case study. However, in the latest version of Abaqus/CAE (v.6.13) this changing become automatically but applying the SPH element to specific domain still needs to be applied.

- 2- The particle motion of SPH region may become unstable when these are in a state of tensile stress. This instability, which is strictly related to the interpolation technique of the standard smoothed particle dynamic method, is especially noticeable in some case of machining orientation. Therefore, however, the three-dimensional FE/SPH developed can be used for a relatively large number of orientation setups, simulation of all arbitrary orientation systems is subject to limitation.
- 3- However, applying the transitional meshes with the element type (C3D8R) and different shape decreased the running time significantly, the whole procedure mentioned in Section 5.2.4 needs to be done in Abaqus/CAE manually for having such an element. This limitation increases the time to prepare models for each case study.
- 4- All PC3D elements with the same section definition are forced to be run in the same parallel domain. Note that the average running time for orthogonal single crystal machining model with 71825 particle numbers is about 72 hours in high performance computers (HPC) system with one CPU. There is not any significant difference between running a job with multi-core CPUs, computers and single one as the whole SPH region should be run is one CPU. It is needed to mention this time is seems reasonable for a large amount of intermediate data in crystal plasticity formulation. The pure SPH technique with the identical cutting parameters with the same geometry needs at least 15 times more in terms of running time or even impossible for the single-crystal machining model.

With the use of developed single crystal machining model the mechanism of deformation was studied in more detail in the next section.

5.3 Mechanism of deformation in single-crystal machining

When the cutting tool advances towards the workpiece, it starts to deform. When a primary shear stress generated by the intrusion action of the cutting tool is larger

than the critical shear stress of a single crystal of copper, slips would be generated in its crystalline lattice to release the strain energy. In the presented crystal-plasticity theory, the material flow on a slip system was represented in a continuum sense as a plastic shear strain γ .

In general, the active slip system for a f.c.c. single-crystal structure consists of $\{111\}$ slip planes and $\langle 110 \rangle$ slip directions as explained in Section 2.3. There is a total number of 12 slip systems for f.c.c. structure, which can be active or not at the same time. Activation of each slip system is determined by a Schmid-factor value obtained by Eq. 4-1. From the Schmid's law, it is apparent that the primary slip system will be the system with the highest Schmid factor. It is possible to calculate the values of $\cos\phi \cos\lambda$ for every slip system and, subsequently, determine which slip system operates first. The Schmid factor for 12 slip systems was obtained for three cutting directions $[100]$, $[110]$ and $[111]$ and shown in Table 5-4.

For determining the magnitude of the Schmid factor two angles λ and ϕ should be defined. λ is the angle between the slip direction and the applied force, and ϕ is the angle between the normal to the slip plane and the applied force. The product $\cos\phi \cos\lambda$ is generated Schmid factor. For example, for the first slip system with applied force direction equal to $[100]$, slip plane normal is (111) and slip direction is $[0\bar{1}1]$. Therefore, the $\cos\phi = 1/\sqrt{3}$ and $\cos\lambda=0$ result in Schmid factor equal to zero. The Schmid factor magnitude is calculated in the VUMAT subroutine for each time increment.

For instance, for a crystal machined in cutting direction $[100]$, the majority of slip systems (eight from twelve) expected to be active as they have the highest Schmid factor value. Only four slip systems-numbers 1, 6, 7 and 10- are not activated. At the same time, more than one slip system is active, and the total strain is the result of summation over all active slip systems. Table 5-5 shows the predicted shear direction for 12 slip systems. For crystal machining in cutting direction $[100]$, the Schmid theory predicts the flow of material in systems 2, 4, 5, 8, 9 and 11 in the 135° (-45°) direction, while systems 3 and 12 let material to slip in the 45° direction.

Table 5-4 Values of Schmid factor for 12 slip systems for three cutting directions [100], [110] and [111].

No.	Slip system		Schmidt factor		
	plane	direction	[100]	[110]	[111]
1	(111)	$[0\bar{1}1]$	0	-0.4082	0
2		$[10\bar{1}]$	0.4082	0.4082	0
3		$[\bar{1}01]$	-0.4082	-0.4082	0
4	$(\bar{1}11)$	$[101]$	-0.4082	0	0.2721
5		$[110]$	-0.4082	0	0.2721
6		$[0\bar{1}1]$	0	0	0
7	$(1\bar{1}1)$	$[011]$	0	0	0.2721
8		$[110]$	0.4082	0.4082	0.2721
9		$[10\bar{1}]$	0.4082	0	0
10	$(11\bar{1})$	$[101]$	0	0	0.2721
11		$[101]$	0.4082	0.4082	0.2721
12		$[\bar{1}01]$	-0.4082	0	0

Table 5-5 Shear-angle prediction for machining in cutting direction [100]

Slip system No.	1	2	3	4	5	6	7	8	9	10	11	12
Shear angle	90°	135°	45°	135°	135°	90°	90°	135°	135°	90°	135°	45°

The crystal begins to deform plastically by slip on these active systems, known as *primary slip systems*. The stress required to cause slip on the primary slip system is the yield stress of the single crystal. The crystal-plasticity framework was discussed in detail in Section 4.2 in order to obtain the shear strains to implement the kinematical concept of shearing in slip directions at each increment. Figure 5:11 shows the distribution of shear strain for 12 slip systems after the

cutting length reached 50 μm . This analysis was set at (010)[100] orientation setup with the cutting depth of 10 μm , cutting tool speed of 1300 mm/s and friction coefficient, $\mu = 0.12$. Clearly the slip systems 4, 7 and 10 were the most active ones, whereas the contribution of other slip systems was comparatively small. It is worth noting that slip systems 1, 6, 7 and 10 also partially contributed to the total deformation, although they are considered to be inactive according to Table 5-5 based on their Schmid factors.

The underlying reason for these discrepancies arises from the fact that the Schmid factors calculated in Table 5-5 are based on a simplifying assumption of uniaxial compression. However, the contribution of slip systems to the overall deformation in FE simulations is computed by imposing boundary conditions locally. This means that throughout deformation the boundary conditions of the material points start to change as a result of strong strain gradients introduced by the cutting tool tip; hence, the Schmid factors start to evolve with deformation and deviate from their initial values. As the load is increased further due to further propagation of cutting tool, critical shear stress may be reached on other slip systems; these then begin to operate.

The above analysis unveiled the basic deformation mechanism in single-crystal machining based on the Schmid factor. Under different combinations of grain orientations and cutting directions the deformation process shows various characteristics in its aspects such as a variation of the force and chip morphology. Mechanics of cutting depends strongly on the crystallography and the orientation of the slip systems in the grain, which is highly anisotropic in terms of both elastic and plastic properties.

Having a well-developed model allows the predictions of the force variation and chip morphology. The shear-strain direction and magnitude, changing after each step of cutting tool's penetration are calculated and updated in the model based on the VUMAT subroutine. The computing time required to carry out a single simulation increases with the number of elements involved and, hence, with

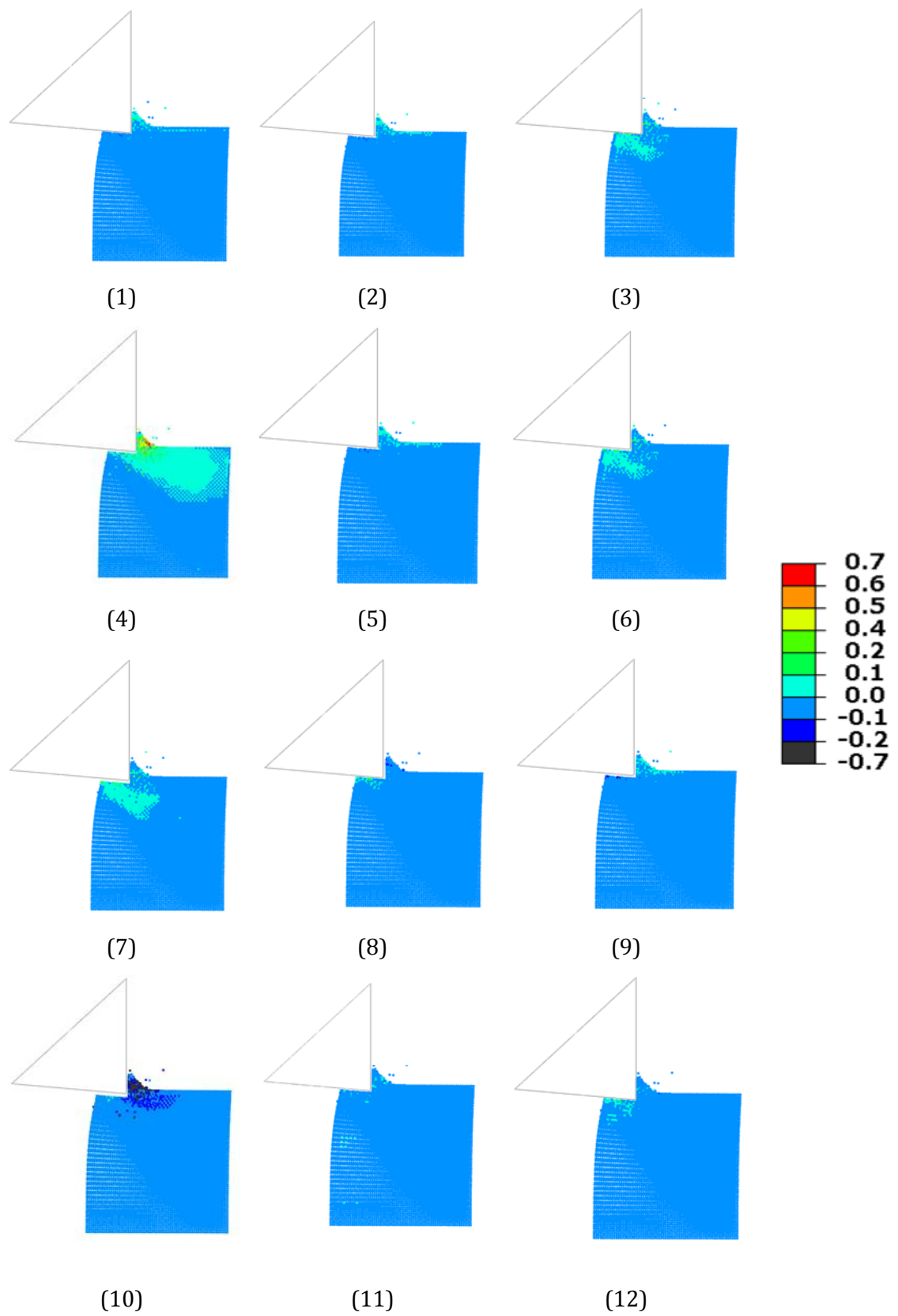


Figure 5:11 Shear strain distribution for 12 slip systems

diminishment of this size. The more elements, the longer it takes for the calculations to complete. In the following section the cutting-force variation and chip morphology for different orientations are discussed in more detail.

5.4 Variation of cutting force and chip morphology

Evolution of the calculated cutting forces with an increasing cutting length for the 0° cutting direction in three cutting planes is shown in Figure 5:12. This result was already valid with experimental observation in Section 5.2.7. This figure indicates the strong effect of crystallographic orientation on cutting force variation. The effect of crystal orientation is evident in the character of this evolution. Initial stages of the tool-workpiece interaction (depicted as Section I in Figure 5:12) demonstrate a marked difference for different crystal orientations. With increasing tool penetration the workpiece material rearranged when the strain energy in the deformed lattice exceeded the binding energy of particles. The direction and value of shear flow can be estimated based on the Schmid's law. During single crystal machining oscillations of the shear angle due to grain rotation resulted in variation in the observed cutting forces (Figure 5:12). The level of fluctuations was less than 8% of the maximum cutting force for the (100) plane, where the finer lamellar slip structure occurred; it was approx. 20% for the (101) and (111) planes, where the coarser lamellar slip type occurred. A comparison of chip morphologies after machining showed a distinct change in the type of chip formed when moving from one direction cutting setup to another. The character of fluctuations in the cutting force was found to correspond fairly well to the pattern of the chip formation. Generation of a spatial angle of chip formation in the workpiece highlighted the importance of 3D formulation for simulation of the machining process in the single crystal of copper to account for realisation of deformation processes for various orientations of the cutting system.

The variations of cutting forces when they are cut under identical cutting parameters with different crystal orientations are due to the variations in the angle

of the most favourable shear plane. Not only the cutting force, but also the mode of chip formation was found to vary dramatically with cutting orientation. Forces and chip morphology are highly orientation dependent. The morphology of the chips contains important information about the mechanics of the cutting process. From the profile view of the chips, the strong effect of crystallographic orientation observed for the same cutting depth. Clearly the chip thickness and lamellae thickness significantly increased after section III for (101) cutting orientation linked to increase the cutting force in this section. This observation indicates that a fundamental change in the chip-formation process occurred during micro machining process, and the force fluctuations were reflected in cut-chip thicknesses.

When the major slip plane is coincident with the cutting direction material glide does not significantly contribute to material removal: chips are formed by fracture along the direction of maximum shear stress. Plastic flow becomes possible when the specimen is rotated so that the slip plane makes an acute angle with the cutting direction. These differences in the material motion lead to significant variations in the nature of plastic deformation ahead of the tool and consequent variation in the magnitude of the forces, force ratio, specific energy, and subsurface deformation.

Interestingly, the chip morphology is heavily influenced by the crystallographic orientation as shown in Figure 5:13. In this study, continuous chips with different chip morphologies were produced for all orientations. As the tool moved forward (Section I), the chip in the (101) orientation exhibited a larger thickness when compared to other two orientations. This phenomenon, in turn, led to a higher maximum value of cutting force for this orientation.

In chip formation, there is a small region, in which the high-strung and high-strain-rate deformation process occurs. Observations of a smaller chip structure in the (100) plane compared to (111) in Section I with a higher amount of force is due to the shear angle. In the (100) orientation, the material is not amended to machining at the beginning of the process resulting in an approximately zero shear angle. When the tool moved forward (Sections II and III), the shear angle increased with a reduction in the cutting force.

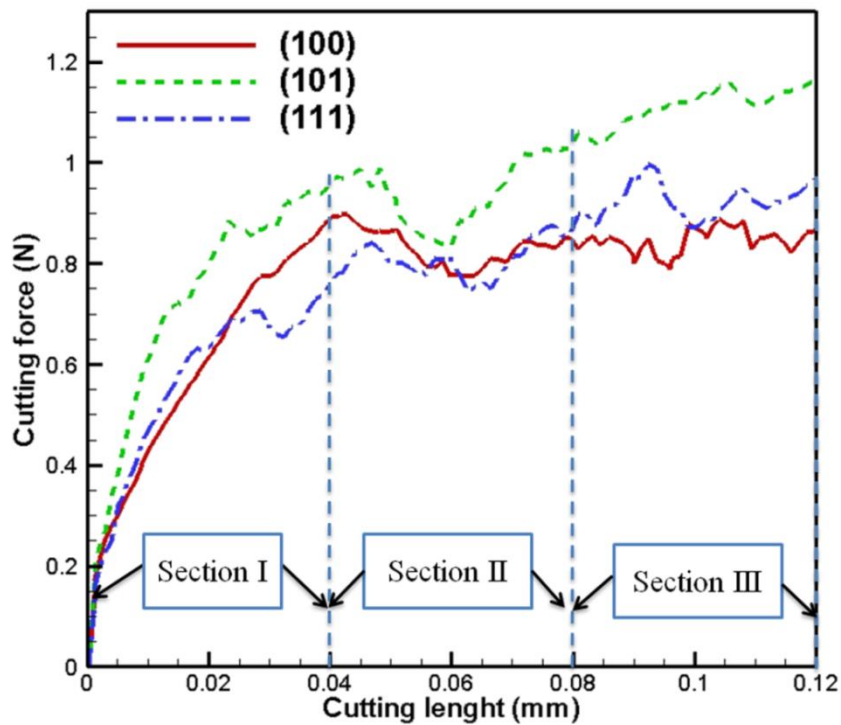


Figure 5:12 Evolution of cutting forces for different cutting planes of 0° cutting direction

The kinematics of material separation are accommodated in SPH in a manner that neither involves the loss of material, requires foreknowledge of the locus of separation, nor requires special numerical treatment. Material damage is incorporated at SPH nodes through a loss of cohesion as neighbouring SPH particles separate from each other. This comes about because once those particles are more than the critical distance, h , from each other, each particle no longer contributes to the strain calculated at the other, and the corresponding cohesive component of the stress disappears.

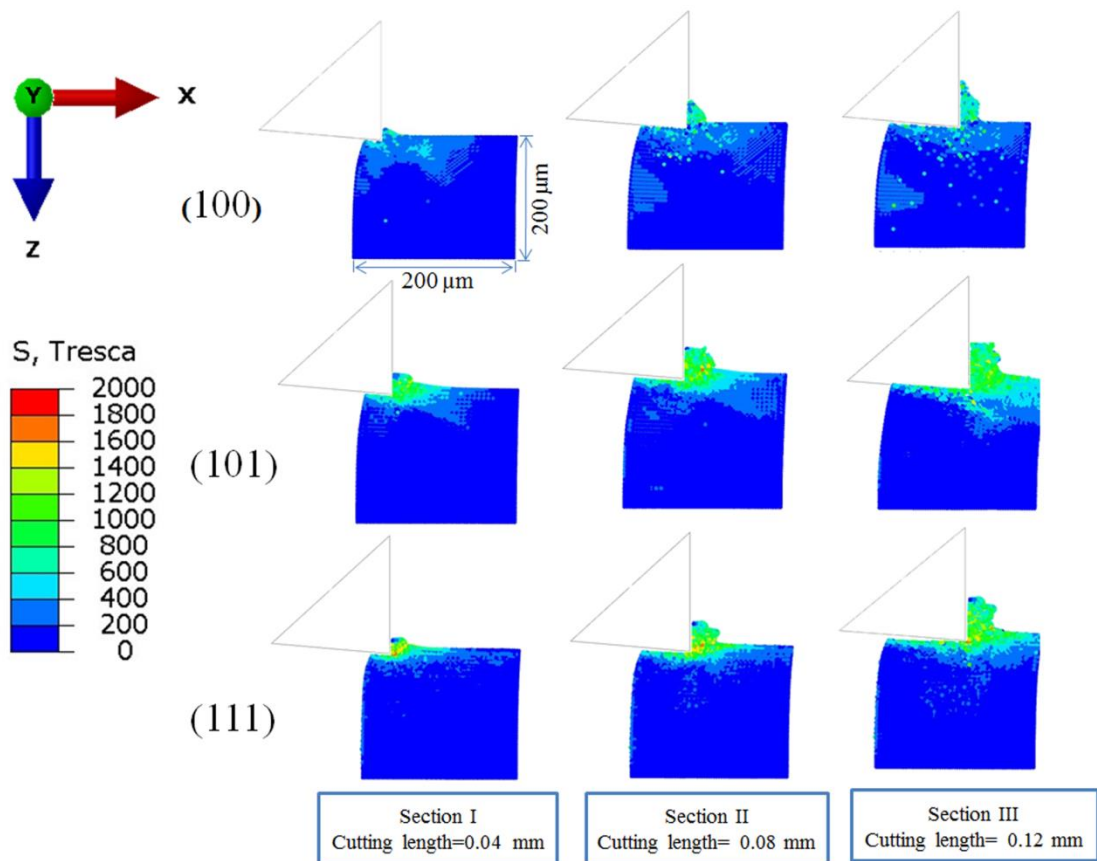


Figure 5:13 Chip morphologies in three planes-(100), (101) and (111)-in 0° cutting direction for different stages of machining (Sections I – III, see Figure 5:12)

Figure 5:14 shows the calculated average values of cutting forces in Section III (Figure 5:12) for the single -crystal of copper for different combinations of planes and cutting directions. The first observation is that for all the planes the 0° direction is characterized by the maximum value of the average force. On the other hand, the variation in the average cutting force values for the (100) plane is smaller than that for other planes due to a basic symmetric structure of the f.c.c crystal in this plane, where this can reach the level of up to 33% (on the (101) plane), a significant value for the micro-cutting process.

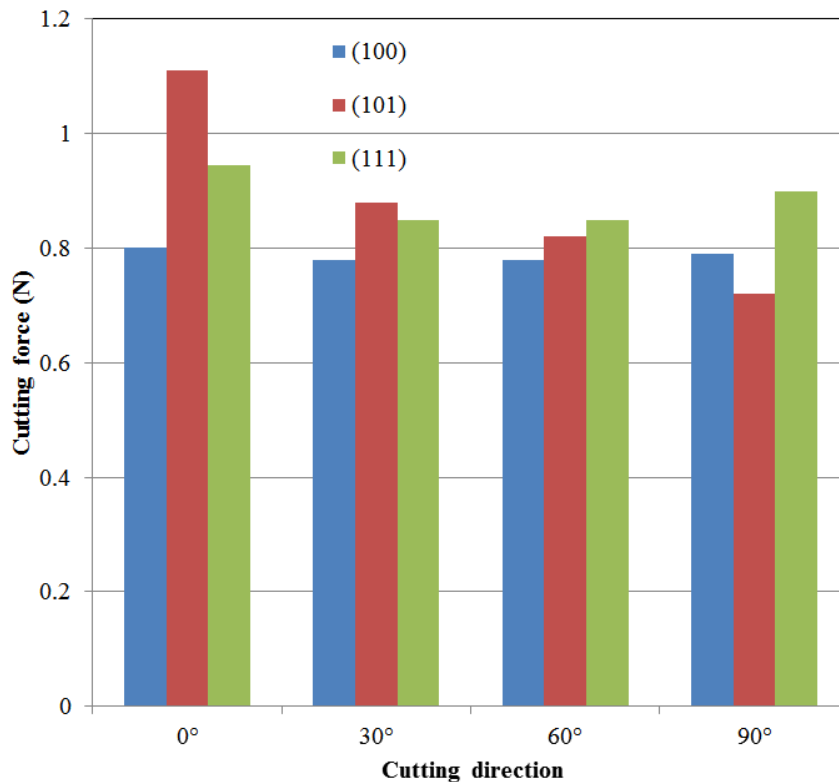


Figure 5:14 Typical variation of cutting force for various cutting directions for copper single crystal machining

5.5 Effect of material property

In order to study the sensitivity of cutting force to variation in material properties, the developed three-dimensional FE/SPH model was used in analysis of aluminium property in this section. The cutting orientation setup for single crystal aluminium machining was selected the same as copper (Table 5-1). The elastic properties of the single-crystal aluminum were represented by three material constants, $C_{11} = 108.2$ GPa, $C_{12} = 61.3$ GPa and $C_{44} = 28.5$ GPa. The strain-rate sensitivity, n , of the material was set to 20 for each set of slip systems for the evolution of the plastic strain-rate $\dot{\gamma}^\alpha$ (Eq. 4-6 and 4-8). It is worth mentioning that the reference stress-rate was taken as 29 MPa. The saturation stress and initial hardening modulus were considered as 48 MPa and 3.4 MPa, respectively. Selecting of these parameters was based on the literature (Groh *et al.*, 2009).

Figure 5:15 was shown the cutting force variation for chosen zone axis. The variation of the material parameters has been observed to have only a little effect on the variation of cutting force in different orientation setups. The magnitude of cutting forces, on the other hand, has a stronger dependence on the material parameters.

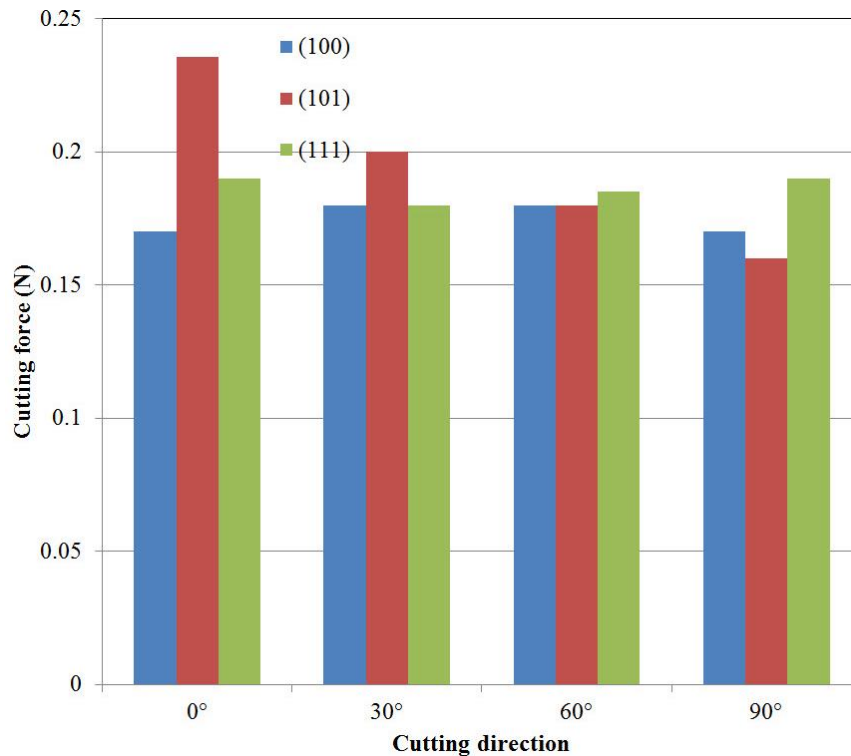


Figure 5:15 Typical variation of cutting force for various cutting directions for aluminum single crystal machining

A part of this difference in cutting force magnitude between copper and aluminium machining single crystal is arisen from different friction material in these two properties (Cohen, 1982). The effect of friction is discussed in more details in the Section 5.6.1 and Section 6.4.1.

The similarity of the trend results for aluminum and copper indicates that the deformation kinematics, which depend on the arrangement of the slip systems, are identical for all f.c.c. metals and play a major role in determining the cutting force.

To explain the observed behaviour, the deformation (slip) mechanism should be considered. The total slip that occurs in all active slip systems for a given state of deformation is nearly the same for f.c.c. structure.

The current model which was validated against experimental results for cutting forces have also been performed to understand the effect of machining parameters on machining responses. The next section the coefficient of friction and tool edge radius is studied in more detail.

5.6 Parametric study of orthogonal machining model

Analysis of cutting forces over a wide range of friction condition and tool-edge radii can help to understand the importance of cutting parameters and conditions. These are investigated by employing the developed FE/SPH model of single-crystal orthogonal machining. In these studies, the coefficient of friction varied from $\mu = 0$ to $\mu = 0.4$ is shown in the present thesis. This range is covered a well lubricated tool-workpiece interface to non-lubricated interface condition in real machining. In order to minimize computational effort, calculations for cutting tool radii of 5 μm , 10 μm and 20 μm are shown to investigate its effect on the output results.

5.6.1 Effect of coefficient of friction

The interaction between the tool and the chip includes forces in the normal and tangential directions. The traditional Coulomb friction model was applied along the chip-tool interface in the present study. It states that friction behaviour is a result of two contacting bodies. If shear stress at a tool-chip contacts point is less than the limited friction stress, no relative motion occurs between the chip and the rake face of the cutting tool. The relative motion occurs in the workpiece as a chip in cutting tool face angle while the shear stress is equal to or greater than the limited friction stress. The critical shear stress was estimated based on Eq. 4-1 and to be associated with the crystallographic orientation of workpiece. In this

section, the results of finite-element simulations are used to investigate the effect of friction.

The experimental result of Zhou and Ngoi (2001) showed that the coefficient of friction was very sensitive to the crystallographic orientation. The coefficient of friction between cutting tools and workpiece materials was measured by a friction test. This difference is not limited only to different crystal planes, but also along various directions on the same plane. The values of the coefficient of friction in three common planes of f.c.c. and three crystal orientations are presented in Table 5-6. These were obtained for single-crystal copper and showed the variation of nearly 40% between the maximum level of friction- 0.130 belonging to (110) [001] and minimum 0.078, for the (111) $[\bar{1}\bar{1}2]$ orientation set.

Table 5-6 Coefficient of friction of crystalline copper for different orientation sets (Zhou and Ngoi, 2001)

Plane	Direction	Coefficient of friction
(100)	[001]	0.115
	[011]	0.081
(110)	[001]	0.130
	$[1\bar{1}0]$	0.123
(111)	$[11\bar{2}]$	0.086
	$[\bar{1}\bar{1}2]$	0.078

Implementing these coefficients of frictions to the FE/SPH model results in the force-displacement diagram presented in Figure 5:16. This diagram was shown the

cutting force variation result in a sensitivity coefficient of friction obtained by experimental study in different crystallographic orientation. The depth of cut was set at 10 μm , and the tool moved with velocity of 1300 mm/s. Between the eight machining orientations cited in Table 5-6, the cutting force in (110)[001] and (111) $[\bar{1}\bar{1}2]$ orientations have obtained same value whiles with having the maximum and minimum friction factor, respectively. Therefore, the increasing Coulomb friction parameters are not the only reason for increasing cutting forces. The cutting plane and direction have a stronger influence on the force-displacement behaviour.

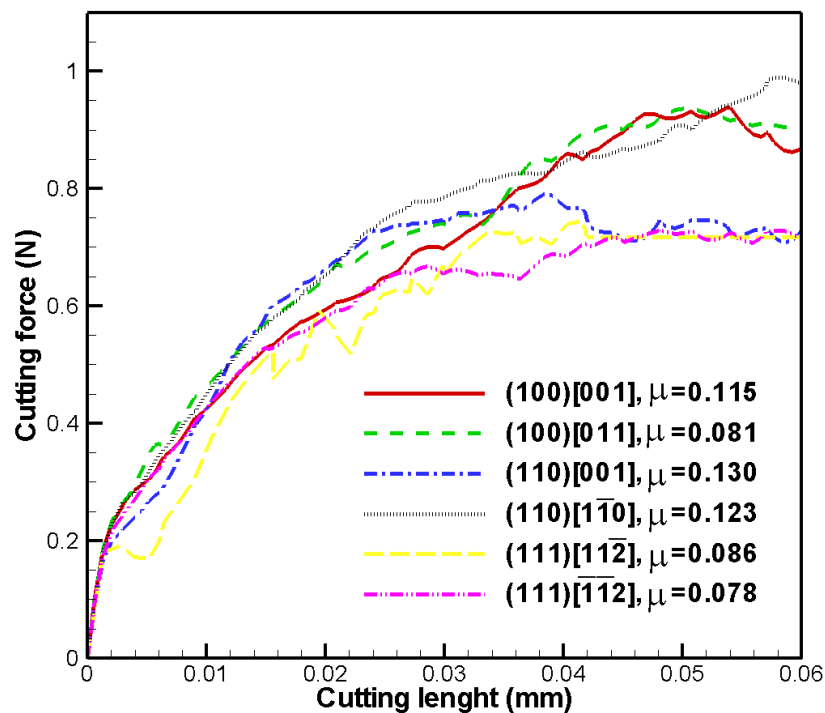


Figure 5:16 Cutting force behaviour of different coefficients of friction in different orientations machining process

For better understanding of the effect of friction condition in metal cutting, three friction conditions in single-crystal modelling were studied. First, the effect of a well lubricated tool-workpiece interface ($\mu = 0$) was considered. After that an average value of the coefficient of friction presented in Table 5-6 ($\mu = 0.12$) was

studied, followed by a dry (non-lubricated interface) condition ($\mu = 0.4$). The crystallographic orientation (001)[100] was selected for these three modelling setups and similar to previous simulation parameters, the depth of cut was fixed at $10 \mu\text{m}$, and the tool moved with velocity of 1300 mm/s . The cutting forces increase rapidly as the tool advances into the workpiece and after certain penetration the forces tend to be constant, indicating a steady cutting state. When the friction coefficient varied between 0, and 0.4, the cutting forces reached at 0.61 N , 0.81 N , and 1.12 N , respectively (Figure 5:17). Increasing the frictions result in to increase nearly uniformly the cutting force signature.

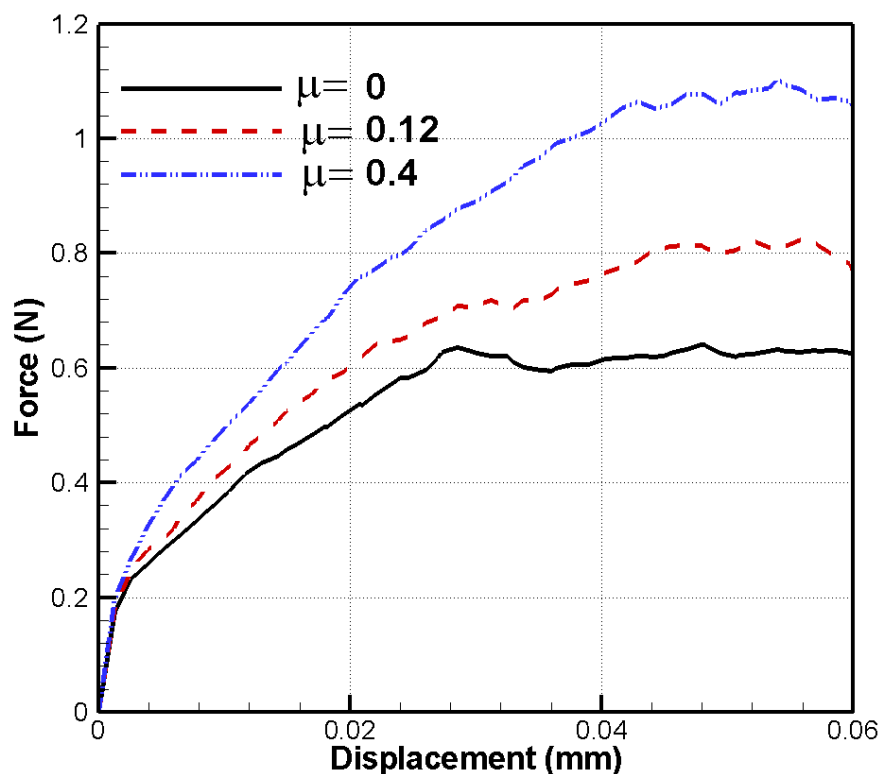


Figure 5:17 Cutting force pattern for different coefficients of friction

The chip tool interface is the main area of concern with respect to friction due to its influence on the resultant forces and the variation of normal and shear stress on the tool's rake face. The effect of friction on the process zone the chip-tool interface is shown in Figure 5:18. The interaction at the chip-tool and workpiece tool play an

important role in the controlling the type of chip formed. When friction vanished, thickness of the removed chip was relatively small, and a lower radius of curvature was observed in the root of the chip (Figure 5:18 a). As a result, the chip flew out and departed from the contact region on the rake face quickly. When the coefficient of friction increased (Figure 5:18 b and c), chip thickness, the radius of curvature at the chip root and the contact length between the tool and the chip on the rake face all increased. As a result, the chip moved out of the rake face with more difficulty. A more detailed analysis of the results demonstrates that friction parameters on single crystal machining can affect machining processes quite similar to macro scale. The friction coefficient increased the cutting force magnitude for all active slip systems during deformation without changing the active slip system in each increment too much.

Study the effect of coefficient of friction at the micro-scale needs for accurate observation of chip radius curvature in order to gain more insight into the cutting mechanism. The coefficient of friction, as stated earlier, affect the ratio of the frictional force to normal force acting. This average friction coefficient was selected between 0 to 0.4 to represent the well lubricated tool-workpiece interface to non-lubricated interface. The chip curve reflects the changes in friction coefficient. The highest coefficient of friction exhibits lowest radius of curvature. The frictional shear at the chip-tool interface mostly effective at the cutting tool faces and characterizes the tool wear. The contact mechanism on a surface has been changed in modelling the cutting tool edge over a workpiece due to changing the friction parameters. As a result, the decreasing sliding velocity and increased in frictional stress occurs by increasing the friction parameter. The uniform increased of cutting force obtained for a selected friction coefficient.

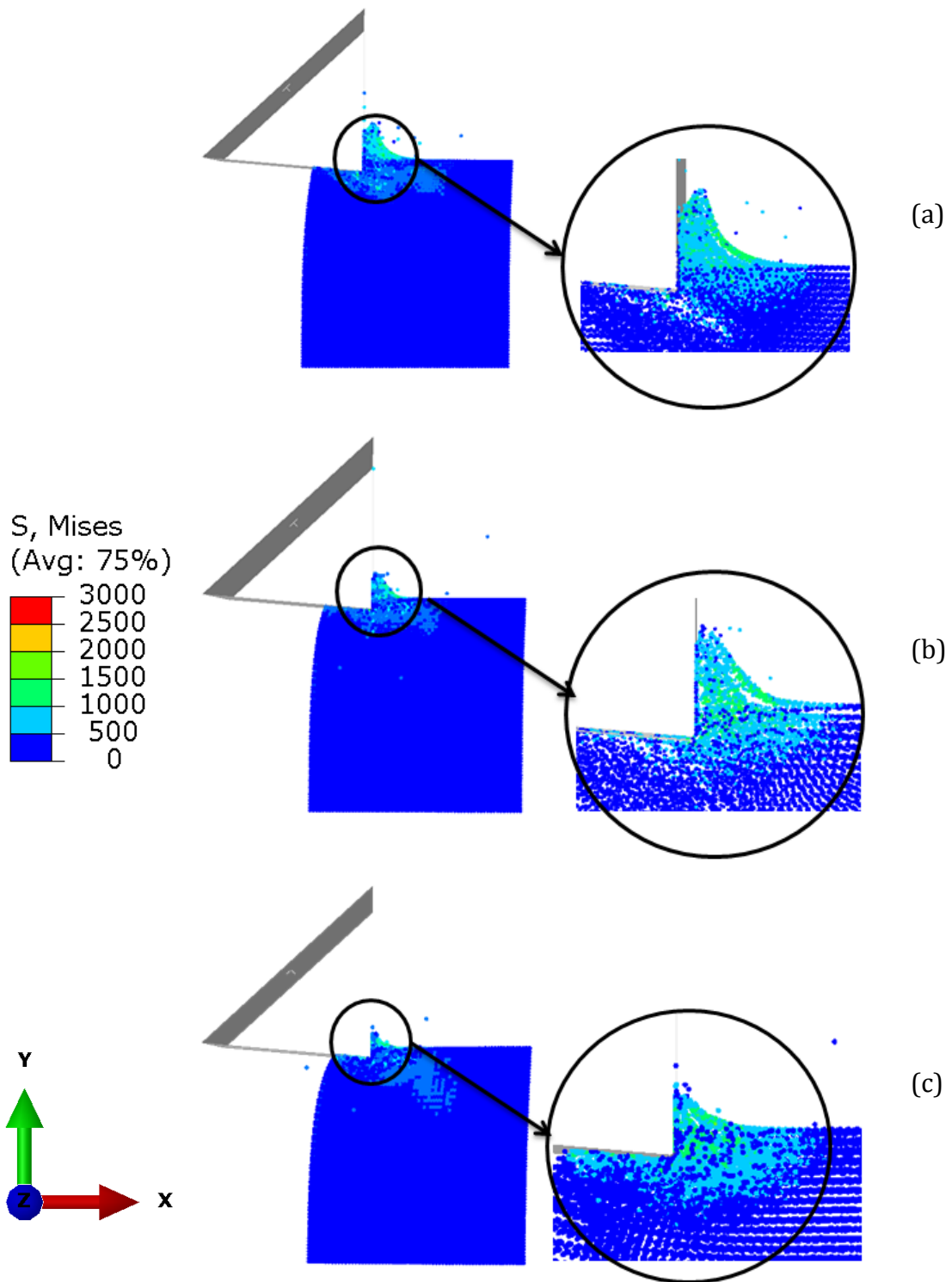


Figure 5:18 Distribution of flow stresses for different coefficients of friction:

(a) $\mu=0$, (b) $\mu=0.12$ and (c) $\mu=0.4$

5.6.2 Effect of tool-edge radius

Machining raises a great number of issues, mainly due to its size or scale. There are two different aspects of size effects of concern. First when the depth of cut is of the same order as the tool-edge radius, and second, where the microstructure of workpiece material in small scale has a significant influence on the cutting mechanism. The first case is studied in this section, and the next one is considered as future works of this thesis.

Three different tools-edge radii -5 μm -10 μm and 20 μm - were chosen to illustrate chip formation and material deformation for three different h_c/r ratios (h_c is the cutting depth and r is the tool-edge radius) equal to 2, 1 and 0.5, respectively, at the initial cutting stage (the cutting length was fixed at 50 μm). In Figure 5:19, the force components, tangential (a) and normal (b) to the cutting direction, are compared for those h_c/r ratios, generated in the simulation of orthogonal cutting of copper single crystal. These were obtained for three cutting planes - (100), (101) and (111) - with keeping average value for three orientations -0°, 30°, 60° and 90° in each plane.

In the orthogonal cutting in macro scale, the tangential force should be higher than the normal force, while for $h_c/r = 0.5$, the normal force becomes larger than the tangential one. This demonstrates that the mechanism of material removal results in plowing rather than cutting in front of the tool for this cutting tool tip.

In the case of small roundness of the cutting edge (compared with the depth of cut), near the tip of a sharp tool, the material of workpiece was divided into two distinct regions: a region transferred to the chip and a remaining part that generated a new machined surface. Hence, the workpiece material was removed by conventional cutting, and the chip-formation process and structural integrity were significantly influenced by the orientation and crystal structures of single grain (Figure 5:20 a). When the depth of cut is nearly equal to the radius of the cutting edge- at $h_c/r = 1$ - both the rounded tool edge and rake edge participated in

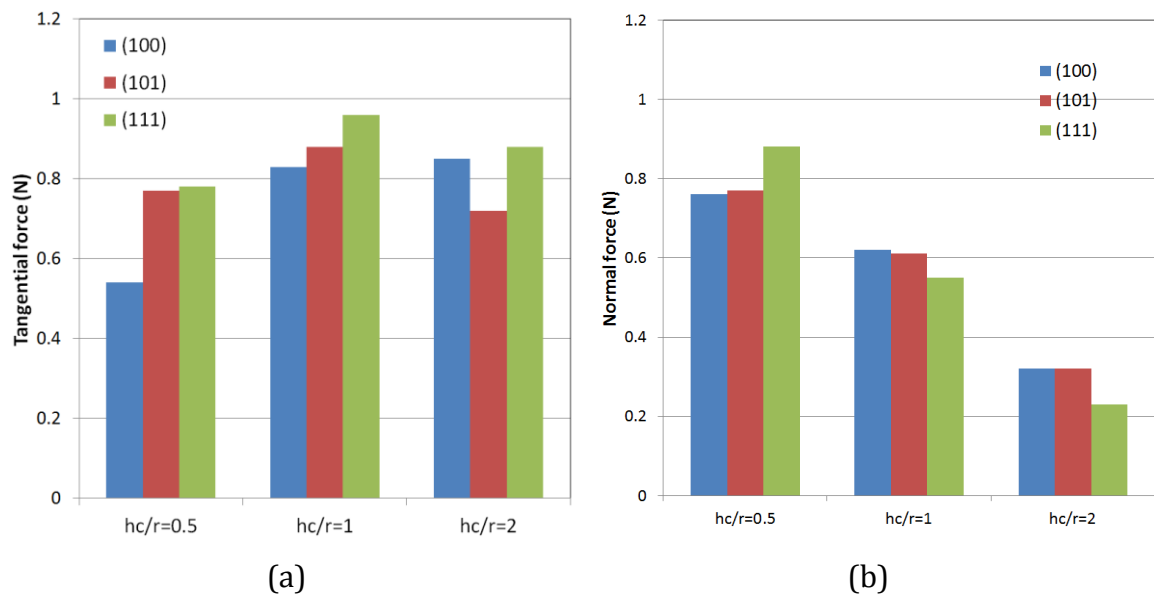


Figure 5:19 The force components tangential (a) and normal (b) for three h_c/r value

chip formation, and the workpiece material was removed by the cutting tool with a large negative rake angle. In this case, plastic deformation such as rubbing or burnishing dominated the process rather than cutting (Figure 5:20 b). As shown in Figure 5:20 c, in case of a larger tool radius ($h_c/r = 0.5$), a small fraction of the particles was separated, forming the chip while a large fraction passed through beneath the tool edge. In addition, the chip layers could not reach the positive rake edge due to the large edge radius and small depth of cut. Therefore, the ratio of undeformed chip thickness to the tool-edge radius is a governing parameter in machining, and material separation greatly influencing cutting forces.

In the micro-machining of single crystalline copper, tool edge radius influenced on chip formation and material deformation mechanism. The changes in the mechanism due to the tool edge radius effect are driven by the combination of h_c and r where the emphasized on either one parameter is not meaningful. This study was carried out by performing finite element analyses at different h_c/r ranging from 0.5 to 2.

When hc/r was reduced below 1, initial machining action was performed by the cutting edge. The workpiece material ahead of the tool edge was found to flow against the cutting tool motion; small amount of material shows upward displacements along edge radius while the remaining fraction of the material is found to flow around the rounded curvature, back into the bulk workpiece material and then being compressed beneath the tool edge. Material in the vicinity of the rounded tool edge undergoes severe plastic deformation, associated with a large plastic deformation zone. The increased size and thickness of the plastic zone is due to the merger of the primary and secondary deformation zone. A smaller chip curl was produced comparing to those at $hc/r > 1$.

By increasing the ratio of hc/r , as the cutting continues the chip was first forms, grows and subsequently flows along the rake face of the tool. Small fractions of the material may escape to deform as chips while the remaining flow back into the bulk material, leading to the formation of the machined surface. Shearing is concentrated in front of the sharp tool edge around the chip root.

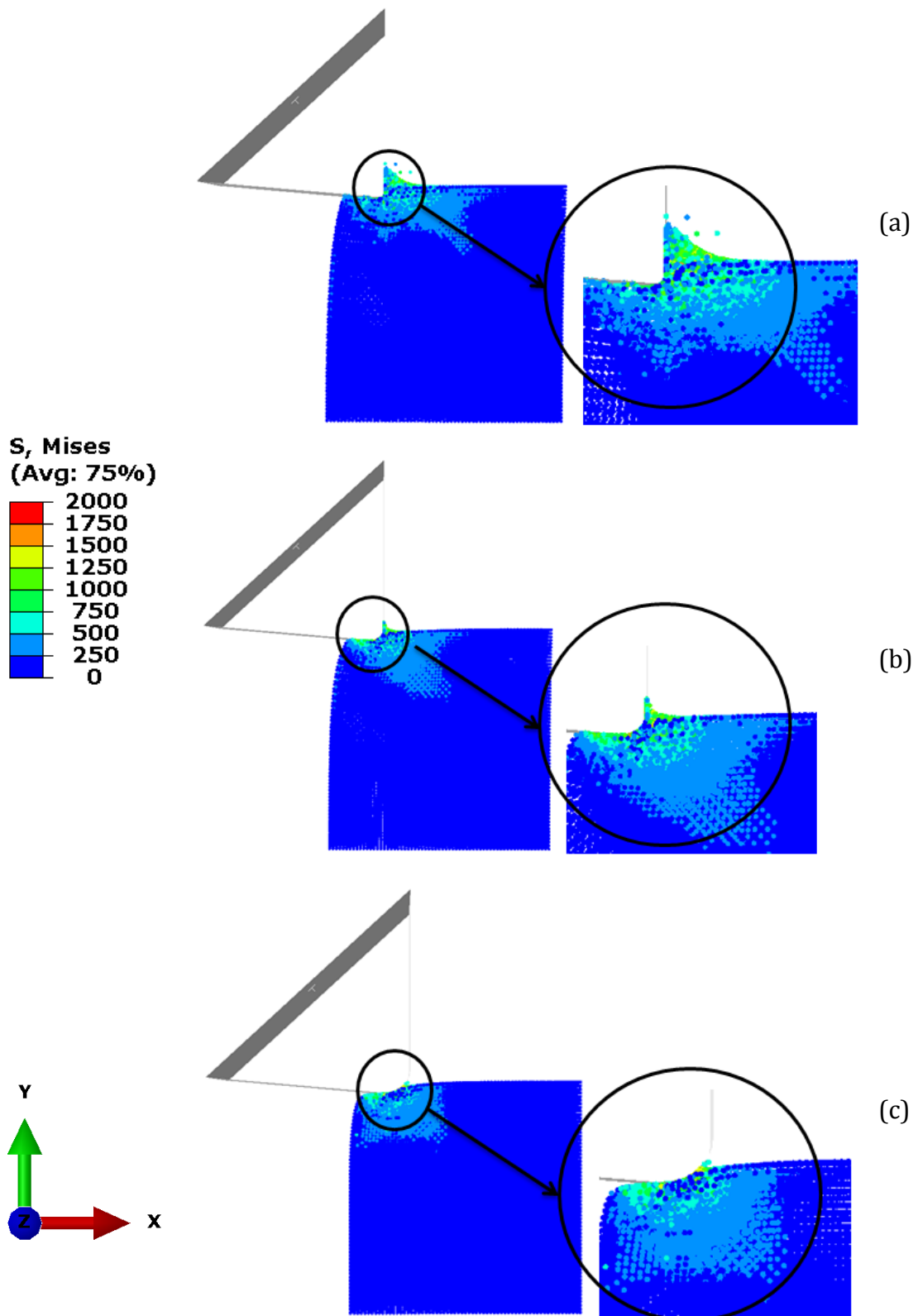


Figure 5:20 Chip shape for various magnitudes of (a): $\frac{h_c}{r} = 2$; (b): $\frac{h_c}{r} = 1$; (c): $\frac{h_c}{r} = 0.5$

In terms of directions, Table 5-7 is shown the ratio of tangential to normal force for three crystal orientations and four cutting directions. Tool-edge radius changes the mechanism of deformation by changing the activation slip systems in each incremental deformation. Cutting force is the main factor governing machining accuracy, surface quality, chip formation, power requirements and tool life. The ability to predict the cutting forces is useful for the design of machine tool structures and cutting tools, as well as for the control and optimization of machining processes to achieve high accuracy and productivity. The resultant force is the components of tangential and normal force. The ratio of tangential to normal force confirmed the change of machining mechanism from cutting to ploughing. However the unique role was not observed for whole data, the (111) crystal orientation recorded the maximum force ratio for h_c/r ratio of 1 and 2 for cutting direction 90° and 30° , respectively, and in terms of $h_c/r=0.5$, the (101) have more cutting ratio magnitude in 30° cutting direction.

Table 5-7 Tangential to normal force ratio in different directions

	(100)			(101)			(111)		
	$h_c/r=0.5$	$h_c/r=1$	$h_c/r=2$	$h_c/r=0.5$	$h_c/r=1$	$h_c/r=2$	$h_c/r=0.5$	$h_c/r=1$	$h_c/r=2$
0°	0.70	1.34	2.26	0.90	1.38	2.21	0.80	1.70	2.60
30°	0.85	1.35	2.55	0.93	1.41	2.42	0.88	1.74	2.70
60°	0.73	1.3	2.60	0.85	1.40	2.30	0.85	1.75	2.66
90°	0.69	1.27	2.35	0.82	1.44	2.35	0.84	1.76	2.5

5.7 Summary

A combination of SPH and continuum finite-elements approaches in a single model of a machining process of crystalline copper and aluminium are presented in this chapter. It is shown that this is a viable and a numerically robust way for solving

large-deformation problems at small length scales without compromising complex underlying physical mechanisms that drive deformation in crystalline materials.

The importance of grain orientation and direction of machining on the overall cutting forces, chip morphology was demonstrated together with the propensity of the workpiece material to generate slips when its grains undergo rotations. Between three selected grain orientations in f.c.c. single crystals – (100), (101) and (111) – the cutting-force variation on the (101) plane was observed to be larger than that on two other planes. The total difference in force for the chosen orientations was 33%, signifying the strength of the effect of crystal orientation in the single crystal machining process.

It is observed that, although the actual values of the cutting force are different for aluminium and copper, the variation trend for both materials were similar. These two materials have the same f.c.c. crystal structure.

In terms of the parametric study various coefficients of friction values were analysed in this chapter and showed the crystallographic of workpiece have stronger influence on the force-displacement behaviour than the coefficient of friction parameter. Increasing the friction caused the increase of the cutting force pattern for each cutting direction uniformly while tool edge radius change the activation of the slip system completely. Having this knowledge helps to predict the cutting force variation in single crystal machining.

Modelling of single-crystal turning

6 Modelling of single-crystal turning

6.1 Introduction

Turning is one of the most widely-used machining methods to produce revolution parts with high precision. This process requires a turning machine called a *lathe*, a workpiece, a fixture and a cutting tool. The parts ranging from pocket-watch components to large-diameter marine propeller shafts can be machined on a lathe (Chua *et al.*, 1993). A schematic of the process is shown in Figure 6:1 and basically indicate the primary process parameters (Yang and Tarng, 1998).

The primary motion of turning cutting is the rotation of the workpiece, and the secondary is the tool's feed per revolution. The workpiece is rotated about its axis, and the cutting tools are fed into it. Turning can be performed to create the external surface of the part as well as internally. Usually, the term "turning" is used for generation of external surfaces by this cutting action, while the same essential cutting action when applied to the internal surfaces like holes is called *the boring*.

Therefore, the terms, 'turning' and 'boring' categorized the larger family of (essentially similar) processes.

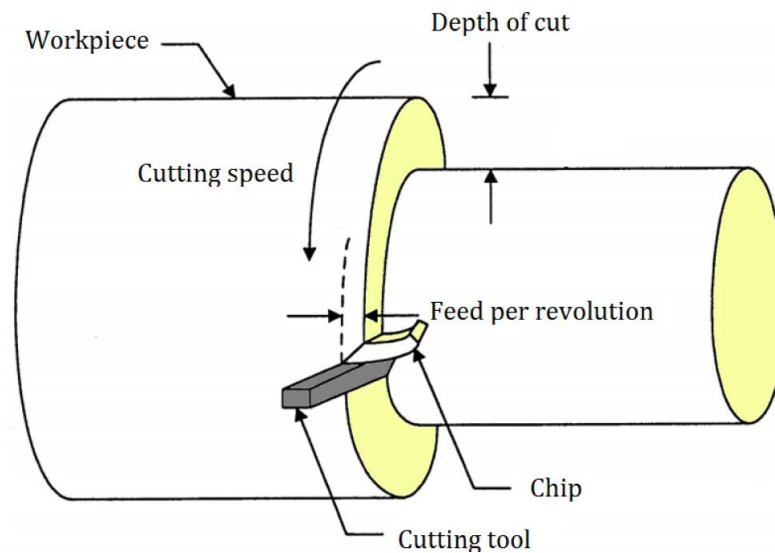


Figure 6:1 Basic turning operation after Yang and Tarnq, (1998)

Modelling of the turning process is quite complex; as a result, the majority of machining studies are limited to an analysis of the orthogonal planning scheme, which is the simplest geometric configuration. Machining accuracy is affected by the workpiece's properties, and there is a need for a fundamental understanding of the material's behaviour under high strains and strain rates, characteristic of the turning process. While experiments with a single-crystal material provide detailed data in terms of cutting energy only for one crystal orientation at a time, the turning configuration provides near-continuous data for the entire range of cutting directions for a given zone axis.

Due to wide application prospects and practical value of turning for the industry, the robust modelling tools with predictive capability to characterize a component's response to mechanical loading states are needed (Huang and Liang, 2005 and Shengfang *et al.*, 2010). This would reduce the need for extensive experimental

studies, which are expensive, and also help to extend the usability envelope of next-generation components to untried levels of load and environment conditions.

Through finite-element simulations, distributions of stresses and strains can be evaluated. The main problem of such a kind of simulations is to introduce the physics of the turning process through a very accurate constitutive model. This chapter describes three dimensional developed FE/SPH model for a turning configuration to study the effect of workpiece crystallinity on a material respond to machining. The crystalline anisotropy is implemented into the turning model using the commercial finite element software ABAQUS/Explicit (v.6.11) by means of a user-defined subroutine VUMAT described in Section 4.2.2.

6.2 Model characteristics

The existing finite-element models for turning processes in literature are somewhat limited (Arrazola and Ozel, 2008). The mesh distortion that happens at the initial stage of running such a model is considered as a main problem for turning simulations. Developing a three-dimensional model based on the FE/SPH technique is a way to overcome the distortion of elements. Moreover, the accuracy of a finite-element solution depends on many factors such as the number and size of elements, proper boundary conditions, realistic material modelling, contact and interaction. These are the main subjects studied in the following sections in more detail.

6.2.1 Descriptions of turning geometry

The tool's material is usually much stiffer than the workpiece material and can be simplified to analytic rigid surfaces in this study; the workpiece was modelled as a deformable body. The turning-model configuration consisted of a disk of single-crystal copper with the cutting tool moving along the disk's perimeter while the disk was fixed. Note that instead of rotation of the deformable disc as in real-life

turning processes, the tool was selected to move along the disk's circumference in a clockwise direction. The reason of this configuration is that there are no rotational degrees of freedom for PC3D element type and so it cannot directly prescribe a rotation degree for constraint of disk in the turning model. In this type of simulation, when the disc as a deformable body turns around cutting tool, it needs to redefine the element type from a deformable element into rigid body element. The rigid elements are not included in the calculation and cannot give any results later on.

While there are some ways of solving this problem like to put all nodes in a kinematic coupling, cover all surfaces with rigid shell and put all nodes in a distributing coupling, the rigid body motion of cutting tool around disc was assumed in the present model of single crystal turning for saving the computational time. Having such a model cut down the computational time by eliminating unnecessary contact and makes the model robust so as to avoid convergence issues. This assumption was considered to have an accurate kinematic movement without any differences in the real turning configuration.

According to experimental observations in Cohen (1982) in one complete revolution the force pattern shows periodicity with four repeating stages. Hence, a quarter revolution of the disc was modelled in this study. A schematic of the cutting model is shown in Figure 6:2. To eliminate the effect of boundary on the predictive capabilities of the developed model, the disc was considered to range from $\theta = -10^\circ$ to $\theta = 100^\circ$. These two additional $\pm 10^\circ$ sectors to a 90° segment (i.e. quarter disc) in the model eliminated the boundary effect on the final results for the cutting energy (force).

To compare results of the experimental study and the present model, it is clear that the outside diameter of the workpiece should be fixed based on the experimental study of Cohen (1982), while for the inside diameter more possibilities were available. The workpiece should be modelled large enough so that the boundary conditions do not influence the physical behaviour at the deformation zone during the machining process. In addition, if an unnecessary large dimension was used to

model the geometry, a solution might be computationally very expensive due to the increased number of elements in the model. By selecting a proper input disc's diameter the number of elements could be minimized, reducing significantly the computational time. The disc's inside diameter was set at 14.8 mm, which created the workpiece part some 10 times thicker than the undeformed chip thickness. The depth of the cut was fixed to 0.11 mm and width of the disc was 0.1 mm. These dimensions were fixed for simulation in this chapter.

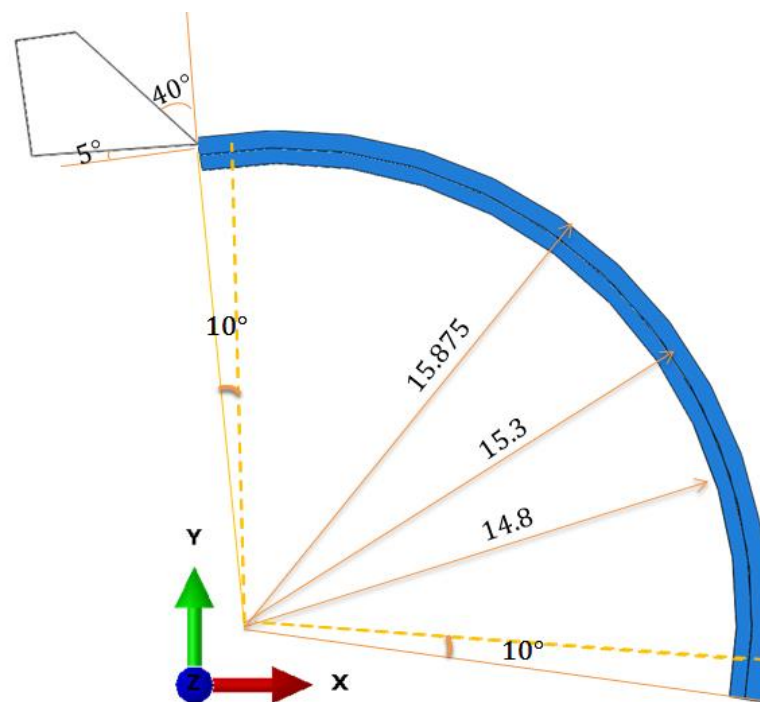


Figure 6:2 Geometry of cutting process (dimension in mm)

The disc was divided into two regions; one representing the SPH domain with inside and outside diameter equal to 15.3 mm and 15.875 mm (see Figure 6:2). The remaining part was used as a continuum FE domain. The simulations were carried out with relevant parameters shown in Table 6-1. The tool's geometry and cutting conditions were fixed based on the experimental study of Cohen (1982).

Table 6-1 Turning simulation parameters

Disc outside diameter: 15.875 mm	Disc inside diameter: 14.8 mm	Tool rake angle: 40°
Width of disc: 0.1 mm	Depth of cut: 0.11 mm	Cutting velocity: 0.55 mm/s

6.2.2 Configuration of coordinate system

The turning system of coordinates used in finite-element simulation is shown in the Figure 6:3. It is an aggregate of two systems of coordinates: crystal and a reference coordinate frame. Both systems are usually defined in terms of 3 orthonormal directions. In the case of crystal system $[hkl]$ is the cutting direction, $[uvw]$ is the cutting plane's normal and $[abc]$ is the zone axis. The reference coordinate system was fixed during the cutting process and was created by the combination of $[pqr]$, $[def]$ and $[abc]$ directions (see Figure 6:3). The cutting direction and the cutting plane normal change with the movement of tool on the disk's perimeter. Therefore, the turning model is able to predict the entire range of changing orientation around one fixed zone axes by covering one quarter of the full disk's tool perimeter.

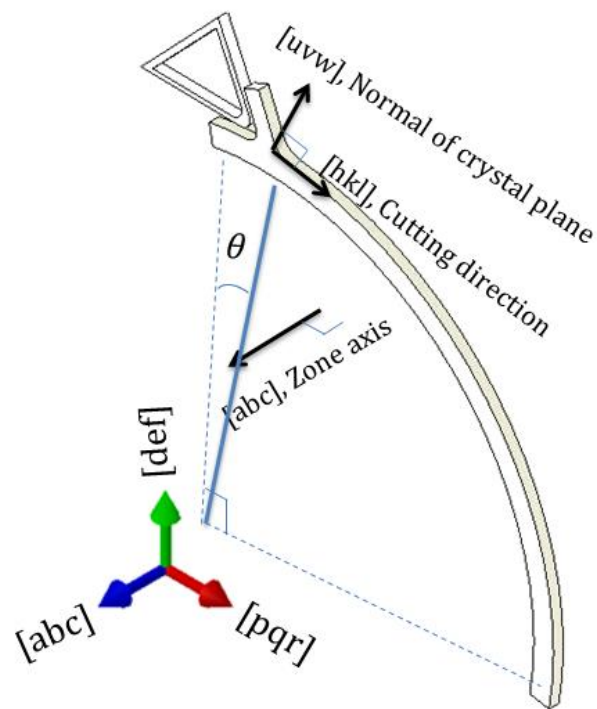


Figure 6:3 Relations between cutting coordinate system and reference cutting frame

One way to link these two coordinate systems is to define an angle (θ) from a reference axis $[def]$ that is perpendicular to the zone axis $[abc]$ to the cutting plane normal, $[uvw]$ as illustrated in Figure 6:3. This angle will be used to denote a position of the cutting plane normal during the turning process. In the turning experiments, the cutting forces were collected for specific orientation of the zone axis ($[abc]$ in Figure 6:3). As it is impossible to simulate all of the crystal orientations, the zone axes were chosen from position uniformly distributed over the standard stereographic triangle.

This triangle is a useful way to demonstrate orientations of the crystal axis. All possible orientations of a cubic-structure crystal can be specified by plotting the position of the specimen's axis within this triangle or along its boundaries (Gambin, 2001). The Figure 6:4 shows the standard stereographic triangle for f.c.c. cubic crystals. It is a two-dimensional drawing of three-dimensional data for basic

crystal orientation of f.c.c. structure. The dimensions of all crystallographic planes and directions are accordingly reduced by one. Hence, as in a typical stereographic projection, planes are represented by their normals and are plotted as points (Reed-Hill and Abbaschian, 1964).

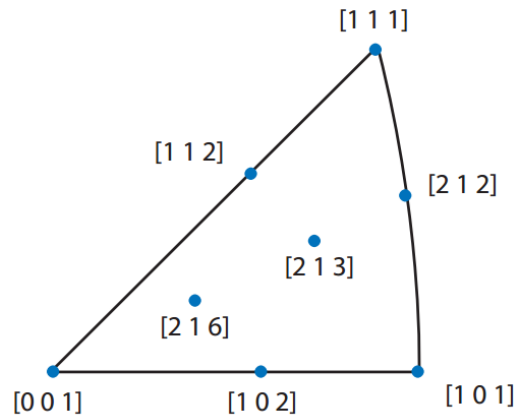


Figure 6:4 Standard-stereographic triangle for f.c.c. crystals

The eight different zone axis, namely, $[001]$, $[111]$, $[101]$, $[112]$, $[212]$, $[213]$, $[216]$ and $[102]$ were chosen. Table 6-2 shows the cutting direction and the normal of the crystal plane for these eight zone axes. These were obtained based on the rule discussed in Section 5.2.2.

Table 6-2 Three orthonormal directions for eight zone axes (see Figure 6:3)

$[abc]$	$[hkl]$	$[uvw]$	$[abc]$	$[hkl]$	$[uvw]$
$[001]$	$[100]$	$[010]$	$[212]$	$[20\bar{2}]$	$[\bar{2}8\bar{2}]$
$[111]$	$[10\bar{1}]$	$[\bar{1}2\bar{1}]$	$[213]$	$[30\bar{2}]$	$[\bar{2}13\bar{3}]$
$[101]$	$[10\bar{1}]$	$[020]$	$[216]$	$[60\bar{2}]$	$[\bar{2}40\bar{6}]$
$[112]$	$[20\bar{1}]$	$[\bar{1}5\bar{2}]$	$[102]$	$[20\bar{1}]$	$[050]$

6.2.3 Contact and boundary conditions

In the developed finite-element model; all the nodes at the bottom of the workpiece (Figure 6:5) were fixed in both the axial and tangential directions. To reproduce pure rotation of the tool around perimeter of the workpiece, the tool's surface should be defined as a rigid body. By selecting a reference point on the tool surface and fixing this to the center point of the workpiece by using a kinematic coupling constraint, one point could be used to define all of the tool's constraints. The center of the workpiece in the local coordinate system was considered as coupling node, and all the constrained degrees of freedom were implemented on it. Therefore, the constraint will enable the tool to rotate along with the reference node and fix its radial motion.

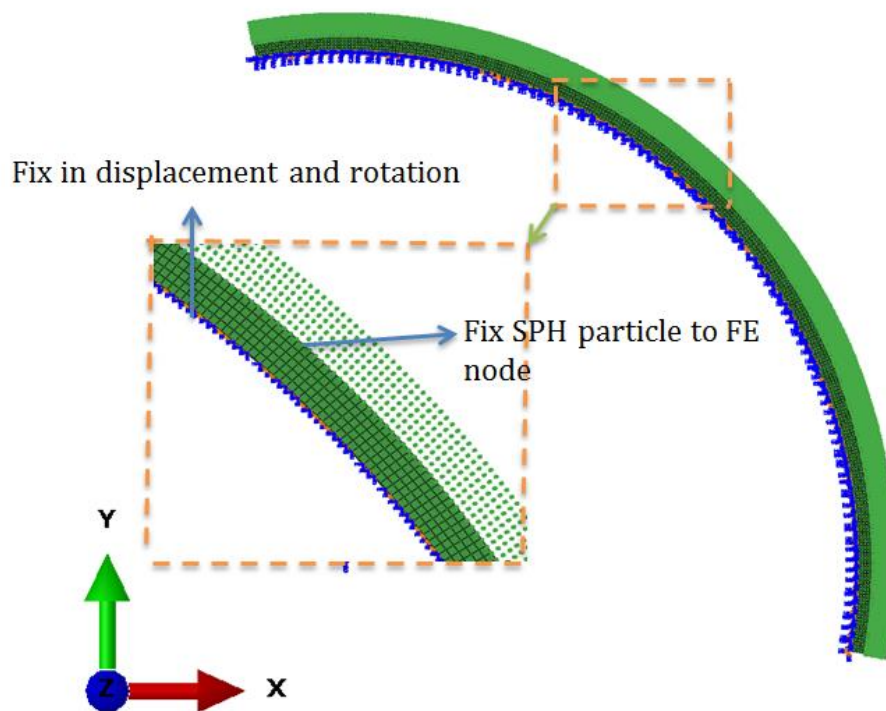


Figure 6:5 Boundary conditions

The connections between the tool and the workpiece were idealized using kinematic contact constraints. In the pure kinematic contact algorithm, the model is advanced into the predicted kinematic configuration in each increment of the analysis, regardless of the contact conditions. After determining, which slave nodes

in the predicted configuration penetrated the master surface, the forces required to oppose this penetration were calculated based on the penetration depth of each slave node, the associated mass, and the time increment. The resisting forces and masses of the slave nodes were distributed to the master surface-nodes, which were used to calculate an acceleration correction form (Kishawy *et al.*, 2002).

In finite-element simulations, a friction model is one of the key input boundary conditions. The classical Coulomb friction model, similar to the orthogonal machining simulation described in Section 5.2.5 was adopted for contact modelling in the normal and tangential directions, while the accuracy and better representing physics of the metal-removal process by implementing different types of friction models is still undetermined and controversial (Özel, 2006).

6.2.4 Mesh

Apparently, the three-dimensional rigid body used to model the tool does not need to mesh, while the disk was meshed with PC3D elements for SPH domain and C3D8R element for the rest of the domain (see Figure 6:5). The important aspect of developing a finite-element model is to select a proper element number to discretize the model. The number of elements should be large enough to make an accurate sensitivity analysis in order to validate numerical results. Generally, an increase in the number of elements means more accurate results. However, if the number of elements is increased beyond a certain number, the accuracy cannot be improved significantly, or, on the contrary, it may produce even less accurate results because of errors introduced by mesh generation (Zienkiewicz and Taylor, 1977).

To find a compromise between the conflicting requirements of accuracy and computational cost, a mesh-sensitivity analysis of the workpiece was performed. Based on that it was found that, a mesh with a minimum element size of 100 μm was sufficient to characterize accurately the behaviour of the developed model during the turning operation. By considering of the disc's inside diameter equal to 14.8 mm, the number of elements was reduced. The workpiece was modelled with

7320 particles. Schematics of the initial finite-element mesh configuration are shown in Figure 6:5.

6.2.5 Experimental verification

The specific cutting energy is defined as the energy required for removing a unit area of material. It is calculated by dividing the measured cutting force by the chip area, which is computed from the product of uncut chip thickness and the width of the cut. In this case, the chip area was equal to 0.011 mm² and considered for all the simulations.

To validate the proposed model, the variation of specific cutting energy obtained from the model was compared to the data by Cohen (1982) obtained in a diamond-turning experiment on a single crystal of copper performed inside a SEM system. As shown in Figure 6:6, the calculated variation of cutting energy matches well with the experimental results. The relatively good agreement between experimental and simulated results suggests that the finite-element model developed in this study can be successfully used to model single-crystal turning. The model was run for the [001] zone axis.

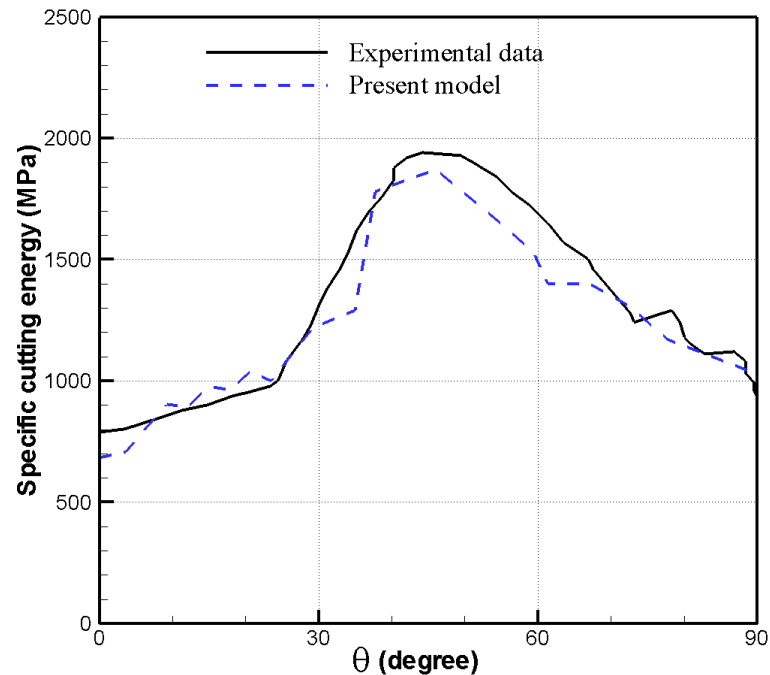


Figure 6:6 Comparison of model predictions and experimental data (Cohen, 1982) for [001] zone axis

The developed model predicted that the maximum cutting force for [001] zone axis happened after 42°-44° degree of initial rotation, and the minimum were at the initial and final stage of 90° rotation. Having two additional segments of 10° each at both ends of the disc geometry (discussed in Section 7.2.1) allowed assessment of the entire range of cutting force over $\theta \in [0^\circ, 90^\circ]$ without the effect of boundary area. The magnitudes of specific cutting energy for machining of these two segments are not presented in Figure 6:6 as well as in the diagrams below.

The practical trend of variation was again successfully captured by the model. The variation in specific energy arises from the crystallographic anisotropy. When interpreting this data, it should be considered that the shear direction (or overall slip direction) would make an angle (shear angle) with the cutting direction at each orientation angle (θ). The approach adopted here to predict the fluctuation in the cutting force was based on the changes in the shear angle and shear strength of the crystallites being cut as discussed in Section 5.3. Figure 6:7 presented the strain distribution for 12 slip system of f.c.c single crystal. Therefore, if the shear

direction is aligned with one of the preferred slip directions, lower forces and specific energies are expected to get.

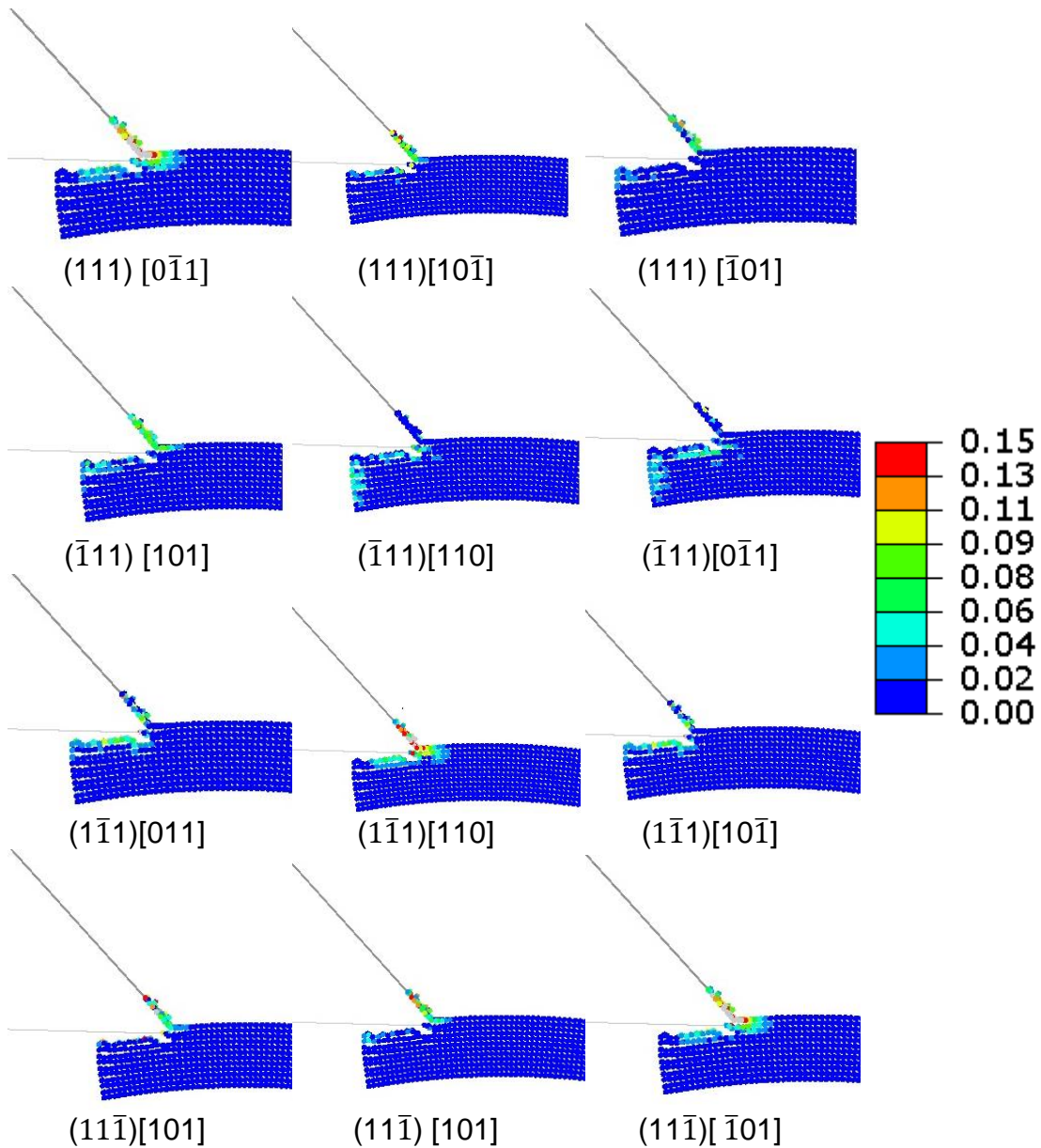


Figure 6:7 Strain distribution over 12 slip systems

6.2.6 Shortcomings of model

A rectangular region was computed at the beginning of the analysis as the bounding box, within which the particles separated from the main model in the

process of material removed were tracked. This fixed rectangular box was 10% larger than the overall dimensions of the whole model, and it was placed at the geometric center of the model. As the analysis progressed, if a particle enters the area outside this box, it behaved like a free-flying point mass and did not contribute to SPH calculations. If the particle returned the box at a later stage, it was once again included in the calculations. The problem aroused that this rectangular region could not be converted to the circle as needed in turning simulations. Therefore, the damage particles flow away; however, they were still in the rectangular region and being computed. Having such particles (see Figure 6:8) increased the calculation time by a significant amount. However, these free particles outside of the contact region did not affect the cutting-force results, but caused each running to take around 7 days using HPC with one core.

Running some parallel jobs is a way implemented in this study to save the time. In the next section, the specific cutting energy variations for eight zone axis are studied.

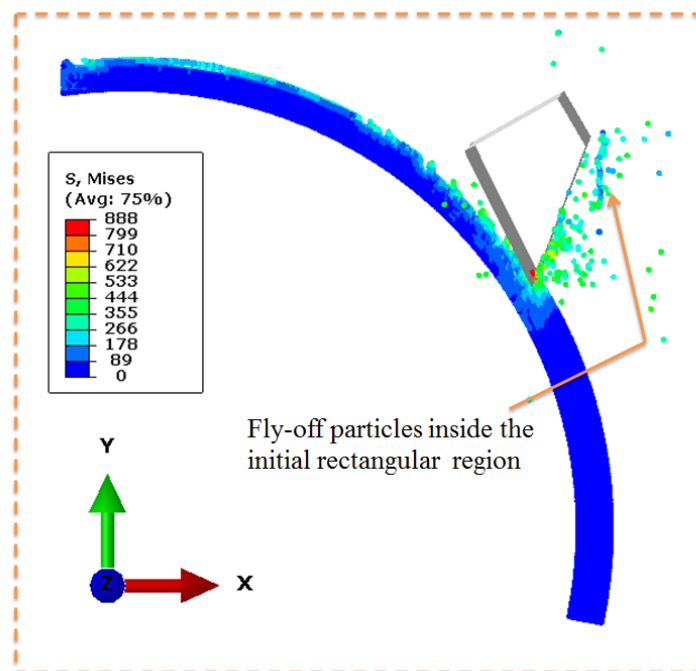
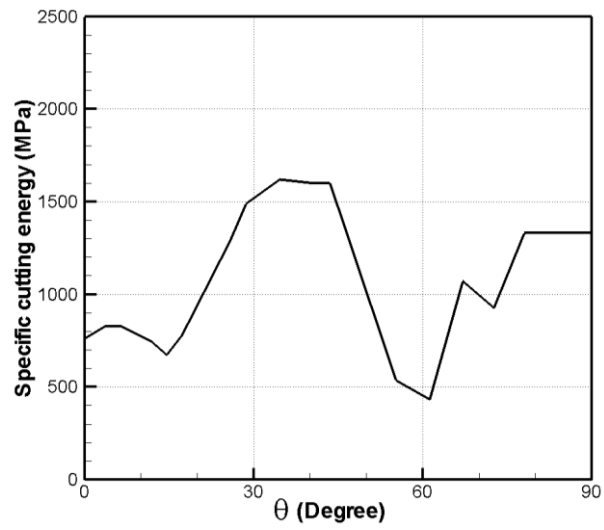


Figure 6:8 Fly off particles inside rectangular box

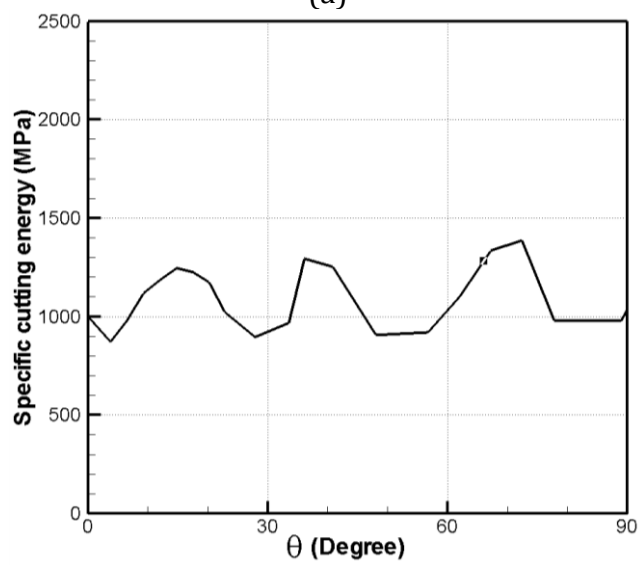
In the turning modelling case, using the finer particles allows a better modelling of the chip curve and a better evaluation of the matter state on the surface. Due to the lack of neighbours, the present model did not correctly calculate the surface roughness. Indeed, a particle located on a free edge of cutting tool only interacts with existing particles. The numerical instability of the SPH method for the turning model was represented as numerical fractures observed in the surface of the machined workpiece. Increasing the number of particles could decrease these instabilities. However, increasing the mesh size caused the increase of the computational time significantly.

6.3 Cutting-force variation for fixed zone axis

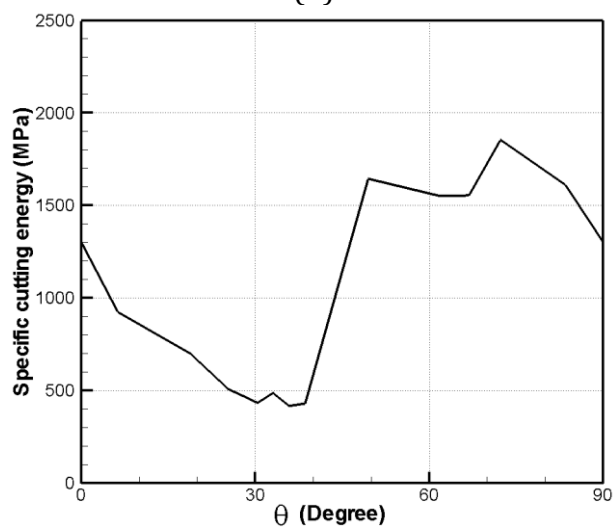
When cutting is performed within a grain, the crystallographic orientation of the materials being cut exerts a significant influence on the cutting mechanism and, hence, the cutting forces. To study the effect of the cutting direction and crystallographic orientation on the cutting energy, eight fixed axes discussed in section 6.2.2 were chosen: [001], [101], [111], [213], [212], [102], [112] and [216]. The calculated cutting energy as a function of crystallographic orientation θ , for a constant cutting speed of 0.55 mm/s is shown in Figure 6:9. The results demonstrate the variation in the specific cutting energy (force) for machining copper crystal for each zone axes.



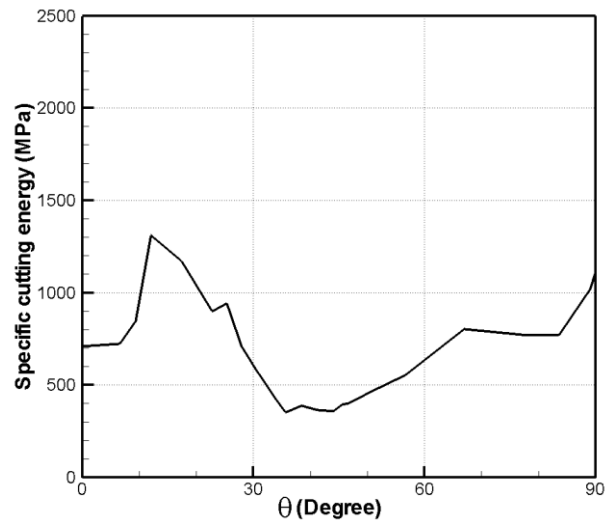
(a)



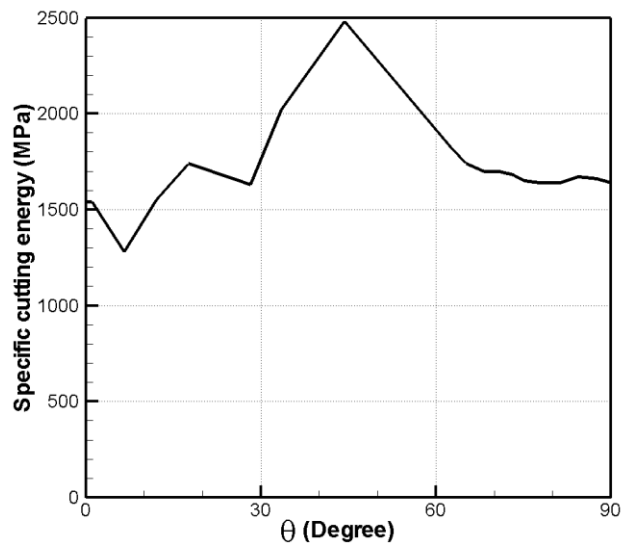
(b)



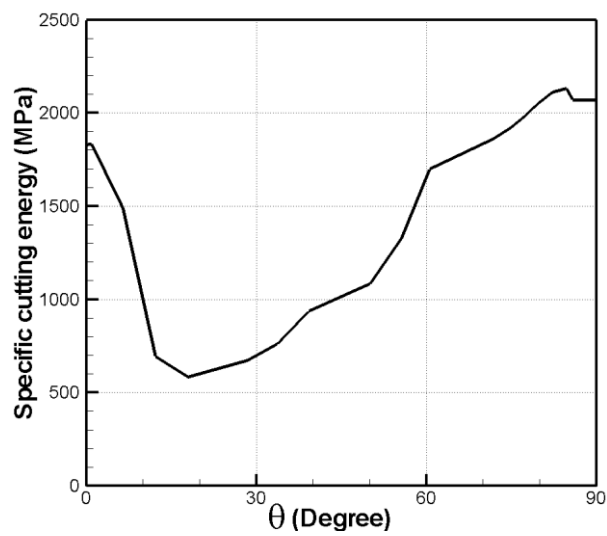
(c)



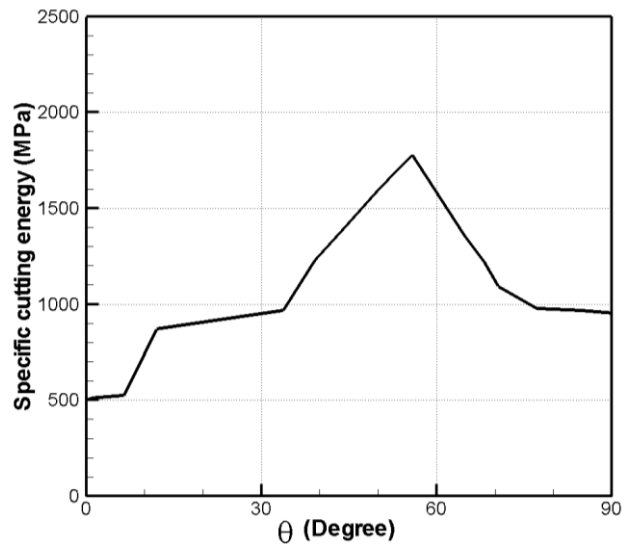
(d)



(e)



(f)



(g)

Figure 6:9 Variation of specific cutting energy in modelling of micro-machining for eight zone axis: (a) [101]; (b) [111]; (c) [213]; (d) [216]; (e) [212]; (f) [112] and (g) [102]

As the disc is continuously in relative rotation, the calculated forces are associated with such variations. The reason of this pattern which is recorded for cutting energy (force) of single copper crystal in different zone axis is the number of the slip system active in each rotation increment. The mechanics of cutting depend strongly on the crystallography and the orientation of the slip systems of the copper single crystal, which is highly anisotropic in terms of both its elastic and plastic properties. Various strains are accumulated from the beginning of the cutting process, including increased strain hardening. After rotation of the cutting tool in the first 10° sector, the cutting force increased from zero to a certain level. By increasing the rotation angle (θ) the state of the stress caused the slip occur on different systems, which have more preferable in the present orientation. The new slip system is also unstable, and it changes by further cutting tool rotation. It is necessary to mention here such a cutting force variation phenomenon was not observed when the large numbers of crystals are involved in turning process (de

Agustina *et al.*, 2013). Since the material behaves isotropic by taking the average mechanical property of crystals.

Due to the above discussion, the specific cutting energies closely follow the related cumulative slip required to adopt the deformation. The amount of shear slips during turning deformation is calculated by Schmid's analysis mentioned in more detail in section 4.15.3. Although the existence of lattice rotations described in Section 5.3 prevents the generalized prediction of the proximity between shear planes and slip direction in advance. For example, it is expected that the lowest specific cutting energy can be gained at a zone axis that would allow the shear plane to be a slip plane, and the shear direction to be a slip direction associated with the slip plane. In order for such a scenario to occur, the slip plane should coincide with the shear plane, and the slip direction should also be aligned with the shear direction. This indicates that both slip planes normal and the slip direction must be perpendicular to the zone axis.

No symmetry is observed in the signature of specific cutting energy for most cases of chosen zone axes. Only [111] crystal orientation demonstrated a slightly symmetric pattern, which rised from crystallographic symmetry about [111] zone axes for f.c.c. structure.

Careful observations of the specific-cutting-energy (force) patterns for each quarter- revolution showed the existence of a major peak and a valley as well as a minor peak and a valley. Table 6-3 present the maximum and minimum value of specific cutting energy followed by an orientation angle (θ) and the average value of specific cutting energy for each zone axes. This is an extremely important observation and indicates the sensitivity of the process to material crystallography. Having the maximum and minimum energy for specific cutting zone axes represented the variation of cutting energy to material crystallography.

Table 6-3 variation of cutting energy versus θ°

Zone axis	Max		Min		Mean
	Val. (MPa)	θ (degree)	Val. (MPa)	θ (degree)	
[102]	1717	50°-55°	502	0°	1029
[112]	2171	86°-90°	583	15-20°	1532
[212]	2481	44°	1277	7°	1764
[216]	1315	12°	350	35 °-40°	718
[213]	1855	72°	435	30°	1021
[111]	1403	10°,40°,70°	753	31°,56°,86°	1102
[101]	1600	35°-40°	431	60°	1065
[001]	1930	42°-44°	685	0°	1207

The mean specific cutting energy provides information on the case of machinability in particular zone axes. The higher average values of specific cutting energy are recorded for those zone axes that have a higher active number of slip systems for accommodating the deformation. For instance, in turning model for the [212] zone axis in the nearly most of the orientation angles at least 5 slip systems active and accommodate the deformation while for [216] zone axis the maximums 4 active slip systems are observed. Hence, the lower average values of the specific cutting energy are expected in this zone axis. Machining in such orientation requires less energy in comparison to other cases studied.

The deviation of the average specific cutting energy from maximum and minimum results from the difference in proximity of slip systems at different orientation angles about a given zone axis. Generally, for selected orientation studied while in the [216] zone axis, around 35°-40° rotation angle produced the minimum cutting force happen via single slip, the maximum one was consistently observed to occur at a constant 44° rotation from cutting direction in [212] zone axis require up to five slip systems to be simultaneously activated, and thus causing high-value cutting force.

The results from the turning studies demonstrate the effect of the anisotropy of f.c.c. crystals on the specific cutting energy, inducing variation of up to 140% for different crystallographic orientations for the selected orientation studied, for the copper crystal. The maximum and minimum difference between average values showed the variations due to crystallographic orientations reaching as high as 150% of the average calculated for all orientations. This behaviour of cutting force was in congruence with the existing literature (Kota, 2011) which was based on the plasticity theory and the Merchant's machining model.

These data can be used, for instance, in an operation like milling, where the rotation of a tool caused continually changing cutting direction about the fixed zone axis. The schematic of the milling operation is shown in the Figure 6:10. Like the turning process, where rotation of the workpiece causes the changing of the cutting direction and cutting plane normal of the single crystal at each time, rotation of the tool in milling has the same effect for a fixed zone-plane normal.

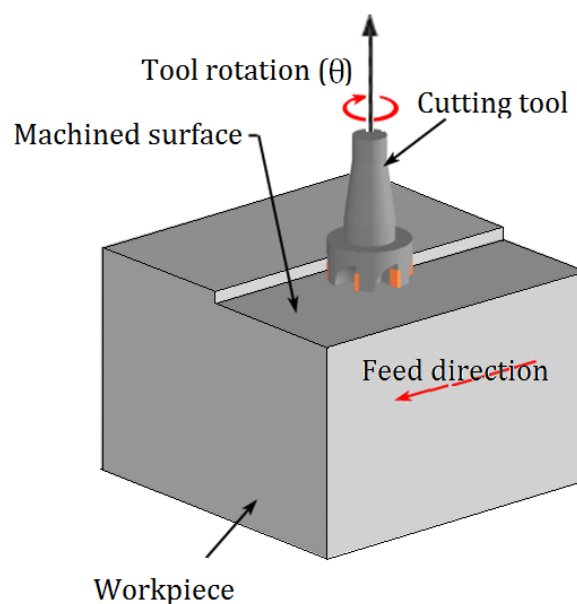


Figure 6:10 Milling operation

6.4 Study of cutting parameters in turning

During a turning operation, it is an important task to select cutting parameters for achieving high cutting performance. Usually, the desired cutting parameters are

determined based on experience or using a handbook. Although the crystallographic structure effects strongly the machining process, the effect of material anisotropy is often not included in the textbooks. The present developed model could be a suitable way to study the effect of cutting parameters on the turning process. The relationships between the cutting parameters of turning with simulations for different crystallographic orientations of the workpiece materials are explored in the next section.

To investigate the effect of cutting parameters on the energy pattern along the tool–chip interface, 18 simulation cases were selected (see Table 6-4). For these 18 cases, a number of comparisons can be made. To show the effect of friction on machining of copper, three magnitudes of the coefficients of friction ($\mu=0$, $\mu=0.12$ and $\mu=0.4$) were compared. This selection was based on frictionless condition, normal coefficients of friction and non-lubricated interface. Additionally, to investigate the effect of cutting speed, three levels of cutting speed (0.45 mm/s, 0.55 mm/s and 0.65 mm/s) were adopted for simulations of machining of copper. To study the effect of single-crystal orientation, each setup was repeated for three cases of cutting for fixed zone axis [100], [101] and [111].

Table 6-4 Simulation setups for study friction and cutting velocity in turning

	Friction			Cutting velocity (mm/s)		
	$\mu=0$	$\mu=0.12$	$\mu=0.4$	0.45	0.55	0.65
[100]	Case 1	Case 2	Case 3	Case 10	Case 11	Case 12
[101]	Case 4	Case 5	Case 6	Case 13	Case 14	Case 15
[111]	Case 7	Case 8	Case 9	Case 16	Case 17	Case 18

Note that due to the limitation of an instability problem (a typical challenge for SPH), it was not possible to further increase the range of cutting speed based on presenting geometry. Decreasing the cutting speed to levels below 0.45 mm/s was also not convenient due to limitation of computation power. For instance, for the

cutting speed of 0.35 mm/s, the run of simulations took 10 days by using the HPC cluster of 1 node and 1 core.

6.4.1 Effect of friction

In order to study the effect of friction along different crystal orientations, the same tool–disc geometry was selected. The values of friction coefficients ($\mu=0$, $\mu=0.12$ and $\mu=0.4$), were chosen, and machining simulations were performed around the fixed [001], [101] and [111] zone axis. Sensitivity of the cutting force to friction was presented in Figure 6:11.

It is seen from Figure 6:11 that the behaviour of the cutting energy (force) curves versus the orientation degree (θ) follows a particular pattern for all the studied cases investigated for one zone axis. The overall shape of the specific cutting energy curves does not vary significantly with friction factor, whereas the mean specific cutting energy increased due to increased require the amount of work for overcoming the friction. The related results deliberated in Section 5.6.1 for one orientation setup confirms this pattern. This study revealed that the higher coefficient of friction, the higher amount of energy required for initiating plastic deformation and shearing of the material. This, therefore, increases the cost of machining as machining force is increased. When a single-crystal copper was being turned, the response of the cutting force to different coefficients of friction in different orientation was a nearly similar pattern.

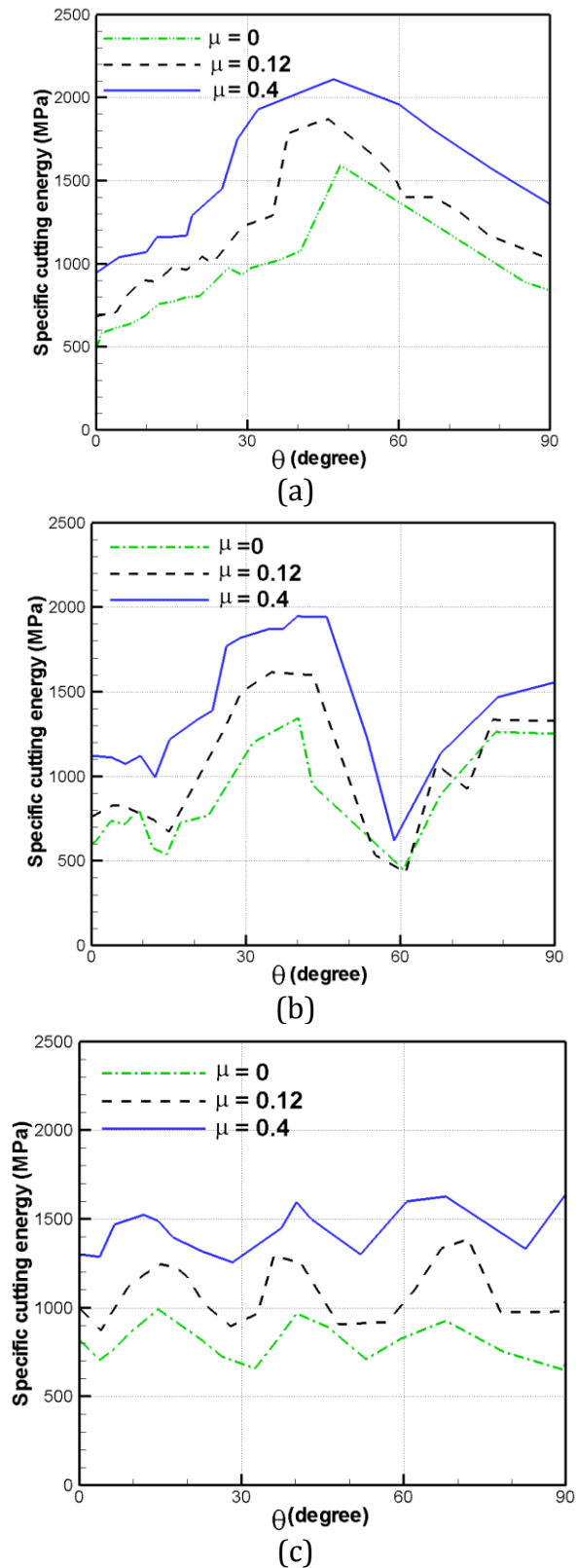
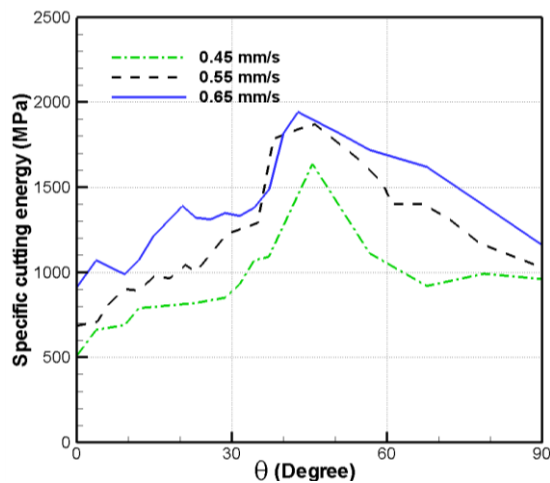


Figure 6:11 Effect of coefficient of friction on specific cutting energy pattern for (a) [001]; (b) [101] and (c) [111] zone axis-(case 1 to 9)

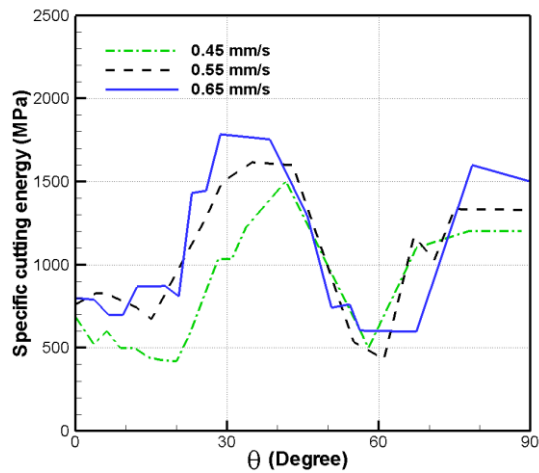
6.4.2 Effect of cutting velocity

The effect of cutting velocity on the specific-cutting-energy data was calculated for machining about [001], [101] and [111] directions and shown in Figure 6:12. In these simulation setups, the coefficient of friction was fixed to 0.12. In the same as the friction factor by increasing cutting speed approximately constant pattern appears for each zone axis. Increasing cutting speeds were observed to produce higher value of the specific cutting energies. However, within the range of cutting velocities considered in this work, the effect of cutting velocity was seen to be small. Averaging over the whole crystallographic orientations, the specific cutting energy is only 30% higher at 0.65 mm/s than at 0.45 mm/s.

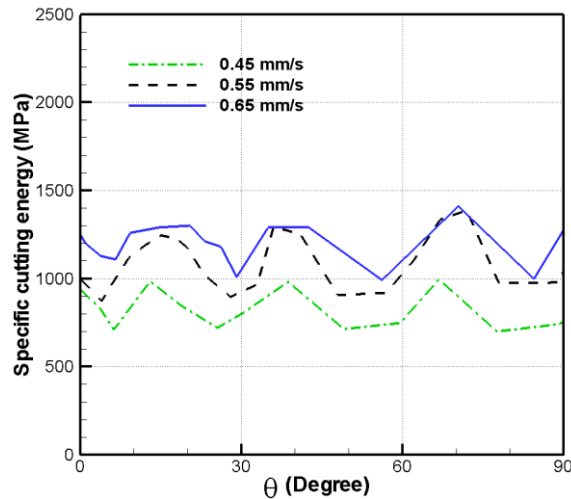
Selecting of 0.55 mm/s for cutting speed was based on an experimental study in Cohen (1982) and the other two cutting speeds were selected based on modelling limitation discussed in Section 6.4. The proposed model was valid for [001] zone axes with 0.55 mm/s cutting speed, and the rest of the results were the model predictions.



(a)



(b)



(c)

Figure 6:12 Variation on cutting speed in specific cutting energy for three different zone axes; (a) [001]; (b) [101]; (c) [111]- (case 10-18)

Generally, a change in the cutting velocity affects the cutting process through two opposing mechanisms. First, a higher cutting velocities increased strain rate deformation. Second, for a wide range of cutting speeds by increasing the cutting velocity the workpiece temperatures started to increase. The softening of material is the result of growth temperatures to reducing the specific cutting energies. The temperature is not incorporated in the presented crystal plasticity formulation. Thus, the relatively low-speed cutting regime followed by low cutting depth is considered in the current study to minimize the effect of the temperature and

hence, the increase strain hardening is considered as a main reason for increased the specific cutting energy.

The increased strain hardening resulted in the material's resistance to deformation and ultimately higher machining cost. The effect of cutting speed is seen mainly on the stress distribution for a given applied strain. The resulting stress distribution is related to the strain rate through a power law relationship, typically in the form of τ and n (Eq 4-9), where τ is the shear stress, $\dot{\gamma}$ is the strain rate, and n is the coefficient of rate sensitivity. The strain rate is directly proportional to the cutting velocity and typical values of n for metals range from 10 to 30. Consequently, the effect of strain rate, and thus, the cutting velocity, on the stress response is relatively small. In the current set of simulations, the increase in specific cutting energy was seen to be 30% for a 45% increase in the cutting velocity.

Since the coefficient of rate sensitivity (n) is commonly independent of the orientation, the effect of speed is expected to be uniform across all orientations. However, the interaction effect between the number of active slip systems on different crystallographic orientation and the level of weight in the cumulative strain at each rotation increment caused slight variation in pattern.

6.5 Summary

This chapter presented the developed turning finite-element model with analysis of cutting forces for machining of single-crystal f.c.c. metals. The orthogonal machining configuration is reported a very limited number of orientations. Therefore, all orthogonal single crystal work draws conclusions from a very limited database. By utilizing single crystal disk specimens and machining around the periphery, an infinite number of orientations may be examined in a systematic manner. This allows for an orderly examination of many orientations as well as an investigation of the patterns which may occur due to the basic triangular crystallography for f.c.c. structure.

The FE/SPH approach in modelling turning processes in the small scale was shown to be a viable method for simulation of large-deformation problems without compromising the underlying physical mechanisms that drive deformation in crystalline materials. An experimental validation of the model was carried out by using data from the literature for machining of copper single-crystals.

The model was then applied to analyse the influence of crystallographic orientation on specific energies for eight crystallographic orientations that are uniformly distributed over the basic stereographic triangle. The variation of cutting energy at different crystallographic orientations can vary by up to 140% for turning process of crystalline copper. The increased levels of speed and friction were seen to increase the mean specific energies relating the similar patterns for the whole data of orientation setups. This means that, for a given zone axis direction, neither friction nor the cutting speed affects the type of variation significantly.

Although the simplified model provides a good accuracy for incorporating the crystallographic anisotropy into the machining model, the computational cost is still a shortcoming of it.

Vibration-assisted-single crystal machining model

7 Vibration-assisted single-crystal machining model

7.1 Introduction

A direct application of vibration in the machining processes is a new technique developed rapidly in the last two decades. Vibration-assisted machining (VAM) is an advanced method developed for machining of tough and brittle materials such as super alloys, ceramics, single crystals and glass (Grzesik, 2008; Babitsky *et al.*, 2003). Although vibration-assisted machining can be used to machine nearly all materials, it is not cost effective for materials of hardness less than 50 HRC (Thoe *et al.*, 1998). It's preferable use is for machining of materials that cannot be machined with conventional processes.

Regarding to the discussion in Section 1.2.2, the application of single-crystal machining is limited not only to micro-machining. Many single-crystal solids are known as high-strength materials with low-thermal creep. The common application of such material is in turbine blades. These are capable to operate at

high working temperatures than crystalline turbine blades and thus can increase the thermal efficiency of a gas-turbine cycle (Pollock and Tin, 2006). The VAM technique can be easily applied to the expanding needs of machining such a material and increasing complex operations to provide intricate shapes and workpiece profiles.

The schematic of VAM is presented in Figure 7:1. The movement of cutting tool in the feed direction of machining operation contains vibrations with a high constant frequency and low amplitude. The tool periodically loses contact with the chip in a case of a right combination of cutting and vibration parameters. Mechanics of Advanced Material Research Group at Loughborough University, UK has worked on the VAM of modern alloys for some 10 years (Ahmed *et al.* 2007). The studies of this team and also other researchers (Singh and Khamba, 2006, Shamoto and Moriwaki, 1999) demonstrate a considerable improvement in surface roughness of the machined workpiece and a significant reduction in the cutting forces by implementing suitable vibration.

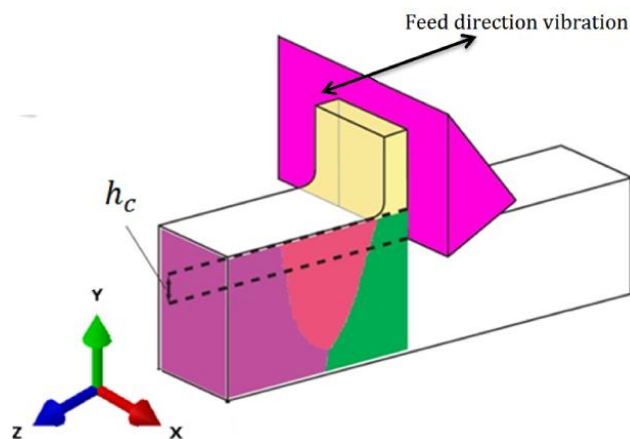


Figure 7:1 Schematic of vibration-assisted machining (VAM)

Accuracy and surface finish plays an important role in modern industry. The characteristics of hard-to-machine material make it difficult to achieve the desired part quality. Based on the literature and the results demonstrated in Section 5.4 and Section 6.3, the crystallographic structure of metals has a

significant effect on the cutting force. In nearly all previous studies, the isotropic material parameters were assumed for the cutting-force analysis of the VAM process. As all the experimental studies were carried out on the real crystalline material, there is an essential need to incorporate the crystalline effects during deformation of material with the machined VAM process in order to get a better understanding of them and also to compare the results.

The high potential for applications and significant improvements when VAM was used in machining of crystalline materials were the main reasons to choose this process as the third case of the process in this study. The effect of crystalline structure in cutting-force evaluation in VAM was deliberated in this thesis for the first time. The details of the developed multi-scale finite-element modelling of VAM single-crystal machining are explained, followed by analysis of the effect of various vibration parameters, i.e amplitude and frequency of vibration, on the cutting forces for various cutting directions.

7.2 Modelling procedure

An approach for a three-dimensional simulation of a VAM process with the use of the FE/SPH method with ABAQUS/Explicit (v.6.11) program is demonstrated in the following sections. The crystallinity formulation described in Section 4.2.2 was implemented in the material property of the workpiece in the form of VUMAT subroutine. In order to compare the cutting-force behaviour, new model for orthogonal conventional machining (CM) was also developed. The main configuration of models for both processes- VAM and CM - was the same. The main difference was that in the VAM model some additional boundary conditions were required to reflect the cutting tool's vibration. Sections 7.2.4 and 7.2.5 describe these differences in more detail.

7.2.1 Geometry configuration

A 3D deformable body was selected as a workpiece while the rigid body was considered for the cutting tool. The length of the workpiece in numerical simulations was $250\ \mu\text{m}$, the height was $100\ \mu\text{m}$ and the thickness was $10\ \mu\text{m}$. The workpiece was divided into two equal regions, one representing the SPH domain ($250\ \mu\text{m} \times 50\ \mu\text{m} \times 10\ \mu\text{m}$) and the remaining part a continuum FE domain (Figure 7:2). The rigid cutting tool had a zero rake angle and cutting edge radius of $2\ \mu\text{m}$. The clearance angle of the tool was equal to 5° . The depth of cut was fixed to $5\ \mu\text{m}$ in nearly all of the simulations in this chapter. A schematic of the three-dimensional finite-element model is shown in the Figure 7:2.

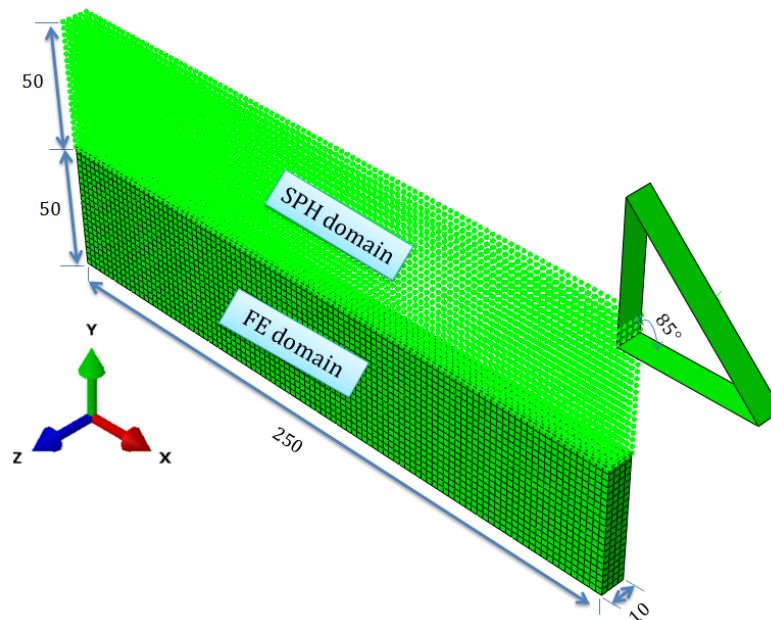


Figure 7:2 Three-dimensional FE/SPH model of VAM (dimensions in μm)

7.2.2 Orientation setup

To set the model orientation with regard to crystalline axes, the same planner configuration used in Section 5.2.2 was assumed. The tool cut along a particular crystal direction $[hkl]$ on a chosen crystal orientation $[uvw]$.

7.2.3 Definition of material properties

The crystal-plasticity constitutive model proposed in Section 4.2.2 was used for definition of the machined material. Single crystals of copper and aluminium were used commonly for crystal-machining study in the literature (see Table 2-3). In order to study VAM, aluminium was selected as a material for this case study. The material properties of aluminium presented in Section 5.5 were used for VAM.

7.2.4 Boundary conditions

The general node-based contact conditions were used for the tool-workpiece interface. The slave surface (SPH domain), which is mechanically less stiff than the master surface (tool), was defined for contact parts. The typical Coulomb friction law with a constant coefficient of friction $\mu = 0.12$ (Zhou and Ngoi, 2001), was used to contact of the cutting tool, with the workpiece.

The tool was rigid and designed to oscillate harmonically in the cutting direction to investigate its effect on the workpiece material. The vibration motion of the tool in the x direction can be written in the following form:

$$x = Vt + a \sin(\omega t), \quad 7-1$$

where a and ω are the vibration amplitude and angular frequency, respectively; V is the constant tool speed. The vibration speed of the cutting tool can be derived by differentiating of displacement, as

$$v_x = V + a \omega \cos(\omega t), \quad 7-2$$

Here, the angular frequency ω is represented by

$$\omega = 2\pi f, \quad 7-3$$

where f is the frequency of vibration. The tool's vibration speed varies from a minimum of $(V - a\omega)$ at any valley to a maximum of $(V + a\omega)$ at midpoint of each cycle. It is upward and downward motion.

In the CM model the cutting-tool motion is limited to

$$x = Vt. \quad 7-4$$

Therefore, the velocity should be constant during deformation as

$$v_x = V. \quad 7-5$$

Sample variations of tool's displacement and velocity in VAM and CM are shown in Figure 7:3. The values $f = 20$ kHz and $a = 20$ μ m were fixed for VAM and $V=1$ m/s is considered for both models presented in Figure 7:3. However, though the final displacement of the cutting tool over 0.2 ms is the same, the way to reach this penetration is different in both scenarios. Based on the presented tool's motion for VAM during the penetration stage, the tool came in contact with the workpiece at the presentation stage, whereas in the retraction stage, the tool separated from the workpiece material. In the CM model, the cutting tool had permanent contact with the workpiece material.

Figure 7:4 shows the regions when the tool contacts workpiece (blue colour) and it is free (red colour). It was concluded that the time of tool-workpiece contact (machining operation) was approximately 43% in one complete cycle of VAM while the rest of the time, the tool was fully separated from the workpiece material.

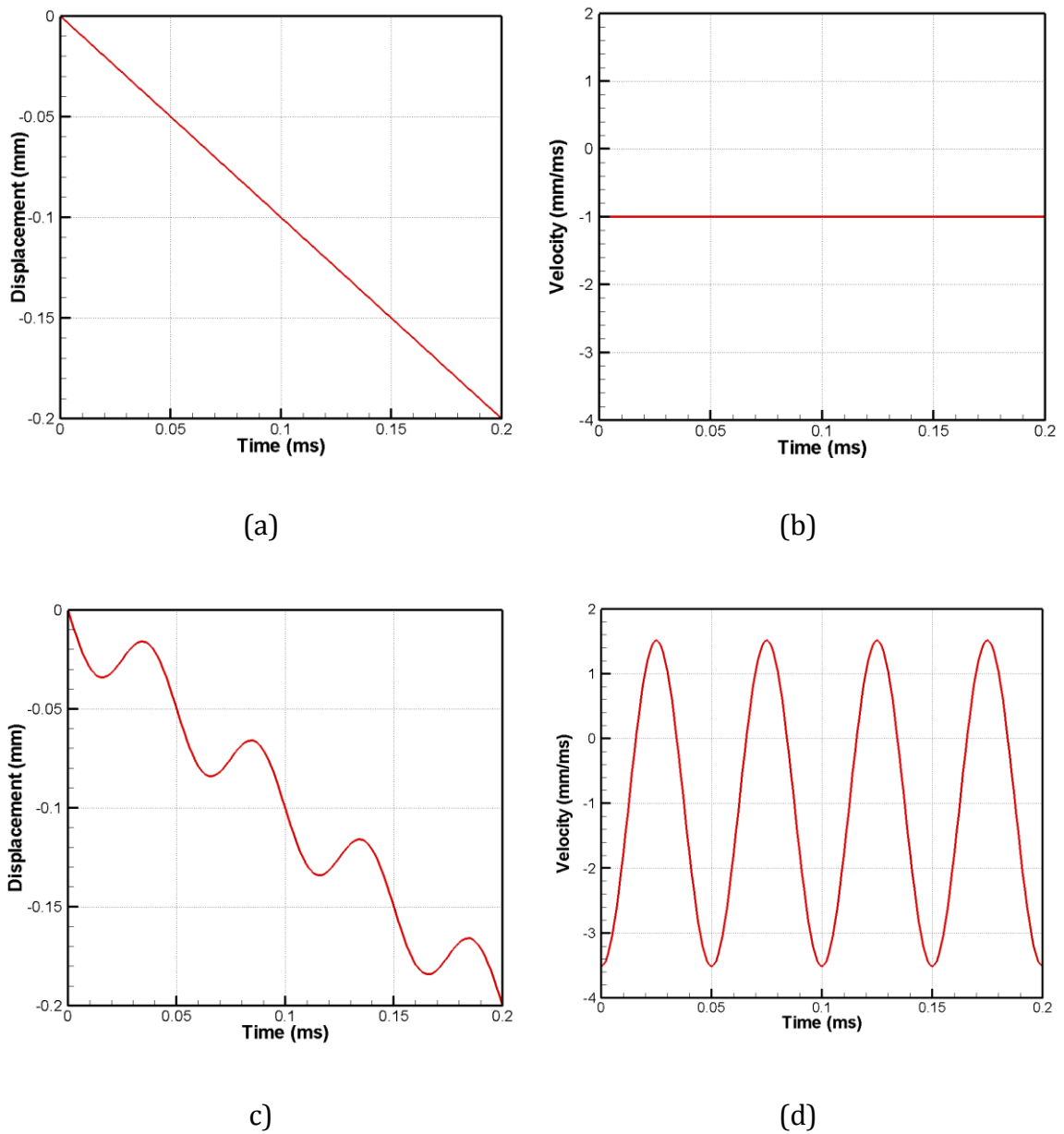


Figure 7.3 Cutting tool's displacement and velocity in CM model ((a) and (b)) and VAM model ((c) and (d))

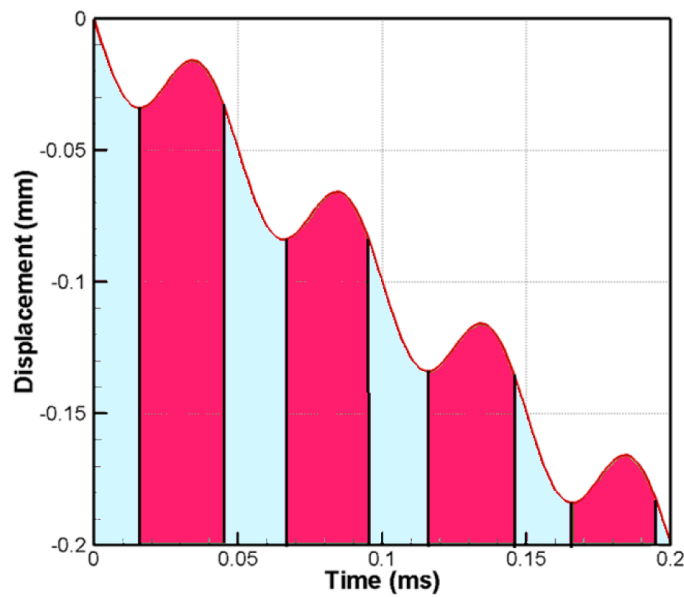


Figure 7:4 Tool-workpiece contact zone for VAM

After implementation of a boundary condition on cutting tool in order to have kinematic simulations of VAM and CM the workpiece needs to have some constraints. The bottom and left-side nodes of the workpiece were fixed with regard to displacements and rotations (see Figure 7:5). A 'tied contact' condition was specified for the interface nodes between the SPH and FE domains (the same contact as mentioned in Section 5.2.5). This condition basically 'ties' together the surfaces of a contact pair.

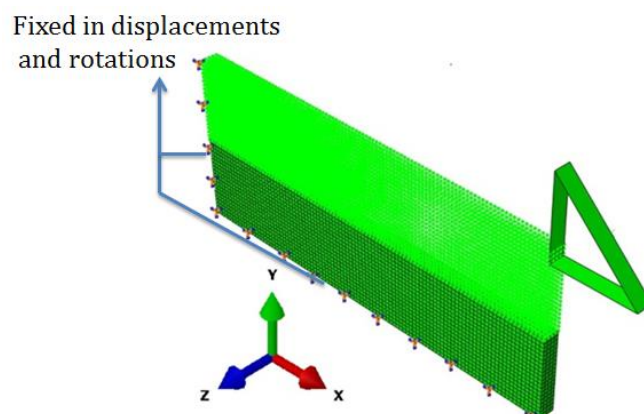


Figure 7:5 Workpiece constraints

7.2.5 Step selection

The cutting-tool velocity has a periodic behaviour over the time for VAM (Figure 7:3 d). Hence, proper contact conditions for the tool-workpiece interface should be well-defined and imposed without affecting the stability of the SPH domain in the model. Implementation of the harmonic velocity in contact with the SPH domain is not as straightforward as in the FE-based numerical models. Abrupt changes of the cutting-tool velocity in contact to the particles in the SPH domain during short time periods caused instability phenomena to happen in the SPH area. For a variety of problems with extremely large deformation, moving boundary or discontinuities, particles in SPH method are very attractive. Instability is a problem that has long troubled conventional SPH method and greatly limited its application. It has been shown that instability in tension for the standard cubic-b-spline kernel function generated whenever $r > 0.6h$ (approximately). This instability of particles in contact with the non-unique velocity area did not allow introduction of a unique step for the whole time domain. This has been regarded historically as one of the weakest points of the particle methods (Cossins, 2010).

For this reason, the model defined a sequence of 50 analysis steps. It provided a convenient way to capture the tool's velocity behaviour using a linear scheme in order to define nonlinear base states. The state of the model at the end of one general step provided the initial state for the start of the next general one. As the tool velocity is constant in CM, the whole procedure can be modelled in one step.

7.2.6 Mesh sensitivity

The continuum domain was meshed with eight-node brick elements with reduced integration (C3D8R), while the PC3D element type was used to represent the SPH area. In the analysis process, when the considered element's size is too small, too many elements are generated. This increases computational intensity, resulting in a model that is either too time-consuming to solve, or in potential errors in the calculated values. Therefore, a reasonable element size (number of elements) is a

main factor that should be considered in a finite-element analysis. Hence, the mesh-sensitivity study was performed, based on Figure 7:6, the optimized model in terms of the number of elements was made by 14491 brick elements with 21517 nodes. The element size of $1.25 \mu\text{m}$ in the continuum FE domain was sufficient to characterize accurately the machining process.

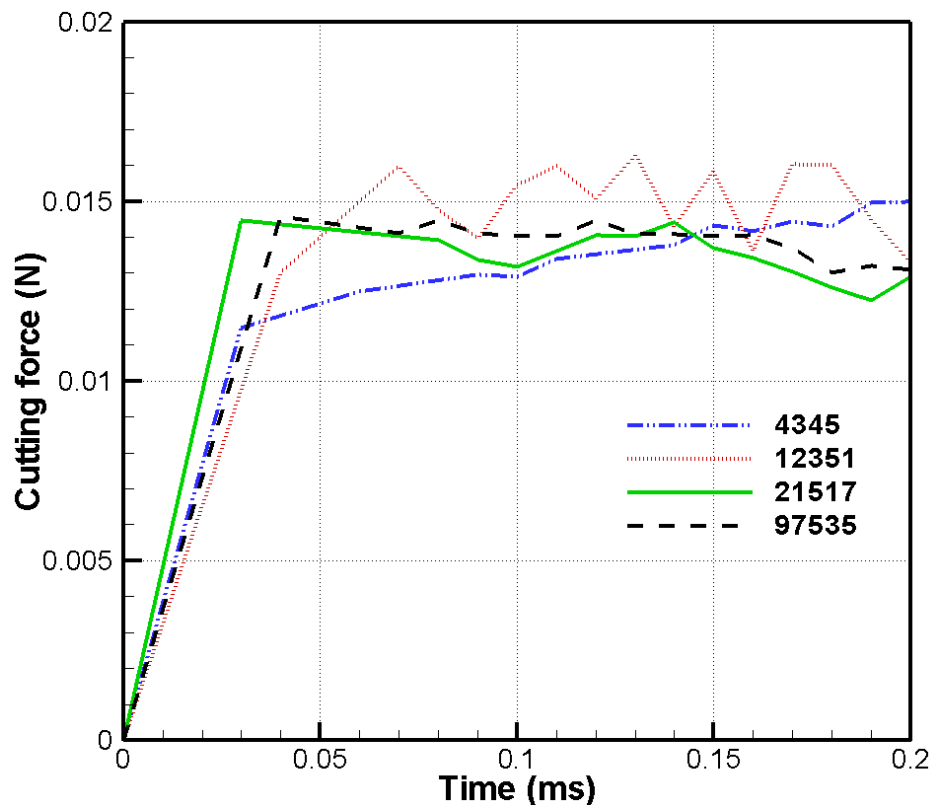


Figure 7:6 Mesh sensitivity analysis of workpeice

It is necessary to mention that the number of nodes in contact with the tool varied during the contact time, depending on its position. At the penetration stage of the tool, the number of nodes in contact was maximized. The number of nodes also changed during the penetration and a retraction stage of the tool movement due to fly-off particles.

7.2.7 Distribution of Von-Mises stress in contact domain

In addition to the mesh-sensitivity study, to find dependence of FE and SPH domains, the distribution of von-Mises stress in the contact region should be considered. It checks the consistence of the computed fields at the interface of the two domains. Has a small stress fluctuation proven that coupling algorithm working well. For this aim, three paths- (A-B-C), (D-E-F) and (G-H-I)- were selected in the contact region. Figure 7:7 presents the distribution of von Mises stress for three chosen paths. These distributions around the contact points- B, E and H- show that the element size chosen for the model was sufficient to meet the conflicting requirements of accuracy and computational cost. The VAM simulation was modelled in (100) [100] orientation setup with the radius tool tip equal to 2 μm , the coefficient of friction 0.12 , frequency 20 kHz and amplitude 20 μm .

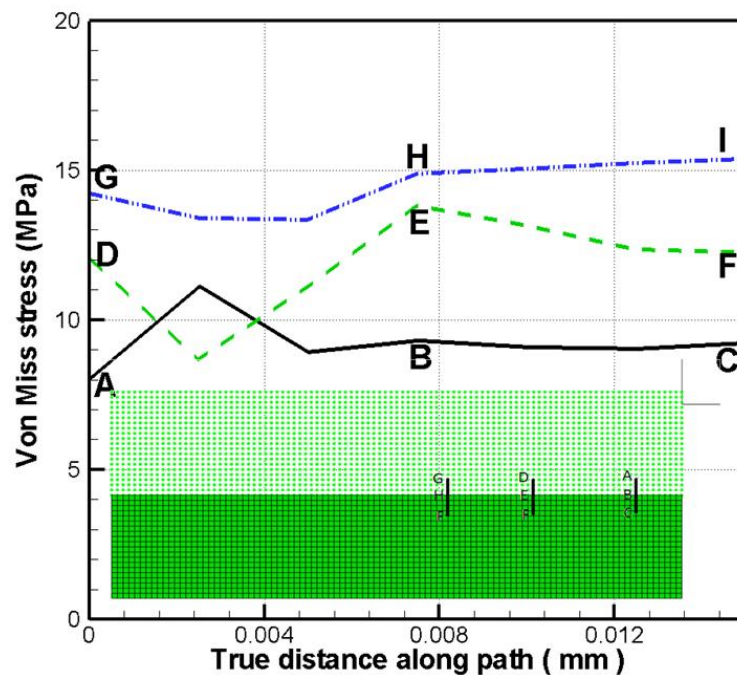


Figure 7:7 Distribution of von Mises stress in contact domain for VAM

7.2.8 Simulation verification

In order to conduct offline process planning by simulation, we need to be able to predict cutting forces that will occur in the actual machining process. A proper experimental report, which can be used for verification of the model of single-crystal VAM did not find in the literature. Therefore, the data for conventional machining was used for verification of the developed model.

Figure 7:8 illustrates the cutting force resulted from simulation with the developed three-dimensional FE/SPH model for CM and the experimental study by Lawson *et al.* (2008) for machining of a single crystal of aluminium. The cutting-force value selected for three crystallographic orientations, namely, $(2\ 7\ 0)$, $(\bar{4}\ \bar{1}\bar{1}\ 0)$ and $(12\ 5\ 0)$ at three cutting directions $[\bar{7}\ 2\ 0]$, $[11\ \bar{4}\ 0]$, and $[\bar{5}\ 12\ 0]$, respectively. The tests were conducted at cutting speed of 5 mm/s with 5 μm chip thickness for each cutting orientation of the workpiece. The acceptable conformity was observed between the results of the presented model and the experimental study by Lawson *et al.* (2008).

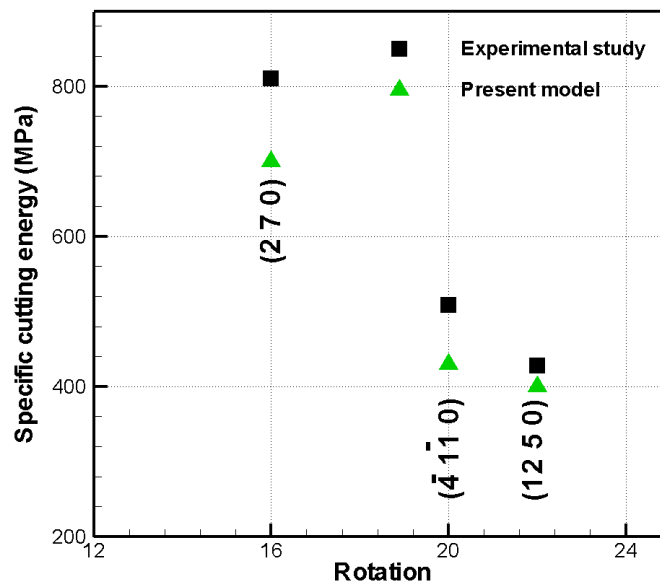


Figure 7:8 Specific cutting-energy magnitudes for presented model and experimental study by Lawson *et al.* (2008)

By changing the cutting tool's motion (Eq. 7-2) and dividing the whole step time into CM 50 sections, the single-crystal aluminium model verified with the experimental study, the VAM model was obtained and can be used as a good basis for understanding of the effects of crystallographic orientations in the VAM process.

7.2.9 Shortcomings of model

Still, though creating multi-step analysis was the only way to implement the harmonic motion of the tool in VAM, it caused some deviations from the original harmonic motion of the cutting tool. Increasing the number of steps to 50 is the suggested way implemented in the presented model to overcome this limitation. Similar to orthogonal cutting and turning process, the fly-off particles increased the computational time in the VAM model. This effect was more pronounced here due to the impact effect of the cutting tool on the workpiece. Therefore, each VAM model took approximately 120% more than CM in HPC with one CPU.

7.3 Comparison of cutting force for CM and VAM

All FE/SPH simulations were performed for VAM and CM processes with identical cutting parameters. The idea was to use CM results as a reference for the VAM process. The intermittent character of the chip-cutting tool contact is the main difference in the cutting force for CM and VAM. Figure 7:9 shows the cutting-force signature for VAM and CM as an example. For VAM, the frequency of tool vibration was 20 kHz and the vibration amplitude 20 μm . This simulation was performed for (100) crystal orientation and 0° cutting direction.

The three-dimensional FE/SPH model developed for CM showed that the cutting force acting on the cutting tool remained practically unchanged after reaching sufficient penetration, as expected, whilst in VAM the force changed during each cycle. The quantitative analysis of the integral level of the interaction forces

between the cutting tool and the workpiece for one full cycle of vibration demonstrated the significant reduction of average forces acting on the cutting tool.

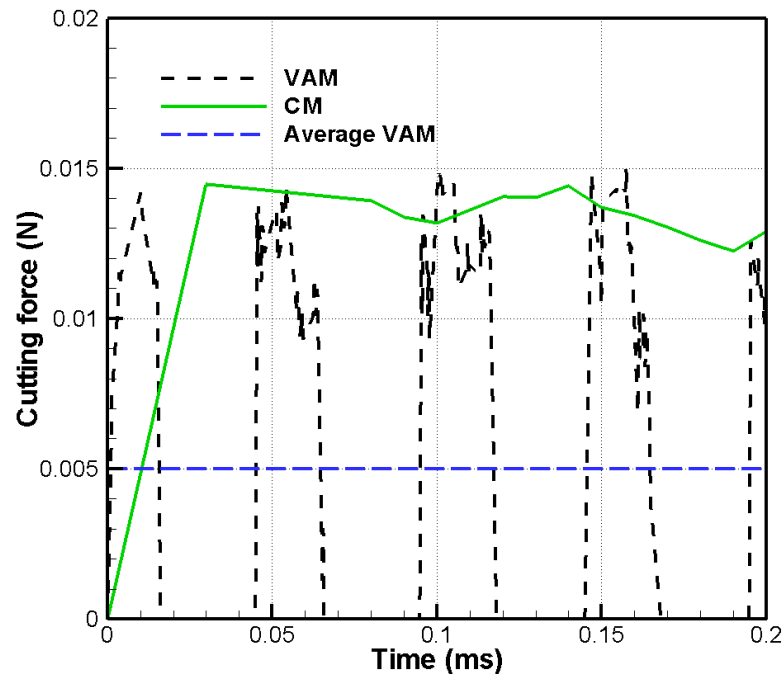


Figure 7:9 Cutting-force variations for VAM and CM (cutting speed 1 m/s and depth of cut 5 μm)

The cutting force in the VAM process during one cycle of vibration could be divided into two main stages. During the first stage, the tool approaches the workpiece, penetrates into the workpiece, causing chip separation from the workpiece. The attainment of the maximum penetration depth is characterized by the highest level of generated stresses in the process zone and marks the end of the first stage. The cutting force grows steadily from the moment of the first contact between the vibrating tool and the formed chip until it reaches the maximum level at the point of maximum penetration.

The second stage is unloading: the velocity direction of the tool changes and it moves backwards. During this phase the full separation of the cutting edge from the chip happens, resulting in a vanishing level of the cutting force. The force

magnitude starts to decline at the unloading stage until it vanishes when the tool separates from the workpiece as the process repeats with the next cycle of vibration.

Since the cutting tool was in permanent contact with the workpiece and has a constant speed in CM simulations, a practically non-changing force was applied to the cutting tool. In VAM, in a single cycle of vibration from the moment of the first contact with the chip, the speed increased with penetration and attained levels somewhat higher than those in CM. Changing the speed at each increment resulted in a non-unique set of slip systems active and, so, the variation in the maximum cutting force observed in VAM. Figure 7:12 provides a view of simulation results for the distribution of shear strains around the cutting tool for 12 slip systems. This figure clearly indicates that two slip systems were activated more than the other slip system.

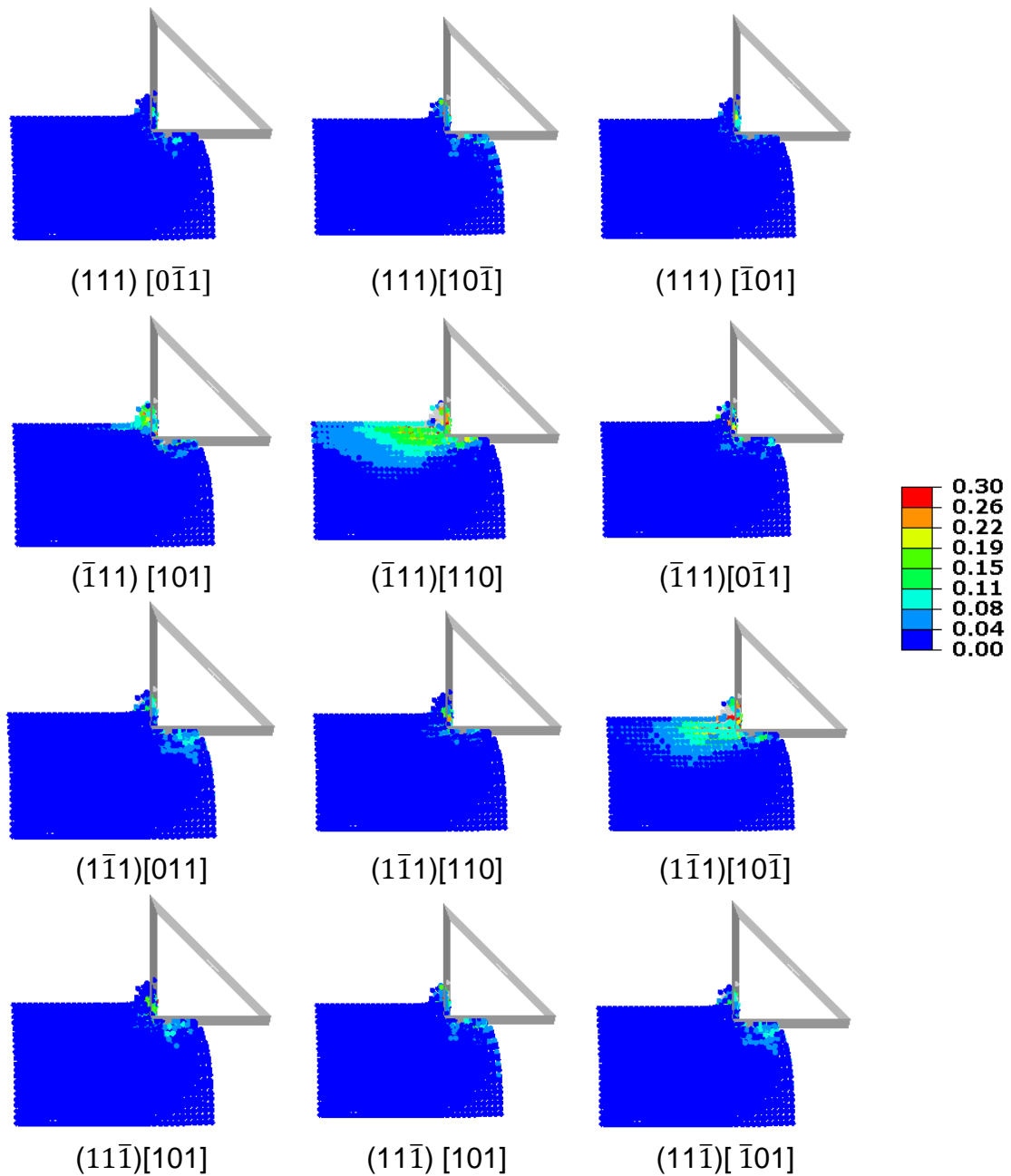


Figure 7:10 Shear strain distribution

In order to study the effect of cutting direction and crystallographic orientation on the cutting forces, four cutting directions - 0° , 30° , 60° and 90° - in three basic crystal orientations of f.c.c. structure - (100) , (101) and (111) - were chosen. The averaged value of cutting force in one completed cycle and the percentage of reduction force in each direction for VAM was calculated and presented in

Table 7-1. In all the cases, the depth of cut was fixed at 5 μm , vibration amplitude fixed at 20 μm and frequency was equal to 20 kHz.

Table 7-1 Cutting force magnitudes (in N) for three basic orientations of f.c.c. in four cutting directions

Ori.	(100)			(101)			(111)		
	CM	VAM	Reduction	CM	VAM	Reduction	CM	VAM	Reduction
0°	0.014	0.0052	62%	0.0160	0.0090	40%	0.010	0.0052	41%
30°	0.014	0.0061	51%	0.0140	0.0033	76%	0.012	0.0051	55%
60°	0.015	0.0062	55%	0.0130	0.0045	65%	0.008	0.0053	41%
90°	0.013	0.0051	60%	0.0110	0.0056	49%	0.013	0.0060	53%

In machining with VAM at (100) and (111) crystal orientation for single crystal of aluminium, the cutting-force values were nearly the same and reached 0.005-0.006 N for all the cutting directions; however, the maximum cutting force recorded in each crystal orientation and cutting direction still had some variation. The possible source of this behaviour is the effect of cutting speed experienced in slip systems and shear behaviour at each increment of deformation in VAM. In comparison to Section 6.4.2 where the change of cutting speed was insignificant, here the cutting speed changes significantly at each cycle. Having different levels of the cutting speed at each time step caused activation of different groups of slip systems at each increment.

The average cutting-force reductions from the level of conventional machining in (111) crystal orientation for these four selected cutting direction reached 47%, while the variations of these reductions in (101) and (100) orientations were recorded around 57%. Both the maximum (76%) and minimum (40%) of force reduction were found for (101) crystal orientation, which showed high-level of the fluctuations of the cutting force. The (101) crystal orientation demonstrated a large value of cutting force variation in the orthogonal-machining study (Section 5.4) and it seems that changing the cutting speed in VAM did not have the effects of reduction of this variation in comparison to two other orientations.

Having the developed and validated model can diminish costly experimental efforts to study the anisotropic behaviour of single crystals in VAM. In order to get a good understanding of the effect of different processing parameters on the cutting operation, a series of different simulations was conducted. It is well known that selection of appropriate vibration parameters such as amplitude and frequency of vibration is critical for VAM. These two process parameters are investigated in more detail in the next section.

7.4 Parametric study of VAM

In order to evaluate the effect of process parameters such as frequency and amplitude on machining of single crystals, three levels of frequency - 15 kHz, 20 kHz and 25 kHz - and three levels of amplitude - 10 μm , 20 μm and 30 μm - were analysed in three basic crystal cutting orientation - (100), (101) and (111) - and four crystal cutting directions - 0°, 30°, 60° and 90°. The selected levels of frequency and amplitude were common for VAM (Thoe *et al.*, 1998). This analysis of the effect of vibration parameters on the cutting forces resulted in-depth understanding of the VAM process.

7.4.1 Effect of vibration amplitude

Three-dimensional FE/SPH simulations were conducted to study the effect of vibration amplitude on the forces acting on the cutting tool. Previously, Ahmed *et al.* (2007) and Nath and Rahman (2008) reported that the cutting force declined with increase in the vibration amplitude for the same frequency but the effect of crystal anisotropy was never performed.

Figure 7:11 shows the cutting-force variation for (100) crystal orientation in different cutting direction. In these sets of simulations the cutting depth was fixed at 5 μm at cutting velocity equal to 1 m/s, with the vibration frequency of 20 kHz. For comparison of results, the cutting force of CM with the same machining parameter was presented for each orientation with different colour.

Basically, the average cutting force decreases with an increase in the amplitude for all the orientation setups. A decrease of approximately 33% in the average force was recorded for an increase in the amplitude from 10 μm to 20 μm , and a low-approximately 10% - decrease was observed when the amplitude was increased further from 20 μm to 30 μm .

A change in the vibration amplitude e in VAM affected the cutting process through two opposing mechanisms. By increasing the vibration amplitude, the maximum value of cutting force of VAM became somewhat higher compared to CM for nearly all of the cases. This is due to the insignificant increase in the level of maximum shear strain in the workpiece for each direction set by the increasing cutting speed (Eq. 7-2). This growth can be attributed to the increased deformation rate and subsequent strain-rate hardening of the workpiece material. Although this increase in the maximum cutting force was different in each case, the maximum of it reached only 4% in (100)[100] orientation compared to CM. On the other hand, the increased amplitude resulted in a larger separation between the tool and workpiece in one complete cycle. Therefore, by quantitative analysis of interacting forces, a higher force reduction in VAM was observed compared to the condition of interminable tool contact in CM.

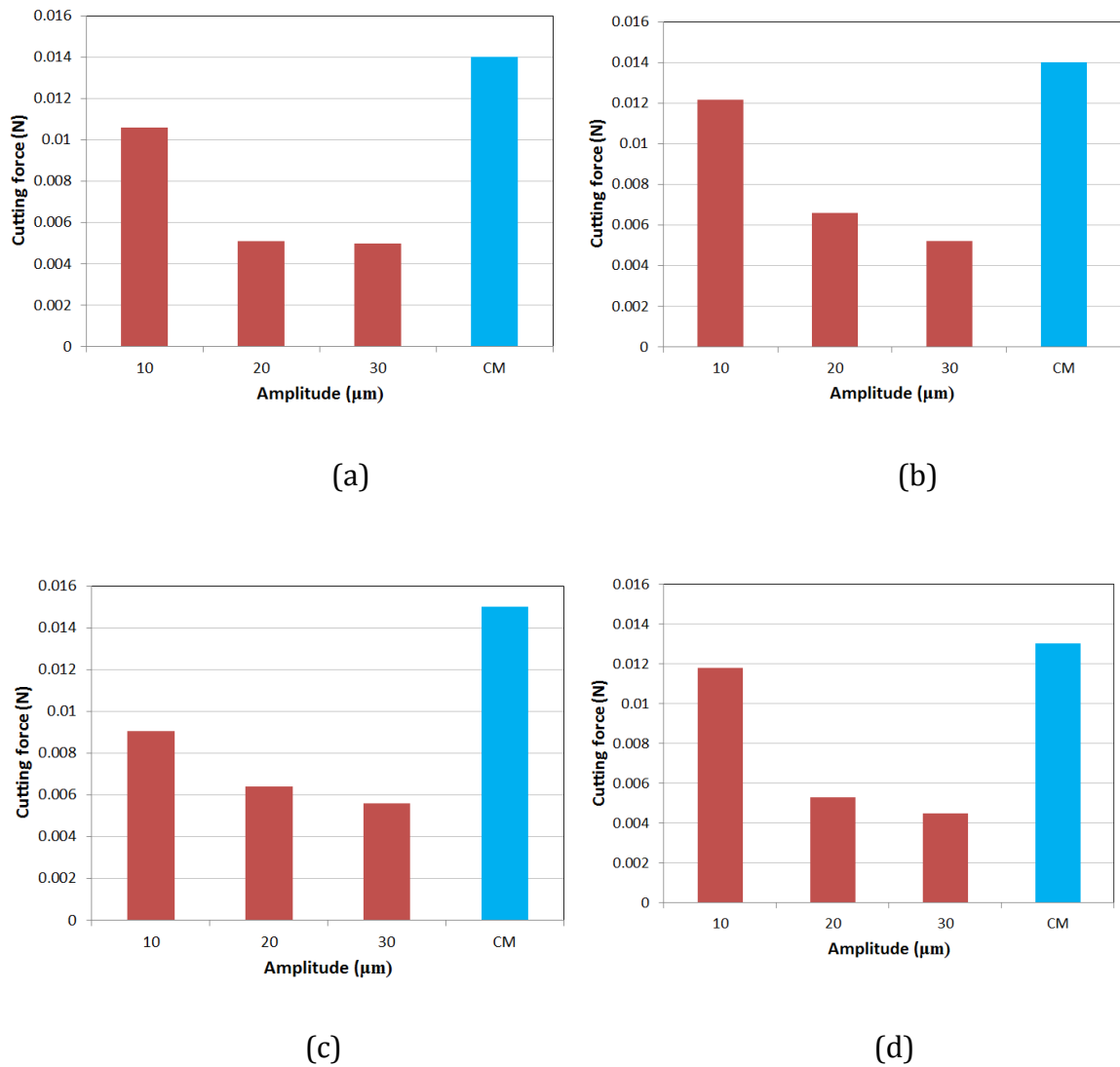


Figure 7:11 Variation of cutting force for fixed frequency of 20 kHz and different vibration amplitudes in (100) crystal orientation with cutting directions: (a) 0°, (b) 30°, (c) 60° and (d) 90°

A separate study was conducted to analyse the effect of vibration amplitude on the cutting forces for (101) and (111) orientations. Figure 7:12 and Figure 7:13 demonstrate the cutting forces for different amplitudes in (101) and (111) crystal orientation, respectively.

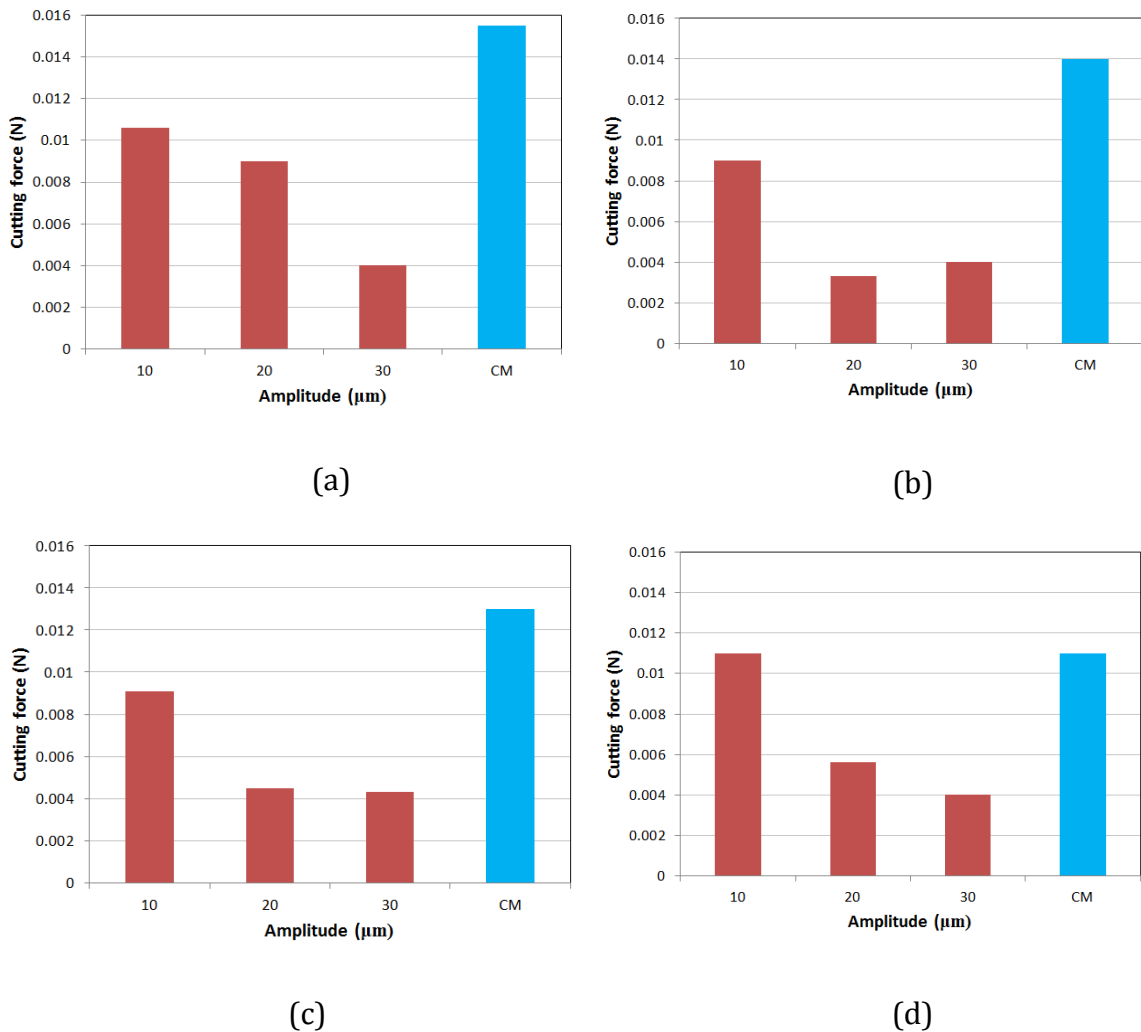


Figure 7:12 Variation of cutting force for fixed frequency of 20 kHz and different vibration amplitudes in (101) crystal orientation with cutting directions: (a) 0°, (b) 30°, (c) 60° and (d) 90°

The level of cutting-force reduction was calculated for each orientation and shown in Table 7-2. However, a unique character was not observed for reduction cutting force in selected orientations: for instance, machining in (101) orientation resulted in a higher force reduction compared to two other orientations for each level of amplitudes. This crystal orientation also recorded the large cutting force variation compared to two others crystal planes. The number of potential active slip system in this orientation seems to be higher than that for two other planes based on the

symmetric orientation of the f.c.c. structure.

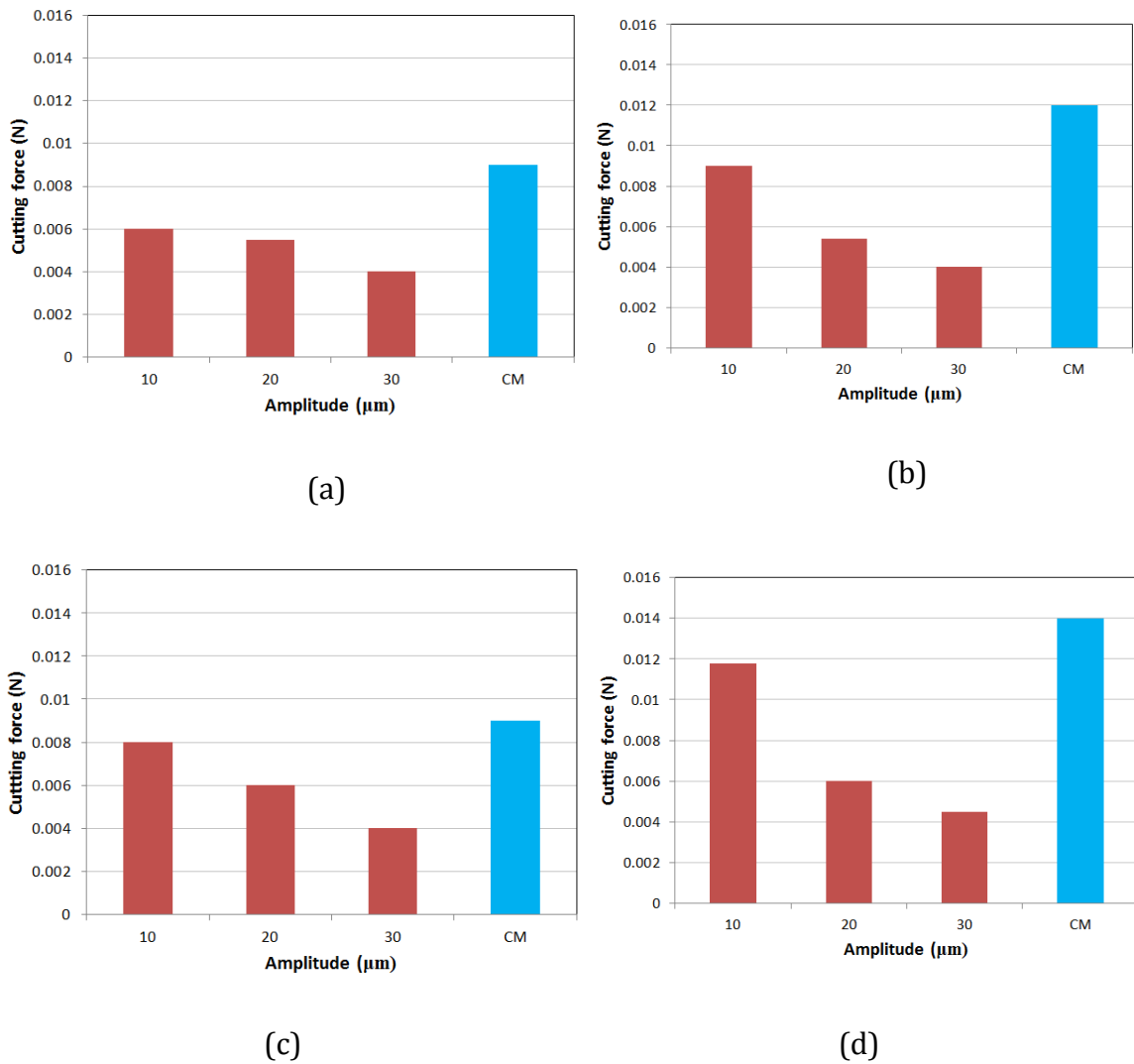


Figure 7:13 Variation of cutting force for fixed frequency of 20 kHz and different vibration amplitudes in (111) crystal orientation with cutting directions: (a) 0°, (b) 30°, (c) 60° and (d) 90°

Table 7-2 Cutting-force reduction for three amplitude (10, 20 and 30 μm)

Cutting direction	100				101				111			
	0°	30°	60°	90°	0°	30°	60°	90°	0°	30°	60°	90°
Amplitude (μm)												
10	24%	13%	34%	10%	31%	35%	30%	10%	33%	25%	11%	15%
	Average 21%				Average 26%				Average 21%			
20	63%	52%	42%	60%	41%	76%	65%	50%	44%	55%	33%	57%

	Average 54%				Average 58%				Average 47%			
30	64%	62%	62%	65%	71%	74%	66%	63%	55%	66%	55%	68%
	Average 63%				Average 68%				Average 61%			

The maximum force reduction happened in (101) crystal orientation at 30° cutting direction for three selected amplitudes. Still, though by using this combination of crystal orientation and cutting direction more energy can be saved with VAM process, a unique role in the minimum force reduction was not recorded for VAM. The possible source of this behaviour is activation of different slip systems near to each other due to the changing cutting speed. When a set of slip systems is active, increased state of stress makes it energetically more preferable for slip to occur in a different system. This led to getting low values of average cutting force in (101) crystal orientation and 30° direction rather than for other cutting direction sets.

The frequency of vibration was also analysed with the developed three-dimensional FE/SPH model and results obtained from simulations a discussed in the following section.

7.4.2 Effect of vibration frequency

The number of contact between the tool and the workpiece in a given period will always be higher for a higher frequency of cutting-tool. To investigate the effect of vibration frequency on the cutting process, three levels of frequencies -15, 20 and 25 kHz - were selected for a case study. The range of selected frequencies was based on an experimental VAM study of Riaz (2012). It is important to mention that though the three cases had different frequencies: they all were modelled for the same whole-time domain. For the purpose of comparison of these cases, the respective CM simulations were models with the same cutting parameters. The average cutting forces are then calculated over the time domain and comparisons were made.

Figure 7:14 starts the comparison with (100) crystallographic orientation. These simulations were for the fixed cutting depth of 5 µm and cutting velocity of 1 m/s.

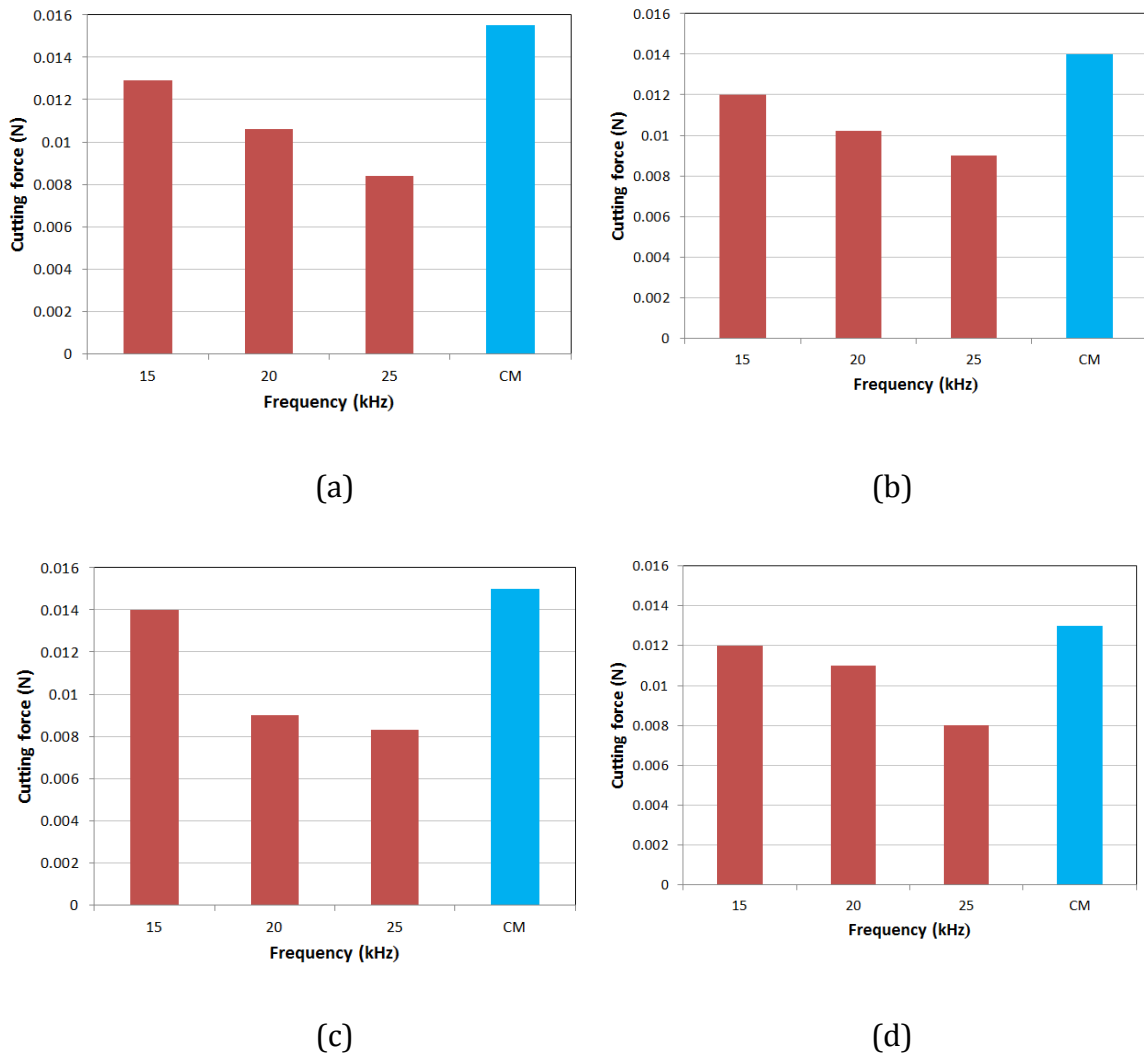


Figure 7:14 Variation of cutting force with constant vibration amplitude of $10\ \mu\text{m}$ for different frequencies for (100) crystal orientation with cutting directions: (a) 0° , (b) 30° , (c) 60° and (d) 90°

For nearly all the cases, a reduction in the cutting forces with an increase in frequency was observed. An average reduction of 8.5% in the cutting forces compared to CM was noted with application of 15 kHz frequency on the cutting tool. A further increase in the frequency to 20 kHz and 25 kHz resulted in an average reduction of 26% and 40%, respectively when compared to CM. The same

simulations were conducted for (101) and (111) crystallographic orientation and presented in Figure 7:15 and Figure 7:16, respectively.

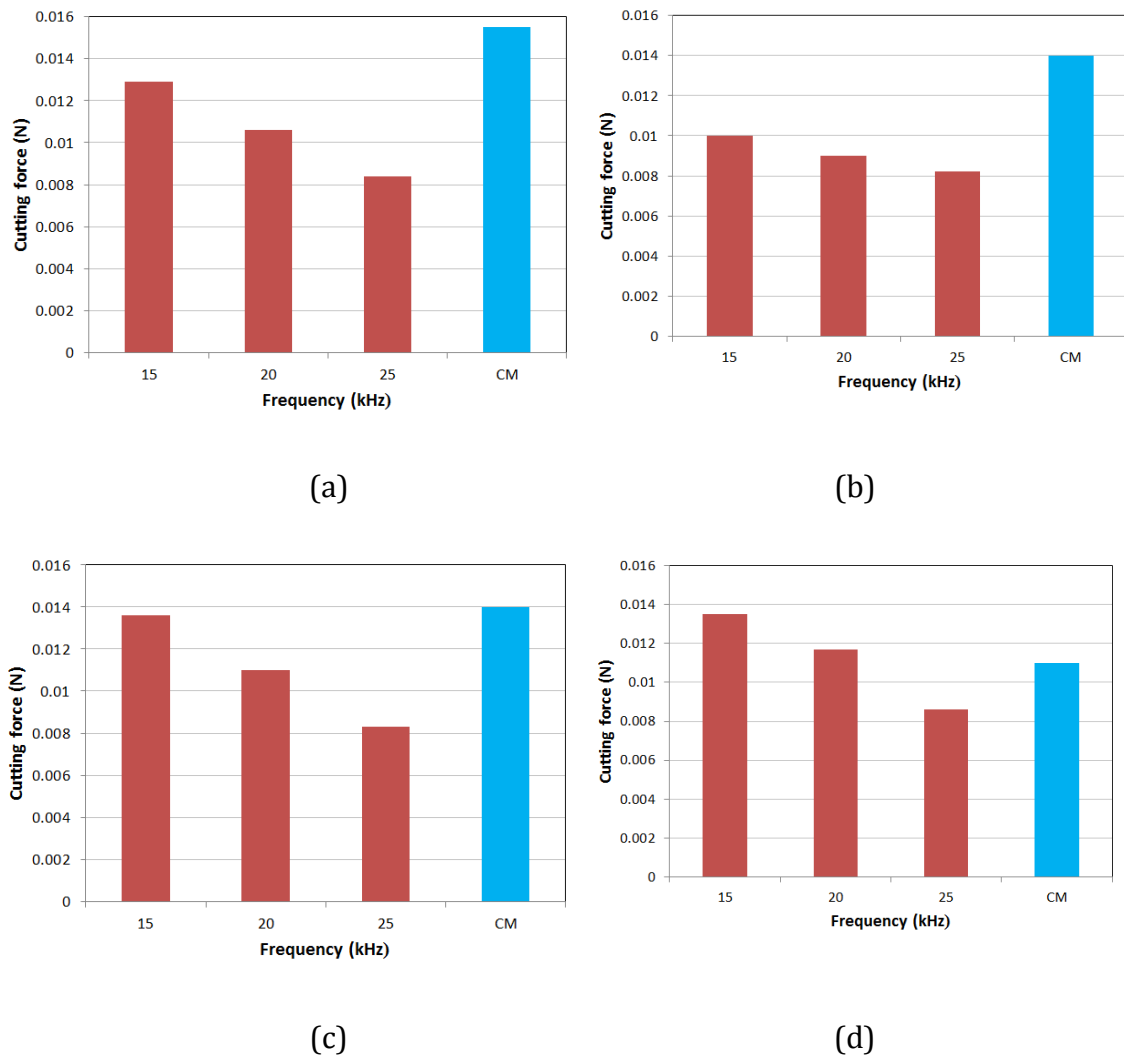


Figure 7:15 Variation of cutting force with constant vibration amplitude of $10\ \mu\text{m}$ for different frequencies for (101) crystal orientation with cutting directions: (a) 0° , (b) 30° , (c) 60° and (d) 90°

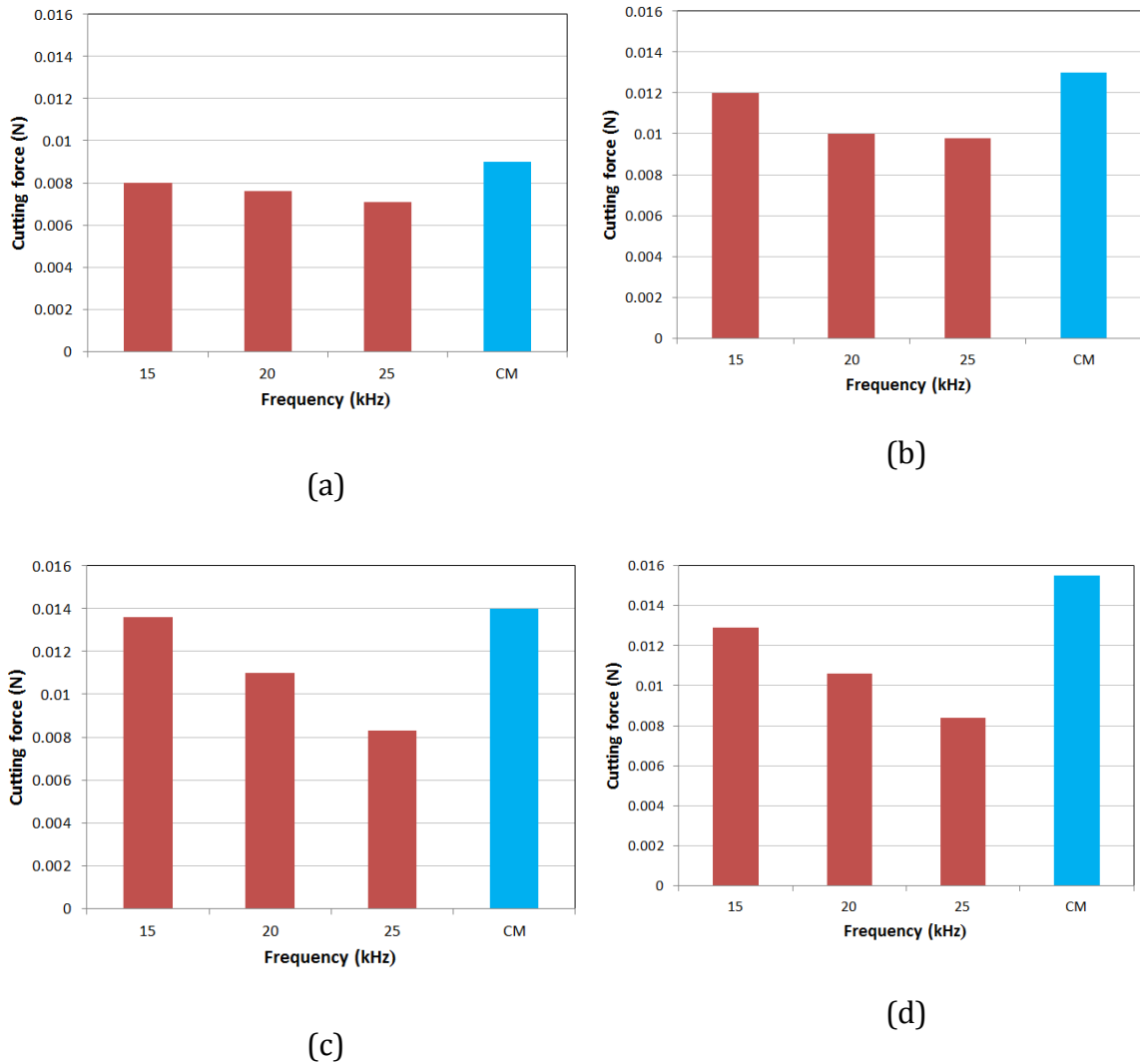


Figure 7:16 Variation of cutting force with constant vibration amplitude of $10\ \mu\text{m}$ for different frequencies for (111) crystal orientation with cutting directions: (a) 0° , (b) 30° , (c) 60° and (d) 90°

With an increase in frequency of the cutting tool by keeping the amplitude constant, a significant reduction in cutting forces arose due to extension of separation between the cutting tool and the workpiece. However, the temperature should increase by increasing the frequency; the effect of it in reduction of the cutting force is insignificant as shown in the experimental study by Ahmed *et al.* (2007). The effect of temperature is not accounted for in this model and considered for the future work.

For better understanding of the effect of orientation on the VAM machining, the percentage of cutting force reduction for various frequencies was calculated and presented in Table 7-3.

Table 7-3 Cutting force reduction for three frequencies - 15, 20 and 25 kHz

Cutting direction	100				101				111			
Frequency (kHz)	0°	30°	60°	90°	0°	30°	60°	90°	0°	30°	60°	90°
15	7%	14%	6%	7%	16%	28%	23%	3%	11%	7%	12%	3%
	Average 8.5 %				Average 17.5%				Average 8.25%			
20	28%	27%	37%	15%	31%	40%	30%	6%	15%	23%	32%	24%
	Average 26%				Average 27%				Average 23%			
25	42%	35%	44%	38%	45%	50%	45%	24%	21%	24%	42%	40%
	Average 40%				Average 41%				Average 32%			

Similar to the effect of vibration amplitude, the maximum cutting-force reduction was observed for (101) crystal orientation and 30° cutting direction. However, by increasing the frequency the magnitude of force reduction in this combination setup is increased and always remains as the maximum force reduction.

As a conclusion, selection of (101) crystal orientation and 30° cutting direction in the VAM process for variety of frequencies and amplitudes can be a reasonable choice for achieving a lower cutting force. In contrary, by selections of this crystal orientation and 90° cutting direction with amplitude of 10 μm and 15 or 20 kHz frequency, the cutting force did not change too much.

7.5 Summary

The simulations of VAM of crystalline material has not been considered and developed before. The three-dimensional FE/SPH model described in this chapter was the first attempt to develop powerful and flexible tool for dynamic analysis of crystalline materials in machining deformation. In the present work, a 3D hybrid

finite-element model of single-crystal copper was developed for VAM and CM to study the level of cutting-force reduction in different orientations. The described model is a viable and numerically robust way for solving large-deformation problems, for such material.

Generally, it was observed that increasing the vibration amplitude and frequency resulted in the growth of force reduction compared to CM with the same machining parameters. This reduction was observed for different crystalline orientations and cutting directions. By comparison between three basic crystal orientation - (100), (101) and (111) - the (101) plane demonstrated a higher cutting-force reduction. In this plane, the 30° cutting direction was always characterised by maximum cutting-force reduction and can be a suitable choice for cutting direction in VAM.

Conclusions and future work

8 Conclusions and future work

8.1 Concluding remarks

Generally, there are two main reasons mentioned in the literature, for the importance of a single-crystal machining study. Firstly, an extended demand from various applications, which need a reduced level of defects (e.g., turbine blades, precision mirrors) and, secondly, the need for developing fundamental understanding of materials and their removal processes, since all crystalline materials are composed of grains and grain boundaries, which, to a large extent, define their mechanical properties.

Conducting experiments of single crystal machining are very difficult. In the last few decades, the finite-element (FE) technique has been extensively used to gain insight into the underlying mechanisms that drive a plastic response in high-deformation problems. Compared to FE approaches, SPH has several advantages, especially in the study of large-deformation processes. To address the matter of

ultra-precision machining of a material by using computational modelling, the combination of SPH and a continuum finite-element model was suggested, where the initial material properties were accounted for, based on some experimental evidence.

The mechanism of material's deformation in single-crystal machining is rather complex. Large deformation is divided into a number of increments, and the plastic work for each of them is determined using a rate-insensitive plasticity approach. For each incremental deformation, the number of active slip systems and amount of slip is identified uniquely in the available 12 slip systems of the f.c.c. structure. Criteria of activation of the slip system are defined based on the Schmid factor at each increment of deformation. The material properties are updated for the subsequent deformation increment to account for hardening. Finally, shear strain is identified for giving cutting parameters (rake angle, cutting velocity, depth of cut, uncut chip thickness and coefficient of friction) and crystal orientation with regard to the tool movement (workpiece zone axis, cutting plane orientation, and cutting direction).

The developed three-dimensional FE/SPH models were implemented in a commercial software ABAQUS/Explicit (v.6.11) using a user-defined subroutine (VUMAT) to incorporate the crystal-plasticity theory and was used to elucidate the effect of crystallographic anisotropy on the response of f.c.c. metals to machining. The cutting force is one of the critical governing parameters defining efficiency of the machining process used to study the influence of crystal orientation. The three-dimensional finite-element models presented in each case were a viable and a numerically robust way for solving large-deformation problems without compromising complex underlying physical mechanisms driving deformation in crystalline materials. This approach can be used for a wide range of cutting speeds, feed rates and tool geometry.

In the present thesis the three common machining processes, namely *orthogonal cutting*, *turning* and *vibration-assisted machining* were studied applied to f.c.c. metals. Based on the orientation setup, the data obtained for the turning model is also valid for a milling operation, which is another common machining process.

The data presented in this thesis are a result of a first study in the use of coupled FE/SPH technique to elucidate the metal cutting process. High purity copper and aluminium were considered for the simulation of machining operations. The general conclusions based on the present study are presented in this chapter, followed by the recommendations for the future work. Although the summary of each chapter was already present and, hence, some extent of duplication was unavoidable, this chapter tries to emphasise the main concluding remarks.

The surface roughness of the machined surface varies considerably with the crystallographic orientation of the material being cut. The dependence of the machined surface roughness on the crystallographic cutting direction was not investigated in this thesis. For this aim, the current model needs to address with finer particle size in SPH domain which caused to increase the computational time. However, there is a fair agreement between the variation of the machined surface roughness, as a result of changing crystal orientation, and cutting force characteristics (Zhou and Ngoi (2001) and Lee et al. (2000)). A large cutting force corresponds to a high surface roughness. The temperature is not incorporated in the presented crystal plasticity formulation. Thus, the relatively low-speed cutting regime followed by low cutting depth is considered in the current study to minimize the effect of the temperature and hence, the increase strain hardening is considered as a main reason for increased the specific cutting energy.

8.1.1 Orthogonal machining

Kinematics and geometry of the orthogonal cutting process is known as a simplest case of machining and is the first choice for a relatively large research study. The FE/SPH model was developed to account for the effect of crystallography of the f.c.c. structure. The transient mesh implemented by the mesh-editing technique in the orthogonal configuration saves the computational time significantly. Between three selected grain orientations for the single-crystals f.c.c. structure – (100), (101) and (111) – the cutting-force variation on the (101) plane was observed to be larger than that for two other planes. The total difference in the cutting force for the (101) orientation was 33%, signifying the strength of the effect of crystal orientation in the single-crystal machining process. This variation obtained was

based on the propensity of the workpiece material to generate slips when its grains undergo rotations.

Investigation of the cutting force for a single grain of aluminium as f.c.c. crystal structure showed that the material parameters have only a little effect on a variation of the cutting force. The detailed analysis of the effect of different levels of the coefficient of friction and tool edge radius demonstrated that while the coefficient of friction did not affect the activation of the slip system significantly, the tool edge radius changed the active slip systems completely.

8.1.2 Turning

By developing the turning model, it was possible to study more orientations for each fixed zone axis. A good match (in terms of amplitude and signature for various zone axes) of results obtained with the developed three-dimensional FE/SPH model and experiment by Cohen (1982) was reported for copper single crystals. The model was then applied to analyse the effect of crystallographic orientation on the specific energies for eight cases of orientations uniformly distributed over a basic stereographic triangle. The variation of the mean specific energy positions of zone axis was seen to reach the maximum of 150%. The deviation (about the mean) of the specific energy with crystal orientation changed significantly with the positions of the zone axis. The minimum deviation was observed for the [111] zone axis, which is characterized by the maximum crystallographic symmetry while the maximum one was found for the [112] zone axis.

The friction and cutting velocity had a small effect on the deviation of the specific cutting energy for a given zone axis. Overall, within the range of parameters tested in this study, the variation due to the effect of the coefficient of friction with crystallographic orientation was 35%. In terms of the cutting velocity, this variation reached the maximum of 30%.

Although the simplified model provided a clear methodology for incorporating the effect of crystallographic anisotropy into the turning model, the computational time was considered as a shortcoming with low importance of the model. The study of single-crystals turning helped to explain realization of the cutting process as well as deformation processes in single-crystal turning at an elementary level enhancing our understanding of the behaviour of polycrystalline materials in machining.

8.1.3 Vibration-assisted machining

The numerical (FE/SPH) investigations were carried out to study the process of VAM in comparison with the CM process. A crystal-plasticity finite-element model for VAM was proposed as an enhancement model to explore microstructural processes at the cutting tool–chip interface for both technologies. A detailed comparison based on numerical analyses of the transient stress distribution during the cycle of vibration in VAM and the steady-state stress distribution in conventional machining showed that the mean level of stresses in the process zone and, consequently, cutting forces were considerably lower for the former. In CM, the cutting tool stayed in a permanent contact with the chip throughout the entire cutting process. In contrast, in VAM the cutting tool remained in contact with the chip for only about 45% of the time, according to the FE simulations.

The performed simulations also demonstrated different values for cutting-force reduction in different orientation setups for VAM as compared to that of CM. An increase in the peak forces with an increase in the amplitude of vibration was observed for nearly all the selected orientations. The average cutting forces in the cutting tool over a single vibration cycle showed that they in fact decreased when the amplitude was increased. Generally, for three crystal-orientations selected, a 31% decrease in the average cutting forces was recorded for an increase in the amplitude from 10 μm to 20 μm , and a further 10% decrease was observed when the amplitude was increased from 20 μm to 30 μm . However, these values had the variation of the minimum 10% cutting force reduction for machining at 90° cutting

direction in (100) and (101) crystal orientation with 10 μm amplitude and 20 kHz and the maximum of 74% force reduction for machining at 30° cutting direction in (101) cutting orientation with 30 μm amplitude and 20 kHz.

The effect of vibration frequency was also analysed, keeping all the other variables of machining constant. A range of frequency values -15, 20 and 25 kHz - was selected. The study of results from the performed simulations with regard to the effect of the changing vibration frequency on the overall forces acting on the cutting tool demonstrated that the average forces over one complete vibration cycle (for selected orientation) had a drop of 15% in the cutting forces for a change in the frequency from 15 kHz to 20 kHz and a further drop of 12% for a frequency increase from 20 kHz to 25 kHz. However, by setting the frequency equal to 15 kHz for three selected crystal orientations and 90° cutting direction the cutting force did not change significantly compared with CM. By keeping the frequency at 25 kHz and selecting the (101) crystal orientation with 30° cutting direction, 50% force reduction was observed. Generally, a variation in the force drop of about 25% was observed for 15 kHz, 34% for 20 kHz and 30% for 25 kHz for different directions of cutting. This value is shown the importance of accounting for crystal plasticity in modelling of VAM.

The study of simulation results demonstrated that the (101) crystal orientation with 30° cutting direction had the highest reduction of cutting force for three levels of amplitude (10, 20 and 30 μm) and three levels of frequency (15, 20 and 25 kHz).

8.2 Impact of study

Micro machining rise as a key technology for the future of manufacturing process due to its many industrial applications in miniaturization, but also for macro scale components with features in the micro world, e.g. micro grooves or micro holes. The use of experiments is costly, difficult to perform, and it is hard to measure parameters at this level. Implementation of current modelling has considered the best alternative for performing the required analysis to reduce the manufacturing

costs and part quality. The results presented in this thesis was dedicated to reducing the need for extensive experimental studies, which are expensive, and also help to extend the usability envelope of next-generation components to untried levels of load and environment conditions. Three machining models developed here can predict the cutting force pattern in different cutting orientations. Analysis of forces plays an important role in characterizing the cutting process, as the tool wear and surface texture, depends on the forces.

Turning operations are common in the automotive and aerospace industries where large metal workpieces are reduced to a fraction of their original weight when creating complex thin structures. The present model of micro-turning has been widely applied in predicting the instantaneous turning forces. The significant advances in turning process have been achieved greatly due to the emergent technologies for precision machining. The simulation results of VAM will support of research studies undergoing at the deformation mechanism at micro scale to select the best possible choices of cutting direction.

8.3 Recommendations for future work

The following topics are suggested for further investigations of the machining process by using the presented model.

1. The extension of the developed model in order to examine other aspects of the machining process, such as chip side flow, cutting depth and cutting-tool geometry.
2. Further development of the VUMAT subroutine to incorporate the thermal effect in order to examine the effect of temperate in the machining model. This would be useful for thermo-mechanical modelling of other materials, which are more affected by temperature and, generally, to elucidate the thermal effect in machining.

3. Further exploration of the frictional conditions along the chip-tool interface. This might clarify the friction paradox at the chip-tool interface, where the coefficient of friction has apparently changed with the change of the contact length of the chip with the cutting tool.

4. The character of material's strengthening at low levels of the uncut chip thickness is an important contributor to the specific cutting energy. The strength of the material is considered as a function of strain, strain rate, strain gradient, etc. (Larsen-Basse and Oxley, 1973). The size effect in machining can be explained with the theory of strain-gradient plasticity since strain gradients in machining are very high. Strain-gradient plasticity suggests that when deformation is large and is constrained spatially to a narrow region, the stress not only depends on strain at a point but also upon the strains in the region surrounding that point. To develop modelling schemes capable of capturing the size effect in specific cutting energy in a machining process, concepts of the strain-gradient plasticity theory should be included into flow-stress equations of the deformation process. It is, therefore, possible to address the size effect in a strain field based on its geometry and gradient. This concept is also suggested for the future study.

References

- Agertz, O., Moore, B., Stadel, J., Potter, D., Miniati, F., Read, J., Mayer, L., Gawryszczak, A., Kravtsov, A. & Nordlund, A. 2007, "Fundamental differences between SPH and grid methods", *Monthly Notices of the Royal Astronomical Society*, vol. 380, no. 3, pp. 963-978.
- Ahmed, N., Mitrofanov, A., Babitsky, V. & Silberschmidt, V. 2007, "3D finite element analysis of ultrasonically assisted turning", *Computational materials science*, vol. 39, no. 1, pp. 149-154.
- Akarca, S., Song, X., Altenhof, W. & Alpas, A. 2008, "Deformation behaviour of aluminium during machining: modelling by Eulerian and smoothed-particle hydrodynamics methods", *Proceedings of the Institution of Mechanical Engineers, Part L: Journal of Materials Design and Applications*, vol. 222, no. 3, pp. 209-221.
- Arrazola, P. & Ozel, T. 2008, "Numerical modelling of 3D hard turning using arbitrary Lagrangian Eulerian finite element method", *International Journal of Machining and Machinability of Materials*, vol. 4, no. 1, pp. 14-25.
- Atkins, A. 2003, "Modelling metal cutting using modern ductile fracture mechanics: quantitative explanations for some longstanding problems", *International Journal of Mechanical Sciences*, vol. 45, no. 2, pp. 373-396.
- Attaway, S., Heinstejn, M. & Swegle, J. 1994, "Coupling of smooth particle hydrodynamics with the finite element method", *Nuclear Engineering and Design*, vol. 150, no. 2, pp. 199-205.
- Azaroff, L.V. 1984, *Introduction to solids*, Tata McGraw-Hill Education.
- Babitsky, V., Kalashnikov, A., Meadows, A. & Wijesundara, A. 2003, "Ultrasonically assisted turning of aviation materials", *Journal of Materials Processing Technology*, vol. 132, no. 1, pp. 157-167.
- Bagci, E. 2011, "3-D numerical analysis of orthogonal cutting process via mesh-free method", *Int.J.the Physical Sciences*, vol. 6, no. 6, pp. 1267-1282.
- Balihodzic, N. 2002, *A numerical investigation of orthogonal machining*. University of New Brunswick (Canada).
- Black, J.T. 1971, "On the fundamental mechanism of large strain plastic deformation: Electron microscopy of metal cutting chips", *Journal of Engineering for Industry*, vol. 93, pp. 507.

- Blochwitz, C., Brechbühl, J. & Tirschler, W. 1996, "Analysis of activated slip systems in fatigue nickel polycrystals using the EBSD-technique in the scanning electron microscope", *Materials Science and Engineering: A*, vol. 210, no. 1, pp. 42-47.
- Bragg, W., Desch, C., Taylor, G., Mott, N., Orowan, E., Andrade, E.d.C., Preston, G. & Hatfield, W. 1938, "A Discussion on Plastic Flow in Metals, 12 May 1938. Opening Address", *Proceedings of the Royal Society of London. Series A. Mathematical and Physical Sciences*, vol. 168, no. 934, pp. 302-317.
- Brinksmeier, E., Preuß, W. & Schmütz, J. 1998, "Manufacture of microstructures by ultrasonic lapping", *13th Annual Meeting of the ASPE*, pp. 169.175
- Callister Jr, W.D. 1997, "Materials Science and Engineering: An Introduction, 4; Callister, Jr., William D", *Materials Science and Engineering: An Introduction, 4th Edition.*, New York: John Wiley & Sons, Inc., copyright, pp. 499-501.
- Campbell, F.C. 2008, *Elements of metallurgy and engineering alloys*, ASM International.
- Campbell, J., Vignjevic, R. & Libersky, L. 2000, "A contact algorithm for smoothed particle hydrodynamics", *Computer Methods in Applied Mechanics and Engineering*, vol. 184, no. 1, pp. 49-65.
- Chae, J., Park, S. & Freiheit, T. 2006, "Investigation of micro-cutting operations", *International Journal of Machine Tools and Manufacture*, vol. 46, no. 3, pp. 313-332.
- Childs, T. 2006, "Numerical experiments on the influence of material and other variables on plane strain continuous chip formation in metal machining", *International Journal of Mechanical Sciences*, vol. 48, no. 3, pp. 307-322.
- Chua, M., Rahman, M., Wong, Y. & Loh, H. 1993, "Determination of optimal cutting conditions using design of experiments and optimization techniques", *International Journal of Machine Tools and Manufacture*, vol. 33, no. 2, pp. 297-305.
- Clarebrough, L. & Ogilvie, G. 1950, "Microstructure by Machining", *Machining Theory and Practice*, ASM, , pp. 110-121.
- Cohen, P.H. 1982, "The orthogonal in-situ machining of single and polycrystalline aluminum and copper, volume 1", PhD thesis.
- Cossins, P.J. 2010, "Smoothed Particle Hydrodynamics", *arXiv preprint arXiv:1007.1245*,.

- de Agustina, B., Bernal, C., Camacho, A. & Rubio, E. 2013, "Experimental Analysis of the Cutting Forces Obtained in Dry Turning Processes of UNS A97075 Aluminium Alloys", *Procedia Engineering*, vol. 63, pp. 694-699.
- De Vuyst, T., Vignjevic, R. & Campbell, J. 2005, "Coupling between meshless and finite element methods", *International Journal of Impact Engineering*, vol. 31, no. 8, pp. 1054-1064.
- Demiral, M. 2012, *Enhanced gradient crystal-plasticity study of size effects in b.c.c. metal*, PhD thesis.
- Donea, J., Huerta, A., Ponthot, J. & Rodríguez-Ferran, A. 2004, "Arbitrary Lagrangian–Eulerian methods", *Encyclopedia of computational mechanics*.
- Dornfeld, D., Min, S. & Takeuchi, Y. 2006, "Recent advances in mechanical micromachining", *CIRP Annals-Manufacturing Technology*, vol. 55, no. 2, pp. 745-768.
- Ellyin, F. 1996, "Constitutive laws for transient and stable behaviour of inelastic solids" in *Fatigue Damage, Crack Growth and Life Prediction* Springer, pp. 205-277.
- Fernández-Méndez, S., Bonet, J. & Huerta, A. 2005, "Continuous blending of SPH with finite elements", *Computers & Structures*, vol. 83, no. 17, pp. 1448-1458.
- Flom, D. 1985, "High-speed machining" in *Innovations in Materials Processing* Springer, pp. 417-439.
- Fries, T. & Matthies, H.G. 2004, "Stabilized and coupled FEM/EFG approximations for fluid problems", *Proceedings of the Sixth World Congress on Computational Mechanics (WCCM VI), Beijing, China*.
- Furukawa, Y. & Moronuki, N. 1988, "Effect of material properties on ultra precise cutting processes", *CIRP Annals-Manufacturing Technology*, vol. 37, no. 1, pp. 113-116.
- Gambin, W. 2001, *Plasticity and textures*, Springer.
- Groh, S., Marin, E., Horstemeyer, M. & Zbib, H. 2009, "Multiscale modeling of the plasticity in an aluminum single crystal", *International Journal of Plasticity*, vol. 25, no. 8, pp. 1456-1473.
- Grzesik, W. 2008, *Advanced machining processes of metallic materials: theory, modelling and applications*, Elsevier.

- Gu, Y. & Zhang, L. 2008, "Coupling of the meshfree and finite element methods for determination of the crack tip fields", *Engineering Fracture Mechanics*, vol. 75, no. 5, pp. 986-1004.
- Guo, Y. & Liu, C. 2002, "3D FEA modeling of hard turning", *Journal of manufacturing science and engineering*, vol. 124, no. 2, pp. 189-199.
- Haasen, P., Haasen, P., Physicist, F. & Haasen, P. 1974, *Physikalische metallkunde*, Springer Berlin.
- Haglund, A. 2005, *On friction modeling in orthogonal machining: An arbitrary Lagrangian-Eulerian finite element model*. University of New Brunswick (Canada).
- Halloran, J.P., Petrella, A.J. & Rullkoetter, P.J. 2005, "Explicit finite element modeling of total knee replacement mechanics", *Journal of Biomechanics*, vol. 38, no. 2, pp. 323-331.
- Harewood, F. & McHugh, P. 2007, "Comparison of the implicit and explicit finite element methods using crystal plasticity", *Computational Materials Science*, vol. 39, no. 2, pp. 481-494.
- Havner, K. & Shalaby, A. 1978, "Further investigation of a new hardening law in crystal plasticity", *Journal of Applied Mechanics*, vol. 45, pp. 500.
- Hill, R. 1966, "Generalized constitutive relations for incremental deformation of metal crystals by multislip", *Journal of the Mechanics and Physics of Solids*, vol. 14, no. 2, pp. 95-102.
- Huang, Y. & Liang, S.Y. 2005, "Modeling of cutting forces under hard turning conditions considering tool wear effect", *Transactions of the ASME-B-Journal of Manufacturing Science and Engineering*, vol. 127, no. 2, pp. 262-270.
- Huang, Y. 1991, *A User-material Subroutine Incorporating Single Crystal Plasticity in the ABAQUS Finite Element Program*, Harvard Univ.
- Hutchinson, J. 1976, "Bounds and self-consistent estimates for creep of polycrystalline materials", *Proceedings of the Royal Society of London.A.Mathematical and Physical Sciences*, vol. 348, no. 1652, pp. 101-127.
- Ikawa, N., Shimada, S., Tanaka, H. & Ohmori, G. 1991, "An atomistic analysis of nanometric chip removal as affected by tool-work interaction in diamond turning", *CIRP Annals-Manufacturing Technology*, vol. 40, no. 1, pp. 551-554.
- Inamura, T., Takezawa, N. & Taniguchi, N. 1992, "Atomic-scale cutting in a computer using crystal models of copper and diamond", *CIRP Annals-Manufacturing Technology*, vol. 41, no. 1, pp. 121-124.

- Inamura, T. & Takezawa, N. 1991, "Cutting experiments in a computer using atomic models of a copper crystal and a diamond tool" in *Progress in Precision Engineering* Springer, pp. 231-242.
- Islam, S., Ibrahim, R., Das, R. & Fagan, T. 2012, "Novel approach for modelling of nanomachining using a mesh-less method", *Applied Mathematical Modelling*, vol. 36, no. 11, pp. 5589-5602.
- James, T.P., Pearlman, J.J. & Saigal, A. 2012, "Rounded Cutting Edge Model for the Prediction of Bone Sawing Forces", *Journal of Biomechanical Engineering*, vol. 134, no. 7.
- Johnson, G.R., Beissel, S.R. & Stryk, R.A. 2002, "An improved generalized particle algorithm that includes boundaries and interfaces", *International Journal for Numerical Methods in Engineering*, vol. 53, no. 4, pp. 875-904.
- Johnson, G.R., Stryk, R.A. & Beissel, S.R. 1996, "SPH for high velocity impact computations", *Computer Methods in Applied Mechanics and Engineering*, vol. 139, no. 1, pp. 347-373.
- Khandpur, R.S. 2005, *Printed circuit boards*, Tata McGraw-Hill Education.
- Khoei, A., Anahid, M. & Shahim, K. 2008, "An extended arbitrary Lagrangian–Eulerian finite element method for large deformation of solid mechanics", *Finite Elements in Analysis and Design*, vol. 44, no. 6, pp. 401-416.
- Kiliçaslan, C. 2009, "Modelling and simulation of metal cutting by finite element method", *Master of Science, Graduate School of Engineering and Science, Izmir Institute of Technology, Izmi*.
- Kim, B., Schmittiel, M.C., Degertekin, F.L. & Kurfess, T.R. 2004, "Scanning grating microinterferometer for MEMS metrology", *Journal of manufacturing science and engineering*, vol. 126, no. 4, pp. 807-812.
- Kim, J.D. & Kim, D.S. 1996, "On the size effect of micro-cutting force in ultraprecision machining", *JSME international journal.Ser.C, Dynamics, control, robotics, design and manufacturing*, vol. 39, no. 1, pp. 164-169.
- Kishawy, H., Rogers, R. & Balihodzic, N. 2002, "A numerical investigation of the chip tool interface in orthogonal machining", *Machining Science and Technology*, vol. 6, no. 3, pp. 397-414.
- Kittel, C. & Kittel, B.C. 1986, "Introduction to solid state physics".
- Klamecki, B.E. 1973, *Incipient Chip Formation in Metal Cutting--a Three-dimension Finite Element Analysis*.

- Ko, T.J. & Kim, H.S. 1999, "Mechanistic cutting force model in band sawing", *International Journal of Machine Tools and Manufacture*, vol. 39, no. 8, pp. 1185-1197.
- Komanduri, R., Chandrasekaran, N. & Raff, L. 2001, "MD simulation of exit failure in nanometric cutting", *Materials Science and Engineering: A*, vol. 311, no. 1, pp. 1-12.
- Komanduri, R., Chandrasekaran, N. & Raff, L. 1998, "Effect of tool geometry in nanometric cutting: a molecular dynamics simulation approach", *Wear*, vol. 219, no. 1, pp. 84-97.
- König, W., Cronjäger, L., Spur, G., Tönshoff, H., Vigneau, M. & Zdeblick, W. 1990, "Machining of new materials", *CIRP Annals-Manufacturing Technology*, vol. 39, no. 2, pp. 673-681.
- Kopalinsky, E. & Oxley, P. 1984, "Size effects in metal removal processes", *Mechanical Properties at High Rates of Strain, 1984*, , pp. 389-396.
- Kota, N. 2011, "Mechanical Micromachining-Effect of Crystallographic Anisotropy on Machining Forces".
- Kuchnicki, S., Cuitino, A. & Radovitzky, R. 2006, "Efficient and robust constitutive integrators for single-crystal plasticity modeling", *International Journal of Plasticity*, vol. 22, no. 10, pp. 1988-2011.
- Kysar, J. 1997, "Addendum to a user-material subroutine incorporating single crystal plasticity in the ABAQUS finite element program", *Mech report*, vol. 178.
- Larsen-Basse, J. & Oxley, P. 1973, "Effect of strain rate sensitivity on scale phenomena in chip formation", *Proceedings of 13th International Machine Tool Design and Research Conference*, pp. 209.212.
- Lawson, B.L., Kota, N. & Ozdoganlar, O.B. 2008, "Effects of crystallographic anisotropy on orthogonal micromachining of single-crystal aluminum", *Transactions of the ASME-B-Journal of Manufacturing Science and Engineering*, vol. 130, no. 3, pp. 316-319.
- Lee, W. & Yang, W. 1993, "Methodology and applications of mesoplasticity in manufacturing sciences", *International Journal of Mechanical Sciences*, vol. 35, no. 12, pp. 1079-1095.
- Levy, N., Marcal, P., Ostergren, W.J. & Rice, J.R. 1971, "Small scale yielding near a crack in plane strain: a finite element analysis", *International Journal of Fracture Mechanics*, vol. 7, no. 2, pp. 143-156.

- Li, S. & Liu, W.K. 2004, *Meshfree particle methods*, Springer.
- Limido, J., Espinosa, C., Salaun, M., Mabru, C., Chieragatti, R. & Lacome, J. 2011, "Metal cutting modelling SPH approach", *International journal of machining and machinability of materials*, vol. 9, no. 3, pp. 177-196.
- Limido, J., Espinosa, C., Salaun, M. & Lacome, J. 2007, "SPH method applied to high speed cutting modelling", *International Journal of Mechanical Sciences*, vol. 49, no. 7, pp. 898-908.
- Ling, X., Horstemeyer, M. & Potirniche, G. 2005, "On the numerical implementation of 3D rate-dependent single crystal plasticity formulations", *International Journal for Numerical Methods in Engineering*, vol. 63, no. 4, pp. 548-568.
- Liu, X., Ehmann, K.F., DeVor R.E. and Kapoor S.G., 2005, "The Mechanics of Machining at the Microscale: Assessment of the Current State of the Science", *Journal of Manufacturing Science and Engineering*, vol. 126 no. 4, pp. 666-678
- Liu, G. "Lecture notes on the smoothed particle hydrodynamics (SPH)".
- Liu, K. & Melkote, S.N. 2006, "Material strengthening mechanisms and their contribution to size effect in micro-cutting", *Journal of manufacturing science and engineering*, vol. 128, no. 3, pp. 730-738.
- Lucca, D., Rhorer, R. & Komanduri, R. 1991, "Energy dissipation in the ultraprecision machining of copper", *CIRP Annals-Manufacturing Technology*, vol. 40, no. 1, pp. 69-72.
- Lucca, D., Seo, Y. & Komanduri, R. 1993, "Effect of tool edge geometry on energy dissipation in ultraprecision machining", *CIRP Annals-Manufacturing Technology*, vol. 42, no. 1, pp. 83-86.
- Ma, S., Zhang, X. & Qiu, X. 2009, "Comparison study of MPM and SPH in modeling hypervelocity impact problems", *International Journal of Impact Engineering*, vol. 36, no. 2, pp. 272-282.
- Mackerle, J. 2003, "Finite element analysis and simulation of machining: an addendum: A bibliography (1996–2002)", *International Journal of Machine Tools and Manufacture*, vol. 43, no. 1, pp. 103-114.
- Masaki, T., Kawata, K. & Masuzawa, T. 1990, "Micro electro-discharge machining and its applications", *Micro Electro Mechanical Systems, 1990. Proceedings, An Investigation of Micro Structures, Sensors, Actuators, Machines and Robots. IEEE*, , pp. 21-28

- Masuzawa, T. & Tönshoff, H. 1997, "Three-dimensional micromachining by machine tools", *CIRP Annals-Manufacturing Technology*, vol. 46, no. 2, pp. 621-628.
- Masuzawa, T. 2000, "State of the art of micromachining", *CIRP Annals-Manufacturing Technology*, vol. 49, no. 2, pp. 473-488.
- Merchant, M. 1998, "An interpretive look at 20th century research on modeling of machining", *Machining Science and Technology*, vol. 2, no. 2, pp. 157-163.
- Michel, Y., Chevalier, J., Durin, C., Espinosa, C., Malaise, F. & Barrau, J. 2006, "Hypervelocity impacts on thin brittle targets: Experimental data and SPH simulations", *International Journal of Impact Engineering*, vol. 33, no. 1, pp. 441-451.
- Moriwaki, T. 1989, "Machinability of copper in ultra-precision micro diamond cutting", *CIRP Annals-Manufacturing Technology*, vol. 38, no. 1, pp. 115-118.
- Movahhedy, M., Gadala, M. & Altintas, Y. 2000, "Simulation of the orthogonal metal cutting process using an arbitrary Lagrangian–Eulerian finite-element method", *Journal of Materials Processing Technology*, vol. 103, no. 2, pp. 267-275.
- Nakayama, K. & Tamura, K. 1968, "Size effect in metal-cutting force", *Journal of Engineering for Industry*, vol. 90, pp. 119-225.
- Nath, C. & Rahman, M. 2008, "Effect of machining parameters in ultrasonic vibration cutting", *International Journal of Machine Tools and Manufacture*, vol. 48, no. 9, pp. 965-974.
- Nemat-Nasser, S. 1979, "Decomposition of strain measures and their rates in finite deformation elastoplasticity", *International Journal of Solids and Structures*, vol. 15, no. 2, pp. 155-166.
- Ng, E., El-Wardany, T.I., Dumitrescu, M. & Elbestawi, M.A. 2002, "3D finite element analysis for the high speed machining of hardened steel", ASME, .
- Okazaki, Y., Mishima, N. & Ashida, K. 2004, "Microfactory: Concept, history, and developments", *Journal of Manufacturing Science and Engineering*, vol. 126, no. 4, pp. 837-844.
- Özel, T. 2006, "The influence of friction models on finite element simulations of machining", *International Journal of Machine Tools and Manufacture*, vol. 46, no. 5, pp. 518-530.
- Patwardhan, P.V. 2003, *Modeling the elastic and plastic response of single crystals and polycrystalline aggregates*, .

- Peirce, D., Asaro, R. & Needleman, A. 1982, "An analysis of nonuniform and localized deformation in ductile single crystals", *Acta metallurgica*, vol. 30, no. 6, pp. 1087-1119.
- Pollock, T.M. & Tin, S. 2006, "Nickel-based superalloys for advanced turbine engines: chemistry, microstructure and properties", *Journal of Propulsion and Power*, vol. 22, no. 2, pp. 361-374.
- Ramalingam, S. & Hazra, J. 1973, "Dynamic Shear Stress—Analysis of Single Crystal Machining Studies", *Journal of Engineering for Industry*, vol. 95, pp. 939.
- Reed-Hill, R.E. & Abbaschian, R. 1964, *Physical metallurgy principles*, Van Nostrand Princeton.
- Riaz M. 2012, *Hot Ultrasonically Assisted Turning of Ti-15V3Al3Cr3Sn: Experimental and Numerical Analysis*, PhD thesis.
- Roters, F., Eisenlohr, P., Hantcherli, L., Tjahjanto, D., Bieler, T. & Raabe, D. 2010, "Overview of constitutive laws, kinematics, homogenization and multiscale methods in crystal plasticity finite-element modeling: Theory, experiments, applications", *Acta Materialia*, vol. 58, no. 4, pp. 1152-1211.
- Sato, M., Kato, Y., Aoki, S. & Ikoma, A. 1983, "Effects of Crystal Orientation on the Cutting Mechanism of the Aluminum Single Crystal: 2nd Report: On the (111) plane and the (112) end Cutting", *Bulletin of JSME*, vol. 26, no. 215, pp. 890-896.
- Sato, M., Kato, Y. & Tsutiya, K. 1979, "Effects of crystal orientation on the flow mechanism in cutting aluminum single crystal", *Transaction of Japan Institute of Metals*, vol. 20, no. 8.
- S, M., Yamazaki, T., Shimizu, Y. & Takabayashi, T. 1991, "A study on the microcutting of aluminum single crystals", *JSME international journal.Ser.3, Vibration, control engineering, engineering for industry*, vol. 34, no. 4, pp. 540-545.
- Sauer, M. 2000, *Adaptive Kopplung des Netzf freien SPH-Verfahrens mit Finiten Elementen zur Berechnung von Impaktvorgaengen (Adaptive Coupling of the Mesh-Free SPH-Method with Finite Elements for the Calculation of Impact Events)*, .
- Shamoto, E. & Moriwaki, T. 1999, "Ultrprecision diamond cutting of hardened steel by applying elliptical vibration cutting", *CIRP Annals-Manufacturing Technology*, vol. 48, no. 1, pp. 441-444.
- Shaw, M. 1995, "Precision Finishing*", *CIRP Annals-Manufacturing Technology*, vol. 44, no. 1, pp. 343-348.

- Shengfang, Z., Na, Z., Zhihua, S. & Xiaoli, J. 2010, "Study on turning simulation technology Based on parametric feature modeling", *Mechanic Automation and Control Engineering (MACE), 2010 International Conference on IEEE*, , pp. 49.
- Shenoy, V., Miller, R., Tadmor, E., Rodney, D., Phillips, R. & Ortiz, M. 1999, "An adaptive finite element approach to atomic-scale mechanics—the quasicontinuum method", *Journal of the Mechanics and Physics of Solids*, vol. 47, no. 3, pp. 611-642.
- Shet, C. & Deng, X. 2000, "Finite element analysis of the orthogonal metal cutting process", *Journal of Materials Processing Technology*, vol. 105, no. 1, pp. 95-109.
- Shih, A.J. 1995, "Finite element analysis of the rake angle effects in orthogonal metal cutting", *International Journal of Mechanical Sciences*, vol. 38, no. 1, pp. 1-17.
- Shimada, S. & Ikawa, N. 1992, "Molecular dynamics analysis as compared with experimental results of micromachining", *CIRP Annals-Manufacturing Technology*, vol. 41, no. 1, pp. 117-120.
- Simulia, D. 2011, "ABAQUS 6.11 Analysis User's Manual", *Abaqus 6.11 Documentation*, pp. 22-32.
- Singh, R. & Khamba, J. 2006, "Ultrasonic machining of titanium and its alloys: a review", *Journal of Materials Processing Technology*, vol. 173, no. 2, pp. 125-135.
- Sun, J., Lee, K. & Lee, H. 2000, "Comparison of implicit and explicit finite element methods for dynamic problems", *Journal of Materials Processing Technology*, vol. 105, no. 1, pp. 110-118.
- Tanaka, M. 2001, "Development of desktop machining microfactory", *Riken Review*, , no. 34.
- Taylor, G.I. 1938, "Analysis of plastic strain in a cubic crystal", *Stephen Timoshenko 60th Anniversary Volume*, pp. 218-224.
- Taylor, G.I. 1934, "The mechanism of plastic deformation of crystals. Part I. Theoretical", *Proceedings of the Royal Society of London. Series A, Containing Papers of a Mathematical and Physical Character*, vol. 145, no. 855, pp. 362-387.
- Thoe, T., Aspinwall, D. & Wise, M. 1998, "Review on ultrasonic machining", *International Journal of Machine Tools and Manufacture*, vol. 38, no. 4, pp. 239-255.

- To, S., Lee, W. & Chan, C. 1997, "Ultraprecision diamond turning of aluminium single crystals", *Journal of Materials Processing Technology*, vol. 63, no. 1, pp. 157-162.
- Trent, E.M. & Wright, P.K. 2000, *Metal cutting*, Butterworth-Heinemann.
- Ueda, K., Iwata, K. & Nakayama, K. 1980, "Chip formation mechanism in single crystal cutting of β -brass", *CIRP Annals-Manufacturing Technology*, vol. 29, no. 1, pp. 41-46.
- Von Turkovich, B. & Black, J.T. 1970, "Micro-machining of copper and aluminum crystals", *Journal of Engineering for Industry*, vol. 92, pp. 130-145.
- Wang, Y., Raabe, D., Klüber, C. & Roters, F. 2004, "Orientation dependence of nanoindentation pile-up patterns and of nanoindentation microtextures in copper single crystals", *Acta materialia*, vol. 52, no. 8, pp. 2229-2238.
- Wenda, A., Beck, M., Huntrup, V., Meisel, M., Rothenburg, M., Rubenach, O., Schmutz, J., Schwietering, C. & Gabler, J. 1999, "möglichkeiten und grenzen der mikrozerspanung", *F & M.Feinwerktechnik, Mikrotechnik, Messtechnik*, vol. 107, no. 11, pp. 64-67.
- Weng, G. 1979, "Kinematic hardening rule in single crystals", *International Journal of Solids and Structures*, vol. 15, no. 11, pp. 861-870.
- Weule, H., Huntrup, V. & Tritschler, H. 2001, "Micro-cutting of steel to meet new requirements in miniaturization", *CIRP Annals-Manufacturing Technology*, vol. 50, no. 1, pp. 61-64.
- William, F.S. & Javad, H. 2004, "Foundations of materials science and Engineering", .
- Williams, J. & Gane, N. 1977, "Some observations on the flow stress of metals during metal cutting", *Wear*, vol. 42, no. 2, pp. 341-353.
- Williams, J. & Horne, J. 1982, "Crystallographic effects in metal cutting", *Journal of Materials Science*, vol. 17, no. 9, pp. 2618-2624.
- Wu, J. & Liu, Z. 2010, "Modeling of flow stress in orthogonal micro-cutting process based on strain gradient plasticity theory", *The International Journal of Advanced Manufacturing Technology*, vol. 46, no. 1-4, pp. 143-149.
- Wu, T., Bassani, J.L. & Laird, C. 1991, "Latent hardening in single crystals I. Theory and experiments", *Proceedings of the Royal Society of London.Series A: Mathematical and Physical Sciences*, vol. 435, no. 1893, pp. 1-19.

- Yang, W. & Tarng, Y. 1998, "Design optimization of cutting parameters for turning operations based on the Taguchi method", *Journal of Materials Processing Technology*, vol. 84, no. 1, pp. 122-129.
- Yuan, Z., Lee, W., Yao, Y. & Zhou, M. 1994, "Effect of crystallographic orientation on cutting forces and surface quality in diamond cutting of single crystal", *CIRP Annals-Manufacturing Technology*, vol. 43, no. 1, pp. 39-42.
- Yuan, Z., Zhou, M. & Dong, S. 1996, "Effect of diamond tool sharpness on minimum cutting thickness and cutting surface integrity in ultraprecision machining", *Journal of Materials Processing Technology*, vol. 62, no. 4, pp. 327-330.
- Zhang, Z., Qiang, H. & Gao, W. 2011, "Coupling of smoothed particle hydrodynamics and finite element method for impact dynamics simulation", *Engineering Structures*, vol. 33, no. 1, pp. 255-264.
- Zhou, M. & Ngoi, B. 2001, "Effect of tool and workpiece anisotropy on microcutting processes", *Proceedings of the Institution of Mechanical Engineers, Part B: Journal of Engineering Manufacture*, vol. 215, no. 1, pp. 13-19.
- Zienkiewicz, O.C. & Taylor, R.L. 1977, *The finite element method*, McGraw-hill London.
- Ziman, J.M. 1972, *Principles of the Theory of Solids*, Cambridge University Press.